Experimental and Numerical Optimisation of a SESAM Mode-locked Holmium Fibre Laser

Alexandros Kolovinos

Thesis submitted for the degree of

Master of Philosophy

in

Physics

at the University of Adelaide

Faculty of Sciences, School of Physical Sciences

December 2022

THE UNIVERSITY of ADELAIDE

Contents

List of Figures

List of Tables

Abstract

The infrared region of the electromagnetic spectrum is an attractive prospect for a variety of pulsed laser applications, including biomedical surgery and imaging, defence, metrology and attosecond science, environmental detection, and range-finding. The aim of this research is to develop a robust, stable, benchtop fibre-based laser source in the mid-infrared region of the spectrum, capable of producing picosecond to femtosecond pulses. This thesis utilises a semiconductor-based absorber to create pulses in concert with various linear and nonlinear optical effects in fibre.

To best optimise the laser source, a multi-step approach utilising both numerical MATLAB modelling in concert with experimental techniques. Firstly, over a half-dozen cavity designs were simulated, assembled, and tested, with each utilising alternate combinations and ordering of various fibre laser components to achieve optimal pulse-to-pulse stability, time duration and spectral quality.

From these experimental results, the most optimal design was chosen and was fully characterised, in addition to a single pass pumped holmium fibre amplifier. This laser produced 2.92 ps pulses at a 20 MHz repetition rate, with a central wavelength of 2029.1 nm and a 3 dB bandwidth of 4 nm at an average power of 20.3 mW.

Lastly, pulse dispersion was optimised using a length of dispersion compensating fibre (DCF). An estimate for the required dispersion compensation was calculated, numerically simulated, and then experimentally implemented via fusion splicing 13 m of DCF and cutting back in 1 m increments, characterising the laser at each length. This process was repeated using 20 cm increments. The optimal length for pulse duration was found to be 7.2 m, where the laser produced 494 fs pulses, and minimised pulse-to-pulse instability indicated by the radio frequency spectrum.

Signed Statement

I certify that this work contains no material which has been accepted for the award of any other degree or diploma in my name, in any university or other tertiary institution and, to the best of my knowledge and belief, contains no material previously published or written by another person, except where due reference has been made in the text.

In addition, I certify that no part of this work will, in the future, be used in a submission in my name, for any other degree or diploma in any university or other tertiary institution without the prior approval of the University of Adelaide and where applicable, any partner institution responsible for the joint award of this degree.

I give permission for the digital version of my thesis to be made available on the web, via the University's digital research repository, the Library Search and also through web search engines, unless permission has been granted by the University to restrict access for a period of time.

I acknowledge the support I have received for my research through the provision of an Australian Government Research Training Program Scholarship.

Signed: **Date:** 01/12/22

Acknowledgements

Firstly, I would like to acknowledge the external support from Defence Science and Technology Group (DSTG), Edinburgh, for their support in material and equipment crucial to undertake the research within this thesis.

Furthermore, I'd like to thank my DSTG co-supervisors Keiron Boyd and Miftar Ganija, whom without their training and support, this project would've been impossible. Likewise, I am grateful for the wealth of opportunities they provided to further my knowledge in both technical and practical respects during my candidature, both in relation to the project and my career in research going forward.

I would also like to thank my principal supervisor, Peter Veitch, for his insightful critique and feedback for both the written content for the thesis, but also bettering its overall structure and flow, in addition to support provided with regards to candidature management and the associated paperwork.

I also give thanks to David McAfee for his support in both inducting me into the lab and teaching me the various characterisation methods crucial to this thesis, but also for providing additional feedback for my work and the various illuminating discussions over concepts in nonlinear laser physics.

I'd also like to acknowledge my student colleagues currently undertaking their M.Phil projects, Henry, Andrew and Jonte for providing a much needed helping hand with regard to setting up the new lab and research centre and for sharing all the excitement that came with it.

Last, but not least, I give my endless thanks to my ever-patient, loving and supportive family and friends, who gave me the emotional and financial support to see me through this entire journey.

Dedication

I dedicate this thesis to my loving family: my parents Millie and George, and my sister Maggie. There are no words to describe how much you all mean to me, and without your love and support none of this would’ve ever been possible.

Chapter 1: Introduction

1.1 Introduction

Mode-locking is a technique to produce ultrashort pulses from a laser, of order picoseconds (10^{-12} s) to femtoseconds (10^{-15} s) long. This is based on producing a fixed phase relation between adjacent longitudinal modes in a laser cavity [1]. The superposition of these phase-locked modes produces an ultrashort pulse [2].

Mode-locking broadly falls under two categories: active and passive [3]. Active methods employ an optoelectronic device synchronised to the laser cavity round-trip time to modulate intracavity energy or phase and force the axial modes to beat with fixed phase, the necessary condition for mode-locking [4]. While intracavity dynamics are electronically controllable via the active mode-locker, the effectiveness of the modulator drops sharply as the pulse duration decreases [3]. Passive mode-lockers use a variety of nonlinear phenomena that mode-lock the laser and produce ultrashort pulses [1, 5].

There are a broad range of applications of ultrashort pulses, as will be reviewed below. In particular, mode-locked lasers with wavelengths in the 2-5 μm band are highly desirable for medical imaging, surgery, materials processing, spectroscopy, ultrafast chemistry, remote sensing, defence and research [6-8]. Although alternative definitions of this terminology exist in other fields (e.g. astronomy), the 2-5 μm band is defined as the mid-infrared (MIR) for the purposes of this thesis. Additionally, development and application of reliable, stable mode-locked laser seed sources is of great importance for use in laser amplifier stages. With an appropriate seed source, such amplifiers can be used in extreme field, high intensity applications such as higher-harmonic generation and soft X-ray generation [9].

Hence, this thesis seeks to investigate, design and construct an ultrashort MIR laser source appropriate for the applications outlined in the following section.

1.1.1 Biomedical Applications

The biomedical applications of ultrashort shortwave and mid infrared radiation is many-fold; of minimising heat dissipation and burning of patient tissue via faster-than-diffusion pulses, and the strong absorption bands of both water and bone near 2 μm [10-15].

Pulsed 2 μm sources, chiefly Ho-doped sources, have been the workhorse lasers for kidney stone ablation and the wider field of medicine for well over 20 years, but further development toward these sources is required [16, 17].

Ultrashort sources at 2 μm are also noted for their significantly reduced carbonisation (damage) of surrounding tissues for laser surgery [13, 18, 19]. For example, Fried & Murray (2005) and Fried (2005) demonstrated a 2 μm pulsed source for ablation and incision of prostate, bladder, and ureter tissue, but with a large thermal damage region down to ~ 500 μm, citing the need for shorter pulse durations at 2 μm to further shrink the damage region [20, 21].

Despite the increased absorption in tissue at 2 μm, Bouma et. al. (1998) found that imaging at this wavelength is desirable due to reduced scatter (prevalent at short wavelengths) [22, 23]. Furthermore, the high efficiency of multiphoton absorption given by ultrashort pulses has been utilised to successfully perform multiphoton microscopy of neural tissues of mice and rats in the SWIR [24-26].

1.1.2 Frequency Combs and Metrology in the IR

The output of a mode-locked laser consists of many discrete and evenly spaced peaks in the spectral domain, forming a regular comb of frequencies [27]. Frequency combs can then be used target specific resonances for atomic clocks, or measure fundamental constants [28, 29]. Broadband spectral features, fundamentally inherent to ultrashort pulsed lasers, also reduce granular interference artefacts in imaging applications [30].

The advantage of an ultrafast frequency comb source in the SWIR-MIR, is the presence of a multitude of vibronic molecular resonances around and beyond 2 μm, known as the ‘molecular fingerprint region’ [31, 32]. To fully understand the structure of molecules with such resonances, precise, accurate and reliable frequency references (i.e. combs) must be available at those wavelengths; hence the attractiveness of mid-infrared combs in particular [17, 31].

1.1.3 IR Supercontinuum Generation and Spectroscopy

Supercontinuum generation (SCG) is the process of ultrashort pulse spectral broadening in a nonlinear medium, spanning several octaves by simultaneously driving several nonlinear effects in the material host [33-36]. These nonlinear processes are easily accessed by the high peak powers of ultrashort pulses, with the SCG Q parameter characterising the breadth of the generated spectrum in Equation 1.1.1 [33]:

$$Q = \frac{n_2 E^2 z}{c\tau} \qquad (1.1.1)$$

where E is the driving laser amplitude, n_2 is the nonlinear index, z is the interaction length and τ is the pulse duration. Thus, pulse durations on the order of picoseconds or less are best suited for SCG [33].

Pushing the envelope of SCG out toward the edge of the MIR at 5 μm is another key application of SWIR mode-locked lasers [12, 17]. Recently, Grassani et. al. (2019) and Scurria et. al. (2020) demonstrated supercontinua out to 3.5 and 4.7 μm respectively, both groups utilising thulium-based laser sources near 2 μm [37, 38].

Broadband 2 μm sources have been noted extensively throughout the literature as suitable for spectroscopy of compounds such as H_2O, CO_2, N_2O, NH_3, CH_4, HF and HCN, in both experimental and theoretical studies [12, 39-42].

For instance, Thorpe et. al. (2007) utilised a NIR (1.5 μm) erbium-doped mode-locked fibre laser for ringdown spectroscopy to access overtone absorption lines of CO2, C2H2 and NH3. Their success hinged on a reliable broadband (i.e. mode-locked) laser source to access the relevant wavelengths [41]. Similarly, Kadwani et. al. (2011) used Tm-Ho codoped and Tm doped fibre lasers to probe the atmosphere for CO_2, owing to the absorption bands near 2-2.2 μm [42].

1.1.4 Materials Processing

Laser machining using controllable, short pulse durations is highly desirable for micro-scale cutting and is well established in the literature [43-48].

Singh & Samuel (2016) describe the major advantage of ultrashort pico and femtosecond sources over nanosecond pulsed sources for laser machining. Ultrashort pulses are shorter than the relaxation time of electrons in a material lattice thus resulting in minimal interaction

and diffusion of heat [49]. Nanosecond lasers are hindered by melting and heat damage due to exceeding this relaxation time, in addition to photoacoustic shocks causing material to fracture [43, 49-51].

MIR ultrafast lasers are particularly attractive for micromachining applications in industry for targeting materials that absorb in the MIR. For example, Mielke et. al. (2010) used an automated erbium fibre mode-locked source to ablate Nitinol (for medical stents) and polytetrafluoro-ethylene (Teflon) [52]. Plastics and glasses also possess high absorption bands in the SWIR and MIR, making these lasers ideal for machining [53]. This was further demonstrated by Voisiat et. al. (2015) and Mingareev et. al. (2012), who utilised pulsed 2 μm lasers to weld various polymers together with improved tensile strengths [54, 55].

One should note that ultrashort pulses often generate plasma due to their high peak powers and can impede drilling speed. Thus, there exists a trade-off between drilling rate and cut quality [56].

1.1.5 IR Pumps for Nonlinear Processes

Development of SWIR lasers with high peak powers (i.e. mode-locked lasers) is key to pushing wavelengths for nonlinear frequency generation further into the MIR [12, 17, 37].

SWIR-MIR laser sources are ideal for pumping nonlinear conversion for infrared wavelength conversion in $ZnGeP_2$ due to the low absorption at wavelengths beyond 2 μm [17, 57]. Gebhardt et. al. (2014) utilised a 2 μm Q-switched Tm system to produce high energy pulses out to 4 μm, owing to the reduced absorption at 2 μm in $ZnGeP_2$ [58]. However, an ultrashort MIR source would afford much higher peak powers due to the decrease in pulse duration.

1.1.6 LIDAR and Atmospheric Detection

Light detection and ranging (LIDAR) is well established technique, using backscattered signal from an illuminated target to measure ranges and velocities [59-62]. The use of 2 μm pulsed LIDAR wind-monitoring systems has existed even commercially since the 2000s [63].

LIDAR and other range-finding applications benefit greatly from the low-loss atmospheric transmission window at 2 – 2.5 μm [64] and pulsed 2 μm systems have been investigated thoroughly throughout the literature [65-68]. Furthermore, monitoring of atmospheric gasses

in the MIR region from 2 – 20 μm is highly desirable due to the existence of many such vibrational resonances of tropospheric pollutants N_2O, CO_2 and H_2O [17]. This requires reliable, broadband (mode-locked) and spectrally pure sources to be developed in the MIR region [67].

1.1.7 IR Seed Sources and Amplification

Lasers at 2 μm also benefit greatly in terms of power scaling versus typical NIR 1-1.5 μm lasers (Yb^{3+} and Er^{3+}) due to multiple effects making them superior for multistage seed-amplifier systems [69]. Firstly, assuming a weakly guiding optical fibre, the mode area grows with λ^2 [69]. This causes the intensity within the waveguide to decrease as the cross-sectional area the light is distributed across increases, causing a reduction in the intensity-squared dependence of various parasitic/scattering nonlinear scattering (Brillouin, Raman, Stokes generated via Raman scattered components) [70]. In turn this increases the damage threshold for the fibre, a major limiting factor for high power fibre lasers.

1.1.8 High Harmonic Generation as a Soft X-ray Source

High harmonic generation (HHG) is a nonlinear process that can generate integer multiples of a driving laser frequency in gas. Discovered in the late 80's by McPherson et. al. (1987), it can be understood as a semiclassical three-step model considering electrons bound to atoms in a gas [71-73]. An electron is liberated by an external strong field (i.e. laser pulse) as the driving laser field distorts the Coulomb barrier and the electron tunnels out. The laser field then coherently drives the free electron until it recombines, releasing the excess kinetic energy as a harmonic of the driving field [72, 74]. Alternatively, instead of the described tunnelling mechanism, atoms may be ionised via a process known as above threshold ionisation (ATI), whereby the bound electron undergoes multiphoton absorption of the pump beam and becomes unbound [75].

The highest energy photon produced by the coherent process depends on the highest feasible ponderomotive energy of the electron [71, 76], given by a semi-classical relation in Equation 1.1.2 below [71, 74, 76]:

$$h\nu_{max} \approx I_p + \frac{3.17}{16\pi^2 c^2}\lambda^2 E^2 \qquad (1.1.2)$$

where I_p is the ionisation potential of the atom, E is the driving laser electric field and λ is the wavelength of the laser light [74].

However, number of HHG photons yielded by this process also drops sharply with increasing wavelength [77]. By considering the semiclassical picture of a continuum electron wavepacket being driven by the external laser field, it is noted that the propagation time of the free electron wavepacket increases with laser driving wavelength, causing a λ^{-3} to λ^{-6} decrease in HHG yield [78]. Other factors contribute to this inefficiency with increasing wavelength, such as increased magnetic drift and the concentration of generated HHG photons about the cutoff harmonic [77].

Furthermore, while HHG has previously been realised using 800 nm laser sources [79-83], this approach has been limited by the low conversion efficiency at this wavelength leading to higher required intensities that cause complete ionisation and thus incoherence of the process [80, 84]. An increase from 1 μm to 2 μm would allow a four-fold decrease in intensities required for the same HHG output, according to Equation 1.1.2. In effect, ultrashort pulsed MIR lasers would pave the way for a HHG-based 'tabletop, coherent version of the Roentgen X-ray tube', critical to medical dosimetry applications [12, 74].

1.1.9 Telecommunication Systems

Infrared pulsed sources are also applicable to free-space communications. In particular, there have been a multitude of studies that confirm low loss propagation of SWIR-MIR signals, owing to the existence of a low-loss atmospheric spectral window around 2.0 – 2.5 μm [12, 53, 64, 85-87].

Li et. al. (2013) developed a thulium-doped fibre amplifier system citing the advantage of a Tm fibre-based system providing the largest gain bandwidth of any rare-Earth doped fibre [88]. Such a system can amplify lasers in the range of 1.8-2.1 μm to allow high bit rate, low noise fibre communications over a larger bandwidth than standard telecom wavelengths. Furthermore, Sorokina et. al. (2014) demonstrated that 2-2.5 μm light outperforms both the 1-1.5 μm, 4 and 10 μm atmospheric windows for free-space communication [8].

1.1.10 IR Pump-probe for Ultrafast Chemistry

As early as 1975, Alfano & Shapiro (1975) realised the importance of ultrafast lasers in studying short lived states in biophysics, plasma, and condensed states, stating that "…the utilisation of the mode-locked laser that emits light pulses of picosecond (10^{-12} sec) duration is the key to the study of rapid processes." [89].

Ultrafast chemical processes occur over distances of tenths of a nanometre or less, necessitating time resolutions on the order of femtoseconds, hence the need for ultrafast laser sources of appropriate wavelength to investigate these phenomena [90]. Typically, this is achieved using femtosecond pulses in a pump-probe experiment, whereby a chemical sample is excited by a pump pulse and the evolution of the sample measured via a delayed probe pulse [91, 92].

The advantage of a SWIR-MIR source near 2 μm is to specifically analyse attosecond dynamics of particles and molecules in the molecular fingerprint region. As noted above, this includes important atmospheric molecules and greenhouse gasses such as carbon dioxide (CO_2), water vapour (H_2O) and nitrous oxide (N_2O) [93, 94].

1.2 Mode-locking with Saturable Absorbers

1.2.1 Saturable Absorbers

Passive mode-locking uses an element or material that favours mode-locking, such as a saturable absorber (SA), which preferentially pass high intensity, pulse-like phenomena and absorb low intensity, continuous wave noise [95, 96]. Passive methods often produce mode-locked pulses on scales of femtoseconds to picoseconds [97].

SAs are typically implemented in a semiconductor device, known as a **se**miconductor **s**aturable **a**bsorber **m**irror (SESAM), pioneered by Keller et. al. (1996) [98]. This specialised optic incorporates a semiconductor SA grown on top of a dielectric reflector to create a saturable reflectivity [99]. SESAMs are often employed both due to their high degree of engineerability during epitaxial growth and their reliability and stability for mode-locking [100]. Note that the concept for an analogous device, the saturable Bragg reflector (SBR) was also developed independently by Tsuda et. al. (1995) [101].

Techniques also may be employed to mimic the behaviour of a material with saturable absorption by exploiting nonlinear optical effects in the cavity, known as artificial saturable absorption [96]. Common examples of such techniques include nonlinear polarisation rotation (NLPR) and Kerr-lens mode-locking (KLM), which are discussed further in Section 2.3.

For a given laser, saturable absorbers may serve either as the only mode-locking device or run in tandem with another mode-locking element or as a self-starting device to enable soliton-based mode-locking [102-155]. Examples from the literature are summarised in Tables 1.2.1 and 1.2.2, with further examples in Appendices A and B.

Tables 1.2.1 and 1.2.2, and the following discussion, provide contrast between the experimental work undertaken in this thesis against the variety of methods used in the literature to mode-lock similar MIR ultrashort pulsed laser systems, in addition to the relative benefits and downsides with each respective method.

1.2.2 SESAM-only Mode-locking

SESAMs are a common choice for mode-locking lasers at a variety of wavelengths, from the shortwave visible to the mid infrared [106, 119, 120, 126, 156]. A SESAM may be used as

the primary mode-locking element as described above, with the possibility of multiple SESAMs or absorbers to provide additional pulse shaping at the cost of additional loss [108].

1.2.3 SESAM-assisted Mode-locking

Methods such as KLM or NLPR alone may sometimes require mechanical perturbation to initiate mode-locking or are unstable and sensitive to environmental disturbances [102, 157]. Thus, a SA or SESAM may be used to assist in self-starting the mode-locking process without mechanical perturbation [102].

SESAMs may also act as a self-starting mode-locker to enable soliton mode-locking [98]. A soliton is a self-stabilising, ultrashort pulse formed from the balance of nonlinear and dispersive effects in an optical medium and is a solution to the nonlinear propagation for pulses [158]. In this case, SESAMs are often used as a self-starting mechanism and as a stabiliser, providing preferential attenuation to any competing CW noise components that may propagate in the cavity, which will be explored further in Sections 2.4 and 2.5.

1.2.4 Free-space SESAM Mode-locking

Recent and contemporary papers have reported successful SESAM mode locking across a range of wavelengths in free-space cavities, from the visible to the mid-infrared [102, 156]. Implementation of absorbers, such as SESAMs, in free space simply involves one of three configurations:

- SESAM replaces a cavity end-mirror providing saturable absorption once per round trip. This provides less SESAM saturation at the cost of less pulse shaping.
- SESAM replaces a cavity mirror whereby the beam undergoes a double pass per round trip. This provides more pulse shaping at the risk of too much SESAM saturation.
- A transmissible absorber is placed in the cavity as a double-pass element.

A summary of five SESAM free-space mode-locked sources in the literature is provided in Table 1.2.1.

Primary author	Mode-locker	Active dopant	Centre wavelength λ_0 [nm]	Pulse duration $\Delta\tau$ [ps]	Pulse energy [nJ]	Avg. power [W]	Peak power [kW]	Rep. rate [MHz]
Hou et. al. (2013) [108]	Double SESAMs	Nd	1064.5	9.97	23.46	2.98	2.21	127
Wang et. al. (2021) [104]	SESAM and SESAM-Soliton	Tm-Ho	2033	0.046	1.55	0.121	31.68	78
Zeng et. al. (2021) [117]	SESAM – KLM - Soliton	Yb	1054	0.094	17.8	1.05	177.86	59
Saraceno et. al. (2012) [105]	SESAM-soliton	Yb	1040	0.096	65.81	5.1	685.48	77.5
Bu et. al. (2017) [106]	SESAM and SESAM-Soliton	Cr	2415	2.08	2.71	0.342	1.30	126.4

Table 1.2.1: Summary of free-space SESAM mode-locked cavities from the literature.

Recently, Wang et. al. (2021) utilised a Tm-Ho:CALGLO gain medium pumped by a KLM-based Ti:Saph laser, with a SESAM performing the passive mode-locking, achieving nJ pulse energies and sub-50-fs pulse durations at 2 μm [104]. Pulse width and mode-locking was maintained using several pairs of dispersive optics, allowing both SESAM mode-locked double-pulsed operation as well as a low repetition rate soliton-based operating regime. A similar cavity architecture was demonstrated by Zeng et. al. (2021), but at 1 μm, also achieving sub-50-fs pulses in the shortwave IR [117]. Interestingly, the Yb:SALLO crystal used provided additional nonlinearity, allowing the Kerr effect to further shape pulses in the gain.

Bu et. al. (2017) used a Cr:ZnSe gain medium to achieve lasing at 2420 nm, utilising a Tm fibre laser at 1908 nm as the pump [106]. The passive mode-locking was provided by a non-commercial SESAM to achieve a low nonlinear absorption to minimise loss. Soliton mode-locking could be achieved via a sapphire plate inserted in the cavity to provide the necessary dispersion balance, resulting in 400 fs soliton pulses.

Hou et. al. (2014) utilised two SESAMs to produce mode-locked 9.97 ps pulses at 1 μm [108]. Operating with a single SESAM yielded pulses of 10.4 ps, indicating that additional SESAMs provide additional pulse shaping. This is, however, at the cost of additional loss from multiple SESAMs, leading to Q-switching instabilities (discussed further in Chapter 3).

Lastly, Saraceno et. al. (2012) utilised a compact, multi-pass configuration with a thin disk of Yb:$LuScO_3$ as the gain medium and a custom designed SESAM as the passive mode-locker [105]. Gires-Turnois-Interferometer mirrors were used to provide dispersion compensation to achieve SESAM-soliton mode-locking

Additional examples of solid-state, free-space SESAM mode-locked systems in the IR are available in Appendix A.

1.2.5 Fibre SESAM Mode-locking

Fully fiberized designs are an interesting prospect due to the small mode within the fibre and long propagation distances (tens of metres to kilometres) allowing ready access to nonlinearity-based absorbers such as NLPR.

These fibre cavities may also incorporate short segments of free space propagation. This is commonly used to incorporate the SESAM as a free-space external element to the cavity along with optics to adjust the incident pulse fluence [147, 148, 150, 154]. Alternatively, a free-space segment may be used for diffraction-based spectral filtering [159].

As for the free-space counterparts, fibre-based lasers may be mode-locked via installation of a SESAM within the cavity. This is often accomplished by:

- Replacing a fibre (loop) mirror with a SESAM (for a linear fibre cavity).
- Using a circulator with a SESAM at the back reflection port (for a ring cavity).
- Utilising a non-reflective saturable absorber that is built into the fibre or mounted between two fibre physical contacts.

Table 1.2.2 summarises some examples of fibre SA mode-locked lasers from the literature.

Primary author	Mode-locker	Active dopant	Centre wavelength λ_0 [nm]	Pulse duration $\Delta\tau$ [ps]	Pulse energy [nJ]	Avg. power [W]	Peak power [kW]	Rep. rate [MHz]
Huang et. al. (2019) [143]	SESAM	Tm	1940	3.93	38.84	0.672	9.88	17.3
Hinkelmann et. al. (2017) [134]	SESAM-soliton	Ho	2052	1.2	0.18	0.005	0.14	27.3
Stoliarov et. al. (2020) [140]	SESAM-soliton	Er	1553	10.4	10 pJ	0.0003	0.0009	1060.9
Afifi et. al. (2016) [148]	SESAM-NLPR	Er	1560	0.206	0.89	0.07	4.04	79
Li et. al. (2015) [153]	SESAM-NLPR	Yb	1030	0.96	37.63	3.15	36.83	83.7

Table 1.2.2: Summary of fibre SESAM mode-locked cavities from the literature.

Hinkelmann et. al. (2017) and Huang et. al. (2019) fiberised 2 μm mode-locked sources, utilising holmium and thulium gain media respectively [134, 143]. Hinkelmann et. al. (2017) utilised a SESAM-soliton operating regime to achieve ultra-stable but low energy soliton pulses, which were then amplified using a Tm-Ho single-pass amplifier stage giving 0.18 nJ pulses with 1.2 ps duration. Huang et. al. (2019) note that pulse energies are fundamentally limited for stable soliton-SESAM based systems and elected to use a purely SESAM mode-locked approach with no soliton effects. This yielded much longer, 3.93 ps pulses but with almost two-hundred times more energy than comparable systems based on soliton-SESAM mode-locking, e.g., Hinkelmann et. al. (2017).

Stoliarov et. al. (2020) recently used a harmonic mode-locking approach in a linear cavity, whereby high repetition rates are achieved by having multiple pulses circulate intracavity [140]. An erbium gain fibre was used to achieve the 1553 nm output, with the harmonic mode-locking allowing repetition rates up to over 1 GHz, at the expense of only 10 pJ pulse energies. The SESAM was used to self-start mode-locking in conjunction with the soliton formation effects to mode-lock the laser.

Lastly, Li et. al. (2015) and Afifi et. al. (2016) achieved non-soliton-like sub-picosecond pulses using a hybrid NLPR-SESAM mode-locking scheme, with 1030 nm and 1560 nm lasing wavelengths respectively [148, 153].

In both cases, utilisation of a fast artificial SA in addition to the stable pulse-shaping of the SESAM led to sub-picosecond pulse durations. Afifi et. al. (2016) measured the pulse-to-pulse timing noise and found that the addition of a SESAM vs. NLPR alone led to a two to four-fold decrease in timing noise [148]. The origin of timing noise is discussed further in Chapter 3.

There are many other examples of fiberized SESAM-mode-locked shortwave and mid IR fibre sources in the literature, with an extended summary in Table B-1 available in Appendix B.

1.3 Project Objectives

The aim of the project is to comprehensively review and investigate the effects of various cavity parameters for a Ho:doped fibre SESAM mode-locked laser, both experimentally and theoretically, on:

- Pulse train stability
- Pulse duration
- Pulse energy
- Spectral purity

To the best of our knowledge, this is the first time this type of source has been characterised and optimised thoroughly in this fashion. While a multitude of literature is readily available on the topic of sources in the shorter near infrared region of the spectrum, largely around the telecom wavelength (1.55 μm), development of sources in the shortwave infrared and beyond, particularly mode-locked systems, is still lacking. There exists a notable gap in the field for a comprehensive review of pulsed laser characteristics at 2 μm, a region which is highly desirable in both pulse duration and spectrum for the wide variety of applications explored in Section 1.1.

Further discussion regarding both experimental and theoretical approaches to optimisation of pulse train stability is also required. Virtually all the discussed applications require that pulses from the laser oscillator are stable in time, free of severe operational instabilities that may distort the output both temporally and spectrally from pulse-to-pulse. This is of great import to applications such as metrology and use as a seed-source for amplifier stages

While stability plays a central role in the investigations of this project, other parameters must be thoroughly investigated, such as pulse duration. It is readily apparent from the literature reviewed in Sections 1.1 and 1.2 that the instantaneous peak power of a pulse, and thus its duration, is eminently crucial to a variety of applications in micromachining, biomedicine, nonlinear frequency shifting and more.

However, while it has been noted that parameters such as group velocity dispersion and nonlinear parameters, comprehensive optimisation of pulse duration both experimentally and theoretically is rare in the literature, especially in the MIR. Along with stability, this project aims to obtain a theoretically and experimentally explore the phenomena that drive pulse duration.

Where applicable, practical experimental changes such as splice quality, fibre length and mechanical isolation are implemented via experimentation with a Ho:doped fibre SESAM-based mode-locked laser.

To summarise, development of such a source through a thorough optimisation-focussed approach is crucial for realising the applications discussed in Section 1.1. We aim to develop a fully comprehensive investigation of a mode-locked 2 μm source for the first time in the literature, with the end product being a stable, reliable, spectrally pure mode-locked shortwave infrared oscillator built largely from commercially available optical components.

1.4 Thesis Outline

Chapter 1 contained a brief discussion of mode-locked lasers and SESAMs, in addition to an extensive review of mode-locked sources from the near infrared to the mid infrared in the literature, of both free-space and fibre-based configurations. A comprehensive review of the applications of ultrashort lasers and the importance of 2 μm to a variety of these applications followed. This included applications for laser ablation surgery for a variety of human tissues, biomedical imaging, micromachining, higher harmonic soft-X generation, MIR metrology, seed-sources in the MIR and MIR spectroscopy for gas sensing and environmental monitoring.

1.4.1 Chapter 2: Theoretical Background

Chapter 2 contains a broad review of the theory behind concepts regarding the project. This includes dispersion and higher-order dispersion, nonlinearity in optical media, optical devices used by the project, semiconductor saturable absorber mirrors (SESAMs) and other saturable absorbers, mode-locking theory and the generalised nonlinear Schrödinger equation (GNLSE) and lastly on simulation of the GNLSE and various approaches from the literature.

1.4.2 Chapter 3: Laser Characterisation

Chapter 3 discusses the relevant methods of measuring a mode-locked laser's output. Discussion of temporal characterisation focusses on radio frequency (RF) photodetectors and oscilloscopes, autocorrelation and thermal power meters, whereas the relevant spectrally resolved instruments discussed are RF spectrum analysers, optical spectrum analysers and frequency-resolved optical gating. Furthermore, a discussion on mode-locking instabilities due to higher order dispersion and nonlinear effects is provided.

1.4.3 Chapter 4: Experimental and Numerical Results

Chapter 4 will cover the experimental and simulation-based theoretical findings of the project. This includes an investigation of a variety of relevant parameters such as fibre lengths, laser cavity design and more. The merits of each parameter varied and observed

improvements or declines in pulse train stability, duration and mode-locked operation are discussed.

1.4.4 Chapter 5: Conclusion

Chapter 5 concludes the thesis with a review of the chapters contain therein, summarising results and discussing relevant plans for future work and improvements to be made upon the experimental and theoretical investigation that took place in Chapter 4.

Chapter 2: Theoretical Background

2.1 Chapter Layout

This chapter contains a broad review of the theory behind concepts regarding the project:

In Section 2.2, a review of concepts underpinning various fibre optical devices used in the project, alongside a discussion of dispersion in optical fibre.

In Section 2.3, the nonlinear response of materials subject to extreme electromagnetic fields is discussed in the context of ultrashort pulses. Key concepts include self-phase modulation, NLPR and stimulated Raman scattering.

Section 2.4 introduces the theory of mode-locking via the principle of mode superposition, as well as introducing the propagation equation of an optical pulse: the generalised nonlinear Schrödinger equation (GNLSE). Soliton theory is also introduced.

Next, in Section 2.5, the theory of saturable absorbers and SESAMs is explored, alongside the various regimes enabled by these mode-locking devices.

Lastly, Section 2.6 discusses the application of a generalised GNLSE in numerically simulating a mode-locked cavity. A brief, comparative review of the two most common numerical schemes is provided. The model described serves as a basis for informing experimental design and is explored in Chapter 4.

2.2 Dispersion, Optical Fibre and Components

2.2.1 Optical Fibres Overview

An optical fibre is a layered cylindrical construct of several materials, often glasses, with differing refractive indices [1]. In step-index fibres, light propagates within the central-most core with refractive index n_1. The core is surrounded by a cladding layer with a refractive index n_2. In the simple ray model, light is confined via total internal reflection (TIR) within the fibre as n_1, is greater than n_2, thus light launched at an angle larger than the critical angle at the core-cladding interface is totally reflected as show in Figure 2.2.1 below.

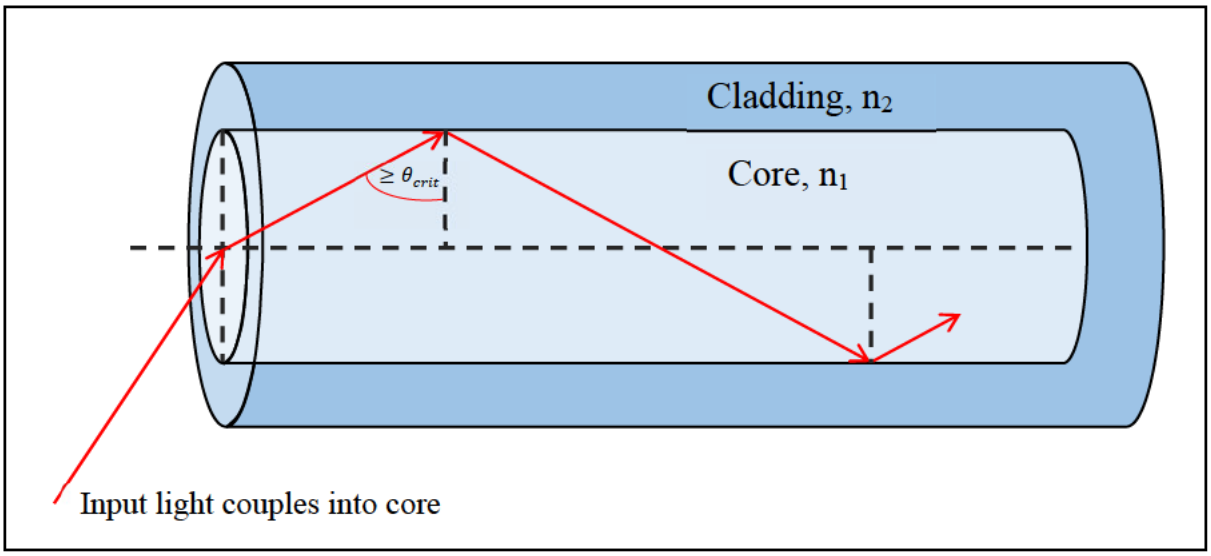

Figure 2.2.1: Cross-section of a typical step-index, singly-clad optical fibre of cladding index n_2 and core index n_1.

These refractive indices may be raised or lowered by introduction of dopants such as germanium (Ge) and boron (B) [2]. Sharp bends in an optical fibre disturbs this TIR condition by decreasing the angle of incidence below the critical angle and can allow light to escape the waveguide through the cladding leading to 'bending' losses [1].

However, it is more accurate to consider the solutions of Maxwell's equations for light within the waveguide instead of the ray picture above. Fibre guided modes are solutions of Maxwell's equations that satisfy the boundary conditions of the cylindrically symmetric waveguide structure [3]. The number of modes that can propagate in a fibre is determined by the normalised frequency; V, given by [1]:

$$V = 2\pi r \frac{NA}{\lambda_0} \quad (2.2.1)$$

where λ_0 is the vacuum wavelength of the propagating radiation, r is the fibre core radius and NA is the numerical aperture, which represents how easily light is coupled into the core given by [1]:

$$NA = \sqrt{n_1^2 - n_2^2} \quad (2.2.2)$$

Single-mode propagation is supported by fibres with a normalised frequency less than $V \approx 2.405$.

A given optical mode has an effective (1/e) mode area, A_{eff}, calculated from the time averaged Poynting vector, S, of the field in the core [4]:

$$A_{eff} = \frac{\left(\iint_{-\infty}^{\infty} S_z dxdy\right)^2}{\iint_{-\infty}^{\infty} S_z^2 dxdy} \quad (2.2.3)$$

where the z direction is aligned with the propagation axis of the waveguide, and the transverse component of the mode is confined to the transverse x-y plane.

It is simpler to characterise the spatial extent of the field within the fibre as the mode-field diameter (MFD). For most practical single-mode fibres, the MFD can be approximated in terms of the normalised frequency V, to within 1% accuracy, using Marcuse's equation, given in Equation 2.2.4 below [5]:

$$M \approx d.\left\{0.65 + \frac{1.619}{V^{\frac{3}{2}}} + \frac{2.879}{V^6}\right\} \quad (2.2.4)$$

where d is the core diameter and M is the MFD of the fibre.

The end-faces of separate fibres can be arc-welded together via a process known as splicing, fusing the cleaved fibres together end-to-end. The net coupling efficiency (η) at the splice-point accounts for various splice losses. This may include MFD mismatch between the fibre ends, or from lateral and angular misalignments during splicing. The coupling efficiency factor due to MFD mismatch between the spliced fibres can be estimated using [5]:

$$\eta_{MFD} = \left(2\frac{M_1 M_2}{M_1^2 + M_2^2}\right)^2 \quad (2.2.5)$$

where $M_{1,2}$ are the MFDs of fibres either side of the splice.

To minimise losses, it is imperative that the MFDs of the fibres, and thus their V numbers, are similar.

Losses due to angular and lateral misalignment of two fibre ends can also be estimated [6,7]. The coupling efficiency due to lateral mismatch in either the x or y directions at a splice joint is given by Equation 2.2.6 [6]:

$$\eta_{lat\ x,y} = \frac{4M_1^2M_2^2}{(M_1^2+M_2^2)^2}\exp\left(-\frac{8\left(\Delta_{x,y}\right)^2}{M_1^2+M_2^2}\right) \qquad (2.2.6)$$

where $\Delta_{x,y}$ is the relative offset between the two fibre ends in either the x or y directions.

For two fibres of MFD, M, the angular mismatch coupling efficiency is given by [5]:

$$\eta_{ang} = \exp\left(-\left(\frac{\pi\Delta_\theta M}{\lambda_0/n_1}\right)^2\right) \qquad (2.2.7)$$

where Δ_θ is the angular separation between the fibre ends.

For this project, those losses were estimated by the commercial FITEL S153 fusion splicer used. This is performed via imaging mutually perpendicular planes to the fibre axis to measure core sizes, lateral and angular mismatch either side of the splice and thus calculate the resultant coupling loss via Equations 2.2.5, 2.2.6 and 2.2.7 above.

2.2.2 Chromatic and Waveguide Dispersion

Chromatic dispersion of light causes different frequencies (ω) to propagate with different phase and group velocities [8, 9]. In fibres, this dispersion primarily arises from the sum of material dispersion and waveguide dispersion [9].

Material dispersion is caused by the interaction of light and electrons in the dielectric material in which the light propagates resulting in a modified, frequency-dependent refractive index [10]. This is characterised by the material dispersion parameter defined by Equation 2.2.8 below [10, 11]:

$$D_m = -\frac{\lambda_0}{c}\frac{d^2n}{d\lambda_0} \qquad (2.2.8)$$

where λ_0 is the central wavelength.

Waveguide dispersion is due to the confinement of the optical modes within the fibre, introducing a frequency-dependent refractive index as the modal area, thus V-number, affects waveguide dispersion [9]. This wavelength-dependent dispersive behaviour is given by [11]:

$$D_w = -\left(\frac{1}{2\pi c}\right) V^2 \frac{d^2\beta}{dV^2} \qquad (2.2.9)$$

This enables the manufacture of dispersion tailored fibre via engineering of the V-number, allowing tailoring of both the magnitude and sign of dispersion [12, 13].

The net (chromatic) dispersion is represented by the propagation constant β, which describes the phase shift per length in the material [9, 14]. Often, an analytical equation for β does not exist, and the parameter is generalised as a series via the Taylor expansion about the central angular frequency of the pulse, ω_0 [9, 14-16]:

$$\beta(\omega) = \beta_0 + (\omega - \omega_0)\beta_1 + \frac{1}{2}(\omega - \omega_0)^2\beta_2 + \frac{1}{6}(\omega - \omega_0)^3\beta_3 + \cdots \qquad (2.2.10)$$

where each term, β_n, is the n^{th} derivative of the dispersion coefficient [12]:

$$\beta_n = \left.\frac{d^n\beta}{d\omega^n}\right|_{\omega=\omega_0}, n \in \mathbb{Z}^+ \qquad (2.2.11)$$

The zeroth order, β_0, produces an arbitrary shift to the absolute phase of the pulse. This is often trivially removed by considering Equation 2.2.10 in the reference frame of the light pulse, as discussed further in Section 2.6.

The first order β_1 term shown is simply the inverse of the group velocity, v_g, and is thus known as the group velocity term:

$$\beta_1 = \frac{1}{v_g} = \frac{1}{c}\left(n + \omega\frac{dn}{d\omega}\right) \qquad (2.2.12)$$

The second order β_2 term quantifies the change in group velocity with angular frequency, as shown in Equation 2.2.13, and is referred to as the group velocity dispersion (GVD). It causes optical pulses to broaden in the time domain.

$$\beta_2 = \frac{1}{c}\left(2\frac{dn}{d\omega} + \omega\frac{d^2n}{d\omega^2}\right) = \frac{d}{d\omega}\left(\frac{1}{v_g}\right) \qquad (2.2.13)$$

It is commonplace to instead express the 2^{nd} order dispersion in terms of the total dispersion parameter D_λ , in units of ps nm^{-1} km^{-1}, [9]:

$$D_\lambda = -\frac{2\pi c}{\lambda^2}\beta_2 \qquad (2.2.1)$$

The third order β_3 term represents third order dispersion (TOD) and produces asymmetrical distortions of the pulse wings. While typically small, TOD dominates in the case of negligible GVD or extremely high intensity, few-optical-cycle pulses (durations ≤ 10 fs).

2.2.3 Anomalous and Normal Dispersion

Waveguide and material dispersion in typical silica glass fibre differ in sign above ~ 1.3 μm [12]. Material dispersion naturally has a zero-crossing point, but waveguide dispersion acts to shift the net chromatic zero-dispersion point as it is the sum of both contributions as shown in Figure 2.2.2 [17]:

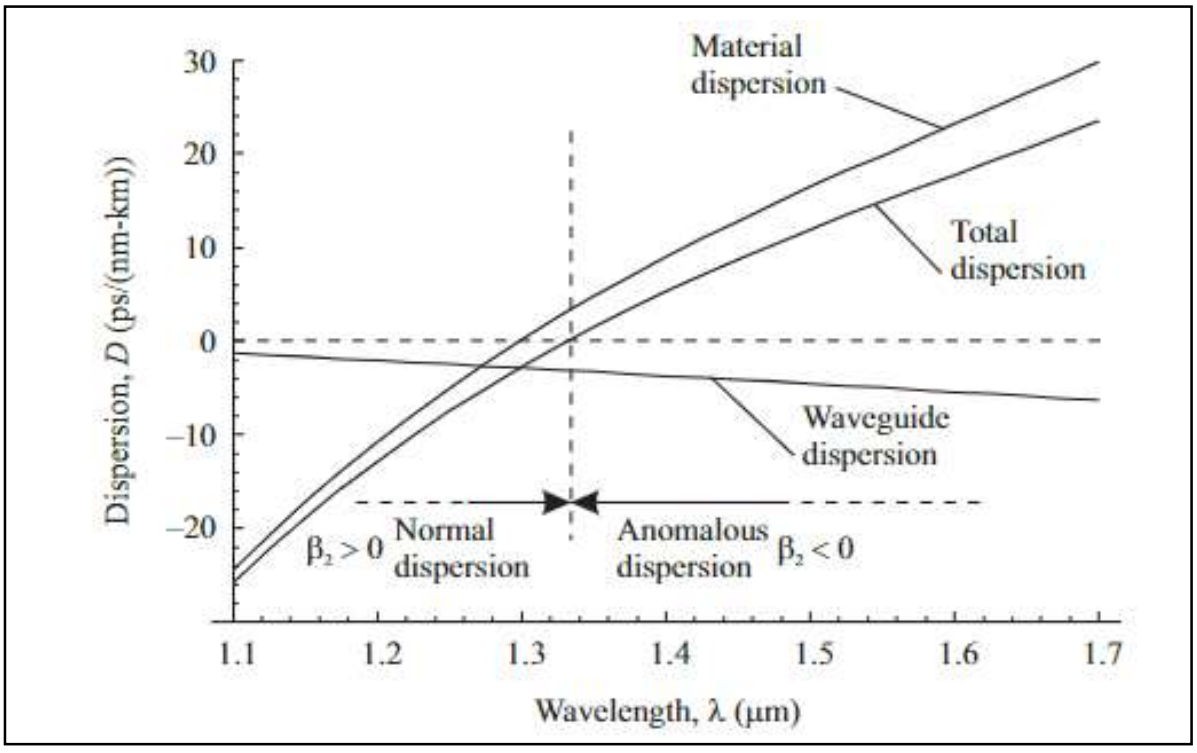

Figure 2.2.2: A plot of material, net (chromatic) and waveguide dispersion versus wavelength.

The region of net positive dispersion β below the zero-dispersion point is known as the normal regime, and the region of net negative dispersion is known as the anomalous regime.

This leads to pulse chirping, defined as the change in instantaneous optical frequency (or wavelength) along a pulse's temporal profile [18].

Long wavelengths travel slower in the anomalous regime, leading to a down-chirp, a decrease in frequency from the leading edge to the trailing edge across a pulse. Conversely, long wavelengths travel faster in the normal regime, causing a pulse to up-chirp, as summarised in Table 2.2.1.

Parameter	**Anomalous Dispersion**	**Normal Dispersion**
β_2	< 0	> 0
D_λ	> 0	< 0
$v_g(\lambda)$	Shorter wavelengths travel *faster*	Shorter wavelengths travel *slower*
Chirp	Down-chirp	Up-chirp

Table 2.2.1: The basic features that define the region of anomalous and normal dispersion.

2.2.4 Dispersion Compensation

Dispersion compensating fibre (DCF) is a specialised fibre that has a tailored dispersion profile to cancel out material or waveguide dispersion.

Waveguide dispersion is also given by [11]:

$$D_{waveguide} = -n_2 \Delta n \frac{V}{c\lambda} \frac{d^2}{dV^2} (\beta V) \qquad (2.2.2)$$

where n_2 is the cladding refractive index, n_1 is the core refractive index and Δn is the refractive index contrast between the core and cladding (Equation 2.2.16):

$$\Delta n = \frac{n_2^2 - n_1^2}{2n_1} \qquad (2.2.3)$$

Thus, by tailoring Δn, the waveguide dispersion of DCF can be engineered to be normal in regions of anomalous material dispersion and vice versa. This allows for net-zero dispersion fibre cavity designs in the near and mid infrared, away from the zero-dispersion point shown in Figure 2.2.2. Dispersion from a length of single mode fibre (SMF) can be offset by the DCFs dispersion parameter [19, 20]:

$$D_{net} = D_{SMF} l_{SMF} + D_{DCF} l_{DCF} \quad (2.2.4)$$

where $D_{\text{SMF, DCF}}$ and $l_{\text{SMF, DCF}}$ are the dispersion parameters and lengths of the SMF and DCF respectively. If the dispersion parameter of a length of SMF is known, it is trivial to approximately balance it against a specifically tailored (positive or negative) DCF dispersion parameter and length to obtain near net zero dispersion via Equation 2.2.4.

In practice, exactly net-zero dispersion is not desirable for several reasons. Firstly, processes such as spontaneous four wave mixing are more readily stimulated when dispersion is close to zero, counteracting stable propagation of ultrashort pulses (see Section 2.6). Intracavity noise may seed four-wave mixing that interferes with the coherent nonlinear processes of the laser pulse interacting with the material, leading to pulse breakup [14, 21, 22].

As early as 1990, Desaix et. al. (1990) noted that operation too close to the (second order) zero-dispersion point may lead to dynamics where third order dispersion leads to pulse splitting, also citing cite that additional stability is afforded by operating at the edge of the anomalous dispersion regime [23, 24]. In addition, oscillatory distortions form in the tail end of the pulse of the pulse intensity [25-27].

Fundamentally, in the anomalous dispersion regime, a small amount of anomalous GVD is also desired to counteract the chirp due to nonlinear processes, leading to stable pulse propagation in the form of a soliton (see Sections 2.3 and 2.4) [28-30].

2.2.5 Intermodal Dispersion

For a waveguide with $V > 2.405$, more than one transverse mode can propagate through the fibre. Each mode will travel with different group velocities due to intermodal dispersion [31]. An optical pulse comprised of many such modes will experience temporal broadening according to Equation 2.2.18 [31]:

$$\Delta\tau = \frac{L n_1}{c}\left(\frac{n_1 - n_2}{2n_1}\right)^2 \quad (2.2.5)$$

where L is the propagation distance and c is the speed of light in a vacuum.

For robustly single-mode fibre (i.e. commercially available SMF-28e+, SM/PM2000 used in this thesis), this effect may be ignored [32]. Single-mode fibre is not truly single-mode however, as it is comprised of an orthogonal (x and y) pair of polarisation modes [11].

2.2.6 Fibre Birefringence and Polarisation Mode Dispersion

Even the fundamental Gaussian transverse mode (TEM_{00}), or fundamental linearly polarised mode in fibres (LP_{01}) is not single mode. This 'single' mode is contains a mode for each polarisation component in the transverse plane of the fibre [15].

While this would not usually pose an issue in an ideal case ($n_x = n_y$), real single-mode fibre is prone to core shape deformation. This is a result of environmental pressures and manufacturing defects introducing ellipticity, thus causing birefringence ($n_x \neq n_y$) [33]. For example, if $n_x > n_y$, y and x are the fast and slow axis for the fibre respectively, along which polarisation is maintained. Due to this we see that a pulse with initially linear polarisation will rotate from linear to elliptical to linear, the distance over which this cycle occurs being the beat length L_B given by Equation 2.2.19:

$$L_B = \frac{\lambda}{|n_x - n_y|} \qquad (2.2.6)$$

This also causes a propagation delay of one of the polarisation modes relative to the other, causing temporal pulse broadening [33]. This effect is known as first order polarisation mode dispersion (PMD) and serves as one of many complications of ultrashort pulsed fibre cavity design, particularly systems that utilise NLPR to achieve mode-locking [34].

PMD may be avoided by using polarisation maintaining fibre (PMF). PMF utilises a large, engineered birefringence such that environmentally induced birefringence is negligible [35]. PMF only preserves linearly polarised light launched into the fibre such that the polarisation is aligned or perpendicular to the strongly birefringent axis [36].

The simplest PMF scheme is the elliptical core fibre, where the core is purposefully deformed spatially along the *x* or *y* cross-sectional axis, introducing a strongly birefringent set of indices due to both stress and geometry of the core [37]. However, this design cannot be extended to arbitrary values of refractive index between core and cladding [38].

Conventional examples of PMF are shown in Figure 2.2.3. It has been shown numerically that the Bowtie PMF structure supersedes the elliptical structure in terms of applied birefringence [35]. Thus, PANDA and Bowtie PMF designs (Figure 2.2.3) are more commonly used. However, PANDA PMF is commonly utilised in industry and research due to its comparable core size to most single-mode fibres [38].

Bowtie and PANDA PMF are drawn with a set of 'stress rods' of differing indices to the core and cladding that run parallel to the circular core. Instead of using a nonsymmetric core, the stress rods introduce the strong birefringence necessary for a PMF architecture via a large thermal expansion coefficient that 'freezes' strain into the fibre after it is drawn and cools, in addition to a form of geometrically applied birefringence due to the rods [37].

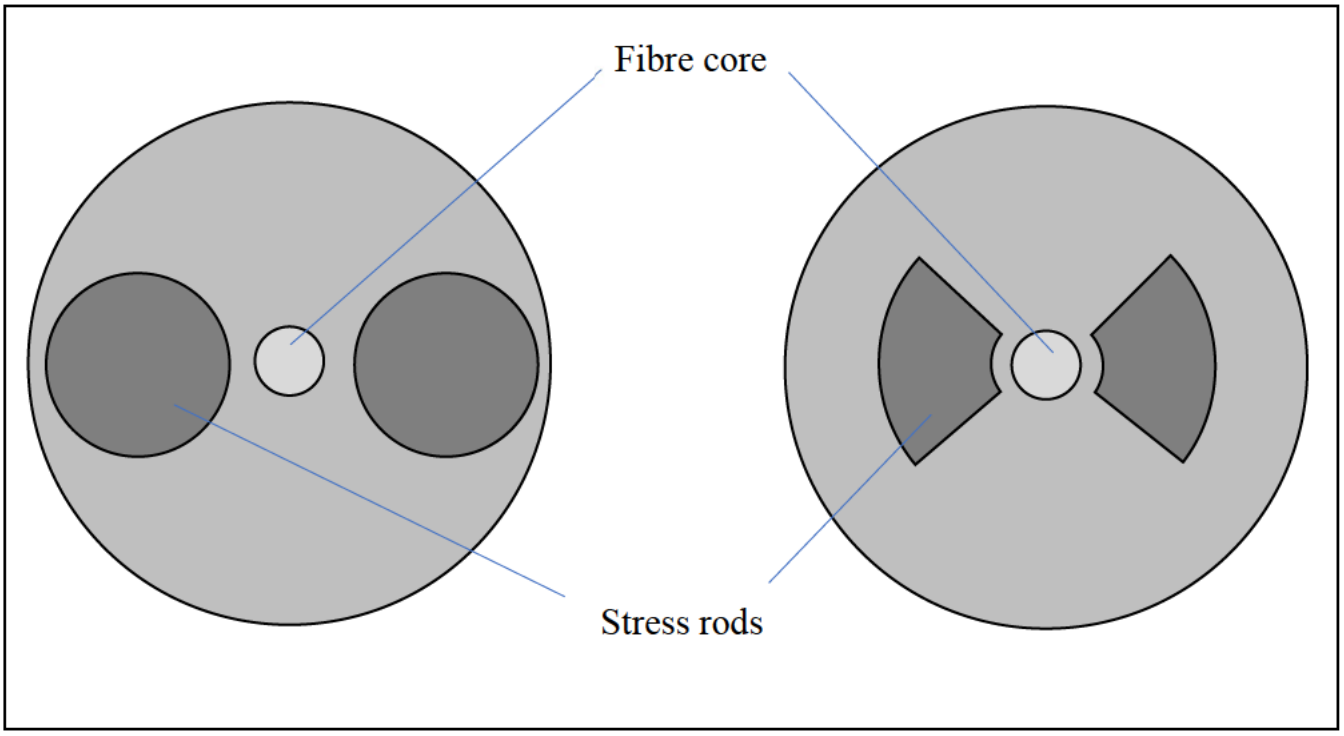

Figure 2.2.3: Transverse cross-section of Panda (left) and Bowtie (right) PMF designs. Stress rods are symmetrically placed around the core to produce strong birefringence.

2.2.7 Polarisation Maintaining Optical Circulators

An optical circulator sequentially sends light from one port to the next while functioning as an optical diode [33, 39]. Typically, circulators consist of three to four ports, such that light entering port 1 leaves port 2, and light entering port 2 leaves port 3 and so on. This is often achieved using non-reciprocal optical paths through the device. An example utilising four Faraday rotators and three polarisation beam splitting prisms is shown in Figure 2.2.4 below [33, 39].

Due to the non-reciprocal polarisation rotation, light that leaves and back-reflects into port 2 takes a different path through the device, ending up at port 3 (spatially separate to port 1). Note that any light entering port 3 will enter the second prism as the o-beam polarisation and transmit through prism 2 at the wrong height (not deflected due to being o-beam), therefore missing rotators 3 and 4 and being rejected.

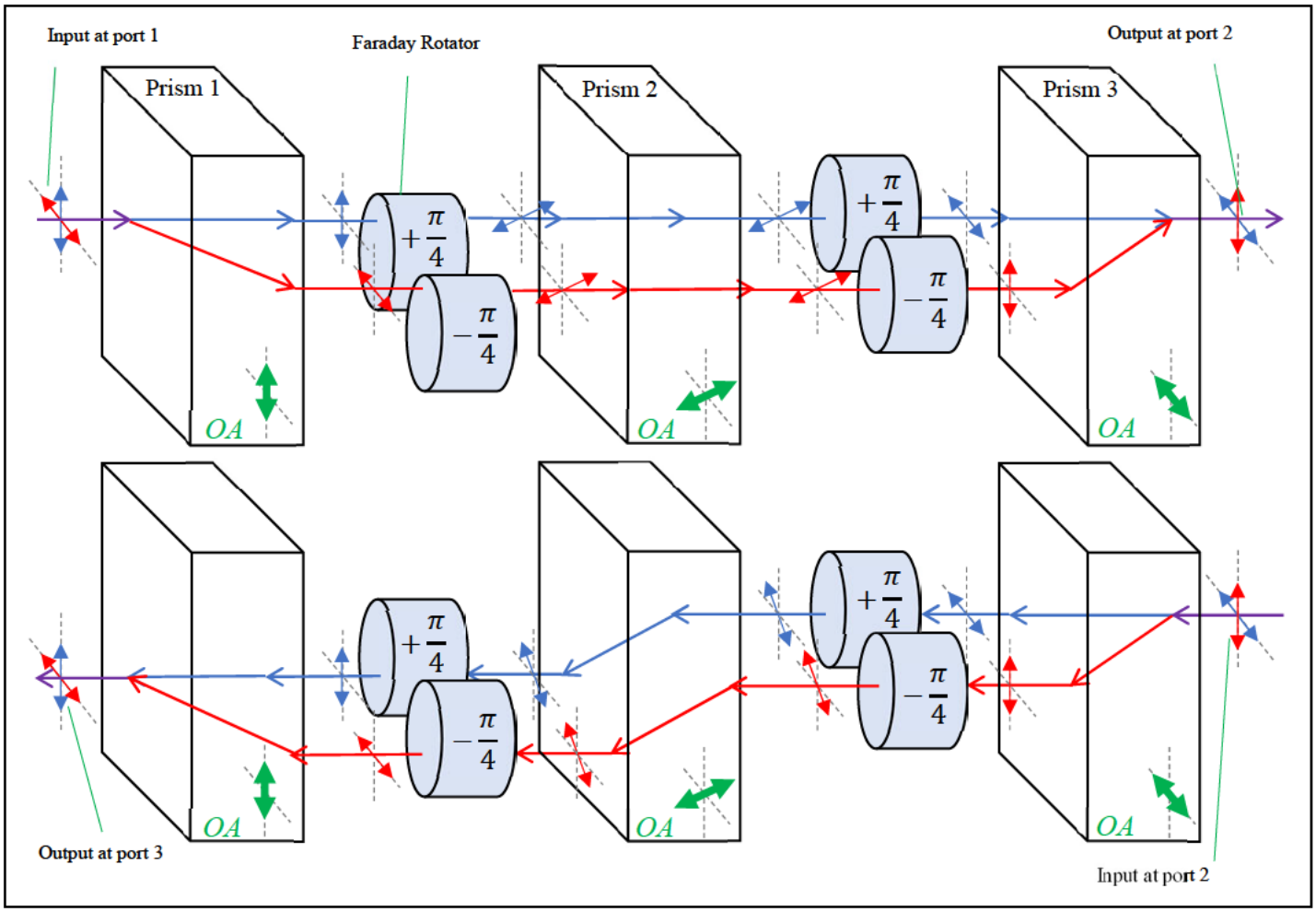

Figure 2.2.4: Schematic of a PM circulator for entry and exit through port 2, with the ordinary axes denoted 'OA'.

2.2.8 Doped Gain Fibres

This project utilised a holmium doped (Ho^{3+} ion) fibre gain medium for generation of 2.1 µm light. This involved stimulated emission between the $^5I_7$ and $^5I_8$ states of Ho^{3+} [40]. There are two transitions that can be pumped to populate the $^5I_7$ state and achieve sufficient inversion for lasing, shown in Figure 2.2.5a below [40, 41]:

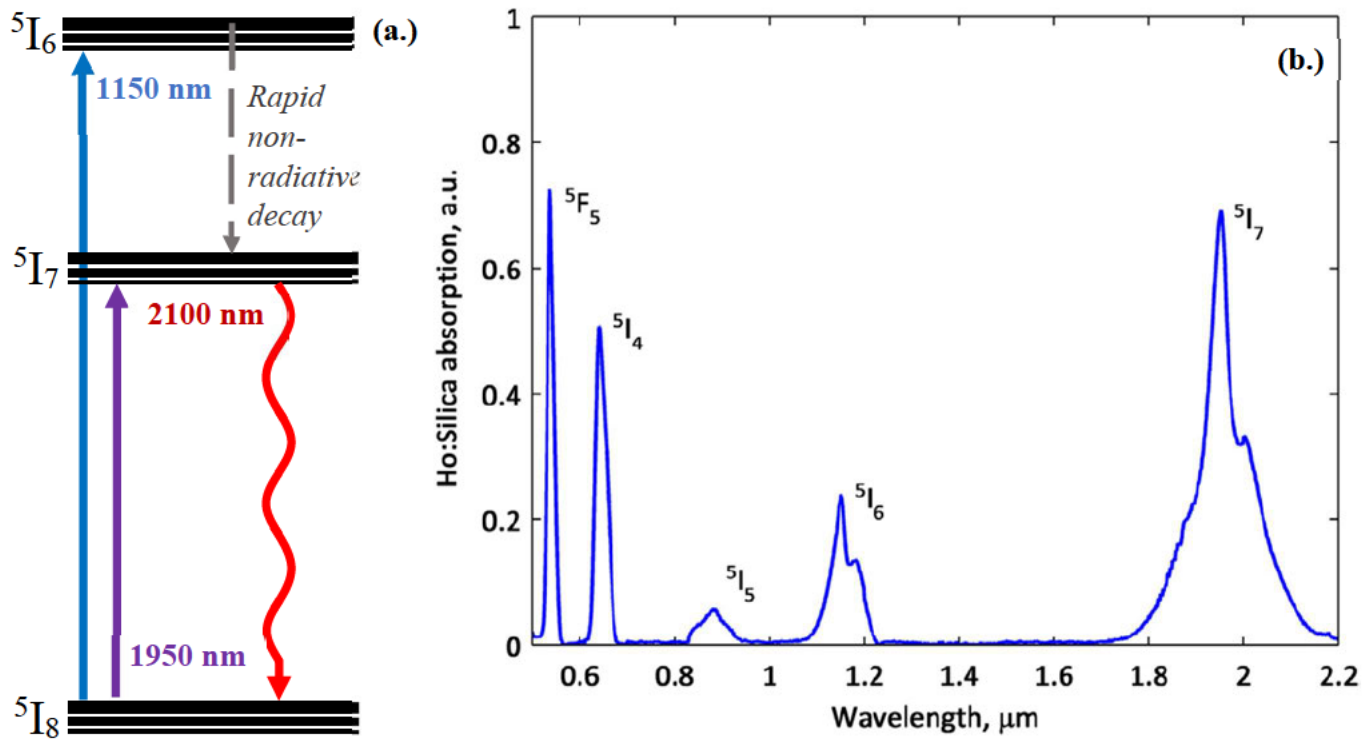

Figure 2.2.5: (a.) Schematic of the relevant lasing states of Ho3+ for a near-IR laser source and (b.) absorption spectrum of Ho:doped silica fibre. Note the non-radiative decay from 5I6 to 5I7 produces a lattice phonon and does not contribute to the field.

This project utilised the $^5I_8$ to $^5I_6$ transition by pumping the Ho-doped gain medium using an Innolume LD-1152-FBG-300 300 mW diode with an emission wavelength of approximately 1150 nm as shown in Figure 2.2.5a above. Atoms excited to the $^5I_6$ state quickly decay via a non-radiative transition to the relevant lasing state shown in Figure 2.2.5, the $^5I_7$ state [40]. Fibre cavities designed for this project utilised a core-pumped scheme where pump light propagates down the core to excite the Ho^{3+} ions as this provides lesser pulse distortion over cladding-pumped schemes [42, 43].

The 1950 nm pumping scheme has a higher slope efficiency as the 1150 nm scheme has a large quantum defect [41, 44]. Quantum defect is an inefficiency arising from a difference in pump wavelength versus the energy of the target state. In future, the 1950 nm pumping scheme would be desirable should laser diodes become more commonly available at 2 μm. CW energies on the order of kW have been predicted using the 1950 nm pumping scheme for a Ho:silica fibre device [41]. Furthermore, Jackson (2006) was able to demonstrate that a slope efficiency of 82% was possible using a thulium fibre laser as a resonant pump for the 1950 nm transition to the $^5I_7$ state [45].

However, the 1150 nm pumping scheme was used due to its relative accessibility and ease of use. Laser diode packages near 1 μm are both commercially available and pre-characterised, both considerable advantages in terms of experimental use and for development of a compact and reliable seed source.

For the 1150 nm transition, Kurkov et. al. (2011) demonstrated a record high 42% pump slope efficiency, close to the theoretically determined limit with a differential quantum defect of ~81% [46]. While a lower slope efficiency than the 1950 nm may pose an issue in terms of thermal management, optical fibres are renowned for their large surface area and thus relative ease of cooling at low pump power [47].

Furthermore, thulium may have also sufficed as an active dopant itself for the gain medium instead of holmium, as Tm^{3+} ions possess a 2.05 μm radiative transition between its $^3F_4$ and $^3H_6$ states. However, holmium was used instead for a variety of reasons, as outlined in Table 2.2.2.

Thulium Advantages (Tm^{3+})	**Holmium Advantages (Ho^{3+})**
Lower inversion threshold for transparency (2-3%) c.f. holmium (20-30%)	Lower parasitic lasing
More mature, extensively documented in literature c.f. holmium	Less mature, gaps in literature to be explored
Prone to amplified spontaneous emission (ASE)	Less prone to amplified spontaneous emission (ASE) losses
Diminishing emission cross section beyond 2 μm	Larger emission cross-section beyond 2 μm

Table 2.2.2: Relative benefits of Ho3+ and Tm3+ dopants.

2.3 Optical Nonlinearity

2.3.1 Nonlinear Polarizability

Thus far we have only considered the linear optical response of materials, where the polarizability is linearly proportional to the electric field (first term of Equation 2.3.1). In general materials display non-negligible higher order nonlinear polarizability terms, as shown in Equation 2.3.1 (assuming instantaneous material response) [48-50]:

$$\boldsymbol{P}(t) = \epsilon_0\left(\chi^{(1)}\boldsymbol{E}(t) + \chi^{(2)}\boldsymbol{E}^2(t) + \chi^{(3)}\boldsymbol{E}^3(t) + \cdots\right) \qquad (2.3.1)$$

where $E(t)$ is the incident field strength [51].

2.3.2 The Optical Kerr Effect

Due to the nonlinear polarizability given by Equation 2.3.1, materials with a high $\chi^{(3)}$ susceptibility will undergo the electro-optical ('AC') Kerr effect, leading to a modified refractive index n [25, 49]:

$$n(r) = n_0 + n_2|E(r)|^2 \qquad (2.3.2)$$

For a Gaussian laser beam, E varies across the transverse cross-section, thus the Kerr effect causes the refractive index to vary with beam radius r. For a nonlinear material with a positive n_2 coefficient we see a positive change in refractive index with increasing spatial intensity [49].

The result is the centre of the beam experiencing a greater optical path than the wings, forming an effective focussing lens, thus focussing the beam and is shown in Figure 2.3.1 below [52-56]:

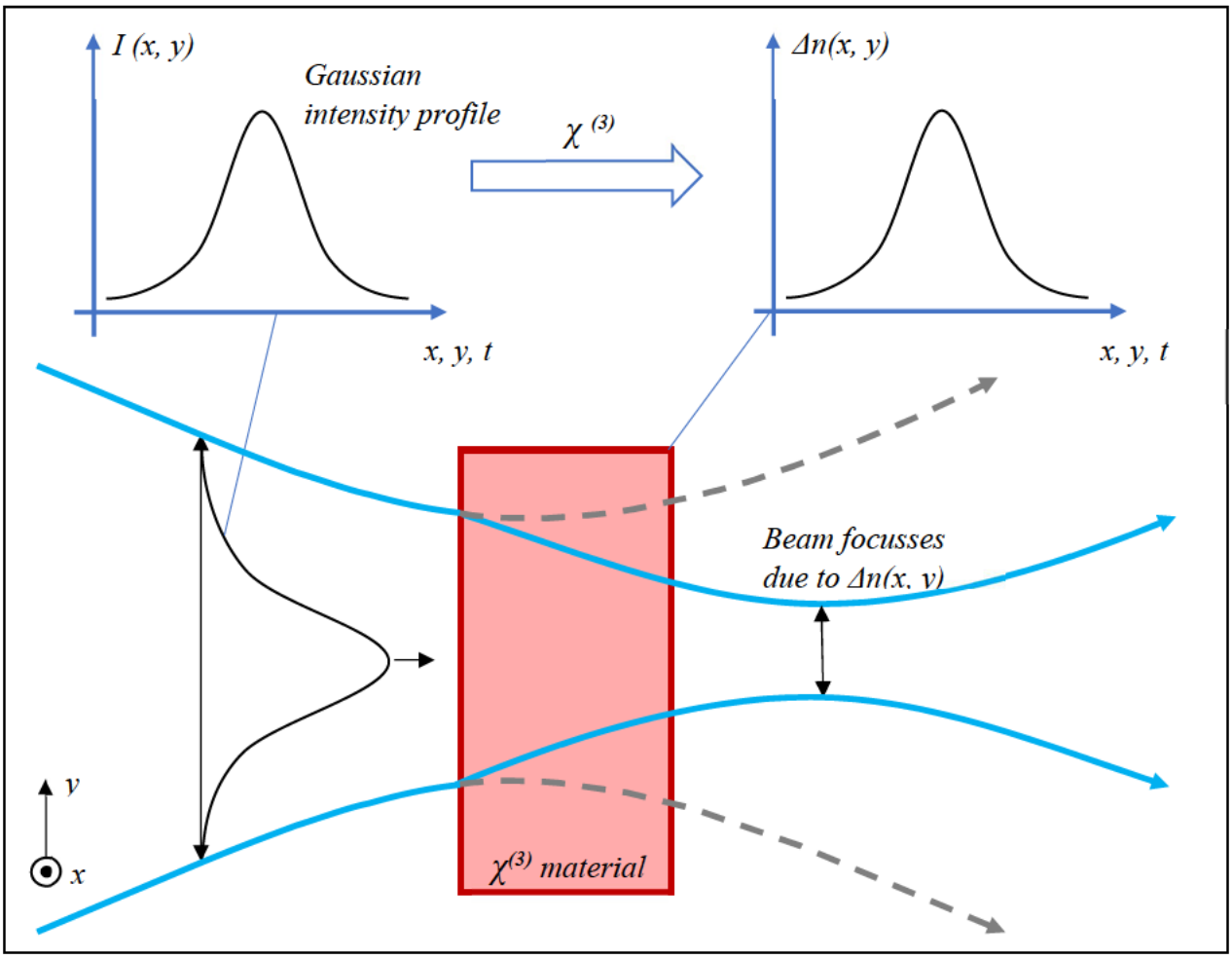

Figure 2.3.1: Diagram of Kerr-lensing focussing a Gaussian beam in a $\chi^{(3)}$ material.

As the Kerr effect produces an intensity-dependent refractive index, note that the intensity profile of a pulse also depends on time (see Figure 2.3.1 above) also. Thus, a laser pulse in a chi-three material will retard its own phase in time also, a phenomenon known as self-phase modulation (SPM) [57].

2.3.3 Self-Phase Modulation

SPM will generate new frequencies caused by a *changing* phase shift over time, given by the time derivative of pulse phase in Equation 2.3.3 below [58]:

$$\frac{\delta\phi}{\delta t} = \delta\omega \qquad (2.3.3)$$

The resulting increased spectral bandwidth is also up-chirped for an initially unchirped or up-chirped pulse [59]. If a pulse is down-chirped then the SPM-generated up-chirp will transfer

energy to the central wavelengths and not generate additional bandwidth [60]. Note that SPM alone does not distort the temporal pulse shape but only its spectrum [61]. An example plot of a Gaussian pulse intensity in the time domain and the resulting SPM-induced chirp is shown in Figures 2.3.2a and 2.3.2b below respectively:

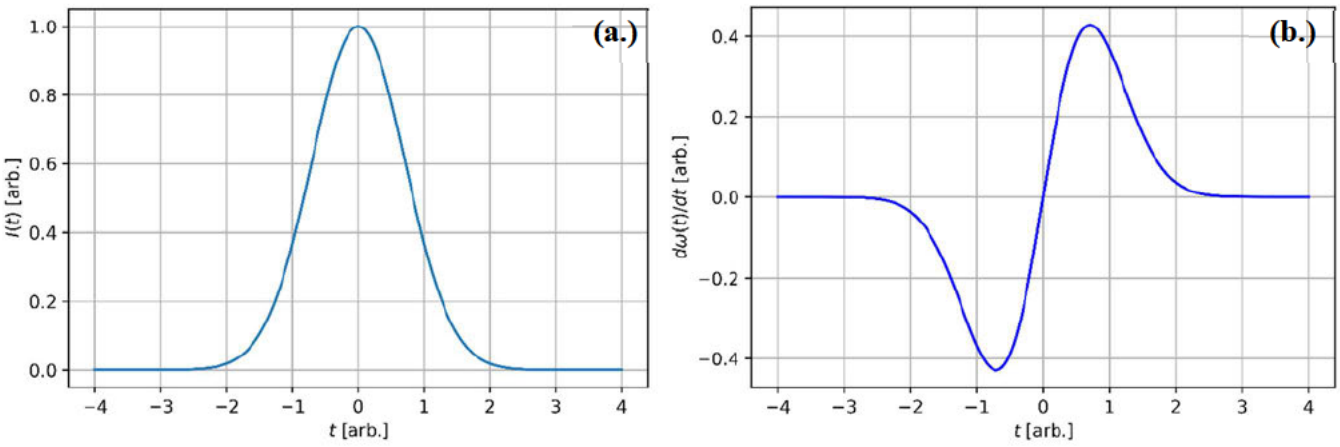

Figure 2.3.2: Plots of (a.) intensity of a Gaussian pulse in time and (b.) the change in instantaneous frequency generated via SPM.

As shown in Figure 2.3.2b above, the leading edge of the pulse will generate lower frequencies, and the trailing edge will generate higher frequencies, thus causing the pulse to be up-chirped through SPM via the generation of these new spectral components.

Also recall that anomalous GVD causes down-chirp. As the chirp of the SPM-affected pulse is opposite to that of the dispersion, anomalous GVD will act to re-compress the pulse [62]. This balance between the two chirps in the anomalous regime creates an ultrashort pulse solitary-wave pulse known as a soliton and is discussed further in Section 2.4.

2.3.4 Nonlinear Birefringence and Polarisation Rotation

The polarisation state of light in a fibre may also rotate due to the chi-three nonlinearity, in a process known as nonlinear polarisation rotation (NLPR) [63]. Recall from Section 1.2 that NLPR may be used as an artificial saturable absorber in combination with a polarisation filter [64]. Thus, despite the work in this thesis being based on SESAMs, NLPR inevitably plays a small role in pulse shaping.

Assuming purely transverse electromagnetic modes (i.e. no skew modes), it is possible to show that the chi-three nonlinearity yields Equations 2.3.4 and 2.3.5 below for the nonlinear change to the x,y refractive indices [25, 65]:

$$\Delta n_x = n_2 \left(|E_x|^2 + \frac{2}{3} |E_y|^2 \right) \quad (2.3.4)$$

$$\Delta n_y = n_2 \left(|E_y|^2 + \frac{2}{3} |E_x|^2 \right) \quad (2.3.5)$$

The left-hand term in the brackets of both Equations 2.3.4 and 2.3.5 represents the Kerr effect (and therefore SPM) as before, where the refractive index in the x or y direction changes depending on the amplitude squared in that direction, as expected [65]. However, the additional terms on the righthand side of the brackets depends on the intensity of the other transverse direction. This cross-coupling of the nonlinear change to the refractive index is known as cross-phase modulation (XPM) and is responsible for nonlinear birefringence in optical fibre [25, 65].

NLPR means that pulses change their own polarisation state dependent on intensity, thus the central, high intensity part of the pulse has a different polarisation than the wings due to the intensity dependence of Equations 2.3.4 and 2.3.5. A polarising device may be used to then discriminate the central-most peak of the pulse and attenuate the wings if used in tandem with a stress-inducing polarisation controller to shift the overall polarisation state of the pulse [64].

2.3.5 Intrapulse Raman Scattering (IRS)

A pulse may also excite molecular rovibrational modes to generate additional shifted frequencies, in a chi-three process known as Raman scattering, either spontaneously or through coherent nonlinear four-wave mixing [66-68]. For coherent (stimulated) Raman scatter, photons from the laser pump undergo wave mixing with Stokes or Anti-Stokes beams in the material via interactions with the ro-vibrational modes of the medium [67].

The Stokes beam is less energetic, and results from lattice optical phonons removing energy from the beam [69]. Conversely, the higher energy Anti-Stokes beam is produced by extracting energy from lattice vibrations. However, the lattice energy is inherently thermal, thus the Stokes process dominates at room temperature [67, 69]. An energy level diagram of both processes and the resultant pulse spectrum is shown in Figure 2.3.3 [68, 70]:

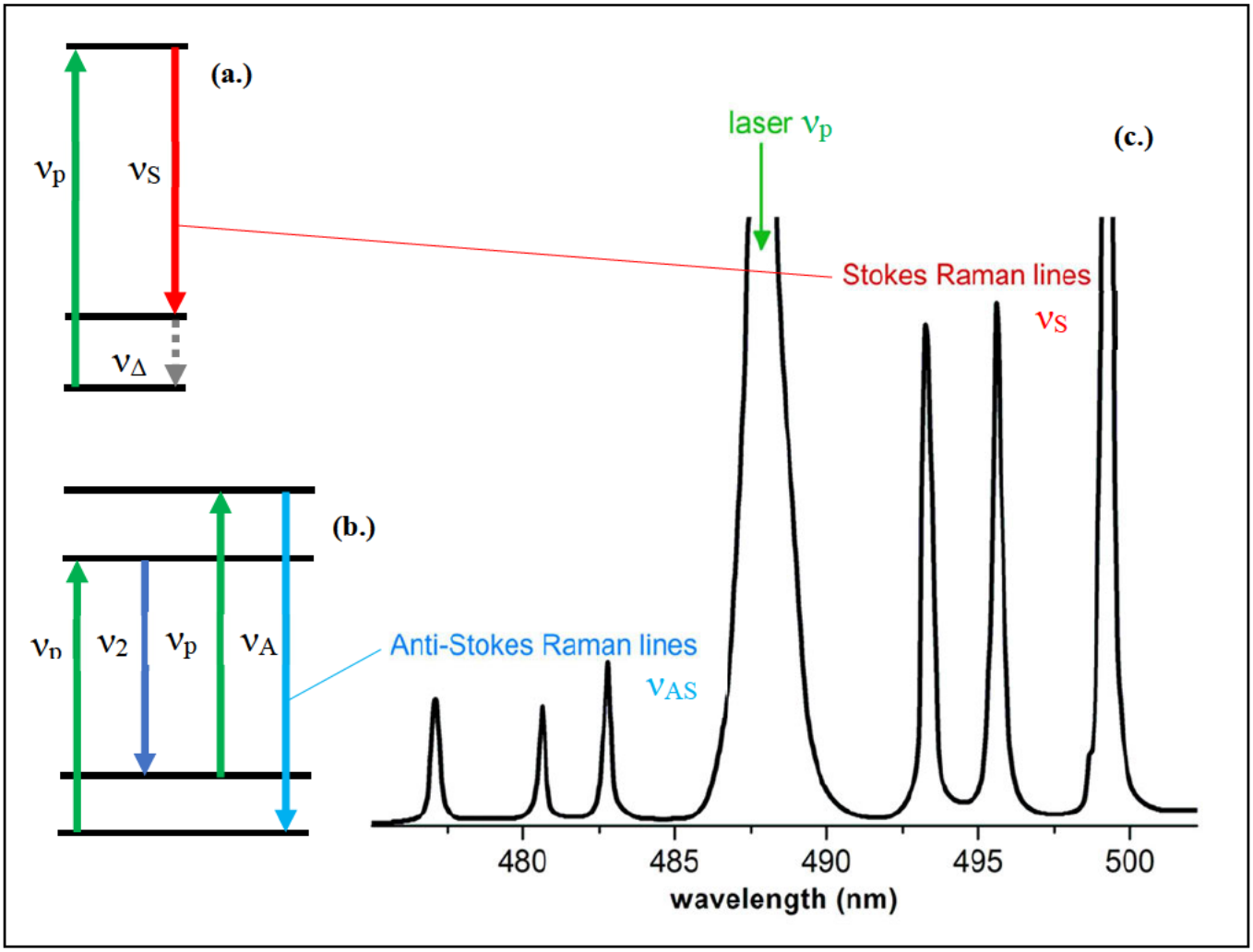

Figure 2.3.3: Energy level diagram of both (a.) Stokes and (b.) anti-Stokes beam generation via SRS, and (c.) the resultant spectrum.

Recall that an ultrafast optical pulse consists of a sharp, high power temporal peak comprised of broad range of frequencies in the spectral domain. In intrapulse Raman scattering (IRS), a pulses high frequency components pump the Stokes wave generating low frequency terms [71]. This leads to a self-induced spectral redshift in the pulse spectrum as the initial pump depletes [71-73].

Silica glass has a large Raman gain spectrum and thus plays a critical role in ultrashort pulse propagation in fibre [71]. The empirical equation which defines the fractional gain of this process in glasses is given by Equation 2.3.6 [74, 75]:

$$R(t) = (1 - f_R)\delta(t) + f_R h_R(t) \qquad (2.3.6)$$

$$where\ h_R = \left(\frac{\tau_1^2 + \tau_2^2}{\tau_1 \tau_2^2}\right) exp\left(-\frac{t}{\tau_2}\right) sin\left(\frac{t}{\tau_1}\right) \qquad (2.3.7)$$

and δ(t) is the dirac delta representing the instantaneous Raman response. The delayed Raman response h_R is given by Equation 2.3.7 where τ_1 and τ_2 are inverse time scales that represent the phonon frequency and the linewidth of the scattering process, respectively [71].

2.4 Mode-locking and GNLSE

2.4.1 Mode Superposition

Recall that the total phase change per round trip in a resonant cavity must be an integer multiple of 2π due to superposition. Axial modes are standing wave resonances whose wavelengths satisfy this condition in the longitudinal direction [76]. However, the modal structure will also change in the tranverse direction, dictated by the structure of the resonator perpendicular to the axial direction (due to mirror curvature etc.). For a given longitudinal mode structure, there are many such transverse modes [77].

Mode-locking is a technique that utilises the superposition principle, whereby a broad band of *M* axial modes are excited and interfere to produce an ultrashort pulse if and only if all modes have a constant phase relation. Consider the resultant complex field *U* is a function of time *t* and propagation distance *z* as a sum of plane waves representing each axial mode [11]:

$$U(z,t) = \sum_m A_m\, exp\left(2\pi i \nu_m \left(t - \frac{z}{v_g}\right)\right) \qquad (2.4.1)$$

$$where\ \nu_m = \nu_0 + m\nu_{FSR},\quad m = \ \ldots -2, -1, 0, 1, 2, \ldots$$

where ν_0 is the central frequency of the gain spectrum, ν_{FSR} is the free spectral range of the cavity and A_m is the real amplitude of the m^{th} mode. Typically, the amplitudes A_m and phase Arg[U] are random as the modes excite and are amplified by different atoms within the gain. However, if the phases (and amplitudes) of *U(z,t)* are fixed then we obtain the following intensity profile [11, 78]:

$$I(z,t) = |A|^2 \frac{sin^2\left(M\pi\left(t - \frac{z}{v_g}\right)/t_{rep}\right)}{sin^2\left(\pi\left(t - \frac{z}{v_g}\right)/t_{rep}\right)} \qquad (2.4.2)$$

where t_{rep} is the repetition time; the time between pulses in a train, and is given by the total round trip propagation length l and the group velocity:

$$t_{rep} = \frac{l}{v_g} \qquad (2.4.3)$$

Equation 2.4.2 is plotted as a function of time in Figure 2.4.1 below, with the resultant intensity field creating a single pulse which is repeats at the repetition period t_{rep}.

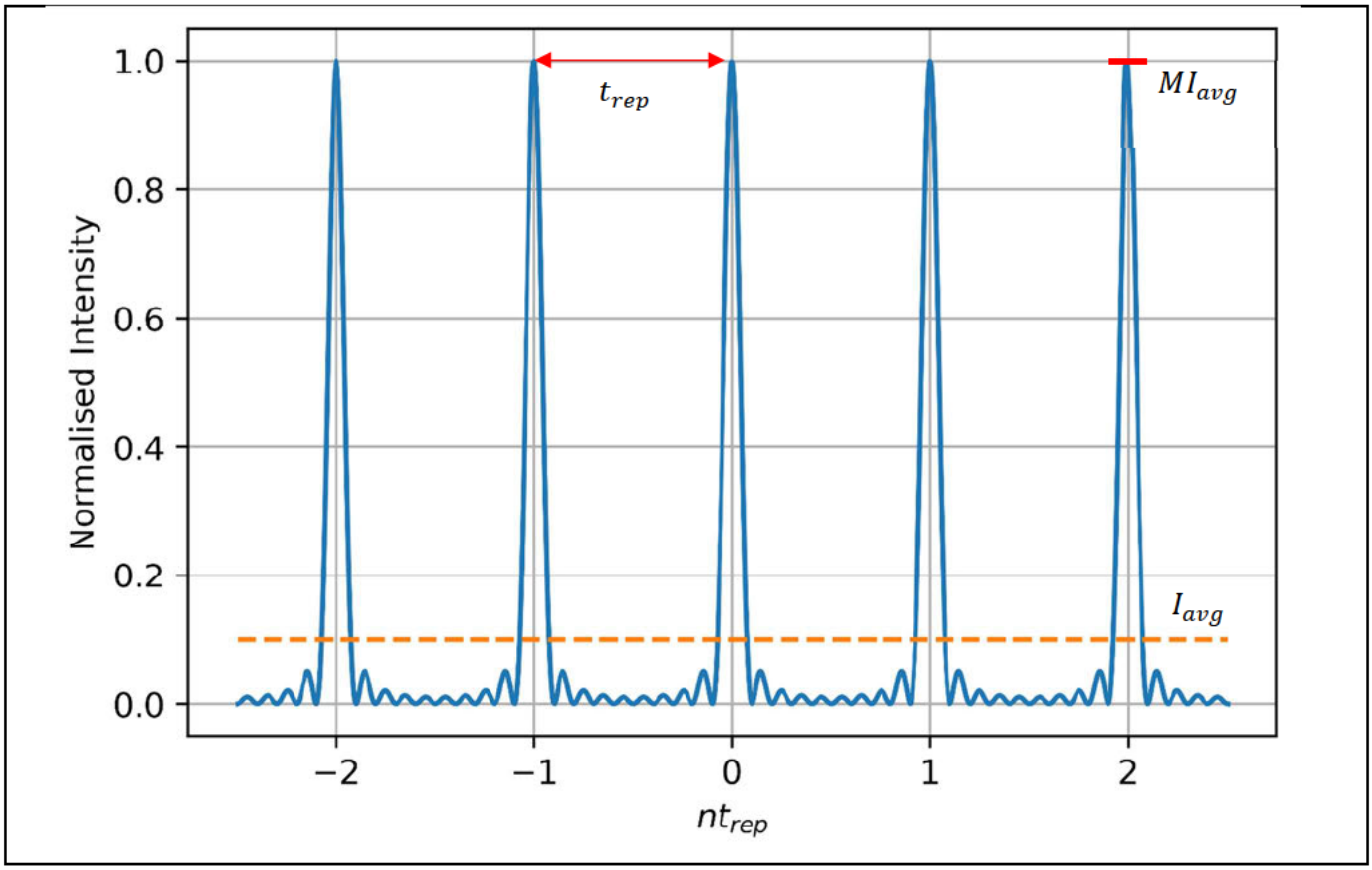

Figure 2.4.1: Mode-locked pulse train for M = 10 modes, with pulses temporally spaced at integer n multiples of the repetition period (eq. 2.4.2)

Thus, as the single pulse circulates through the cavity at timing t_{rep}, a fractional outcoupled copy is observed at the laser output, resulting in an observed pulse train shown in Figure 2.4.1 above. Note that as the number of modes M increases (i.e. spectral bandwidth) the pulse duration decreases via an inverse proportionality [11]. Similarly, the peak intensity of the pulse is proportional to the number of modes (spectral bandwidth) and average intensity as shown in Figure 2.4.1.

2.4.2 The Generalised Nonlinear Schrödinger Equation

In practice, the propagation of mode-locked pulses is described by the generalised nonlinear Schrödinger equation (GNLSE). This is derived by considering Maxwell's equations in the slowly varying pulse envelope approximation (true for most pulses > 1 fs), giving the nonlinear PDE in Equation 2.4.4 [25, 79-81]:

$$\frac{\partial A}{\partial z} + \frac{1}{2}\left(\alpha(\omega_0) + \frac{\partial}{\partial t}\right)A - i\sum_{n=1}^{\infty}\left(\frac{i^n\beta_n}{n!}\right)\frac{\partial^n A}{\partial t^n} = i\left(\gamma(\omega_0) + i\gamma_1\frac{\partial}{\partial t}\right)\left(A(z,t)\int_0^{\infty} R(t')|A(z,t-t')|^2 dt'\right) \quad (2.4.4)$$

Here $A(\omega,t)$ is the pulse amplitude, β_n represents the n^{th} order Taylor expansion term of the dispersion coefficient, $R(t)$ is the Raman response function, α represents linear cavity losses and the bracketed $\gamma_{0,1}$ terms represent the nonlinear coefficient and self-steepening respectively.

By solving Equation 2.4.4 one can obtain the spectral and temporal evolution of a mode-locked pulse in a theoretical cavity model. Equation 2.4.4 and variations thereof have been explored extensively throughout the literature in a variety of contexts such as plasma physics, optics, quantum mechanics and water waves [79-86].

Via inclusion of the n^{th} order expansion of the dispersion coefficient, $\beta(\omega)$, solving the GNLSE becomes a matter of solving an n^{th} order nonlinear partial differential equation, and is thus not easily solved [25]. Note that soliton pulses are a family of analytical solutions to Equation 2.4.4 [82-84, 86]. However, due to intracavity effects such as gain saturation and saturable absorption these analytical solutions no longer apply, and numerical methods are required, discussed further in Section 2.6 [87, 88].

2.4.3 Solitons

Soliton-like optical pulses have field envelopes that are a solution to the NLSE, whereby the balance of anomalous GVD and SPM cancels to create an ultrashort, self-stabilising pulse capable of propagation over long distances without distortion [89, 90].

Recall that SPM introduces spectral broadening for up-chirped and unchirped pulses and that anomalous GVD produces a downchirp [91, 92]. Thus, these two effects may be balanced in

the anomalous regime to produce an ultra-stable pulse known as a soliton [93]. Generally, the soliton pulse shape is described by a hyperbolic secant-squared intensity profile [94]:

$$I(z = 0,\ t) \sim \operatorname{sech}^2\left(\frac{t}{\tau}\right) = \left(\frac{2e^{\frac{t}{\tau}}}{e^{\frac{2t}{\tau}} + 1}\right)^2 \qquad (2.4.5)$$

where τ characterises the pulse duration.

Solitons under ideal conditions maintain their optical power and pulse shape while propagating even at very short pulse durations (~fs to ps) hence they are of great interest both theoretically and practically to many of the applications outlined in Chapter 1 [95].

In reality, solitons lose energy as they propagate due to various intracavity elements such as saturable absorbers, intrinsic losses, filtering etc [95]. This energy perturbation couples into a low power dissipative wave which, unlike the pulse, will be of insufficient intensity to drive SPM to counter GVD and will thus spread out temporally. The resultant low intensity background is known as continuum or the dissipative wave [95-97]. The continuum, when amplified by the gain medium of the laser, may compete for gain in the cavity against desired soliton-like pulses and destabilise them, therefore destabilising mode-locked operation [98]. Suppression of this undesirable component is discussed further in Section 2.5.

2.5 Semiconductor Saturable Absorber Mirrors

2.5.1 Saturable Absorbers (SAs)

A saturable absorber (SA) is a material for which the absorption decreases with increasing optical intensity [99]. Thus, SAs may act as a mode-locking device by preferentially transmitting mode-locked pulses while blocking CW operation, which has a lower intensity. In a mode-locked laser, when the laser modes have no fixed phase relation, lasing is supressed by the absorber, and conversely the SA promotes pulse-like operation, i.e modes are locked [100, 101], shown in Figure 2.5.1 below.

SAs are commonly made from semiconductors, carbon nanotubes, graphene or artificial nonlinear elements based on self-focussing or SPM. Semiconductor and graphene absorbers provide saturable absorption via Pauli blocking, whereby incident light saturates the charge carrier population via promotion to an upper state [102].

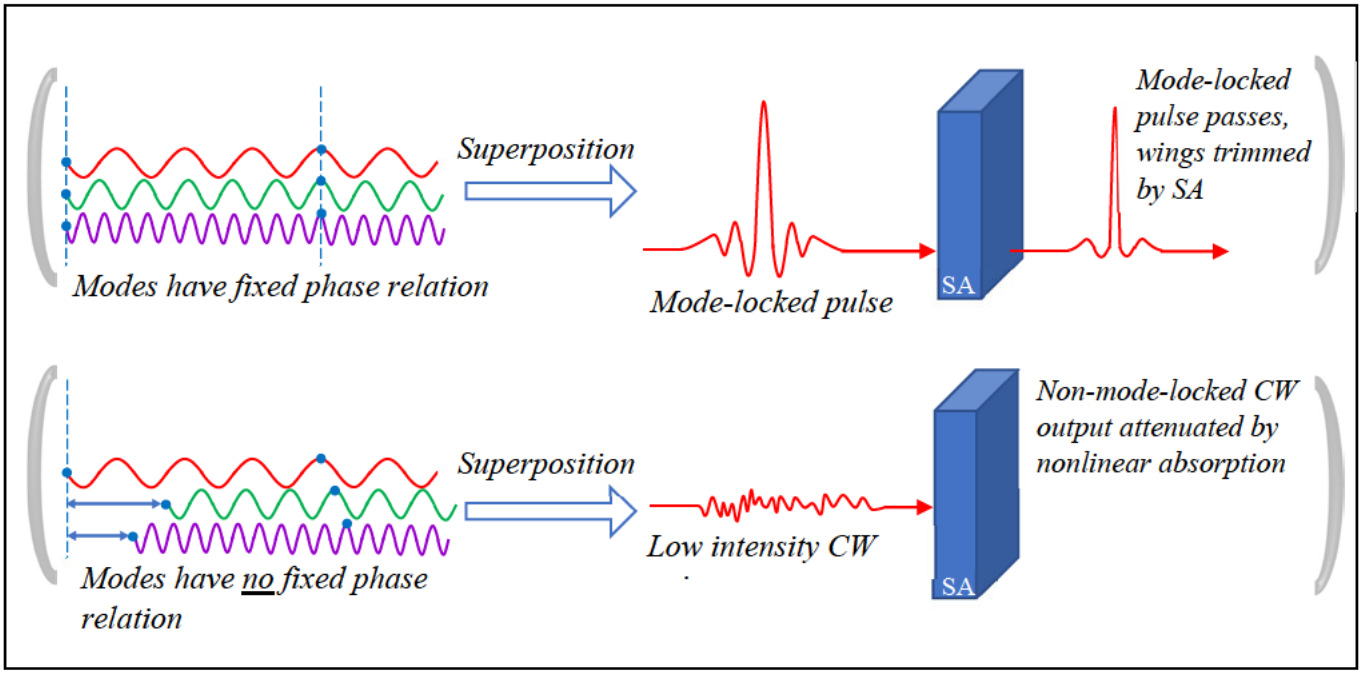

Figure 2.5.1: Diagrammatic representation of an intracavity saturable absorber creating a mode-locked pulse in a laser cavity.

An optical pulse is comprised of low intensity wings with a high intensity peak at its centre. Therefore, the role of an SA is two-fold; to self-start mode-locking from high intensity noise peaks and to sharpen pulse shape with each pass through the absorber [103, 104].

2.5.2 Semiconductor Saturable Absorber Mirrors (SESAMs)

The **s**emiconductor **s**aturable **a**bsorber **m**irror (or SESAM) is a semiconductor SA device typically consisting of four components, as shown in Figure 2.5.2 below:

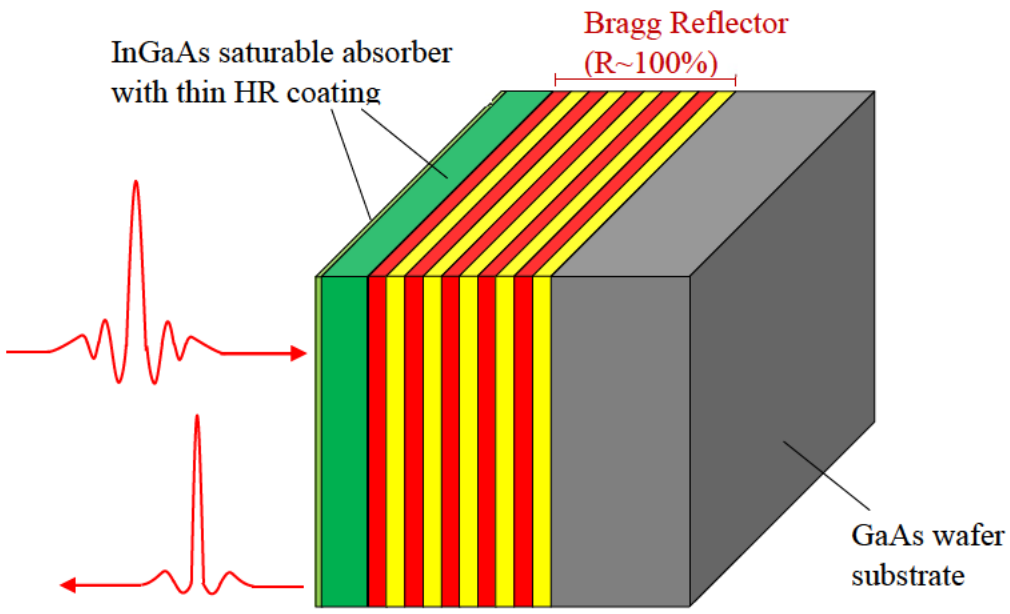

Figure 2.5.2: Architecture of a semiconductor saturable absorber mirror.

The topmost layer is a HR film applied to a semiconductor saturable absorber, which is grown onto a stack of quarter-wavelength Bragg reflectors, with the final layer being a InGaAs substrate [102, 105, 106].

A high reflectance (HR) coating is applied to the air-surface interface of the absorber as a controlled method of increasing the saturation and damage fluences of the device, as it reduces the amount of intracavity radiation that enters the structure [105].

The saturable absorber provides the nonlinear absorption required for mode-locking a laser cavity, as outlined in Section 2.5.1 above. In SESAMs the nonlinear absorption is provided by electron (charge carrier) bleaching in the semiconductor, whereby the absorption centre population is depleted as the optical field excites charge carriers to the conduction band in the absorber [102].

The Bragg reflector component provides high reflectance as a wavelength-tailored quarter/half wave dielectric stack, as is typical for a Bragg mirror [102, 106]. Diebold et. al. (2015) demonstrated that SESAMs with the substrate removed after growth exhibit superior surface quality and superior thermal contact between the Bragg reflector and a heatsink [107, 108]. Further details on SESAM design are available in Appendix C.

SESAMs are commonly installed into an optical cavity by replacing one of the cavity mirrors [106, 109-113]. In the case of fibre systems, this is achieved by placing the SESAM at the reflection port of an optical circulator [103, 104, 114, 115].

2.5.3 Characteristic Parameters of a SESAM

The key physical properties that characterise the behaviour of the SESAM are summarised in Table 2.5.1 These are tuned by changing the growth conditions for the SESAM or via the addition of coatings [105, 116].

The recovery time of the SESAM, τ_S, is defined as the time for the absorber to regain 1/e of its full absorption [102]. Note that this definition loses meaning for an SA saturated at a repetition rate faster than its inverse recovery time, where absorption is no longer exponentially defined [102]. This time is a characteristic related to the recovery time of the charge carriers across the bandgap in the material and may be tuned by introducing quantum well or quantum dot defects into the semiconductor structure [117-130].

The modulation depth, ΔR, is the maximum change in absorption (or reflectivity) of the SESAM's absorption (or reflectivity) curve; the 'height' of the curve from its highest value to its lowest [108]. This is represented in Figure 2.5.3 below, where a SESAM's nonlinear reflectivity is plotted against time after pulse incidence.

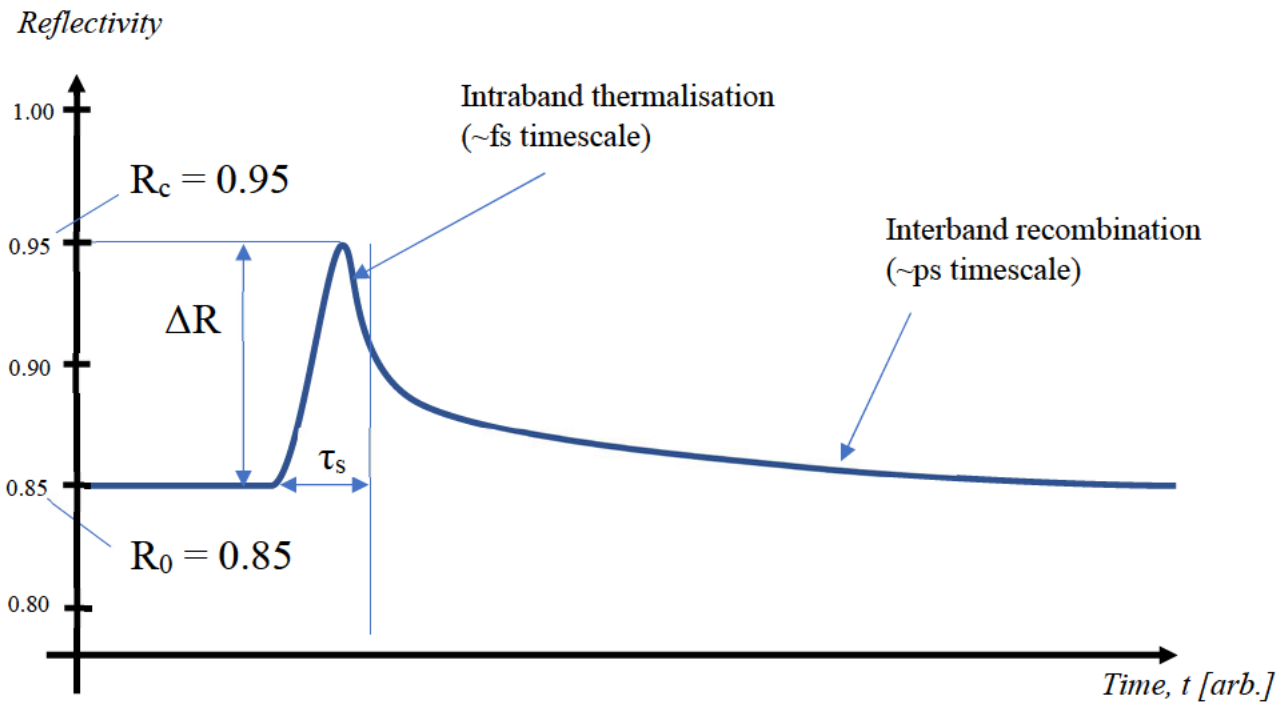

Figure 2.5.3: Example of a SESAMs nonlinear reflectivity profile with a modulation depth of 10%.

As shown on Figure 2.5.3 above, the linear (unsaturated) reflectivity R_0 is the reflectivity of the SA when completely unsaturated [131]. Similarly, the saturated reflectivity R_c is the reflectivity of the SA when it is completely saturated: its maximum reflectivity value [132]. The modulation depth, ΔR, is then defined as the reflectivity change between the unsaturated and fully saturated reflectivity, given by Equation 2.5.1 [132, 133]:

$$\Delta R = R_c - R_0 \qquad (2.5.1)$$

Lastly, the saturation intensity I_{sat} is the intensity at which the SESAM reflectivity (or absorption) falls to 1/e of its fully unsaturated value, as indicated on Figure 2.5.3 [132]. The saturation intensity is defined by the recovery time and absorption cross section (σ_{abs}) of the SESAM in Equation 2.5.2 below [106]:

$$I_{sat} = \frac{h\nu}{\sigma_{abs}\tau_s} \qquad (2.5.2)$$

where $h\nu$ is the incident photon energy and τ_s is the recovery time of the SESAM absorption.

These parameters dictate the behaviour of Equation 2.5.2 below: the equation for the SESAM's nonlinear absorption. Equation 2.5.3 is given by writing the rate equation for the conduction and valence populations of the SA [98, 128, 131, 134, 135]:

$$\frac{d\alpha(t)}{dt} = -\frac{\alpha(t)-\alpha_0}{\tau_S} - \frac{\alpha(t)P(t)}{E_{sat}} \qquad (2.5.3)$$

where α is the SESAM absorption, α_0 is the unsaturated SESAM absorption, *P(t)* is the incident pulse power, and E_{sat} is the saturation energy of the SESAM. This may be solved directly to obtain Equation 2.5.4 [74]:

$$\alpha(t) = \alpha_c + exp\left(-\frac{1}{\tau_s} - \frac{|A|^2}{E_{sat}}\right)\left(\alpha_0 + \frac{\alpha_0}{\tau_s} exp\left(\frac{1}{\tau_s} + \frac{|A|^2}{E_{sat}}\right)\right) \qquad (2.5.4)$$

where *A* is the pulse field amplitude and α_c is the fully saturated SESAM absorption.

Summary of SESAM Parameters

Parameter	Definition	Controlled by
E_{sat}	Incident pulse energy at which the SESAM absorption drops to 1/e of its maximum value [102].	HR coating at the surface-air interface, semiconductor material [102, 108].
τ_s	The exponential time constant of the nonlinear absorption [108].	Intrinsic to the SA's quantum well/dot structure [108, 136].
α_c	The absorption of the SESAM when its nonlinear absorption is fully saturated; i.e. for high pulse intensity [133].	Absorber thickness and material, radiation penetration into device [108].
α_0	The absorption of the SESAM for low pulse intensity; the unsaturated, linear absorption [133].	Undesirable defects/insertion losses.
ΔR	The change in reflectivity (or absorption) from the maximum unsaturated reflectivity to the minimum fully saturated reflectivity [133].	Absorber thickness and material [108] [137].

Table 2.5.1: Summary of SESAM characteristic parameters.

The wide range of parameters outlined in Table 2.5.1 that dictate SESAM behaviour may span a wide range of values due to their engineerability [138, 139]. Thus, intracavity dynamics will depend broadly on the above parameters in addition to dispersion and nonlinearity in the cavity [140-143]. There exist three distinct SESAM mode-locked regimes: fast, slow and soliton [101].

2.5.4 Fast SESAM Mode-locking

The recovery time is another critical SESAM parameter, and its value dictates the type of mode-locking that occurs in the laser cavity.

A 'fast' SESAM is an SA that has a recovery time on the order of or shorter than the incident mode-locked pulse [135]. As such, as the nonlinear absorption recovers fast enough to maintain absorption over the entire pulse duration, the SESAM is both able to shape the trailing and leading edges of a pulse [98]. The behaviour of the fast saturable absorption versus the pulse intensity over time is shown in Figure 2.5.4b below:

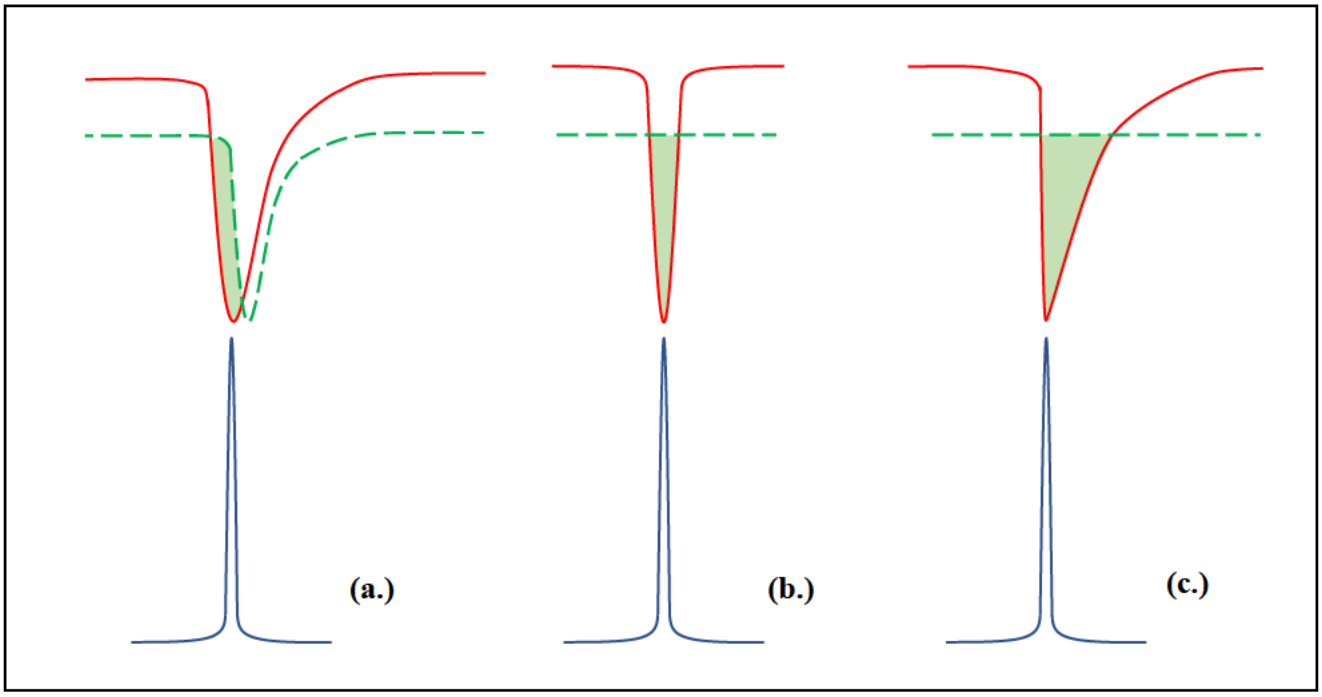

Figure 2.5.4: SESAM absorption and laser gain saturation due to an ultrashort pulse for a) slow SESAM mode-locking ($\tau s >> \tau_{pulse}$), b) fast SESAM mode-locking ($\tau_s << \tau_{pulse}$), c) soliton-SESAM mode-locking.

As shown in Figure 2.5.4b, the nonlinear SESAM absorption recovers fast enough to constantly shape the pulse, leading to a symmetrical hyperbolic secant-squared pulse intensity profile [135, 144].

2.5.5 Slow SESAM Mode-locking

‘Slow’ SESAM mode-locking is where the SESAM recovery time is much slower than the pulse [145]. Naively, as shown by the loss curve in Figure 2.5.4a, it appears that due to the slow recovery time of the SESAM would create an open net gain window that leaves the pulse asymmetrically unshaped [98]. Instead, the trailing edge of the pulse is shaped by the saturable gain, with the resultant net gain window indicated by the shaded area on Figure 2.5.4a [98, 145-147].

However, the mechanism described above would otherwise still produce some asymmetry in the pulse shape [144]. However, the leading wing of the pulse is attenuated such that the peak of the pulse is shifted back relative to the trailing wing [98, 147]. Thus, asymmetry is avoided, keeping the pulse stable with a characteristic sech-squared intensity profile [98, 147].

2.5.6 Soliton-SESAM Mode-locking

Lastly, a SESAM may assist in soliton mode-locking by self-starting pulse formation from noise and by stabilising the resulting soliton pulse [96, 98, 148]. Furthermore, SESAM parameters are somewhat non-critical outside of initial self-starting behaviour, and SPM and GVD based pulse-shaping dominates [98, 148] with recovery time only factoring in ~10% of the resultant soliton pulse duration [149].

Recall that physical (quasi) solitons shed energy as they propagate through lossy elements in cavity, causing a dissipative continuum component to grow and destabilise the pulse. Thus, a fast SESAM prevents the growth of the low-intensity, temporally broad continuum via its saturable absorption [148]. For slow SESAMs the devices dispersion causes the continuum to broaden spectrally into spectrally lossy regions of the cavity, until the recovering absorption ‘cleans up’ by attenuating this residual continuum [98, 148, 149].

Soliton-SESAM based mode-locking is noted to result in the shortest pulse duration of the three categories above, achieving up to a factor of 20 shorter pulse duration than fast absorber mode-locking [148].

2.6 Nonlinear Cavity Modelling

2.6.1 Introduction to Nonlinear Modelling

Optimisation of a mode-locked laser cavity is a complicated multi-dimensional global optimisation problem [150, 151]. To better understand these devices, we therefore look to computational methods to guide the laser design.

However, recall Equation 2.4.4, the generalised nonlinear Schrödinger equation (GNLSE), including nth order dispersion [25]:

$$\frac{\partial A}{\partial z} + \frac{1}{2}\left(\alpha(\omega_0) + \frac{\partial}{\partial t}\right)A - i\sum_{n=1}^{\infty}\left(\frac{i^n \beta_n}{n!}\right)\frac{\partial^n A}{\partial t^n} = i\left(\gamma(\omega_0) + i\gamma_1\frac{\partial}{\partial t}\right)\left(A(z,t)\int_0^{\infty} R(t')|A(z,t-t')|^2 dt'\right) \quad (2.4.4)$$

Recall that Equation 2.4.4 is an nth order partial differential equation, thus it is not trivially solved in the general case.

While there exist a growing number of methods to solve the GNLSE, such as numerical methods [25, 152], case-specific analytical techniques [153-155], and machine-learning algorithms [156, 157] we will focus on two predominant 'pseudo-spectral' numerical methods seen in the literature: the split-step Fourier method and the Runge-Kutta 4th order interaction picture.

2.6.2 Split-step Fourier Method

The split-step Fourier (SSF) method reduces Equation 2.4.4 to a set of linear and nonlinear operators, providing a simpler and relatively efficient way to computationally evaluate the GNLSE for pulse propagation. Consider the GNLSE represented in its most basic operator form [25]:

$$\frac{\partial A}{\partial z} = \left(\hat{D} + \hat{N}\right)A(z,t) \quad (2.6.1)$$

where the non-commuting operators $\hat{D}$ and $\hat{N}$ represent the dispersive and nonlinear terms of the GNLSE (Equation 2.4.4) respectively. One can then approximate the solution for the pulse field amplitude after a propagation step h [25]:

$$A(z+h,T) \approx exp\left(h\widehat{D}\right) exp\left(h\widehat{N}\right) A(z,T) \qquad (2.6.2)$$

At each step, only one operator is applied while the other operator is set to zero, with the operators applied stepwise in an alternating pattern. For example, the first step of the simulation would be carried out with only nonlinear effects, so $\hat{D} = 0$, and the next step would have $\hat{N} = 0$ instead, and so on, reducing the nonlinear PDE in Equation 2.4.4 into two separate ODEs [25, 158].

The dispersive ODE is solved in the frequency domain via a Fourier transform, and thus the SSF method is referred to as pseudo-spectral. While the dispersive operator contains differential terms in time space, these are reduced to much simpler multiplicative frequency terms in frequency space, and thus easily solved by the computation fast Fourier transform (FFT) [159]. The main benefit of the SSF method is its relative efficiency when compared to most popular finite-difference methods (e.g. Hopscotch method) due to use of the FFT algorithm [160].

Accuracy of the SSF method may also be further improved by using a more explicit form of Equation 2.6.1, known as the symmetrised SSF method, whereby the nonlinear exponential operator is replaced by a definite integral over the step of size h, thus incorporating the dependence of the nonlinear operator on propagation distance z [25].

A notable downside of the SSF method is the approximation made in Equation 2.6.2 whereby the GNLSE is split and approximated by two multiplicative exponential operators. This step has an estimated error given by Baker-Hausdorff theorem for two non-commuting operators, given by Equation 2.6.3 [25, 161]:

$$exp\left(h\widehat{D}\right) exp\left(h\widehat{N}\right) = exp\left(h\left(\widehat{D}+\widehat{N}+\frac{1}{2}\left[\widehat{D},\widehat{N}\right]+\frac{1}{12}\left[\widehat{D}-\widehat{N},\left[\widehat{D},\widehat{N}\right]\right]+O\left\{\left(\widehat{D}\right)^2\right\}+O\left\{\left(\widehat{N}\right)^2\right\}\right)\right) \qquad (2.6.3)$$

We see that Equation 2.6.3 predicts that using a split-step method will produce global errors limited to second order in the dispersive operator. While this is negligible for laser cavities with low nonlinear index n_2, or for pulses with temporal FWHM in the picosecond range and above, simulation of nonlinear mode-locked cavity dynamics may be hindered by this order of error [162].

At large step sizes the alternating application of the operators can lead to unphysical variations in field amplitude, particularly when simulating complicated nonlinear processes such as supercontinuum generation [163]. This is remedied somewhat by decreasing the step size until the associated artifacts are negligible, however doing so further increases computation time for the already computationally intensive procedure of cavity simulation.

2.6.3 Runge-Kutta 4th Order Interaction Picture (RK4IP)

Direct integration of the GNLSE without adaptive step-size ODE solvers is also, in general, difficult as the GNLSE contains a 'stiff' term in the dispersive portion of the equation [152]. Stiff ODEs are those for which the solution does not converge unless an arbitrarily small step-size is taken [164, 165]. Small step sizes necessitate longer computational times required per round trip simulated in the cavity thus bottlenecking computation when applying direct ODE solving routines to the GNLSE, which is a nonlinear PDE.

The method known as 4th Order Runge-Kutta Interaction Picture (RK4IP) remedies this stiffness by performing a change of variables in the time domain from the lab frame to a comoving frame that follows the optical pulse, $T = t - \beta_1 z$. In this 'interaction picture' representation (analogous to that used in quantum mechanics) the stiff dispersion term simplifies. A further simplification can then be achieved by rewriting the nonlinear and linear terms in a frequency (ω) dependent form, thus obtaining a modified version of Equation 2.4.4, ready for direct integration via an ODE solving routine [152, 166]:

$$\frac{\partial \widetilde{A}'}{\partial z} = i\bar{\gamma}(\omega)\, exp\left(-\hat{L}(\omega)z\right)\mathcal{F}\left\{\bar{A}(z,T)\int_{-\infty}^{\infty} R(T')|\bar{A}(z,T-T')|^2 dT'\right\} \qquad (2.6.4)$$

where $\bar{\gamma}$ represents a form of the frequency-dependent nonlinear coefficient, $\bar{A}(z,T)$ is proportional to the Fourier transform of the amplitude in frequency-space and $\tilde{A}'(z,\omega)$ is the frequency dependent field amplitude $\tilde{A}(z,\omega)$ multiplied by the linear operator in frequency space.

In comparison to the PDE in Equation 2.4.4, we now have Equation 2.6.4, an ODE which is directly integrable by (most commonly) the Runge-Kutta 4th order numerical technique with all 'stiff' components removed.

The greatest advantage of the RK4IP method is its use of direct integration on the modified GNLSE, Equation 2.6.4, whilst not making assumptions such as the exponential expansion

used in SSF methods and halving the number of FFTs per step, while simultaneously removing the stiff part of the GNLSE [160].

Furthermore, the RK4IP method is limited by the error of the ODE solver (Runge-Kutta 4th order) and is thus limited by only fourth order error [80, 167]. Numerical studies have shown that among a variety of other alternate split-step and integration schemes for solving the GNLSE, the RK4IP method possesses some of the lowest average relative error in computation for simulations of 1000 steps or more [159].

While the RK4IP method requires at least 8 Fourier transforms per step and the SSF method requires (depending on the scheme of SSF) at minimum 2 Fourier transforms, the number of steps used per round trip is much larger for SSF [167]. This exacerbates the computation time issues due to the already large number of numerical steps needed to simulate the multiple hundreds of cavity round-trips.

The largest drawback of the RK45IP method is the more complicated nature of its implementation (ala. Equation 2.6.4) compared to simpler SSF method schemes. Again, the RK4IP method requires twice as many FFTs per propagation step. However, once implemented, the RK45IP method can obtain higher computational accuracy while using larger propagation, and thus less overall, propagation steps [160].

2.6.4 Custom RK45IP Cavity Simulation

The details of the model used in this thesis is based on the RK45IP method as described by various authors, namely Dudley (2010), Mamyshev & Chernikov (1990) and Hult (2007) [152, 159, 168]. However, the original code is a MATLAB script written by Dan Nguyen (2021) and was adapted for assisting design of the experimental laser cavities described in Chapter 4 of this thesis [74]. A copy of this code is available in Appendix D, with a short summary of the parameters used given in Appendix F. Note that the estimation of the third order dispersion for all fibre simulations in this thesis is also outlined in Appendix F, with a short discussion on the effects on the pulse quality for an example simulation.

The code takes a variety of fibre parameters such as dispersion coefficients (second order and above), nonlinear coefficients, lasing wavelength, Raman gain coefficients and more. Cavity components are represented as functions that process inputs such as the above parameters, in addition to an inputted field amplitude, and compute the resultant pulse spectrum and

temporal profile after propagation via solving Equation 2.6.4 via MATLAB's 4th order Runge-Kutta ODE solver, 'ode45'.

Once the amplitude has been passed through each consecutive cavity component, i.e. after one round trip, the amplitude is fed back to the first element of the cavity and the process is repeated until a specified number of round trips (code loops) are completed.

Dispersion-compensating fibre DCF is simply modelled as SMF with a large and negative value of second order dispersion coefficient, β_2, corresponding to the specs of the DCF used.

Active fibre is necessarily more complicated due to the addition of dynamic gain effects, in addition to regular propagation ala. the SMF propagation routine described above. The time-dependent gain of the active fibre was modelled by Equation 2.6.5 [74]:

$$g = \frac{g_0}{1 + \frac{|A(z,T)|^2}{E_{sat,G}}} \qquad (2.6.5)$$

where g_0 is the small signal gain and $E_{sat,G}$ is the saturation energy of the gain medium.

Recall Equation 2.5.3 for the nonlinear absorption of a SESAM [86] [74, 102]:

$$\frac{d\alpha(t)}{dt} = -\frac{\alpha(t) - \alpha_0}{\tau_S} - \frac{\alpha(t)P(t)}{E_{sat}} \qquad (2.5.3)$$

In our model, no assumptions are made for the recovery time of the SESAM versus pulse duration. Instead, recall that the equation is directly solved by the below integrable equation for each round trip, given by Equation 2.5.4 [74]:

$$\alpha(t) = \alpha_c + \exp\left(-\frac{1}{\tau_s} - \frac{|A|^2}{E_{sat,SESAM}}\right)\left(\alpha_0 + \frac{\alpha_0}{\tau_s}\exp\left(\frac{1}{\tau_s} + \frac{|A|^2}{E_{sat,SESAM}}\right)\right) \qquad (2.5.4)$$

where α_c is the fully saturated absorption, α_0 is the unsaturated absorption, τ_s is the recovery time and $E_{sat,SESAM}$ is the saturation energy of the SESAM.

Lastly, the outcoupler is handled via simple multiplication of the field amplitude. Recall the fraction of the field amplitude which is outcoupled per round trip given by Equation 2.6.6 [74]:

$$A_{out}(z,T) = \left(\sqrt{1-f}\right)A_{in}(z,T) \qquad (2.6.6)$$

where *f* is the fractional amount of light outcoupled per round trip. The spectrum and temporal profile plotted in the simulation is A_{out}, the output of the outcoupler, analogous to measurement of a real laser cavity.

Lastly, spectral filtering is implemented similarly to Equation 2.6.6, but with a Gaussian function defining the fractional, wavelength-dependent attenuation shown in Equation 2.6.7 below:

$$F \sim exp\left(-\left(\frac{(\lambda - \lambda_0)}{\Delta\lambda}\right)^2\right) \qquad (2.6.7)$$

where $\Delta\lambda$ is the filter bandwidth, λ is the input wavelength and λ_0 is the filters centre wavelength. The code for the spectral filtering and insertion losses is at the end of Appendix D.

Chapter 3: Laser Characterisation

3.1 Chapter Layout

Chapter 3 will discuss the various performance characteristics of a mode-locked fibre laser in ideal and non-ideal operating regimes.

In Section 3.2, the equipment, methods, and noise characterisation used for the project is discussed in detail, including time domain voltage photodiode response, radio frequency spectra, optical spectra, and intensity-gated pulse traces.

In Section 3.3, unstable and stable operation modes of a holmium fibre mode-locked laser are discussed, along with the key characterisation results that identify these regimes in practice and how they are best avoided via experimental design.

3.2 Laser Output Characterisation

3.2.1 Pulse trains in the Time Domain

When analysing a pulse train output there are two characteristic noise types that exist pulse-to-pulse: relative intensity noise (RIN) and timing jitter [1]. RIN characterises the pulse-to-pulse variation in energy that is intrinsic to the laser's performance and stability [2]. It may be defined as the pulse energy standard deviation over the pulse energy mean, shown in Equation 3.2.1:

$$RIN = \frac{\sigma_{energy}}{\mu_{energy}} \qquad (3.2.1)$$

Clearly, we seek to minimise this quantity by minimising the variation in the pulse energies. Fibre cavity parameters and designs which affect the RIN will be discussed in chapter 4. RIN produces an oscilloscope trace similar to Figure 3.2.1.

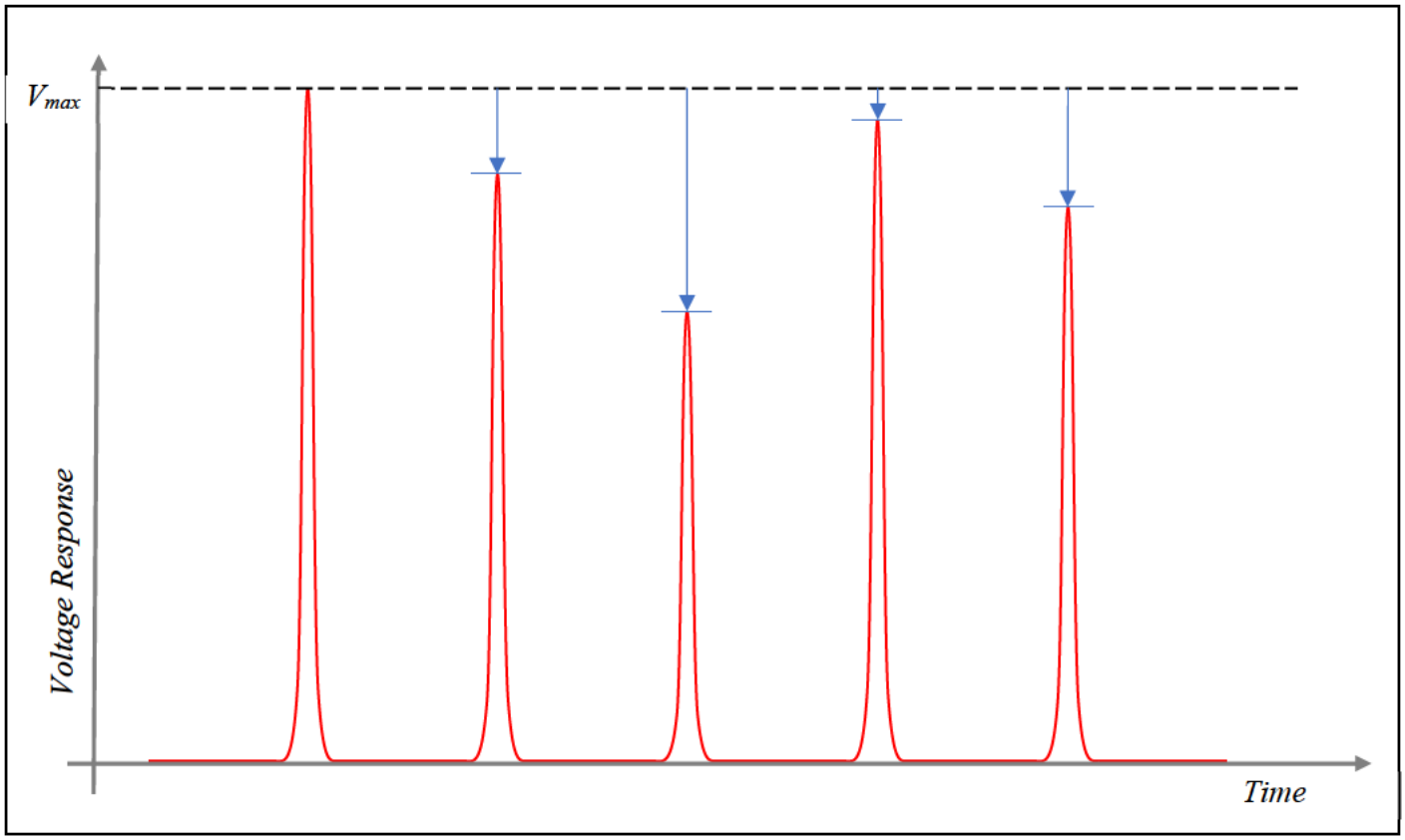

Figure 3.2.1: Example time-domain pulse train trace with random amplitude modulation (RIN) between pulses vs. the maximum recorded voltage response, Vmax.

Timing jitter is another such source of pulse train noise. While RIN describes pulse modulations in intensity, timing jitter describes pulse modulations in time; it is defined as the temporal noise of pulses relative to the laser's repetition rate [3].

This noise exists as a modulation to the pulse timing phase, and thus manifests itself in the radio frequency domain as undesirable sidebands [4]. Physically this arises from quantum effects of the gain medium, optical losses, amplified spontaneous emission (ASE) and thermomechanical disturbances [4].

Note that timing phase and optical phase are linked but not identical quantities [3]. A change in pulse frequency causes a change in GVD, and therefore a fluctuation to timing phase [5]. Furthermore, timing jitter and RIN are also coupled through nonlinear effects such as the Kerr nonlinearity, thus minimising timing jitter also involves minimising RIN [6].

Timing jitter is readily measured in the spectral domain of the pulse train which is discussed further in Section 3.2.3. An example of timing jitter in the time domain is shown in Figure 3.2.2 below.

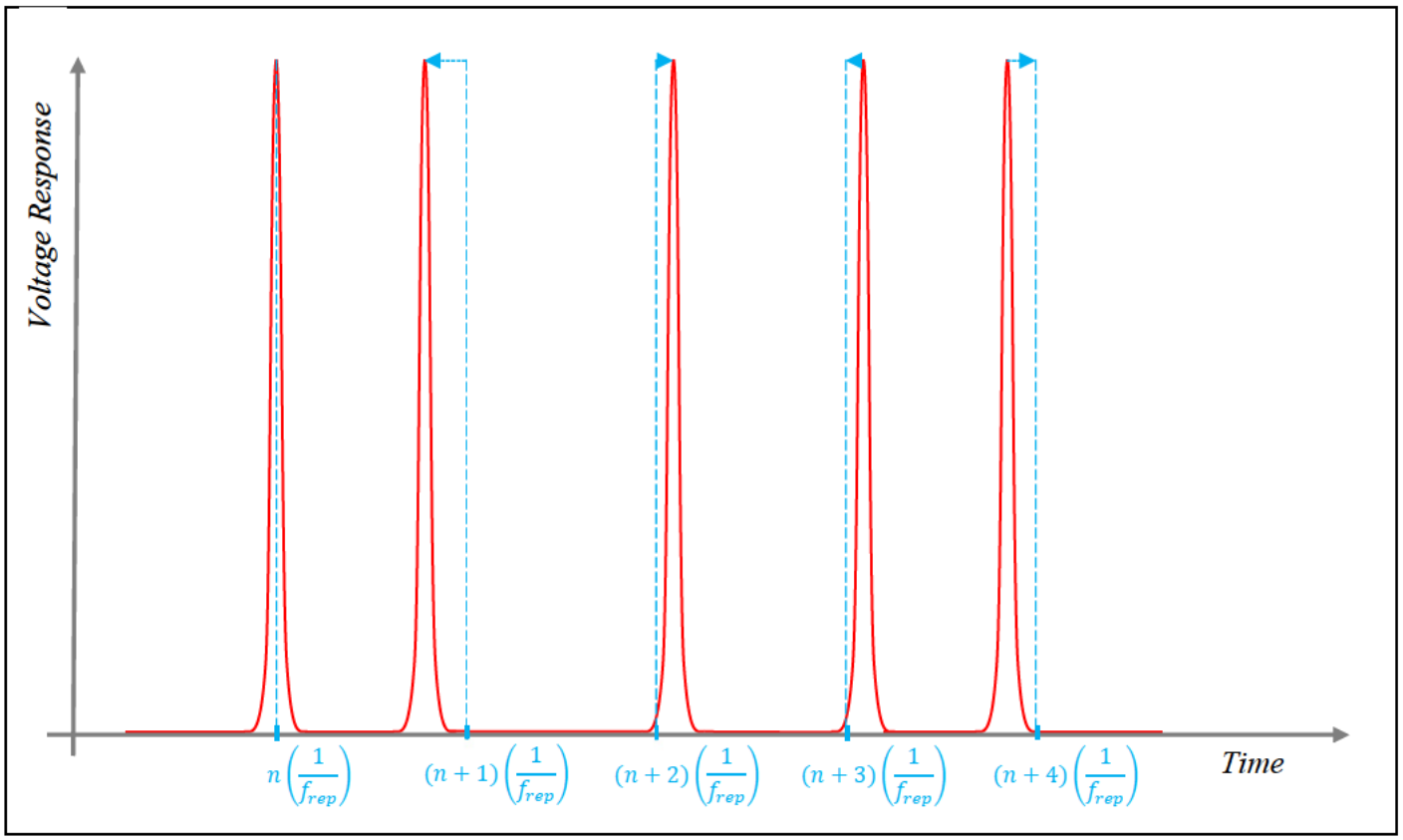

Figure 3.2.2: Example time-domain pulse train trace with random timing jitter between pulses and their ideal timing based on integer n inverse multiples of the pulse rep. rate, f_{rep}.

3.2.2 Oscilloscopes and Photodetectors

Real-time optoelectronic visualisation of the pulse train output of the laser was measured using a DSC-R202-59-FC/APC-K-2 6 GHz bandwidth photodetector. The voltage response signal output was fed to one of two devices via a 50 Ω coaxial cable terminated with 50 Ω for impedance matching:

- RIGOL DS1102E oscilloscope, 100 MHz bandwidth, 1 GSample/s
- R&S-FSP-30 RF spectrum analyser

However, the photodetector is unable to accurately sample the ultrafast (~fs to ps) mode-locked pulse shape due to the limited bandwidth (6 GHz). This is due to the limited response times of available optoelectronic devices [7-9]. However, due to energy conservation it

remains a sufficient tool for measuring RIN and as a simple time-domain check for the operating regime of the laser (see Section 3.3.).

3.2.3 Radio Frequency Spectrum Analyzer (RFSA)

A radio frequency spectrum analyser (RFSA) measures the frequency content of the pulse train signal itself [10]. Under ideal, mode-locked operation, frequencies measured by the RFSA are harmonics of the cavity round-trip repetition frequency [11, 12].

The spectrum produced by the RFSA represents stability in three key ways:

- Decrease of RF power from peak-to-peak over a set bandwidth (e.g. 1 GHz)
- Signal-to-noise ratio (SNR) of the fundamental repetition frequency
- Sideband noise (timing jitter)

The decrease (or 'roll-off') of RF spectral power with increasing frequency represents the overall stability of the pulse train, the frequency at which the spectral RF power decreases by 3 dB being a benchmark for the bandwidth/Q-factor for pulse train stability in the RF domain, or equivalently, a measured RF roll-off over a set bandwidth [13, 14]. This project considers roll-off over a span of 1 GHz in the RF PSD.

Recall that the Fourier transform of a delta comb in time is another delta comb in the frequency domain, thus a similar transform applies for a pulse train [15]. However, ultrashort pulses have finite width on the order of pico or femtoseconds. This finite width transforms to the frequency domain as an intrinsic envelope (or 'roll-off) over a frequency span proportional to the inverse of the pulse duration [16]. However, this roll-off is on the order of μdB for a span of 1 GHz for a train of picosecond pulses and is thus negligible compared to instabilities.

Additionally, noise performance is also characterised by considering the SNR of the fundamental repetition-rate frequency in the RF spectrum. This is obtained by considering a narrow span about the fundamental frequency and measuring the difference (in dB) from the fundamental peak power to the largest noise power present and characterises broadband phase noise [17-19].

Lastly, recall that timing jitter in the time domain manifests as harmonic sidebands in the frequency domain [4]. Narrowband (stationary) timing jitter is then readily estimated from these sidebands, with the root mean-square jitter J_{RMS} defined by Equation 3.2.2 [20]:

$$J_{RMS} = \frac{10^{\frac{S}{20}}}{f\pi\sqrt{2}} \quad (3.2.2)$$

where *f* is the carrier frequency (the repetition rate in this context) and *S* is the sideband amplitude. RF PSD data was obtained via photodetector RF output fed to a R&S-FSP-30 RF spectrum analyser, using a resolution bandwidth of 3 kHz and a video bandwidth of 10 kHz. This leads to sweep times (automatically set by the RFSA) on the order of minutes but enables sufficient resolution to measure the spectral content between harmonics (~ MHz apart).

3.2.4 Optical Spectrum Analyzer (OSA)

Optical spectra for the laser output were measured by a Yokogawa AQ6377 Optical Spectrum Analyser. Laser input is delivered by a series of focussing and collimating mirrors and a rotating diffraction grating [21]. By sweeping the grating, the optical analyser scans through the laser beam's spectral content monochromatically to build a full spectrum. The wavelength resolution used in all experiments was 0.01 nm. The optical spectrum reveals several key features of the laser output:

- Spectral bandwidth
    - See different features based on operating regime (see Section 3.3)
    - Calculate time-bandwidth products (TBPs)
- CW components
- Spectral (Kelly) sidebands

There exists a fundamental lower limit to the multiplication of temporal duration and spectral bandwidth, analogous to the famous Heisenberg uncertainty principle, known as the time-bandwidth product (TBP). The TBP provides a unitless measure of how close the pulse is to the compression limit, and therefore the relative amount of chirp, as defined by Equation 3.2.3 [22]:

$$TBP = \tau\Delta\nu \quad (3.2.3)$$

where τ is the pulse time FWHM (duration) and Δν is the FWHM of the optical spectrum. The TBP has a fundamental lower bound set by Fourier theory, equal to a unique quantity depending on the pulse type [22]. Examples of various TBP for different pulse types is shown in Table 3.2.1 [23]:

Pulse	**Functional Amplitude**	**TBP**
Gaussian	$A(z=0,\ t)=\exp\left(-\frac{t^2}{2\tau^2}\right)$	0.4413
Hyperbolic secant	$A(0,\ t)=\operatorname{sech}\left(\frac{t}{\tau}\right)=\frac{2e^{t/\tau}}{e^{2t/\tau}+1}$	0.3148
Lorentzian	$A(0,\ t)=\frac{1}{1+\left(\frac{t}{\tau}\right)^2}$	0.2206
Table 3.2.1: Common pulse types, with their amplitudes and TBP.		

The optical spectrum also reveals structures intrinsically linked to soliton-like propagation. Solitons experience discrete perturbations to nonlinearity and GVD as they propagate through fibre elements in the cavity, in addition to energy loss and gain perturbations [24]. These perturbations cause the soliton to shed energy, which couples into a low power dispersive wave that co-propagates with the pulse.

Since the soliton is much more intense by comparison it experiences high nonlinearity, and a relative phase change develops due to SPM. Certain frequencies between the dispersive wave and the pulse will then be phase matched by this process, whereby frequencies experiencing a relative 2π phase change between successive dispersive waves and the soliton become resonantly enhanced and therefore amplify, manifesting as symmetrical peak pairs in the optical spectrum of the pulse [24, 25]. Kelly sidebands act as an indicator for non-dispersion-managed soliton propagation [26].

3.2.5 Intensity Autocorrelation

The temporal characterisation of any event necessitates an event shorter than itself, the same is true for ultrashort pulses [23, 27]. Optoelectronic instruments offer 3dB bandwidths toward the 100 GHz range at best, thus picosecond and femtosecond pulses must be measured with similarly ultrafast events [28]. One such method to achieve this is to measure the pulse with itself by intensity gating in a nonlinear medium over a variable delay, known as autocorrelation [29].

As shown in Figure 3.2.3, an input pulse is split into two copies at a beam-splitter, where a variable delay is imposed on one copy via a set path length delay. The pulses are focussed to a point inside a nonlinear material to generate an ultrafast response, with mechanisms such as second harmonic generation (SHG), third harmonic generation (THG), self-diffraction being used for generating the overlap response [30, 31].

The typical beam geometry for an SHG intensity autocorrelator setup is shown in Figure 3.2.3 below:

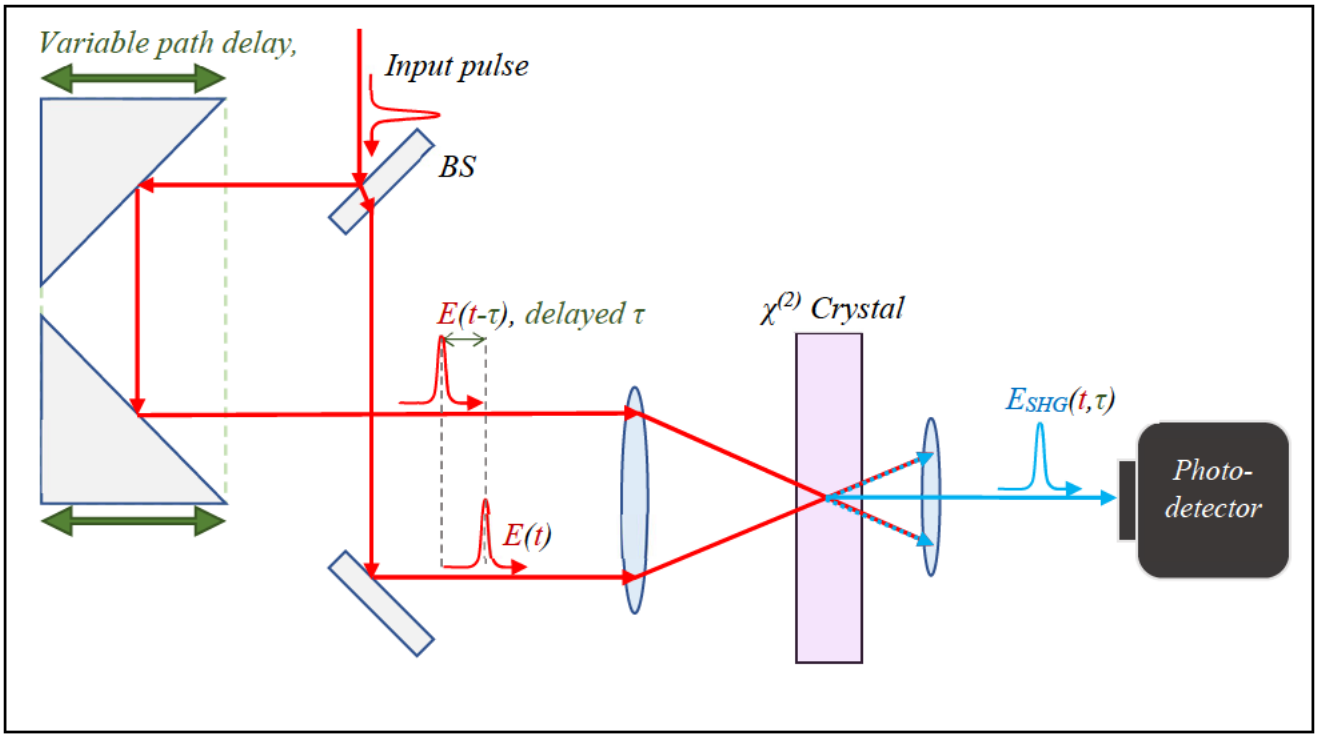

Figure 3.2.3: Schematic of an intensity (noncolinear) autocorrelator.

This intensity-gating in the crystal produces a signal proportional to the overlap of the two pulses, known as the autocorrelation function (ACF) given by Equation 3.2.4 [32]:

$$A^{(2)}(\tau) = \int_{-\infty}^{\infty} I(t)I(t-\tau)dt \qquad (3.2.4)$$

Thus, by varying the delay and recording the intensity for a range of delays, an approximate true pulse width can be determined by only assuming the pulses temporal profile and dividing the autocorrelation FWHM by a shape-related deconvolution factor [33].

However, Equation 3.2.4 does not contain a full description of the pulse's temporal or spectral phase, or even its spectral amplitude, in addition to a trivial ambiguity in the direction of time (symmetrical temporal trace about zero delay) and thus more advanced methods are often employed [34].

Autocorrelation in this project utilises ACF traces as a method to characterise pulse temporal shape and duration.

3.2.6 Fringe Resolved Autocorrelation (FRAC)

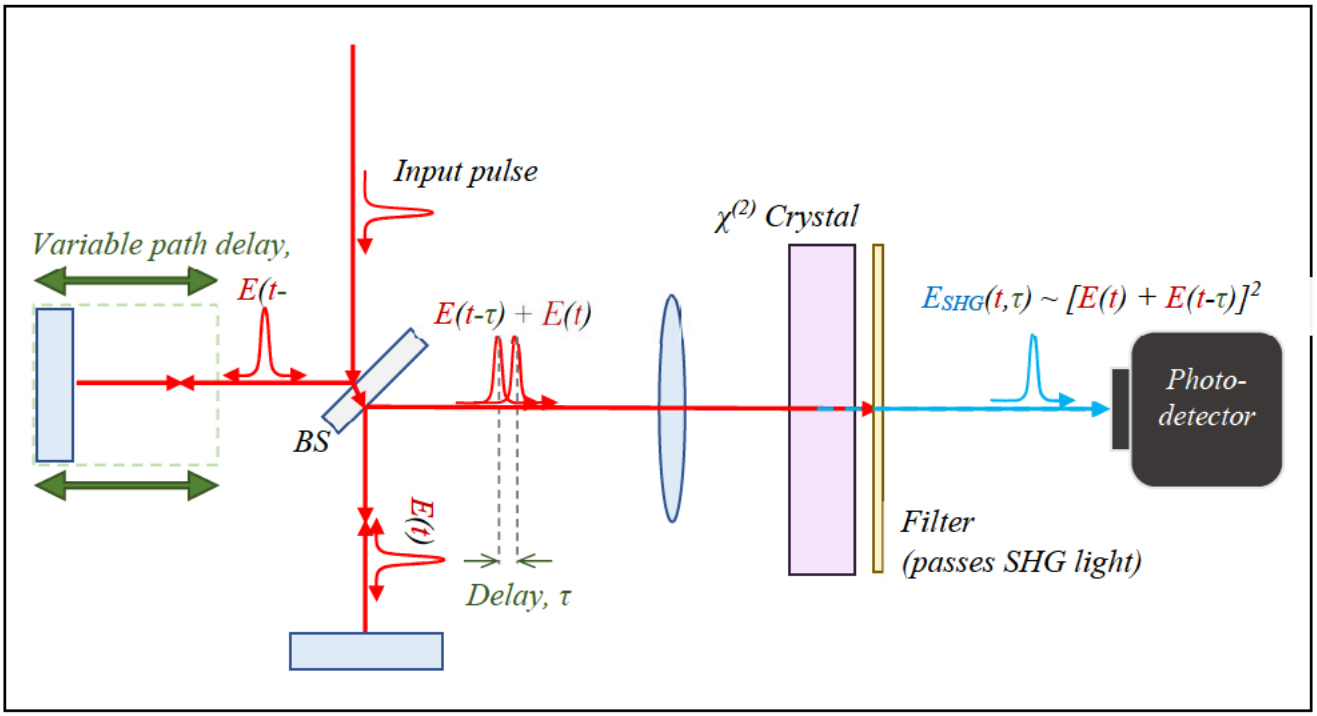

Figure 3.2.4: Schematic of an interferometric (colinear) autocorrelator.

Fringe-resolved autocorrelation (FRAC) instead uses a colinear Michelson interferometer geometry, shown in Figure 3.2.4 As before, an input pulse is split into two copies, one with a variable delay.

However, due to the collinear propagation of the beams from the Michelson interferometer, the SHG signal produced by the two beams interacts coherently with the SHG signal from each beam alone, thus generating a set of interference fringes of both the fundamental (input) frequency and its second harmonic [34].

By obtaining the SHG fringe intensity for each value of variable delay, the fringe-resolved autocorrelation function is obtained in Equation 3.2.5 [34]:

$$I_{FRAC}(\tau) = \int_{-\infty}^{\infty} |[E(t) + E(t-\tau)]^2|^2 \, dt \qquad (3.2.5)$$

$$= \int_{-\infty}^{\infty} [I(t)^2 + I(t-\tau)^2] \, dt + \int_{-\infty}^{\infty} [I(t) + I(t-\tau)] \, \Re\{E(t)E^*(t-\tau)\} \, dt$$

$$+ \int_{-\infty}^{\infty} \Re\{E(t)^2 E^*(t-\tau)^2\} \, dt + \int_{-\infty}^{\infty} I(t)I(t-\tau) \, dt$$

where $\mathscr{R}$ indicates the real component, E^* represents the complex conjugate of the field and τ represents the variable delay.

The first term of Equation 3.2.5 is a constant approximately equal to 8, the second term is proportional to an interferogram of the field amplitude E, the third term represents an interferogram of the 2nd harmonic of E and the fourth term is simply the intensity autocorrelation of the pulse [34].

Thus, the FRAC retrieves parts of the phase information via the interferograms, eliminating some ambiguities of the pulse information obtained [27]. However, FRAC still has trivial time direction ambiguity and no information about the pulse's spectral phase and amplitude, as well as still producing ambiguity of the pulse's temporal phase [35].

While algorithms exist that, in principle, completely solve for the pulse shape, spectrum and chirp based on information from the FRAC, these algorithms fail to converge or are otherwise stiff [27]. Thus, an even more advanced measurement technique is required for full characterisation of a pulse's temporal and spectral intensity and phase. This is discussed further with the introduction of frequency resolved optical gating (FROG) in Appendix E.

FRAC was used for alignment purposes in the experimental work of this thesis due to the sensitivity of the interferometric setup but was not used to produce the autocorrelation data in Chapter 4.

3.2.7 Summary

To summarise, the type of equipment, the model used in the project and its use is outlined in Table 3.2.2 below:

Equipment	**Model**	**Use**
Photodetector	DSC-R202-59-FC/APC-K-2 (6 GHz)	Linear optoelectronic voltage response of laser output
Oscilloscope	RIGOL DS1102E	Voltage/time domain visualisation of photodetector response: RIN characterisation
RFSA	R&S-FSP-30 RF	PSD of photodetector response: timing noise and jitter performance
OSA	Yokogawa AQ6377	Pulse optical spectrum: FWHM and sidebands
ACF	PulseCheck 150 MIR	Time domain pulse-shape reconstruction/measurement
FRAC	PulseCheck 150 MIR	Time domain pulse-shape reconstruction/measurement for alignment

Table 3.2.2: Summary of equipment/methods used in the project.

3.3 Operating Regimes of a Mode-locked Fibre Laser

3.3.1 Introduction

A laser with mode-locking elements can operate in several different regimes, some of which are not mode-locked [36, 37]. This includes continuous wave, q-switched (QS), q-switched mode-locked (QML), multi-pulsed mode-locked (MPML) and 'continuous-wave' mode-locked (CML) operating regimes. Results and characterisation of such regimes obtained with the Ho:fibre mode-locked laser are reviewed in this section.

3.3.2 Continuous-wave Mode-locked (CML)

A continuous-wave mode-locked (CML) laser has axial resonator modes that are continuously driven at constant power such that pulse-to-pulse energy remains constant [38]. Therefore, an ideal CML laser source has minimal RIN.

An measurement of a CML pulse train in the time domain is shown in Figure 3.3.1.

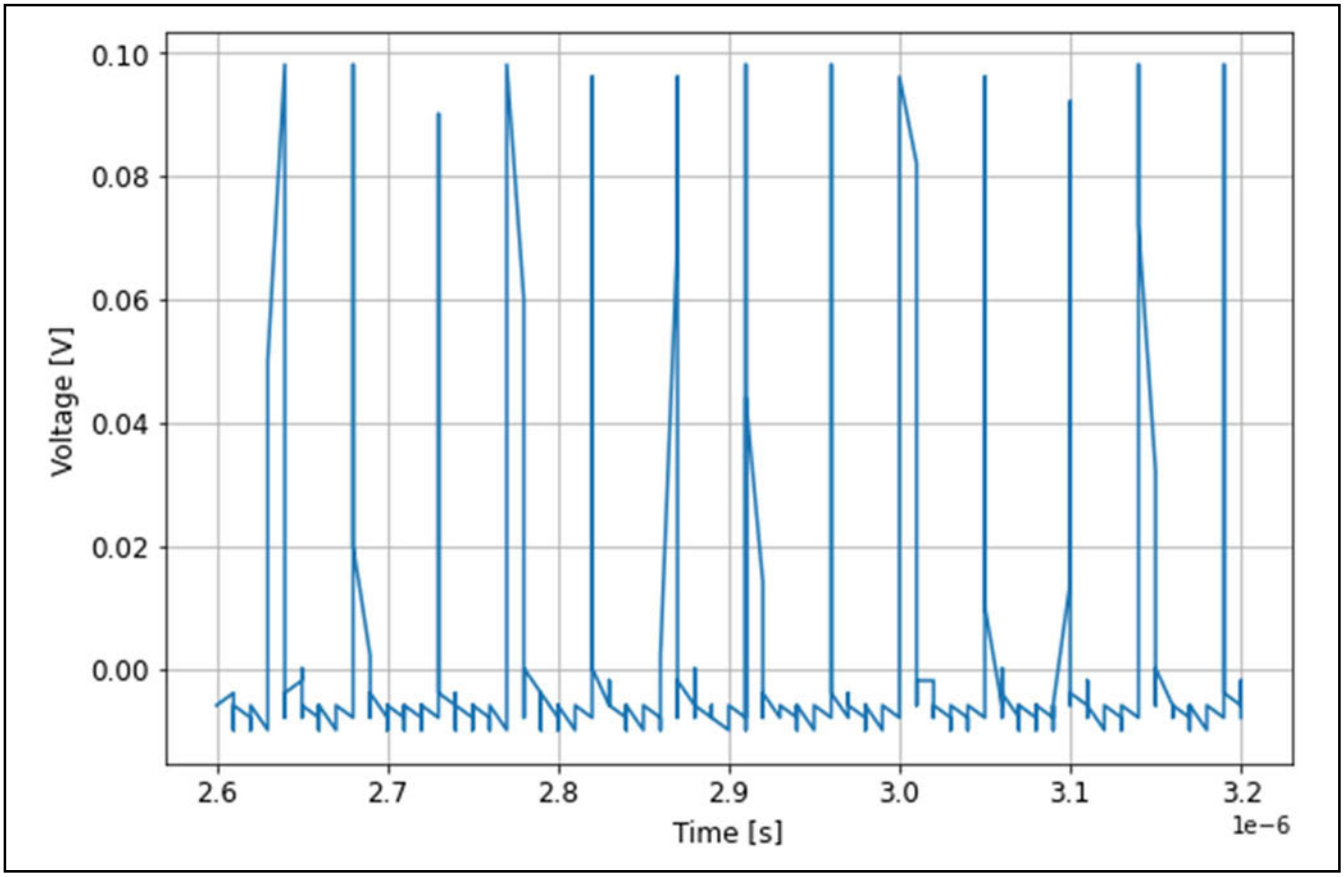

Figure 3.3.1: 1 GSa/s oscilloscope trace of CML laser output measured with a 6 GHz-BW photodetector.

Note that a slight peak modulation is present in the CML trace of ~ 5% due to the sources of RIN discussed in Section 3.2.

An 'ideal' train of ultrashort (delta-like) pulses in time will Fourier transform to a frequency comb, with the frequency of the fundamental peak equal to the repetition rate and the comb being harmonics of the repetition frequency [23]. The repetition frequency of a single-pulse mode-locked ring-cavity laser is given by Equation 3.3.1:

$$f_{rep} = t_{r.trip}^{-1} = \frac{v_g}{l} \qquad (3.3.1)$$

where $t_{r.trip}$ is the round trip time and l is the cavity length. Modulations or instabilities in the time-domain pulse train may manifest as two features in the RF spectrum:

- A relative decrease in power uniformity from peak-to-peak
- A reduced signal-to-noise ratio (SNR) of the fundamental frequency peak

An example RF spectrum measurement of a CML output is shown in Figure 3.3.2 below:

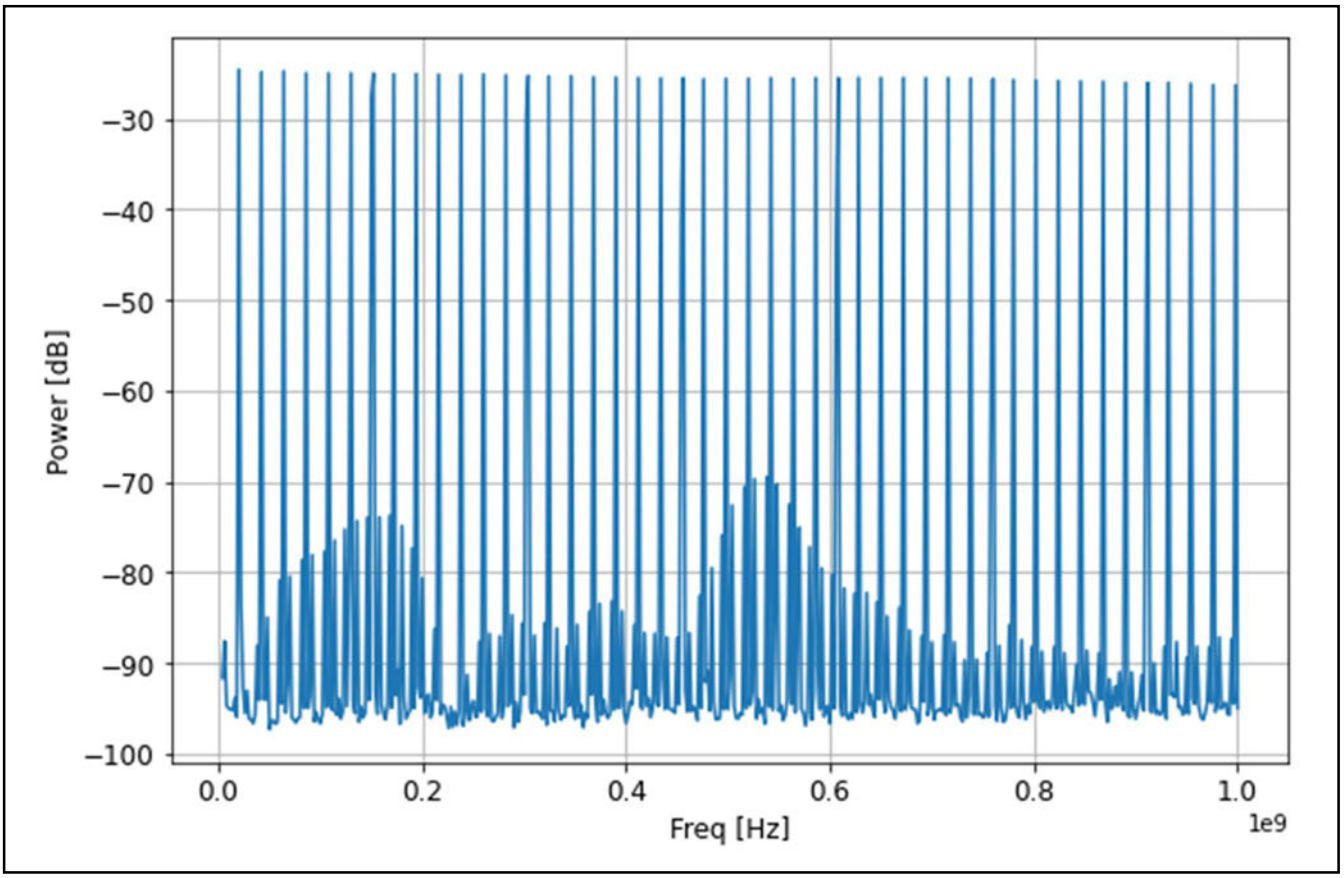

Figure 3.3.2: 3 kHz RBW RF spectrum measurement of CML laser output measured with a 6 GHz-BW photodetector.

The sideband sub-structure at and below -70 dB is due to phase noise as described in Section 3.2. Figure 3.3.1 demonstrates the excellent pulse-to-pulse RIN in a CML regime, showing an RF roll-off of only ~ 2 dB across 1 GHz and a SNR of the fundamental peak of 68 dB.

The optical spectrum of a CML regime is another important indicator of stability as it displays several key features. Firstly, mode-locking requires broad optical bandwidth, with the bandwidth itself necessary to derive a TBP value for the regime. Recall that TBP is a measure of pulse chirp, and therefore the optical spectrum characterises the compression limit (in tandem with an autocorrelation trace) [22].

For a CML regime we expect to see broad spectra on the order of ~ 10 nm wide. An example of a CML optical spectrum is shown in Figure 3.3.3 below, displaying the expected broadband structure, with a 3 dB bandwidth of ~ 4 nm.

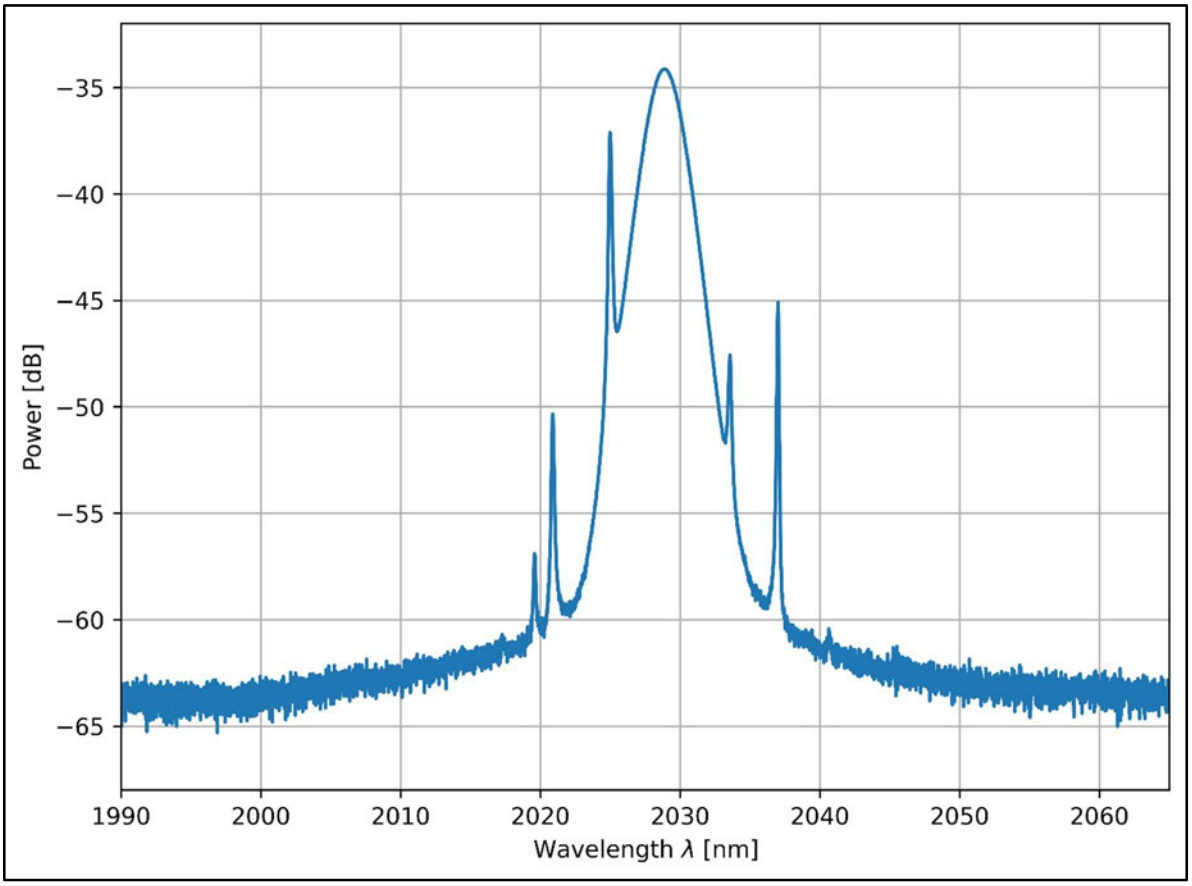

Figure 3.3.3: Optical spectrum of a pulse from a CML pulse train.

Furthermore, recall the presence of Kelly sidebands as an indicator of soliton-like (steady-state) pulse propagation, and therefore laser stability. Such sidebands are visible in Figure 3.3.3, symmetrically spaced about the central wavelength of 2029 nm. Theoretically, these

sidebands are predicted to occur at wavelengths either side of the central wavelength, λ_0, given by Equation 3.3.2 [25]:

$$\Delta\lambda_N = \pm N.\lambda_0\sqrt{\frac{2N}{cDL} - \frac{0.0787\lambda_0^2}{(c\tau)^2}} \qquad (3.3.2)$$

where τ is the pulse temporal FWHM, D is the dispersion coefficient, L is the propagation distance and N is an integer representing the sideband order. For example, Figure 3.3.3 has sidebands up to second order (N = 2).

Lastly, the autocorrelation trace sampled from a CML pulse train is shown in Figure 3.3.4 below:

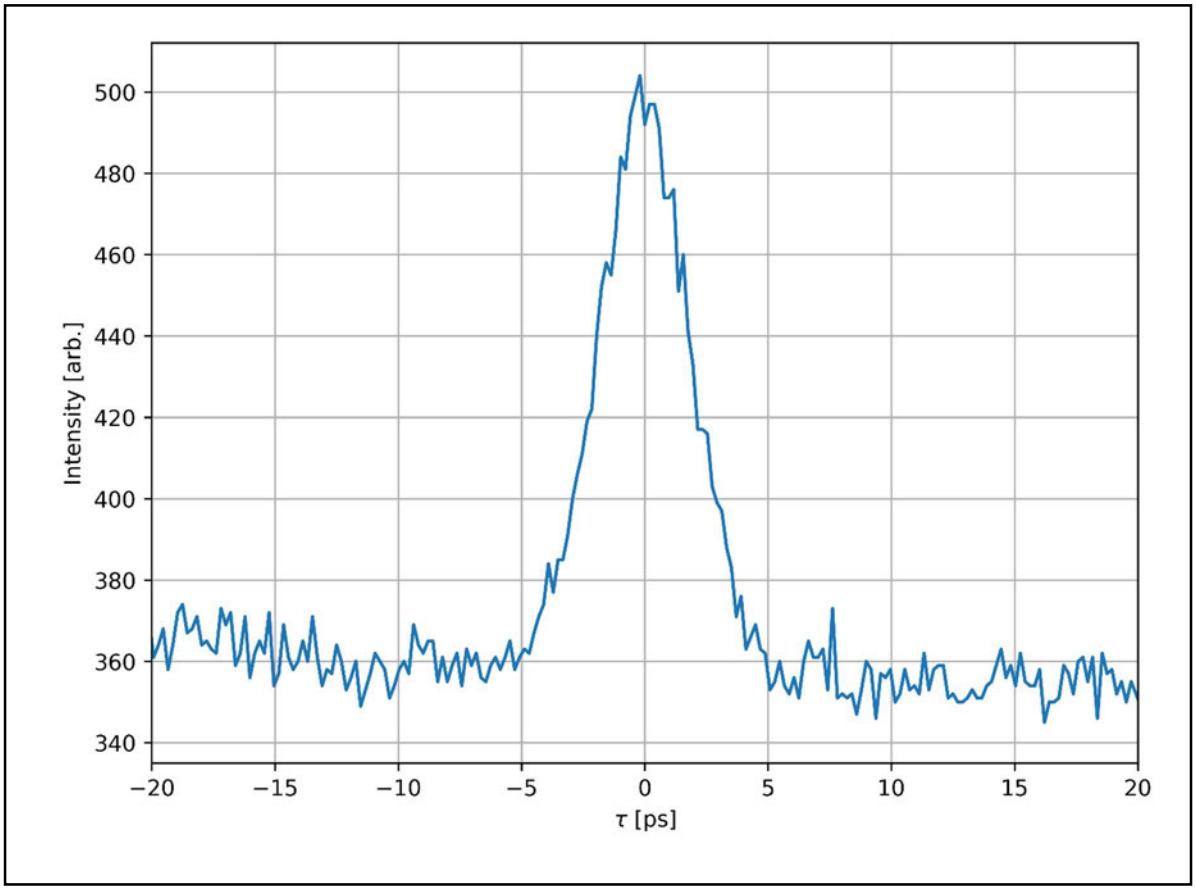

Figure 3.3.4: Intensity autocorrelation of a pulse from a CML pulse train.

Figure 3.3.4 represents the pulse shape of a CML pulse. In the case of soliton-like propagation, recall that this is often a sech^2 pulse intensity given by Equation 2.4.5 [39]:

$$I(t) \sim sech^2\left(\frac{t}{\tau}\right) = \left(\frac{2e^{\frac{t}{\tau}}}{e^{\frac{2t}{\tau}}+1}\right)^2 \qquad (2.4.5)$$

Recall that for sech^2 pulses the true pulse duration is 0.647 times the ACF FWHM due to the inherent convolution integral performed for an autocorrelation (0.647 is known as the deconvolution factor for a sech^2 pulse) [29].

Note that this pulse shape may evolve into a Gaussian depending on the nonlinearity in the cavity, or mode-locking dynamics of the absorber [40, 41]. Nonetheless we look for a symmetric, satellite-free ACF in the CML regime and interpret pulse duration from it.

3.3.3 Q-switched (QS) and Q-switched mode-locked (QML)

It is well known that a SA may act as a passive Q-switch or as a mode-locker [42-45]. Q-switched operation is achieved by the saturable absorption supressing lasing until the gain medium is pumped to a sufficient level, at which point the gain exceeds the loss and a short (~ns) pulse is formed [46]. Systematically, the net result of the SESAM is to undamp relaxation oscillations of the gain with respect to fluctuations in pump power, thus providing the initial instability for Q-switched operation [47, 48]. The threshold intracavity power for this behaviour is given by the Equation 3.3.3 [48]:

$$P^2 > F_{sat,L}F_{sat,A}\Delta R A_{eff,L}A_{eff,A}\left(\frac{1}{T_R^2}\right) \qquad (3.3.3)$$

where P is the average intracavity power, $F_{sat\ L/A}$ and $A_{eff\ L/A}$ are the saturation fluences and effective mode areas of the gain medium and saturable absorber respectively, ΔR is the modulation depth of the absorber and T_R is the round-trip-time of the cavity.

Similarly, QS behaviour may develop into an intensity-limiting envelope over a train of mode-locked pulses, known as QS mode-locking (QML) [47]. For the purposes of this thesis, QS and QML behaviour are considered undesirable effects.

Oscilloscope, OSA and RF traces of a QML regime are shown in Figure 3.3.5.

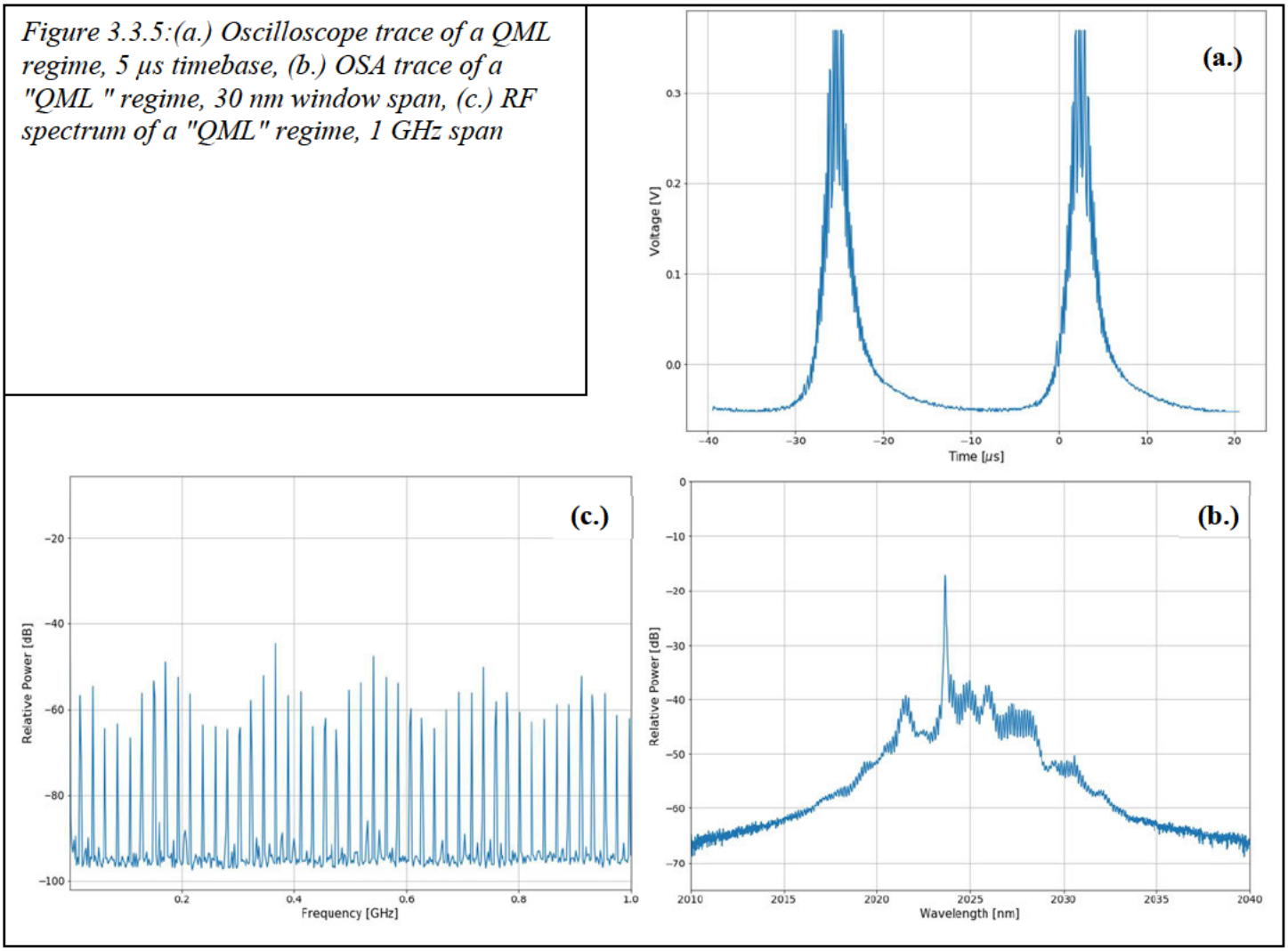

Figure 3.3.5:(a.) Oscilloscope trace of a QML regime, 5 μs timebase, (b.) OSA trace of a "QML " regime, 30 nm window span, (c.) RF spectrum of a "QML" regime, 1 GHz span

Note the sharp, ultrashort peaks under an asymmetric QS pulse shape in Figure 3.3.5a, encompassing ultrashort pulses over multiple microseconds. The effects on the optical spectrum are observed in Figure 3.3.5b,c. In the optical spectrum (Figure 3.3.5b), a narrow peak-like structure forms atop a pedestal. Oscillations in the pedestal structure may arise from SPM [49]. Thus, CML operation is indicated when narrowband, peak-like structures are avoided alongside fringe-like pedestal features seen in Figure 3.3.5b.

Lastly, in the RF domain, periodic 100 MHz oscillations are seen enveloping the harmonic structure, with an SNR of approximately 40 dB. In obtaining an ideal CML pulse train we then seek to avoid a modulating envelope in the RF domain as such structure, as seen in Figure 3.3.5c above, is representative of QS/QML instabilities.

QS and QML instabilities are therefore avoided by satisfying the power threshold given by Equation 3.3.3, which is achieved in practice by:

- Amplifying intracavity energy to above the threshold value
- Minimising losses to ensure the SESAM experiences sufficient fluence given by Equation 3.3.3

3.3.4 Multi-pulse Mode-locked (MPML)

Mode-locking as described in Chapter 2 produces a singular, ultrashort pulse in the cavity, with the fraction of light outcoupled every round trip producing a train of pulses, hence the harmonic spacing being one repetition rate apart in the RF domain. However, there are many such instabilities which can perturb the desired stable, single-pulse operation of a ML laser.

Modulation instability is one such multipulse instability that arises from nonlinear effects in the spectral domain. Recall that in the anomalous dispersion regime, SPM imposes a positive chirp through generation of new frequencies which opposes the negative chirp of the GVD [50]. If these effects exactly cancel such that the imposed phase change on the pulse is zero, phase matching may occur for a number of nonlinear processes. Most notably, four-wave mixing between amplified spontaneous emission and the pulse itself may occur. These new frequency components appear as sidebands in the spectrum, leading to generation of a sinusoidal temporal perturbation which destabilises the pulse such that pulse breakup occurs [50].

In the absence of sufficiently large dispersion and with high peak powers, the Kerr effect also plays a role in destabilising pulses known as self-steepening. Recall that the nonlinear Kerr effect causes a intensity dependent refractive index, and thus propagation speed. This spatio-temporal intensity-velocity coupling means that the most intense part of an optical pulse, the peak, will experience significant retardation (for positive n_2) compared to its wings, thus leading to a relative lagging of the peak toward the trailing edge [51, 52].

The resultant spectral broadening due to SPM at the intense, steep edge broadens the spectrum, where dispersion acts to broaden the pulse. In the absence of dispersive pulse broadening however, this causes the pulse shape to distort into a sharp triangular shape as shown in Figure 3.3.6 below [52].

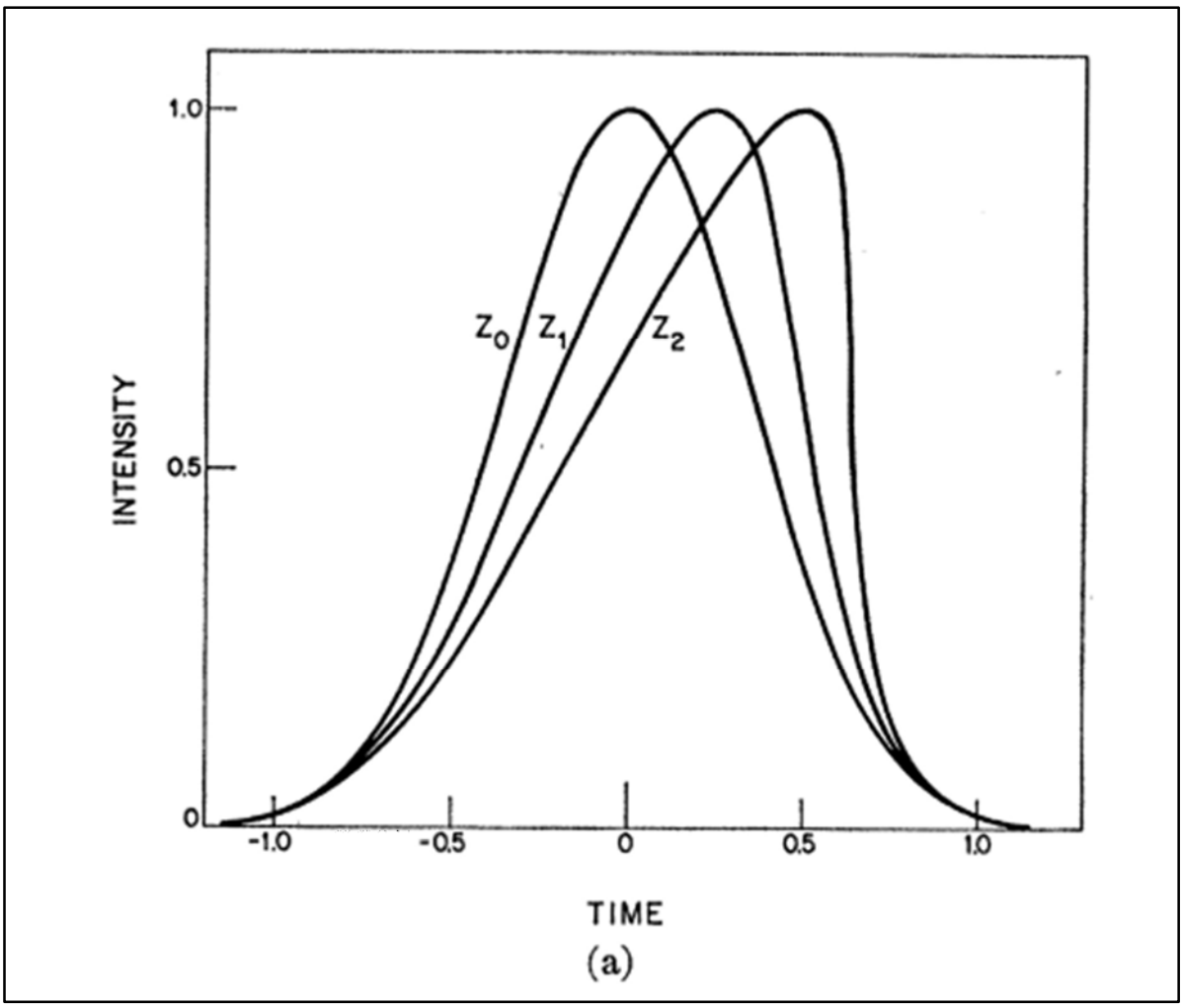

Figure 3.3.6: Pulse temporal intensity profiles after propagating distances z0 < z1 < z2.

Without re-broadening the pulse intensity combined with the K err effect will drive the pulse's trailing edge and cause pulse breakup [53].

Third-order dispersion (TOD) also plays a role for cavity designs close to the zero-dispersion point or with large TOD coefficients. TOD leads to a decrease in the pulse's peak power and the generation of an oscillatory tail in the time domain amplitude [54]. The shape of this tail is well described by an Airy function, and is shown in Figure 3.3.7 below [54].

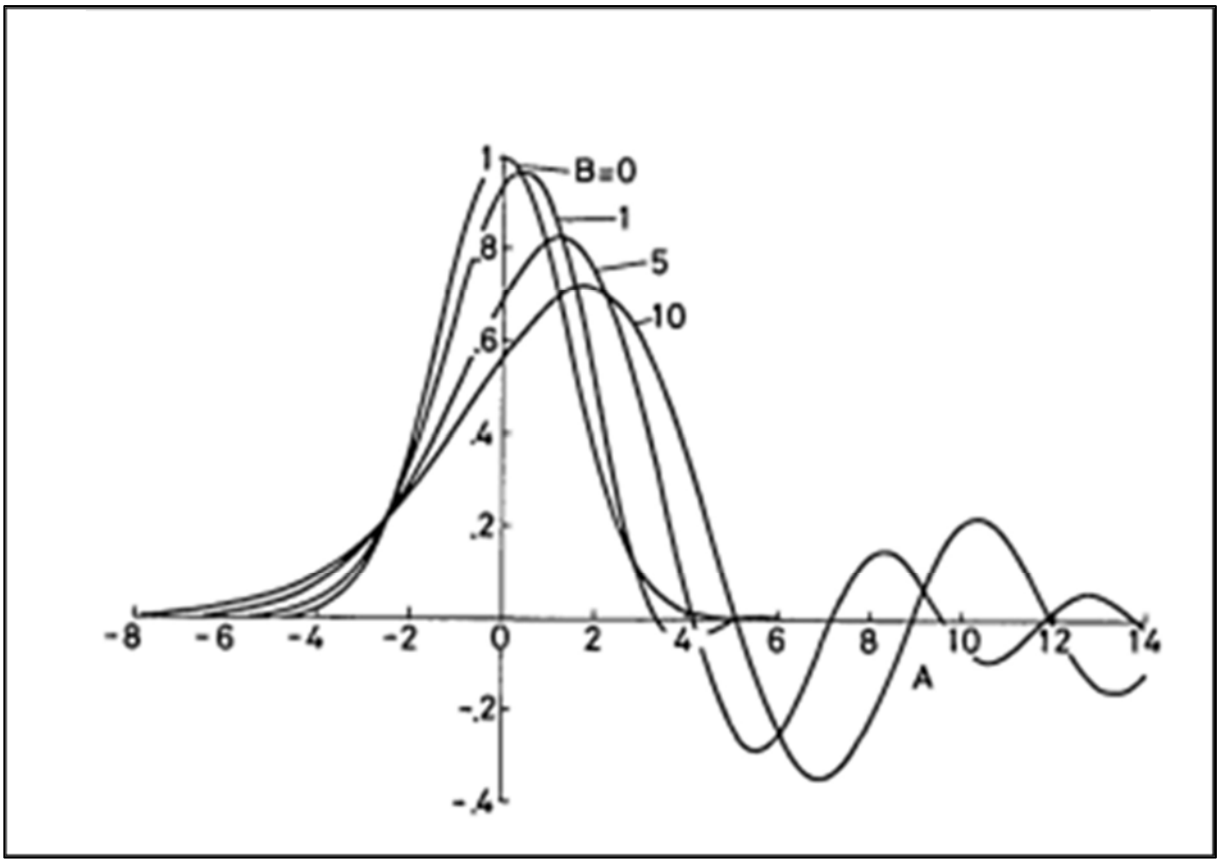

Figure 3.3.7: Propagation model demonstrating the distortion of a pulse's temporal tail into an Airy function due to varying degrees of TOD (B ~ β(3)).

An example of a characterised multipulse operating regime is shown in Figure 3.3.8 below:

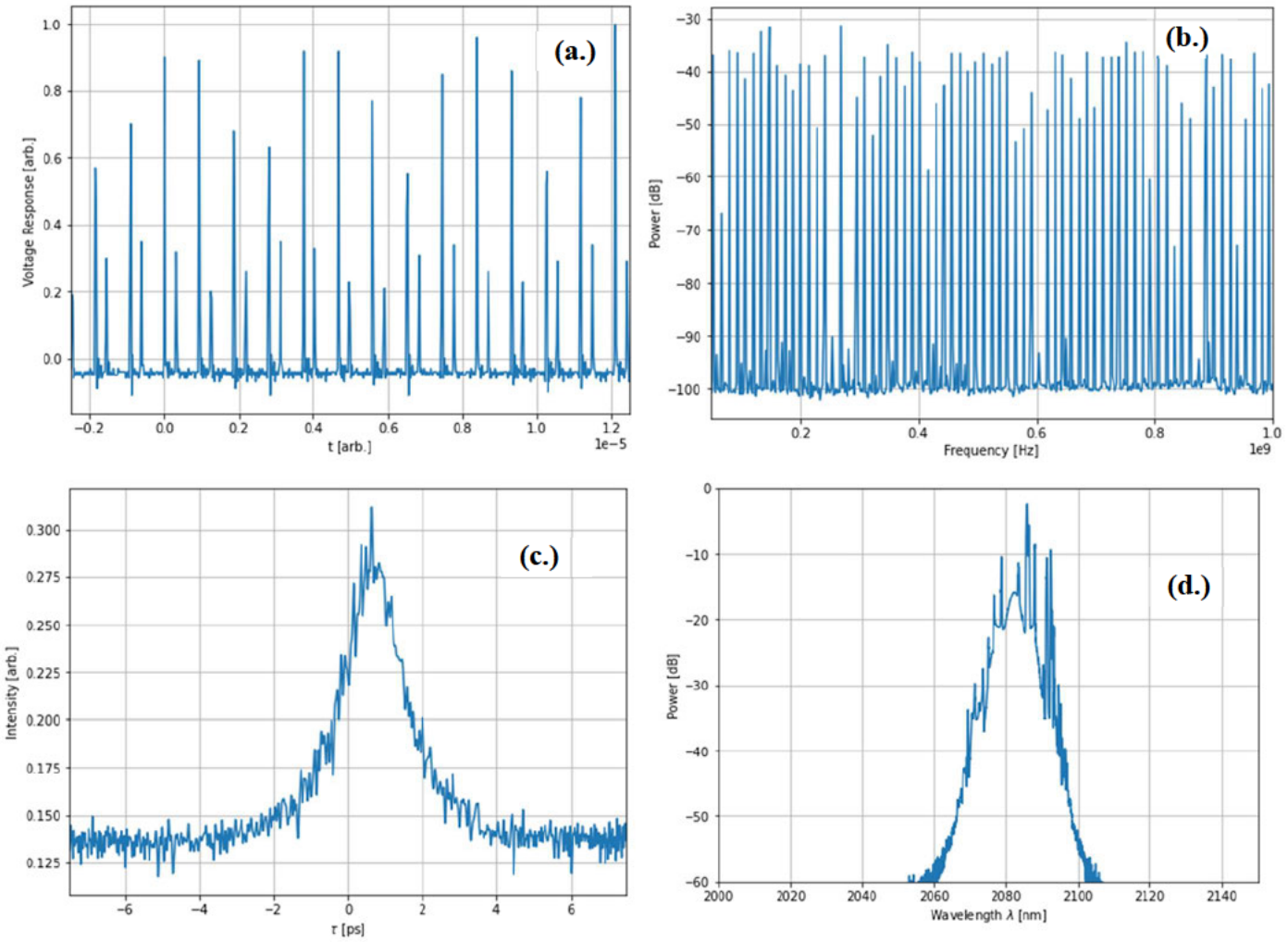

Figure 3.3.8: (a.) Oscilloscope trace, (b.) RF spectrum, (c.) AC trace and (d.) optical spectrum of an MPML regime.

Multipulsing is readily evident from the oscilloscope trace shown in Figure 3.3.8a, whereby a secondary, satellite pulse is observed co-propagating with approximately 20-30% of the main pulse power in addition to extreme RIN of 30%. This manifests in the RF domain (Figure 3.3.8b) as chaotic comb of frequencies with fluctuations from 5 to 60 dB across 1 GHz. Noise sidebands (spurs) are also visible, but with no repetitive structure, indicating the inherent timing instability of the main and satellite pulse.

Figure 3.3.8c displays the ACF trace of this regime, where the primary pulse is seen with several noise-like distortions to the pulse shape along with a CW background.

Lastly, the optical spectrum of this regime is observed in Figure 3.3.8d. The broad structure with overlayed Kelly sidebands familiar to the CML regime remains but contains several sharp distortions. These sharp peaks may represent the Kelly sidebands of multiple quasi-soliton pulses which experience different nonlinearities due to their relative power differences, producing multiple sets of sidebands [55]. Note that the larger, asymmetrical peaks may also represent CW components in the intracavity power [56].

Multipulsing can therefore be avoided by ensuring modulation instability, self-steepening, and higher order dispersion is managed by:

- Keeping pump power low to keep nonlinearity sufficiently low
- Appropriately balancing dispersion (see Chapter 4) to avoid TOD-related oscillations

Chapter 4: Experimental and Numerical Results

4.1 Chapter Layout

Chapter 4 presents the experimental and numerical results, categorised into three parts in addition to a brief literature review of optimising mode-locked sources.

In Section 4.2, a short literature review is provided, exploring the key parameters of a fibre mode-locked laser as explored in the literature. These parameters include dispersion management, cavity design and component arrangement, gain and amplification.

In Section 4.3, seven different preliminary fibre laser designs are presented, with numerical predictions outlining the intent behind each design's architecture with regards to filtering, SESAM saturation and output. Each design is then explored experimentally, with the oscilloscope trace RIN, RF roll-off and SNR, optical FWHM and ACF trace FWHM presented for each design as described in Chapter 3.

Section 4.4, an eighth design presents the first successful cavity design that is used as a basis for the work in Section 4.5, displaying record stability for the project. Again, the numerical predictions of this design are presented along with an experimental demonstration of its performance.

Lastly, Section 4.5 explores optimisation of dispersion compensating fibre (DCF) through both numerical and experimental methods. Numerically, the DCF length is tuned in increments to explore the pulse shaping dynamics that occurs due to the added normal dispersion of the DCF. Experimentally, an estimate is made for the approximate zero dispersion point, and a length of DCF is spliced to the cavity. This length is cut back in increments, with the resulting performance characterised at each length such that an optimum length may be found for either stability or pulse duration. Near net-zero dispersion and pulse stability is achieved through careful characterisation of the experiment.

4.2 Fibre Laser Parameters Review

4.2.1 Preamble

Optimisation of a pulsed fibre laser is a complex multidimensional problem, with efforts focussed on finding optimal parameter regions for characteristics such as gain, dispersion, component (insertion losses and bandwidth) and output power for application purposes [1-7]. In the following section we briefly review both experimental and theoretical insights into key parameters and their optimisation, chiefly: amplification, dispersion management and cavity design.

4.2.2 Dispersion Management

As discussed in Chapter 2, dispersion is a critical parameter to the generation, stabilisation, and propagation of ultrashort and short laser pulses. Not only does the sign of dispersion fundamentally dictate the pulse shaping dynamics, but the absolute quantity also [6, 8]. This is utilised throughout the literature to manage both the temporal and spectral widths of mode-locked laser pulses in cavities, both in fibre and free-space [8-14].

Recall that Chapter 2 discussed the concept of a dispersion compensated fibre (DCF), whereby the waveguide dispersion is tuned according to Equation 2.2.15, with the total dispersion given multiplication with the length of DCF (Equation 2.2.17) [15-17]:

$$D_w = -\left(\frac{1}{2\pi c}\right) V^2 \frac{d^2\beta}{dV^2} \tag{2.2.15}$$

$$D_{net} = D_{SMF} l_{SMF} + D_{DCF} l_{DCF} \tag{2.2.17}$$

The sign and quantity of dispersion is defined by Equation 2.2.15 and is chosen as desired, and the net amount of dispersion is then easily tweaked by altering the length via Equation 2.2.17. Thus, the pulse duration can be managed directly, in addition to optimising the balance of dispersion to support soliton-like pulses in the cavity [13].

4.2.3 Gain and Amplification

Realisation of high average fibre oscillator power continues to drive forward technology in both CW and pulsed fibre systems [18]. This may be achieved by directly designing and manufacturing a fibre with a controlled doping concentration of active ions, or by adopting

alternate pumping and core geometries to further optimise pump absorption in the core [19-21].

More simply, net power scaling is easily adjusted in a controlled fashion by removal of discrete increments intracavity of gain fibre length [20, 21] or by addition of an external single-pass amplification stage connected to the output [20, 22, 23].

4.2.4 Cavity Design and Component Layout

Nonlinear and dispersive evolution of ultrashort pulses leads to drastically different pulse shape, spectra, timing and energy during a single round trip, i.e. operators for different cavity components are generally non-commutative due to the nonlinear dynamics [24-27]. Thus, cavity design involving component choice and the order through which pulses propagate remains an interesting and oft unexplored prospect in the literature. Shtyrina et. al. (2015) thoroughly investigated the importance of ring cavity element order via simulation, finding that pulse energy was maximised by placing the absorber directly after the gain medium, which was followed with an outcoupler [27]. Nady et. al. (2019) report similar results, citing the necessity of high energy fluence on the saturable absorber to saturate it and minimise losses (while still ensuring it isn't oversaturated, etc.) [25].

4.2.5 Other Parameters

Optimisation of fibre parameters is challenging to isolate in practice, as any given change can result in a wealth of changes in nonlinear and linear dispersion effects on the resulting intercoupled pulse dynamics [5, 28]. However, there exist other, largely tuneable methods of further improving pulsed fibre laser output.

Control of passive or active modulation is one such key parameter. For instance, acousto-optic or electro-optic modulators may be used to introduce an active, electronically modulated mode-locking element, capable of introducing further timing and amplitude stability [29, 30]. Alternatively, direct engineering of the parameters of the passive mode-locking element (SESAM) itself during manufacture is possible given the appropriate manufacturing capability and facilities to do so [31-33].

Lastly, outcoupling fraction is a key parameter that has interesting applications for both intracavity energy and the average output power of the oscillator [7]. As the nonlinear effects

are driven by the intensity of the pulse, decreasing or increasing the outcoupling fraction provides a controlled, fractional change in nonlinear phase for the pulses. Spectral bandwidth and filtering also play a critical role in suppression of dissipative soliton sidebands, stability, and desired spectral purity [34, 35].

These methods, however, fall outside the scope of this project and are discussed as future prospects in Chapter 5.

4.3 Fibre Cavity Design

4.3.1 Overview

To design a mode-locked fibre ring laser, the splicing, order and number of fibre components in the ring cavity is crucial to optimising the pulsed output parameters. As alluded to in Section 4.2, several studies have indicated the importance of non-averaged pulse (soliton) dynamics in mode-locked cavities [24-27]. Thus, it is imperative that various arrangements of WDMs, circulators, SESAMs and additional gain fibre, with bi-directional pumping schemes are investigated to find an optimal arrangement.

Note that pump power was driven at a constant ~1000 mA across all pump diodes used for consistency resulting in approximately 300 mW 1150 nm output.

The most stable design, not included here, is presented in Section 4.4, serving as the basis for the experiments carried out in Section 4.5. A single-pass amplifier stage was also designed and used for obtaining sufficient optical power for characterising the lasers in this chapter. The design of the amplifier is discussed further in Section 4.4.

Every cavity investigated was built in a ring cavity configuration using several components, as listed below.

Firstly, a polarization-maintaining (PM) circulator circulates intracavity power to the SESAM, as described in Section 2.2. The SESAM used for each design is a fibre-coupled BATOP GmbH SAM-2000-30-10ps-25.4g SESAM, with a recovery time $\tau \sim 10$ ps with a modulation depth of ~ 18% and an operating bandwidth of 1910 - 2080 nm.

A 25% 2100 nm broadband splitter outcouples a fraction of the energy to be observed at the output.

Lastly, 1150/2000 nm wavelength division multiplexers (WDM) are used for one of two purposes: to couple 1150 nm pump diode light into the cavity for gain pumping, or for use as an additional intracavity spectral filter (i.e. with the 1150 nm port terminated). According to the manufacturer, the transmission spectrum of the 2000 nm port has a Gaussian spectral profile with a bandwidth of 40 nm, plotted in Figure 4.3.1 below [36]:

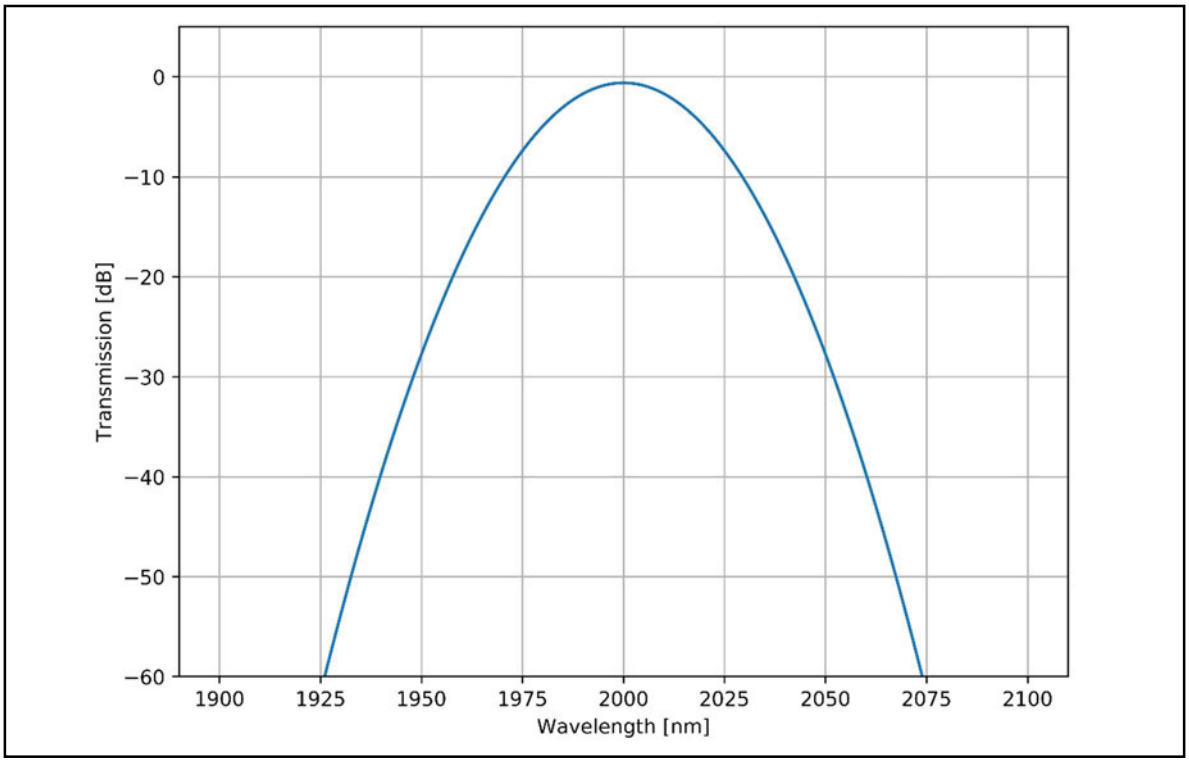

Figure 4.3.1: Transmission spectrum of the 2 μm port of the WDMs used in the experiment.

4.3.2 Design and Numerical Modelling

Eight total designs were considered for the ring cavity, with the least stable seven presented in this section. Figures 4.3.2a. through 4.3.8a. show the schematic for each design consisting of a unique arrangement of components, where 4.3.2b,c,d to 4.3.8b,c,d show the numerical models predictions for each design. Numerical modelling is done via the model discussed in Section 2.6 using a Runge-Kutta interaction-picture MATLAB script from Appendix D. Appendix F contains a short discussion to justify the parameters used in the simulation along with relevant calculations not contained in Appendix D.

Simulation results of each design for the second to six-hundredth round trip are available in Appendix G in Figures G.1 – G.8. While we are interested in the steady state performance of each design, the transient, pulse-shaping behaviour of the laser is nonetheless interesting.

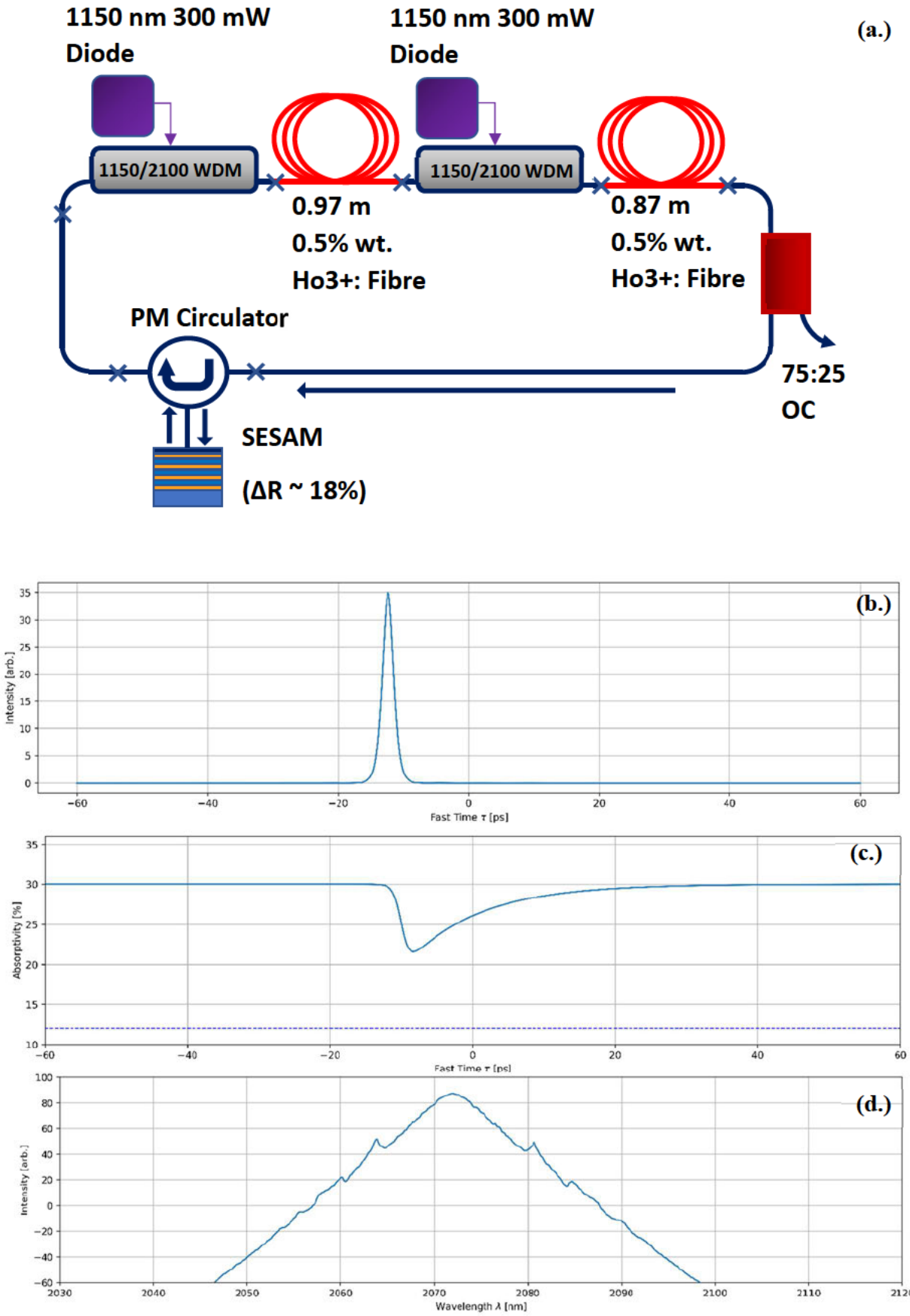

Figure 4.3.2: (a.) Schematic of Design #1, (b.) time domain trace, (c.) SESAM absorptivity profile and (d.) optical power spectrum after 600 round trips.

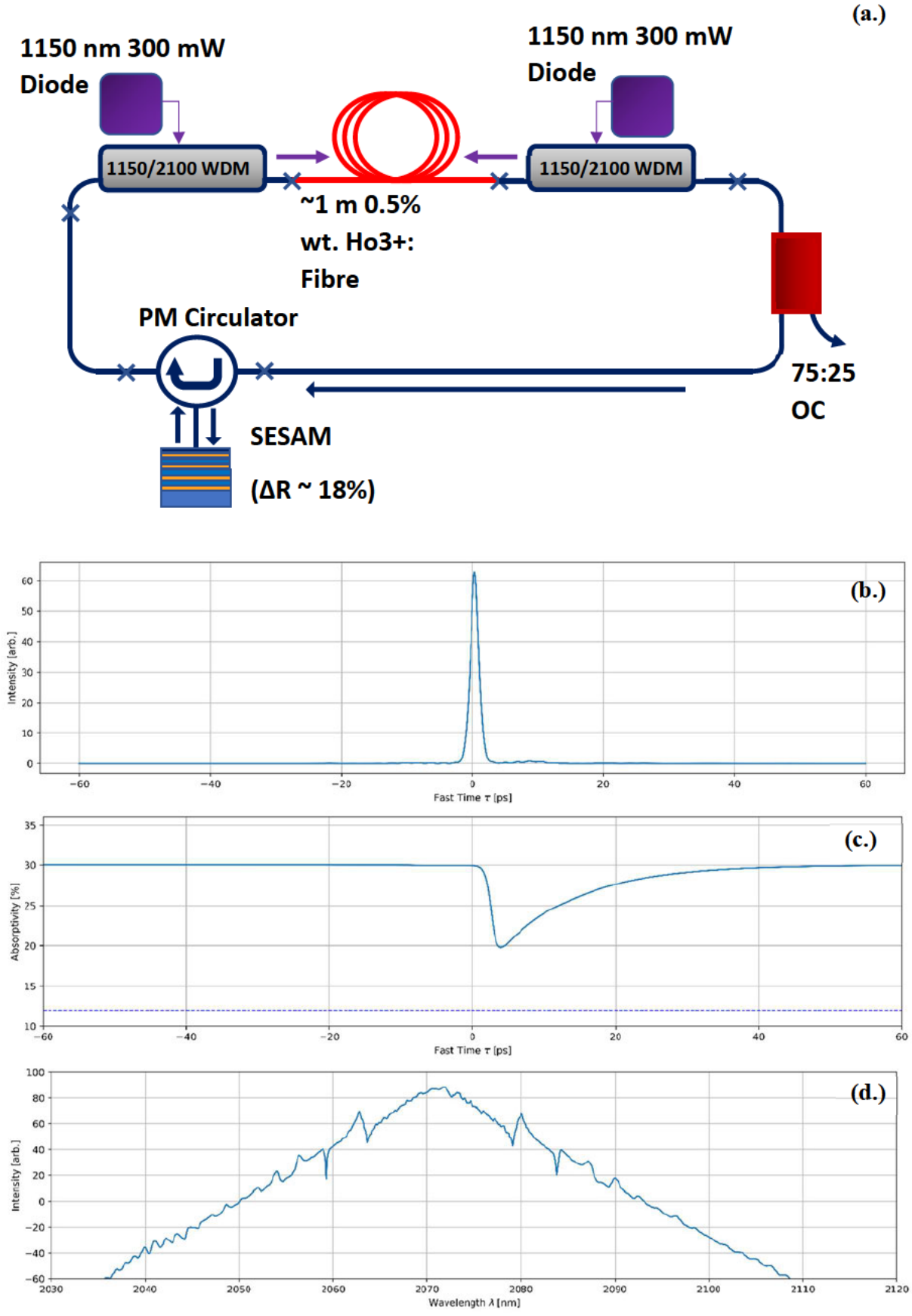

Figure 4.3.3: (a.) Schematic of Design #2, (b.) time domain trace, (c.) SESAM absorptivity profile and (d.) optical power spectrum after 600 round trips.

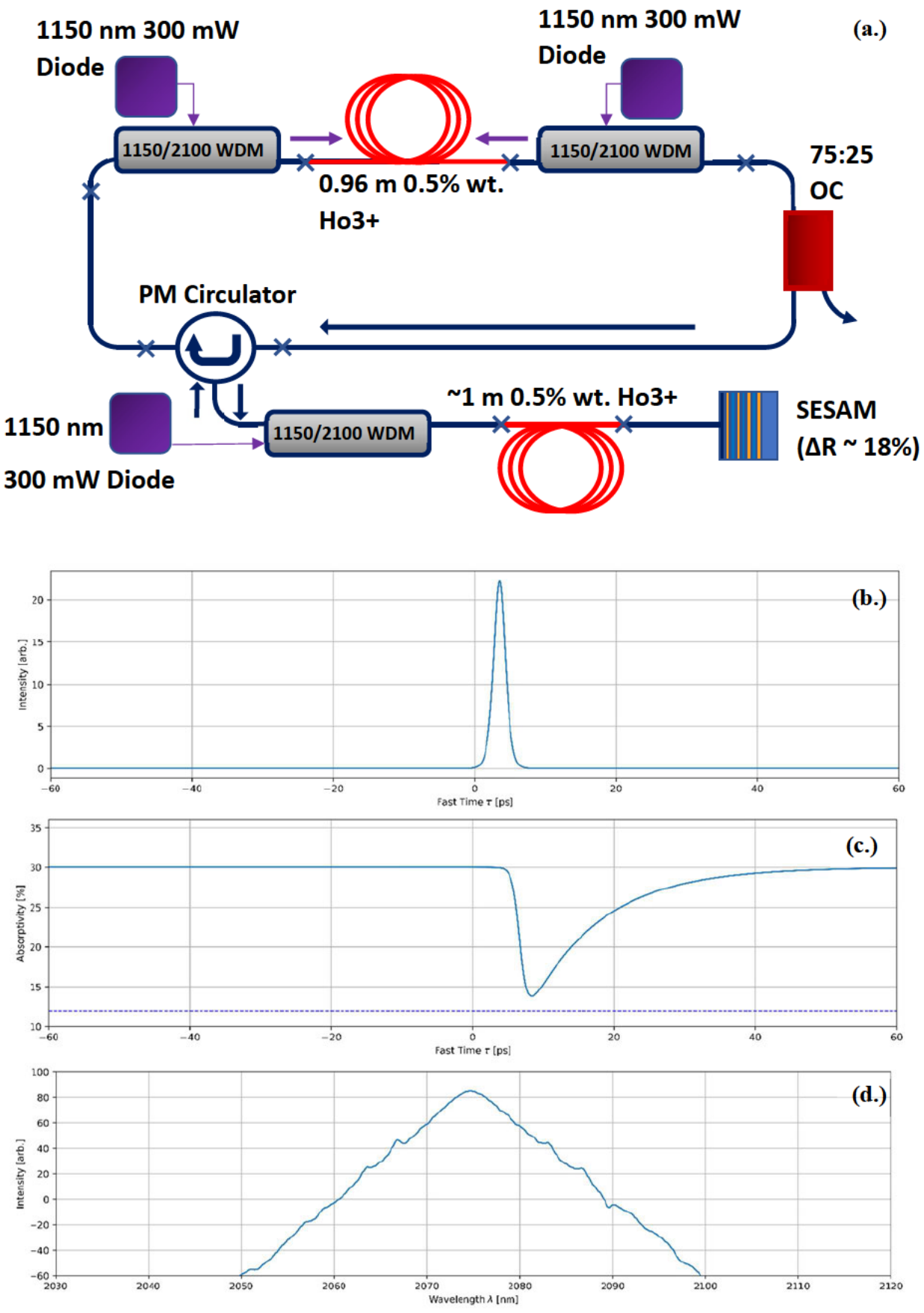

Figure 4.3.4:(a.) Schematic of Design #3, (b.) time domain trace, (c.) SESAM absorptivity profile and (d.) optical power spectrum after 600 round trips.

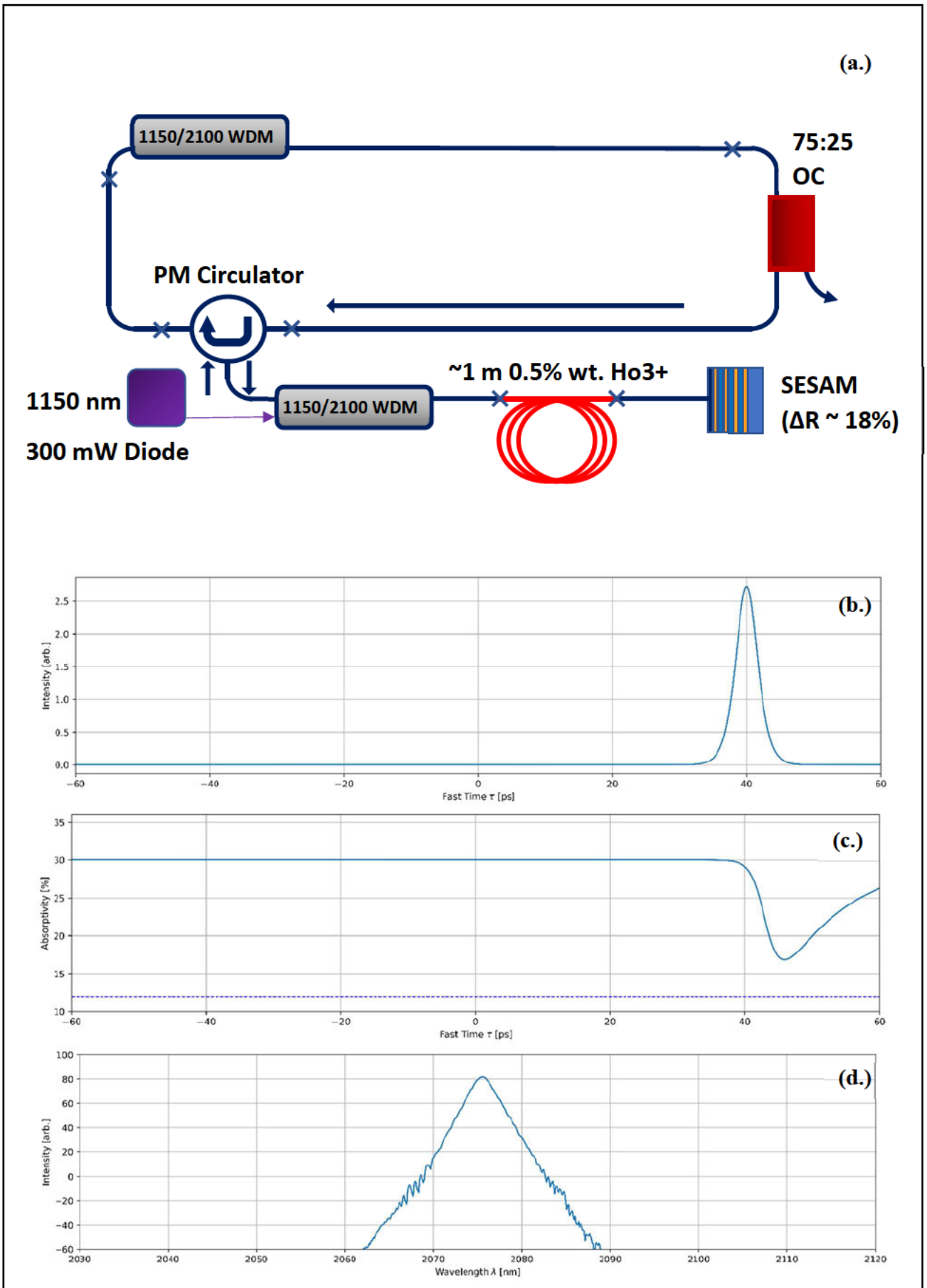

Figure 4.3.5: (a.) Schematic of Design #4, (b.) time domain trace, (c.) SESAM absorptivity profile and (d.) optical power spectrum after 600 round trips.

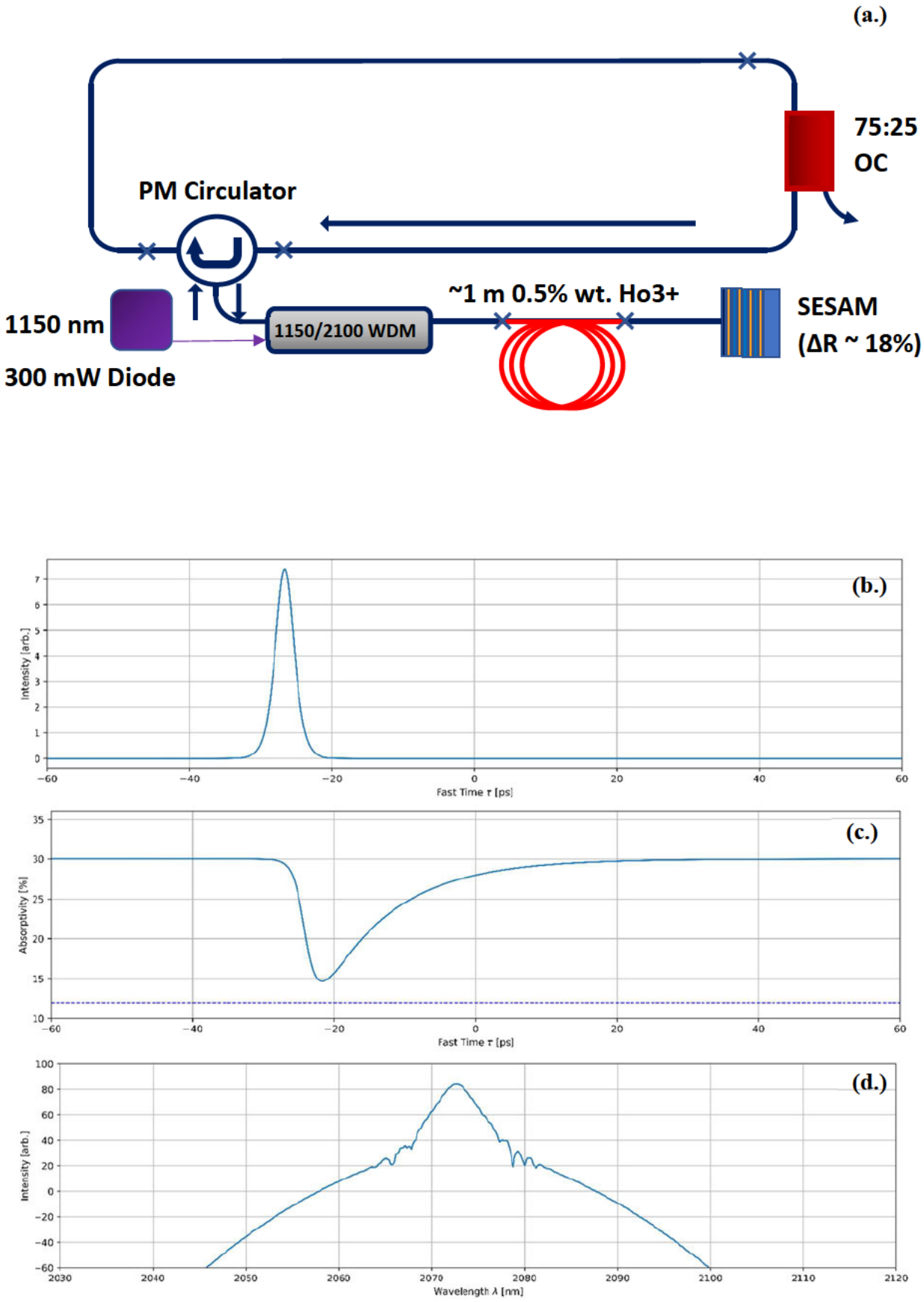

Figure 4.3.6: (a.) Schematic of Design #5, (b.) time domain trace, (c.) SESAM absorptivity profile and (d.) optical power spectrum after 600 round trips.

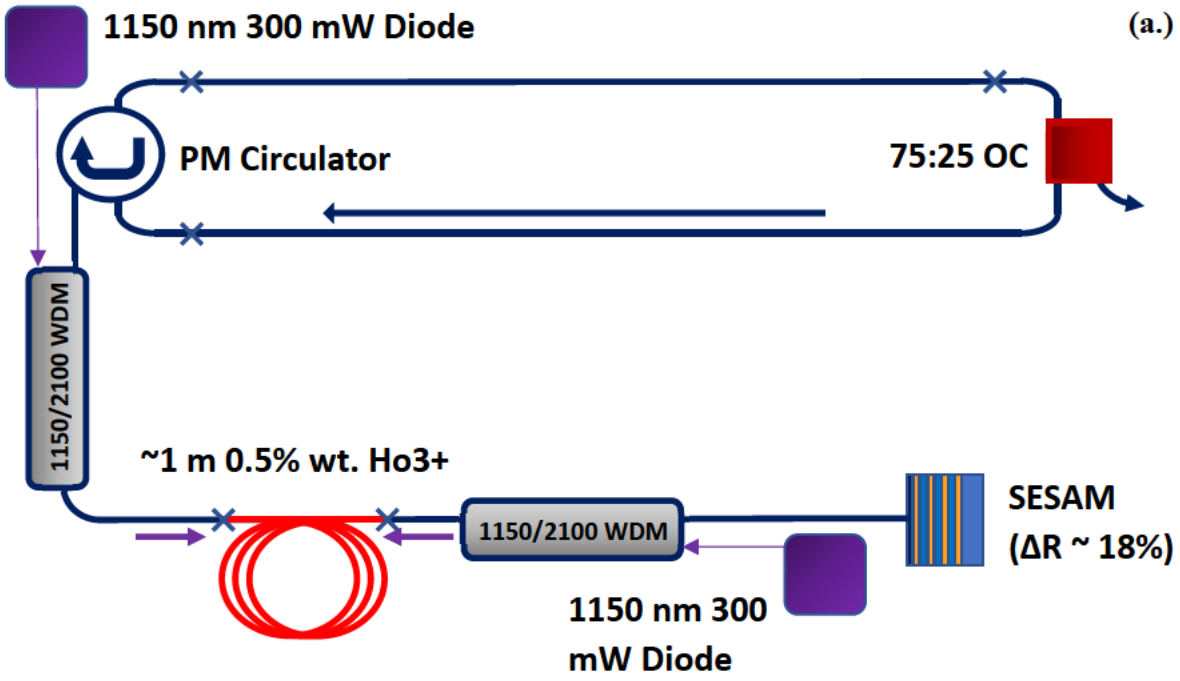

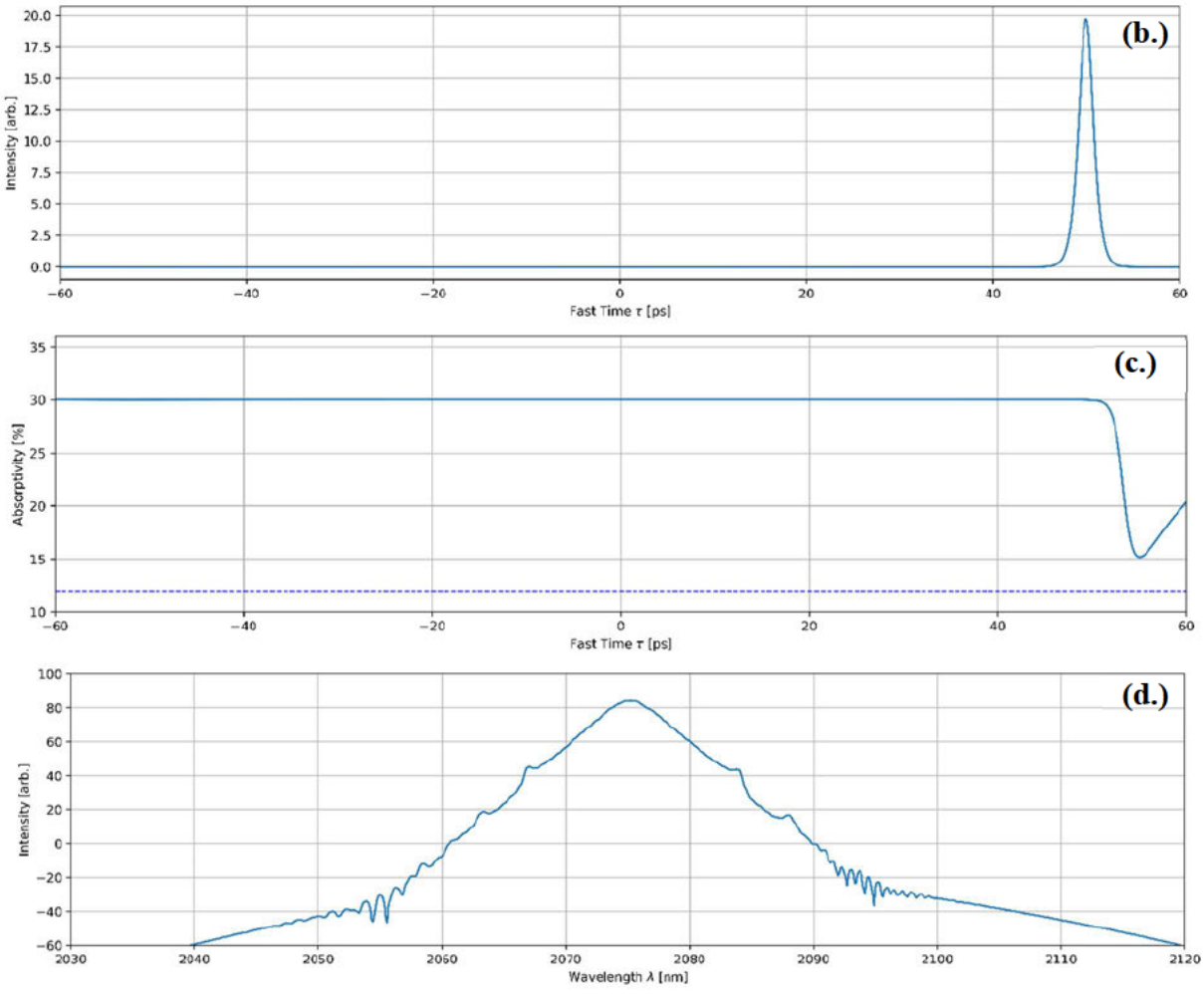

Figure 4.3.7: (a.) Schematic of Design #6, (b.) time domain trace, (c.) SESAM absorptivity profile and (d.) optical power spectrum after 600 round trips.

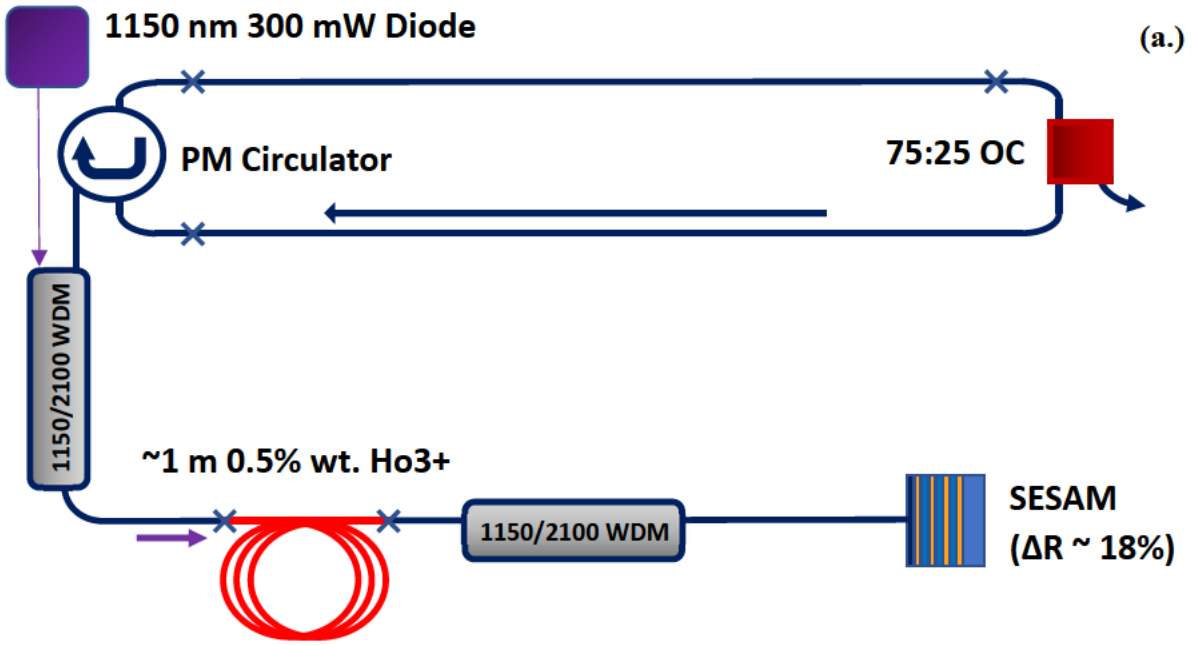

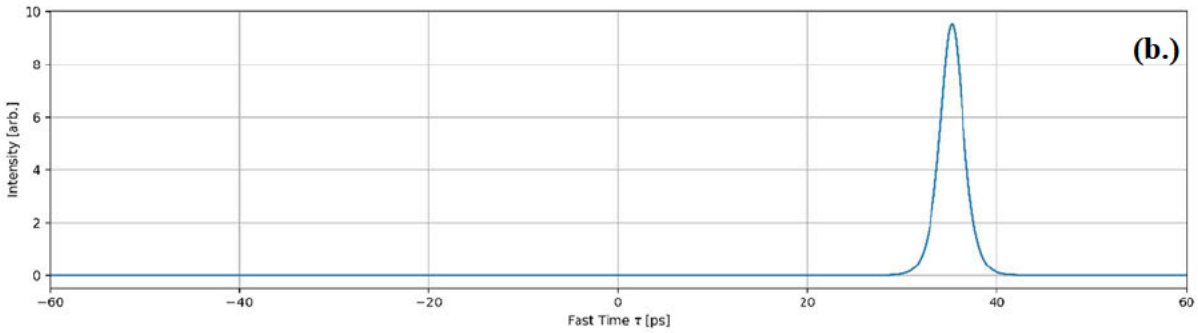

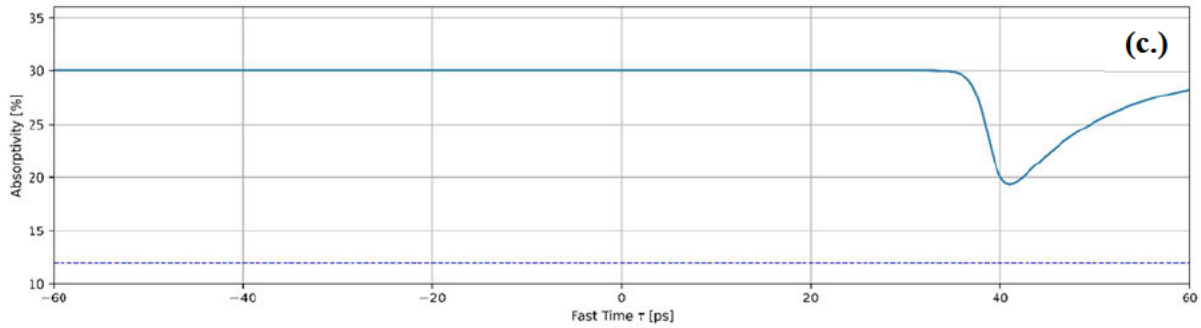

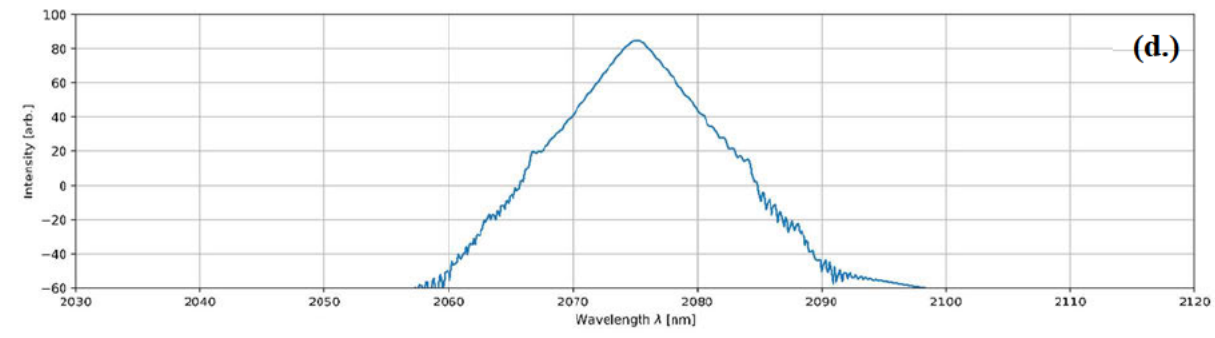

Figure 4.3.8: (a.) Schematic of Design #7, (b.) time domain trace, (c.) SESAM absorptivity profile and (d.) optical power spectrum after 600 round trips.

Design 1 aimed to increase intracavity power in the main loop outside of the circulator by providing two gain passes for each cavity round trip, with the schematic shown in Figure 4.3.2a. Simulation results predict a pulse duration of ~2.01 ps (Figure 4.3.2b.) and a spectrum centred near 2070 nm featuring symmetrical sidebands (Figure 4.3.2c.). SESAM saturation is predicted to reach ~21.6% shown in Figure 4.3.2d., indicating that the laser operates at but not far beyond the saturation fluence (1/e) of the SESAM's full modulation depth of 18%. No satellite pulses are predicted for this design.

Design 2 was an alternative design to utilise only one gain fibre, with a bi-directional pumping scheme to achieve higher intracavity power by further extraction of the gain, with the schematic shown in Figure 4.3.3a. The simulation of the time intensity domain in Figure 4.3.3b. predicts that the intracavity power, and thus nonlinearity allows for pulse compression down to 1.48 ps, the shortest predicted time of any design. However, this comes with an added instability visible in both the time and spectral domain (Figure 4.3.3c.), with a small satellite pulse appearing on the trailing edge, with small distortions growing in the spectrum in addition to the familiar pair of sidebands. SESAM saturation reaches 19.8% for this design (Figure 4.3.3d.), implying slightly more SESAM saturation as desired, but still insufficient for near full saturation.

Design 3 was designed similarly to Design 2, but with an additional segment of singly pumped gain fibre before the SESAM in order to increase the saturation toward 12%. The simulations show that this results in a singly pulsed operation shown in Figure 4.3.4b due to the higher saturation of the SESAM in Figure 4.3.4d. (at 13.81%, almost fully saturated). Taking steps to implement a fully saturated SESAM is desirable for obtaining shorter pulses but may prove difficult in practice due to component and gain limitations [37].

Designs 4 and 5 are nearly identical, and are both variations of Design 3, the key difference being removal of the gain fibre within the main ring cavity loop. Design 4 uses an additional WDM in the loop for the purposes of spectral filtering, shown in Figure 4.3.5a. Design 5 does away with this WDM, shown in Figure 4.3.6a. As expected, slightly less saturation is achieved as a result of reducing the overall gain in both cases (Figures 4.3.5d., 4.3.6d.), resulting in minimum SESAM absorptivities of 16.8% and 14.6% respectively. As expected, the net effect of the additional filter WDM in Design 4 results in additional clipping of spectral content in the wings, leading to a more narrowband spectrum in Figure 4.3.5c, whereas this lack of additional filtering in the main loop allows Design 5's output to feature

broader spectral wings shown in Figure 4.3.6c. In both cases no multi-pulse structures are observed.

Design 6 takes the bi-directional pumping scheme of 1 m of gain fibre ala. Design 2 and places it before the SESAM. The predicted result is 1.85 ps pulses, shown in Figure 4.3.7b. As desired, this design allows for higher saturation of the SESAM, down to ~ 15.2 % absorptivity as shown in Figure 4.3.7d. Again, single pulse operation is obtained, and the spectrum shows only minor distortions out toward 2050 nm and 2090 nm, with a broad spectrum centred around 2075 nm.

Design 7 uses the same architecture as Design 6, but with only a singly pumped scheme, with the second WDM serving as a filter. Interestingly, the time domain output of this design is predicted to be 2.83 ps, a full picosecond longer than that provided by the dual pumping scheme of Design 6. Similarly, the reduction in intracavity power due to only using one pump results in only a minimum of 19.4% SESAM absorptivity. The resulting spectrum is similarly centred about 2075 nm as shown in Figure 4.3.8c., and analogously to Designs 4 vs. 5, the filter WDM serves to narrow the spectrum content significantly, specifically in the wings.

4.3.3 Experimental Results

The ring cavities shown in Figures 4.3.2a – 4.3.8a were constructed using a FITEL s153 fusion splicer, with estimated splice losses kept to 0.01 dB and below. Components were chosen with matching MFD of ~ 7.4 μm. The resulting oscilloscope trace, RF spectrum, intensity autocorrelation and optical spectrum are shown in Figures 4.3.9 – 4.3.15.

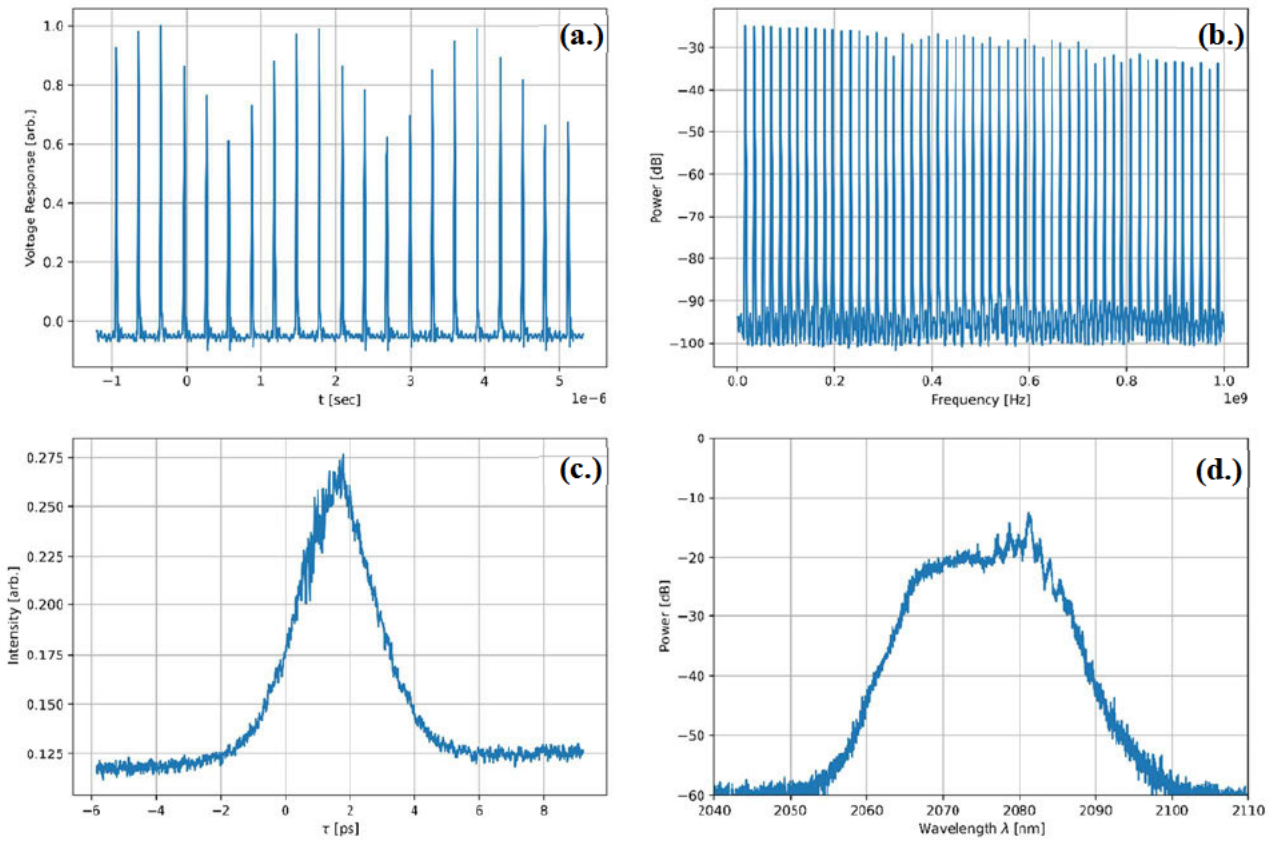

Figure 4.3.9: (a.) Oscilloscope trace, (b.) RF spectrum, (c.) ACF and (d.) OS of 'design 1'.

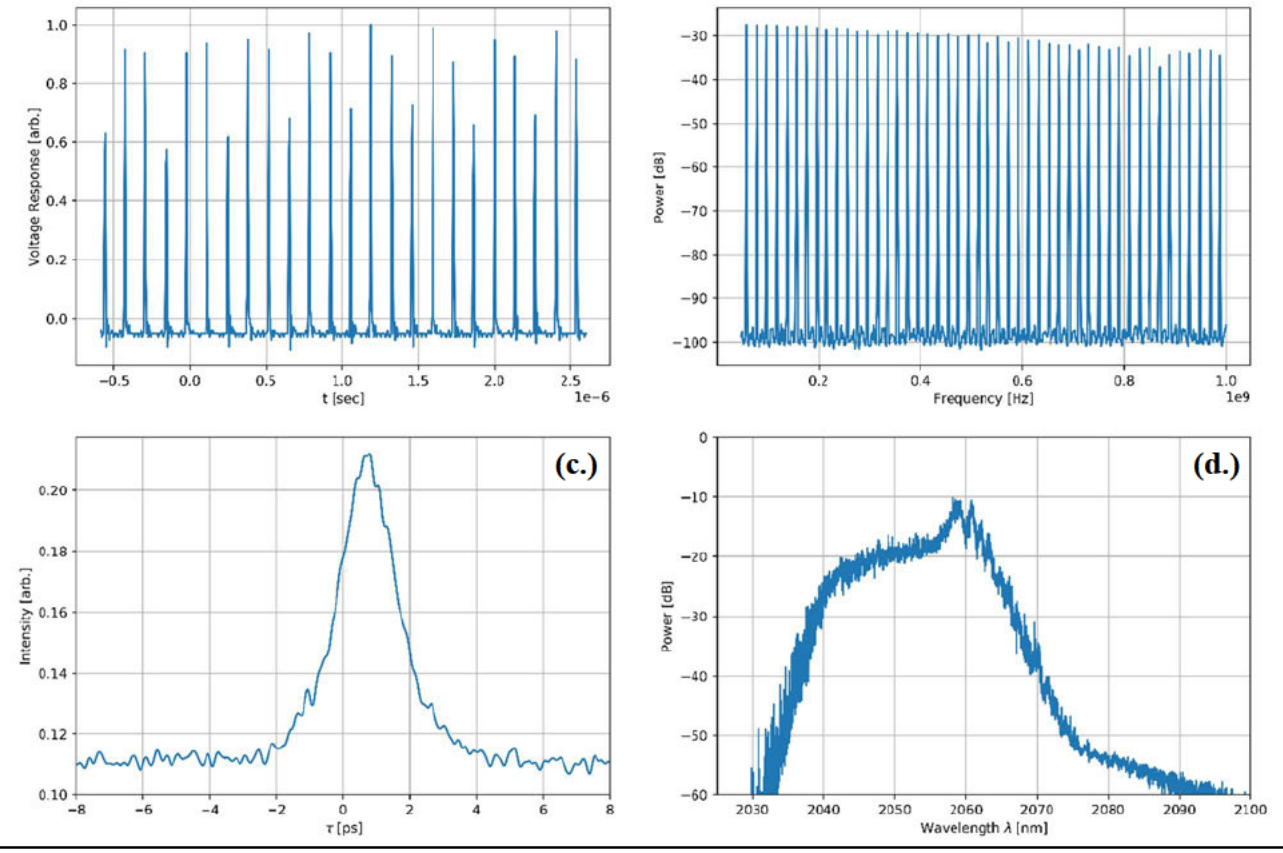

Figure 4.3.10: (a.) Oscilloscope trace, (b.) RF spectrum, (c.) ACF and (d.) OS of 'design 2'.

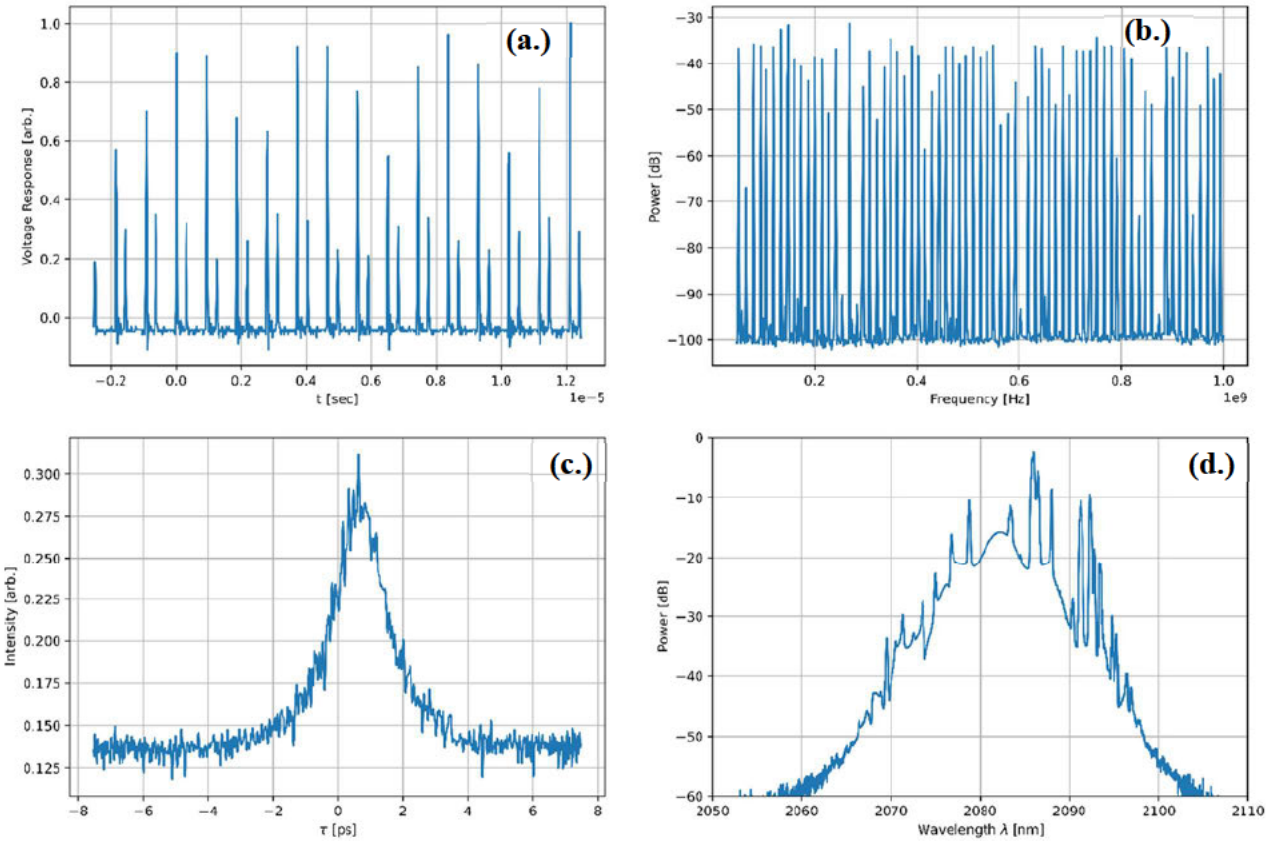

Figure 4.3.11: Oscilloscope trace, (b.) RF spectrum, (c.) ACF and (d.) OS of 'design 3'.

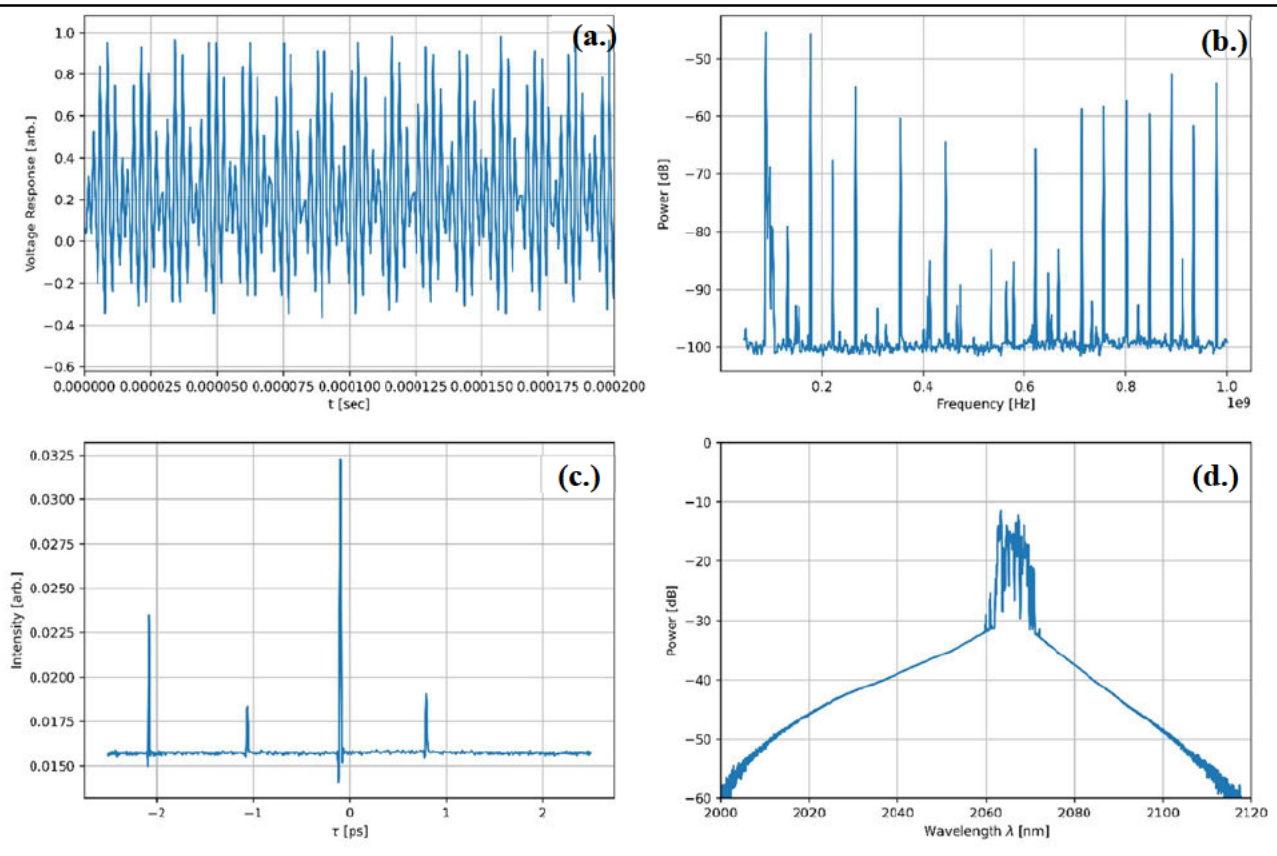

Figure 4.3.12: (a.) Oscilloscope trace, (b.) RF spectrum, (c.) ACF and (d.) OS of 'design 4'.

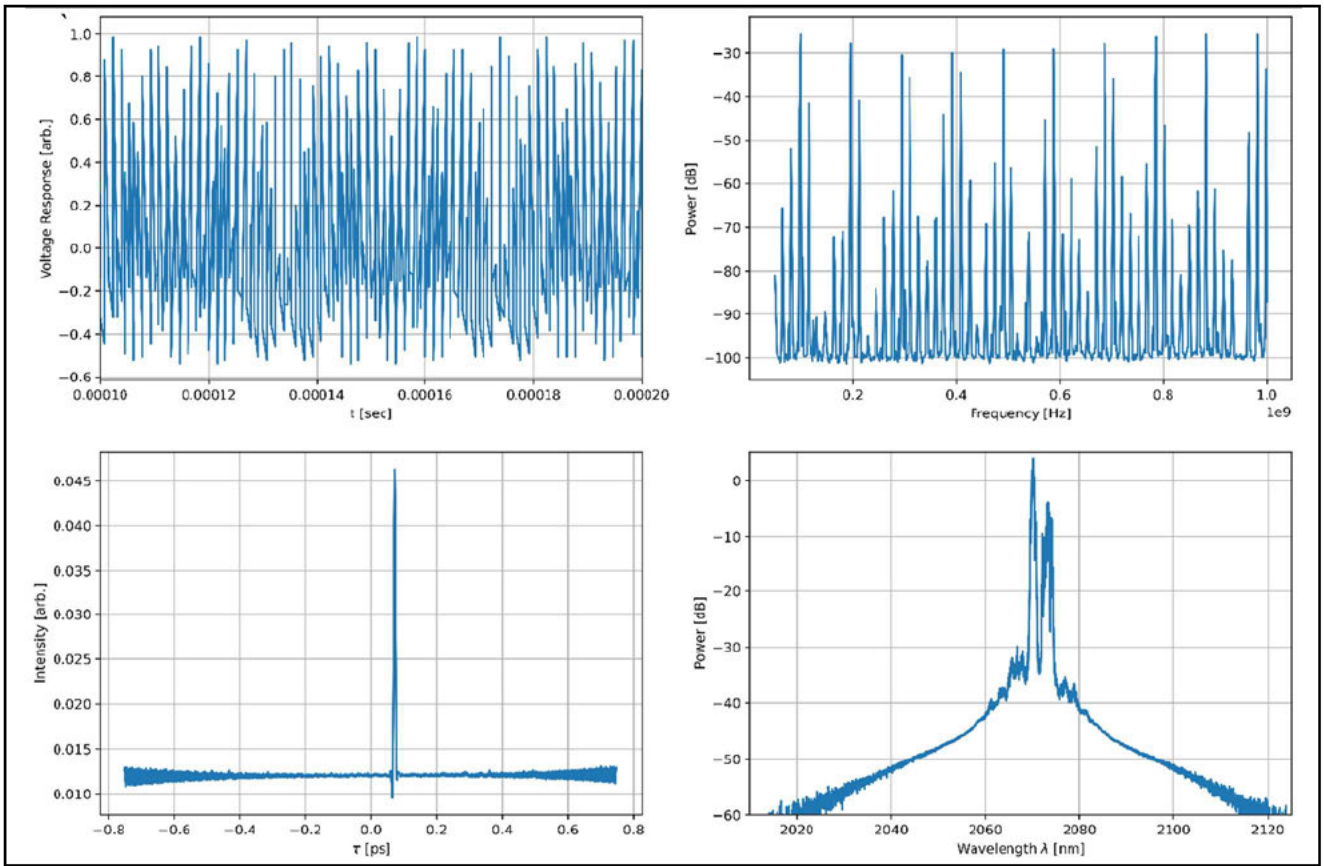

Figure 4.3.13: (a.) Oscilloscope trace, (b.) RF spectrum, (c.) ACF and (d.) OS of 'design 5'.

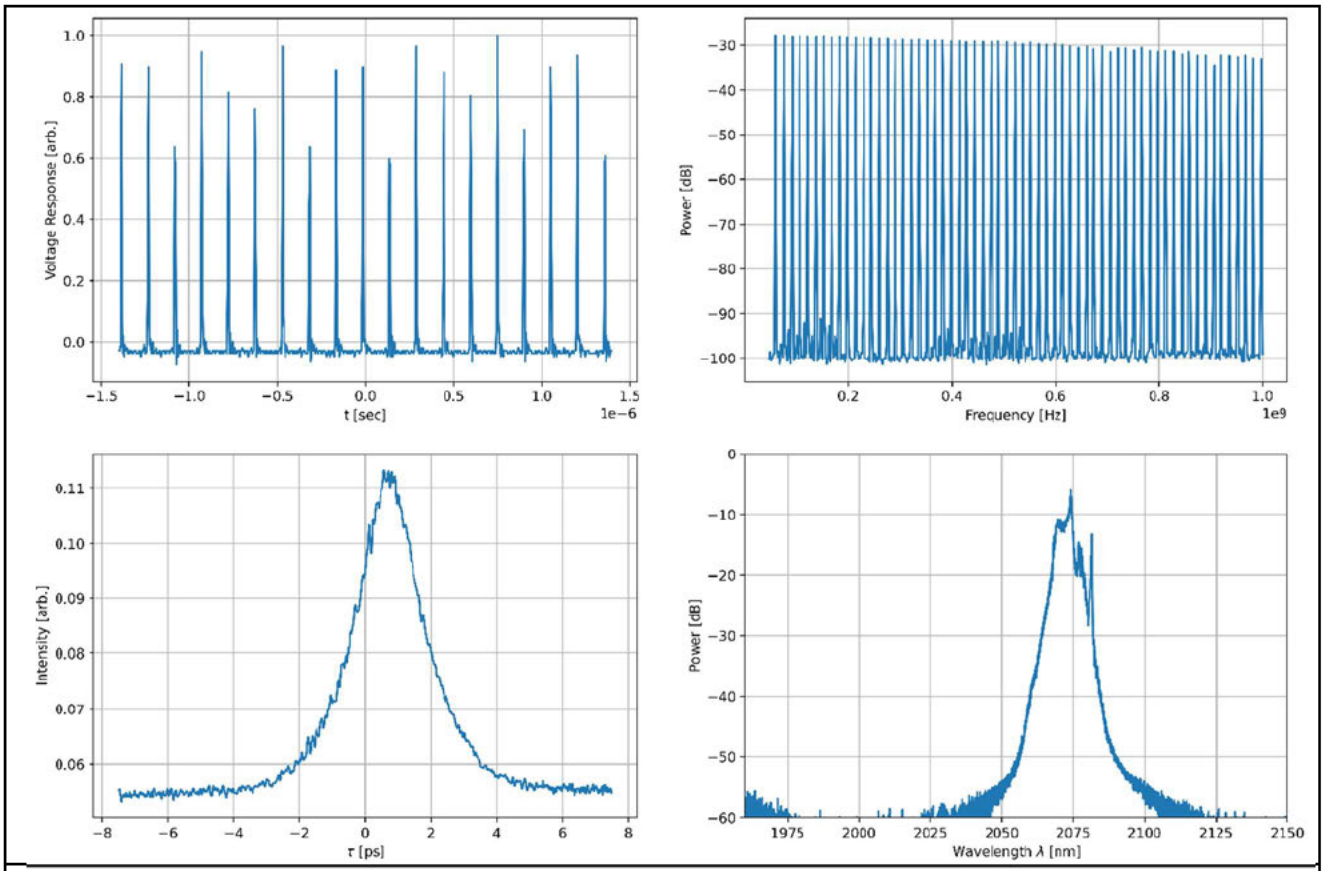

Figure 4.3.14: (a.) Oscilloscope trace, (b.) RF spectrum, (c.) ACF and (d.) OS of 'design 6'.

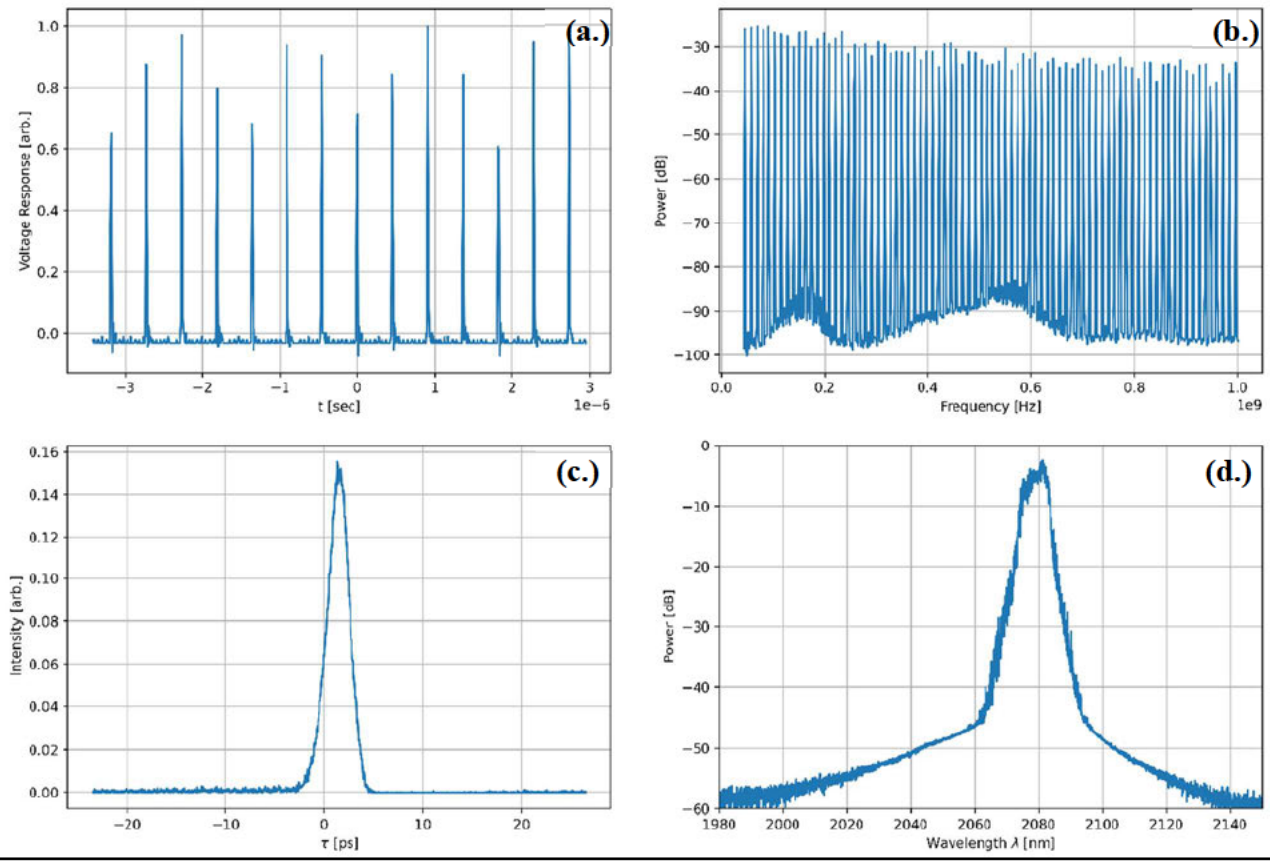

Figure 4.3.15: (a.) Oscilloscope trace, (b.) RF spectrum, (c.) ACF and (d.) OS of 'design 7'.

4.3.4 Discussion: Design 1

Design 1 displays significant instabilities in the time intensity domain trace on the oscilloscope, with a RIN of ~39%, indicating that intracavity energy fluctuates approx. 10% between cavity round trips, possibly due to multipulsing as indicated by the 17.8 MHz repetition rate. This instability is mirrored in the RF spectrum, with both a uniform 1 GHz RF roll-off of 9 dB, and several fundamental harmonic peaks with several dB drops relative to their neighbouring peaks. The RF SNR of this design was 62.5 dB, indicating that the design was largely stable. However, a minor sidepeak structure is also visible below -90 dB, related to phase noise as discussed in Chapter 3.

The intensity autocorrelation showed a hyperbolic secant-squared shape with a true temporal pulse FWHM of 2 ps with no pedestal or satellite features present. The optical spectrum had a FWHM of 16.9 nm, indicating significant spectral broadening. Several peak-like distortions are visible around 2080 nm in lieu of Q-switching instabilities, possibly indicating the tendency of this design toward the Q-switching threshold. This is reflected in the low average output power of 13.2 mW (after amplification).

By comparison, the simulation results from Figure 4.3.2 agree well with the experimental results in Figure 4.3.9 in many respects, such as predicting mode-locked operation at 2075.7 nm (versus the prediction at 2072 nm), in addition to predicting a pulse temporal FWHM of 2.01 ps versus the experimental value of 1.99 ps. However, the asymmetric and broad spectral features of the experimental results are unexpected, as the simulation predicts a smooth, symmetric structure with small Kelly sidebands.

4.3.5 Discussion: Design 2

Design 2 showed notably improved stability over Design 1 despite the higher intracavity power, and therefore increased nonlinearity, with the bi-directional pumping scheme providing doubled average power output, with RF roll-off and SNR of 7 dB and 69.2 dB respectively. RIN was however slightly higher at ~ 43%, but this may be attributed to the evident multipulsing with a repetition rate of 19.6 MHz. The phase noise sideband structure is also less pronounced, with a reduction in this component of ~ 5 dB versus Design 1.

The autocorrelation trace shows a sech-squared profile with a 1.57 ps FWHM. Such a reduction in temporal FWHM is expected due to the higher intracavity power, supported by more highly driven SPM-induced spectral broadening and up-chirp compared to Design 1. The optical spectrum displays several spurs with a broad, blue-shifted shoulder to the spectrum ala. Design 1.

Again, the simulation accurately predicts the pulse temporal FWHM of 1.48 ps, versus the experimental value of 1.57 ps. However, the large, blue-shifted spectral shoulder is unexpected, and may have resulted from additional nonlinear effects not predicted by the simulation. This is supported by the relative discrepancy in spectral FWHM, with the simulation underestimating this figure by 4 nm.

4.3.6 Discussion: Design 3

Design 3 is the first to utilise gain positioned just before the saturable absorber, thus we expect a more saturated SESAM by partially bypassing the insertion losses of the circulator and outcoupler of 1.5 dB and 2 dB respectively.

This design results in an even shorter pulse duration due to the additional gain toward the SESAM, with a deconvolved ACF FWHM of 1.44 ps, the shortest of all designs in this section. However, this appears to come at the cost of even higher instabilities, with a interpulse RIN of 45%, RF roll-off of ~ 10 dB and a RF SNR of 59.6 dB. Furthermore, the

RF spectrum does not display a stable comb of harmonics, but instead several valleys of low power/missing harmonics, and modulations of dozens of dB from peak-to-peak, comparison to the simulation which predicts relatively stable single-pulse operation with RIN on the order of ~ 20%.

Given a fundamental RF peak (rep. rate) at 26.8 MHz and the oscilloscope trace in Figure 4.3.11(a), it appears that further saturation at the SESAM has led to an inability to supress satellite pulses.

Evidence of this is further indicated by the complex structure present in the optical spectrum of Figure 4.3.11(d). The broad, underlying structure in lieu of the simulated predictions is overlayed with both the expected Kelly sidebands in addition to a noisy, peak-like structure towards the red shoulder of the spectrum beyond 2090 nm. Multiple sets of different Kelly sidebands are expected and observed here in the multisoliton regime, with each pulse may shed dispersive waves that periodically phase match to the individual pulse spectra. The peaks around 2090 nm do not appear to be paired clearly with a shorter wavelength counterpart as expected with Kelly sidebands, indicating some possible noisy CW component passed by the oversaturated SESAM.

The bandwidth of this laser design is significantly large at 12.3 nm compared to the prediction of 2.4 nm. The central operating wavelength of the experiment is noticeably longer at 2085.3 nm than the simulation, which was predicted to be 2074.7 nm. The temporal FWHM of 1.44 ps is in relatively good agreement with the prediction of 1.9 ps, however.

4.3.7 Discussion: Designs 4 & 5

Stable mode-locking was unobtainable with Designs 4 & 5. The RF spectra contained very few harmonics in both cases and resemble those associated with QS operation in addition to large numbers of sidebands with the relevant peaks. However, typical QS RF spectra have roll-off intrinsically limited to the kHz range, whereas these spectra show harmonic content out to 1 GHz with a drop of 10 dB. Measuring the repetition rate from the sparsely peaked spectra gives repetition rates of 90 and 98 MHz for Designs 4 and 5 respectively, and would otherwise indicate an interesting, if physically complex noise like pulsing regime in lieu of other characterisation.

However, in both cases the autocorrelation reveals structures of only 1 – 10 fs duration despite the narrowband optical spectra to support such pulses being insufficient, giving

unphysical TBP values well below the theoretically possible limit, indicating that these are in fact coherence spikes and do not represent a real pulse duration. Recall that the autocorrelation of a noise-like pulsing regime tends to a broad envelope with a coherence spike, which was observed.

Interestingly, Designs 4 & 5 disagree with their simulation results. The GNLSE predicts that these cavity designs should be stable, however the experiment strongly demonstrates noise-like pulsing with unstable spectral and temporal structure, in contrast to the well-defined mode-locked operation seen in the simulation. This unexpected disagreement may be due to issues with the experiment itself, such as SESAM oversaturation or damage. However, the predictions as seen in Figures 4.3.5 and 4.3.6 reveal only 16.8% and 14.6% SESAM absorption, well within acceptable operating range for both lasers.

4.3.8 Discussion: Design 6

Design 6 utilised a bi-directional pumped gain to achieve more uniformly pumped gain, higher pulse energy just before the SESAM, as well as amplification on the subsequent reflection from the mirror. In terms of performance, we see that this design has the lowest RF spectrum roll-off of only 5.38 dB, with few modulations to peak height and a reduced phase noise floor compared to the other designs. Similarly, the RF SNR was 69.1 dB, competing with all other designs for one of the highest peak SNRs, in addition to the smallest RIN (38.3%) of the five stable, mode-locked oscillators presented here.

Considering the repetition rate of 15.4 MHz versus that of an identical fibre length in Design 7 (11.8 MHz), it is apparent that the additional, bi-directionally pumped gain both provides needed saturation for the SESAM at the cost of multipulsing. The simulations predict an additional few percent saturation as desired to provide uniform pulse shaping.

The autocorrelation FWHM of 1.78 ps is somewhat similar to other designs, but moreover there are no apparent pedestal or satellite features despite the increased repetition rate. Given the well-defined temporal separation of the pulses in the oscilloscope trace, no ACF distortions should be immediately expected. Lastly, the optical spectrum displayed a FWHM of approx. 5.55 nm, with a few peak-like structures present.

The simulation agrees well with the results as outlined in Table 4.3.1, presenting near identical pulse temporal FWHM and central wavelength. The predicted temporal FWHM is 1.85 ps versus the experimental value of 1.78 ps, and the predicted central wavelength is

2075.2 nm versus the actual value of 2074.2 nm. Again, only the spectral FWHM is underestimated by approximately 4 nm, likely due to underestimation of nonlinear processes or gain bandwidth justified in Appendix F.

4.3.9 Discussion: Design 7

Lastly, Design 7 showed one of the most stable outputs, indicated by the 70.6 dB RF SNR at 11.6 MHz, with a roll-off of 7.67 dB. The accompanying interpulse RIN was 39.4%. This is further supported by the lack of satellite or side pulses in the oscilloscope and autocorrelation traces in Figure 4.3.15(a.) and (d.) respectively. As this design bypasses the insertion loss of the circulator and outcoupler a fuller saturation of the absorber is achieved without significant oversaturation. However, this design did report a marked increase in phase noise in the RF spectrum below -80 dB, indicating an increase to timing instability between the individual pulses.

The optical spectrum displayed few abnormalities, revealing a relatively clean trace with a FWHM of ~5.71 nm. Strangely, Kelly sidebands or any peak structures are not observed, presenting two possibilities. One, this cavity arrangement may not support soliton-like pulsing, or two, the dispersive-wave soliton resonant interference is disrupted or are spread to regions outside the operating linewidth of the cavity.

Again, the simulation predicts the central wavelength within 3 nm accuracy but underestimates the bandwidth by 4 nm. This lack of bandwidth in the simulation also leads to an overestimation of the temporal FWHM, yielding a duration 1 ps longer than the experimental result. Interestingly, similar spectral structure with minimal sideband structure is observed between the experiment and numerical results, excluding the pedestal which is absent in the simulation.

4.3.10 Summary and Conclusion

Summaries of the simulation and experimental results are provided in Tables 4.3.1 and 4.3.2 below respectively:

	SESAM Absorption	Central Wavelength [nm]	OS FWHM [nm]	Temporal FWHM [ps]
Design 1	21.6%	2072	2.1	2.01
Design 2	19.8%	2071.8	2.0	1.48
Design 3	13.8%	2074.7	2.4	1.90
Design 4	16.8%	2075.5	1.3	3.83
Design 5	14.6%	2072.2	1.6	3.07
Design 6	15.2%	2075.2	2.4	1.85
Design 7	19.4%	2075.2	1.7	2.83

Table 4.3.1: Tabulated summary of simulation predictions for designs 1 – 7.

	RIN	OS FWHM [nm]	Central Wavelength [nm]	ACF FWHM [ps]	TBP	RF roll-off [dB]	RF SNR [dB]	Rep. Rate [MHz]	Avg. Power [mW]
Design 1	39.1%	12.3	2075.7	1.99	1.69	9.0	62.5	18.0	13.2
Design 2	42.6%	6.74	2058.1	1.57	0.748	7.0	69.2	19.8	23.6
Design 3	45.0%	12.3	2085.3	1.44	1.22	5.5	59.6	13.8	25.4
Design 4	49.1%	4.64	2063.4	~	~	20.2	28.8	90.0	20.5
Design 5	26.7%	~	2069.3	~	~	8.1	31.9	98.0	20.6
Design 6	38.3%	5.55	2074.2	1.78	0.677	5.4	69.1	15.4	43.0
Design 7	39.4%	5.71	2072.5	1.66	0.66	7.7	70.6	11.8	35.8

Table 4.3.2: Tabulated summary of performance of designs 1 – 7.

To summarise the experimental performance of each design:

- Design 1 utilised multiple lengths of gain fibre in series, displaying the longest pulse duration, a broad, asymmetric spectrum and generally middling stability characteristics, in addition to the lowest average power. The TBP shown in Table

4.3.2 above indicates the largest amount of chirp of all designs, well over the minimum of 0.315.

- Design 2 utilised a bi-directional pump scheme, leading to the second shortest pulse duration, while attaining largely stable multi-pulsed operation indicated by the RF spectrum, along with a smaller TBP (and thus chirp) of 0.748.
- Design 3 iterated on Design 2 with an additional gain fibre toward the SESAM, leading to further improved RF roll-off and the shortest pulse duration.
- Designs 4 and 5 had gain fibre only before the SESAM and, unexpectedly, did poorly. Simulations indicated performance similar to that of Design 3 owing to superior SESAM saturation, but these designs did not mode-lock successfully, as indicated by the chaotic RF spectra, unresolvable AC traces and sharp, peak-like optical spectra as is typical for QS instabilities. This could be indicative of damage to the system (i.e. the SESAM) or degradation of splice quality, or attributed to SESAM bleaching and subsequent absorptive roll-over not accounted for in the simulation.
- Designs 6 and 7 utilised bidirectionally and unidirectionally pumped dual-WDM architecture with a single gain fibre, placed at the SESAM. These systems displayed the highest average powers in agreement with the simulation, in addition to markedly improved stability shown by RF SNR of over 69 dB each, as expected by the increased saturation of the SESAM.
- Design 8 demonstrated the most optimised stability performance over all designs in this section and is discussed in detail in Section 4.4.

4.4 First Stable Ho:fiber SESAM-mode-locked Laser

4.4.1 Master Oscillator Design

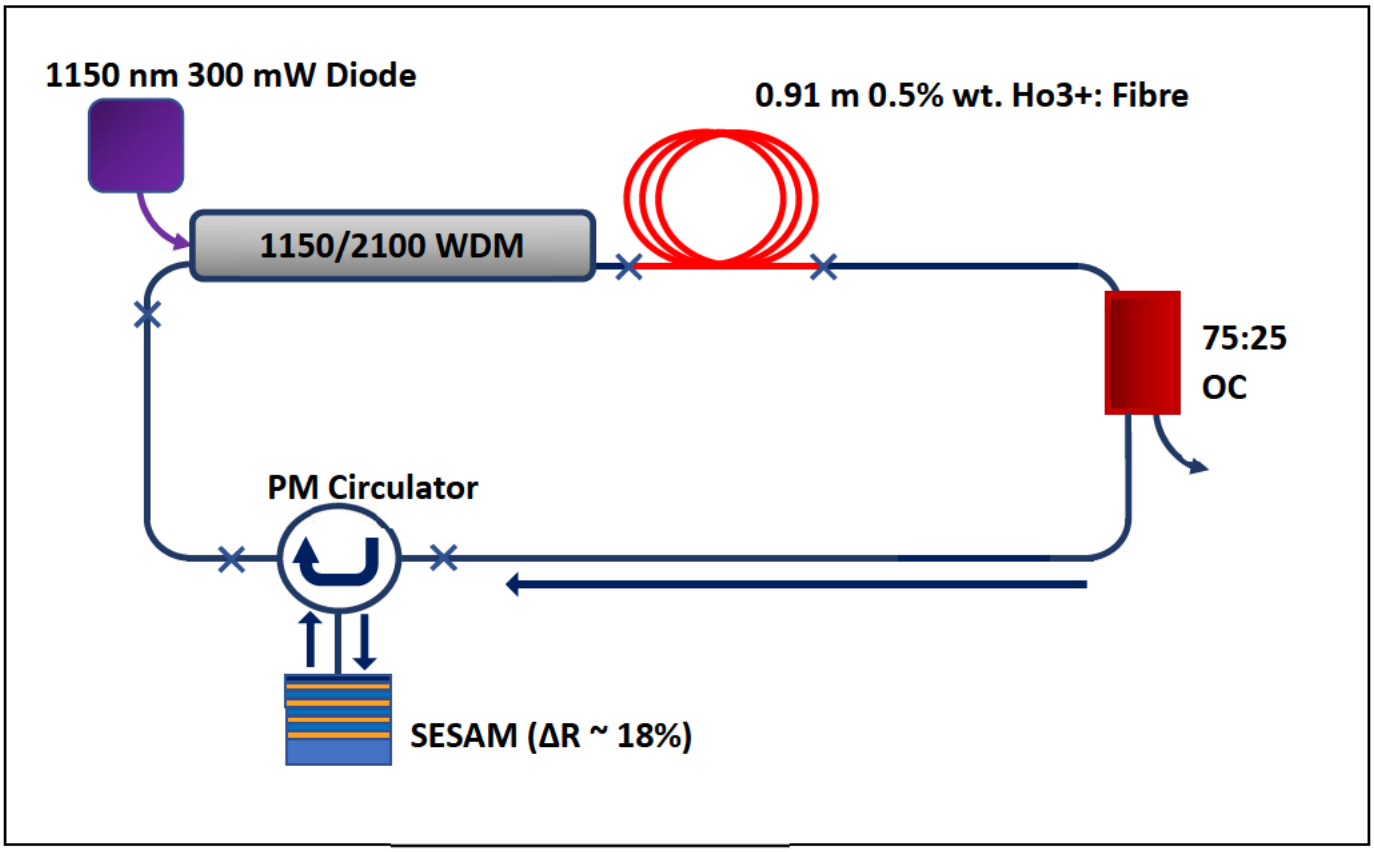

Figure 4.4.1: Schematic of the Ho-doped SESAM-mode-locked fibre laser. Fusion splices are marked with an 'X', and propagation direction is indicated by the arrows.

After considering the alternate architectures in Section 4.3, the cavity design shown in Figure 4.4.1 above was found to be the most stable. It incorporated ~10 m of SM2000 passive fibre, spliced to 0.91 m of custom active 0.5% wt. Ho-doped active SM fibre.

The PM circulator acts to direct light to the SESAM, which is in physical contact with the cleaved fibre face from port 2. The PM circulator additionally acts as a polarisation gate due to its Faraday-rotator based non-reciprocal polarisation rotation structure as shown in Chapter 2, providing some amount of polarisation-based saturable absorber action by preferentially attenuating based on polarisation state across the pulse [38, 39]. Note that due to the complicated implementation and further increased computational load, such a mechanism was not accounted for in the simulation, the model of which is discussed further in Chapter 5.

The BATOP GmbH SAM-2000-30-10ps-25.4g SESAM has a recovery time $\tau \sim 10$ ps with a modulation depth of 18%. The Bragg-reflector of the SESAM is grown to have a high reflectance band from 1910 to 2080 nm.

Similar to the designs in Section 4.3, a 1150/2000 nm wavelength division multiplexer (WDM) is spliced to the cavity, with one input connected to a 1150 nm pump diode, thus coupling light into the cavity to pump the gain medium via the core (rather than the cladding). Lastly, a 75/25 2100 nm broadband output coupler permits 25% of the mode-locked pulse to leave as the laser output.

4.4.2 Numerical Modelling

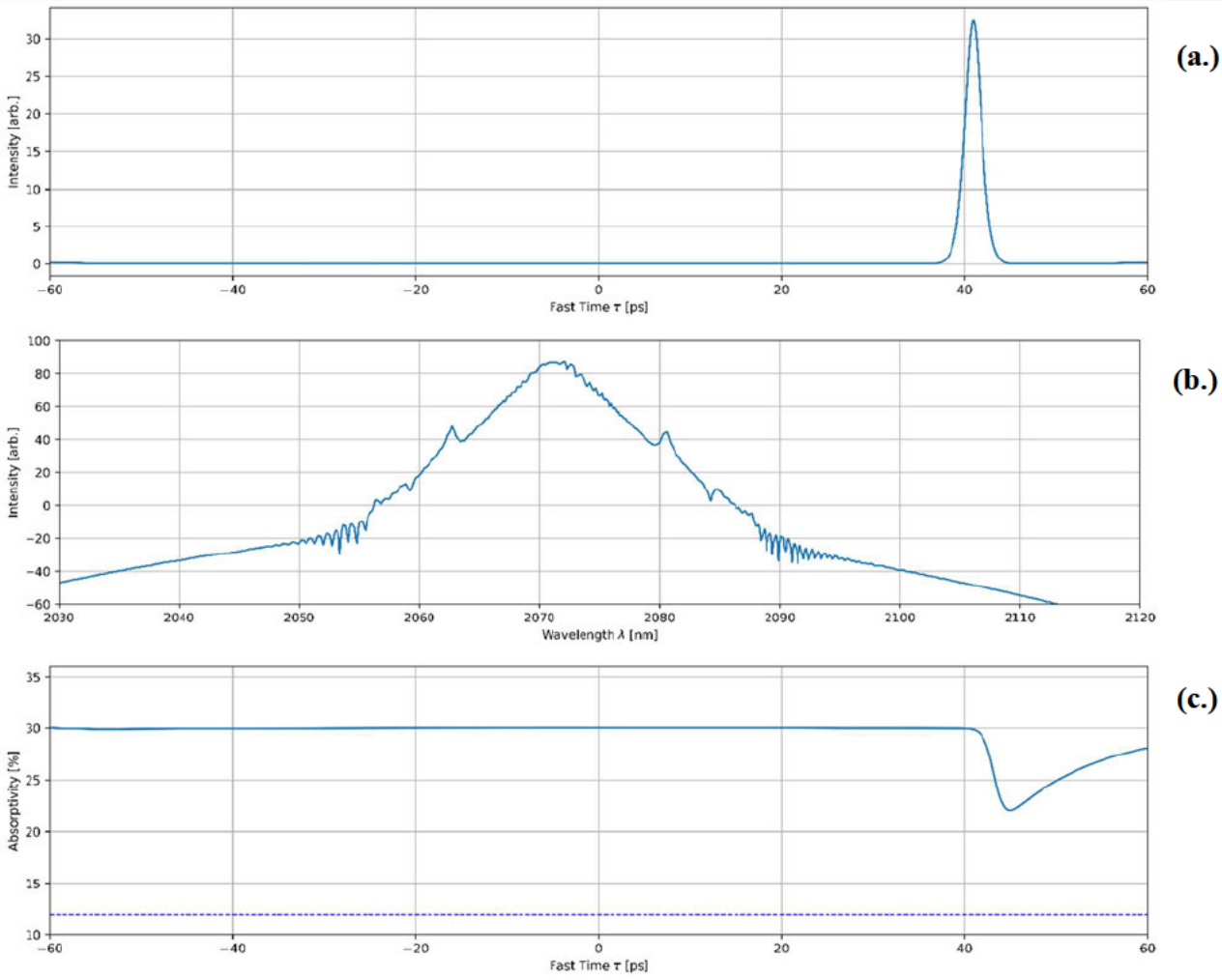

Figure 4.4.2: Numerical simulation results of (a.) time domain intensity, (b.) optical spectrum and (c.) the SESAM absorptivity vs. comoving pulse reference frame time for the laser design in Figure 4.4.1.

The cavity in Figure 4.4.1 was numerically simulated, and produced the following time-intensity trace, optical spectrum and SESAM absorptivity profile in Figures 4.4.2 (a), (b) and (c) respectively. The minimum SESAM absorptivity (saturated) reaches 22%, thus it is apparent that this design operates at approximately the saturation fluence given by the approximate 1/e saturation shown in Figure 4.4.2c. This partial saturation nonetheless does not lead to significant satellite features in Figure 4.4.2a. However, a small pedestal feature appears toward 60 ps delay which may explain the oscillatory multipulse-like structures observed in the optical spectrum in Figure 4.4.2b in combination with those typically seen with significant SPM. Pairs of symmetric sidebands are visible in Figure 4.4.2 in accordance with the results presented in Section 4.3.

4.4.3 Amplifier Stage Design

The autocorrelation/pulse-gating measurement techniques discussed in Chapter 3 requires sufficient input optical power to drive the ultrafast nonlinear response they use for detection and characterisation. As such, a single-pass Ho:silica fibre amplifier stage shown in Figure 4.4.3 was designed to amplify the output of the master oscillator:

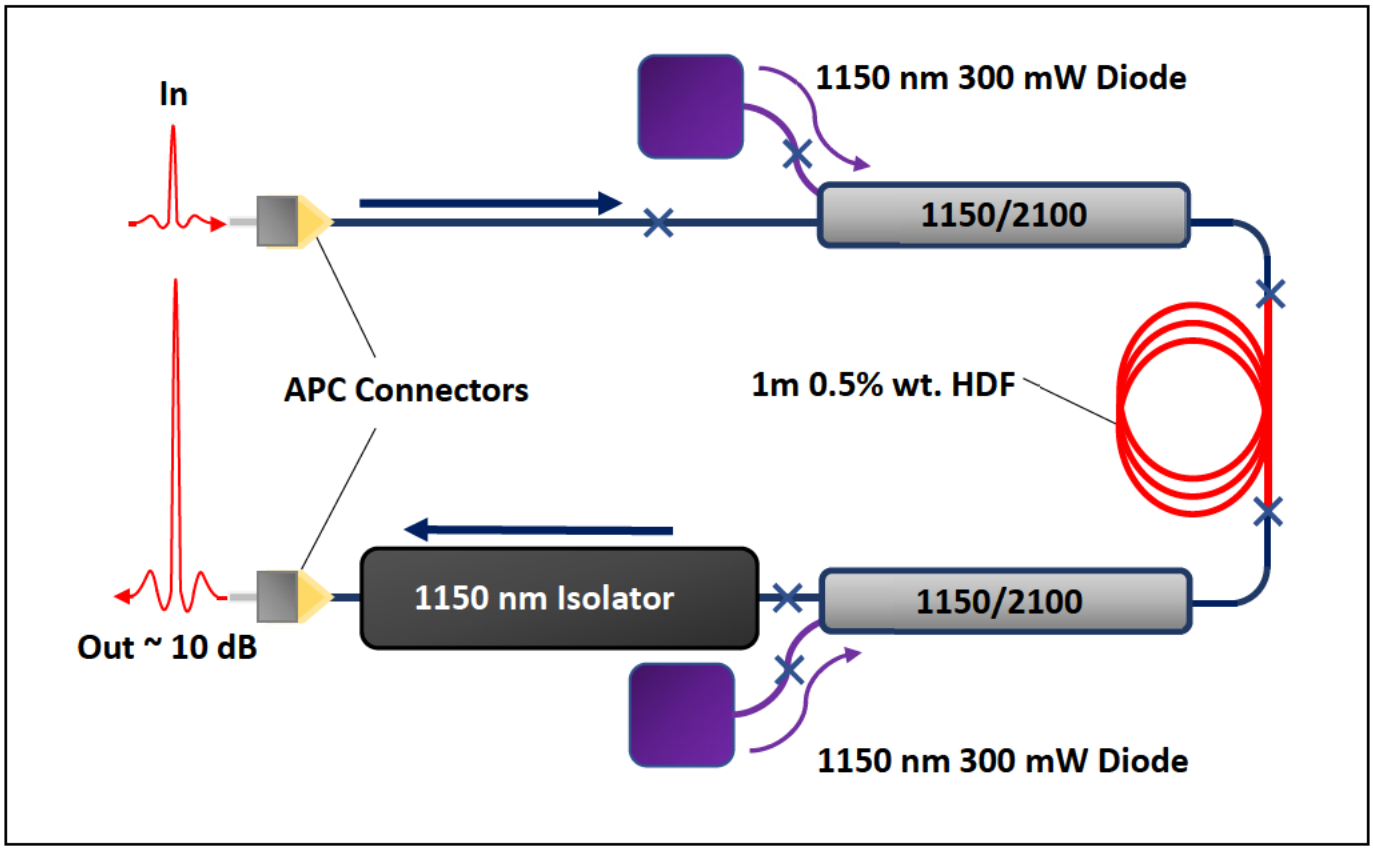

Figure 4.4.3: Schematic of the Ho:fiber single-pass amplifier stage. Output is amplified by approximately 10 dB.

The amplifier consists of ~ 10 m SMF spliced to ~ 1 m of active HDF. Two 1150/2100 WDMs provide bi-directional core pumping for the Ho:fiber gain medium. Isolation/protection for the master oscillator against the unabsorbed back-propagating pump light is provided by the first WDM, as the pump light will travel into the 2.1 μm port and will be rejected, and thus prevented from passing to the input APC and into the master laser. A set of identically specified ~300 mW 1150 nm butterfly diodes are used as pump sources.

4.4.4 Experimental Results

With a pump diode current of 1000 mA and with the amplifier, the average power output was 20.3 mW, producing a train of stable pulses shown in the oscilloscope trace in Figure 4.4.4 below:

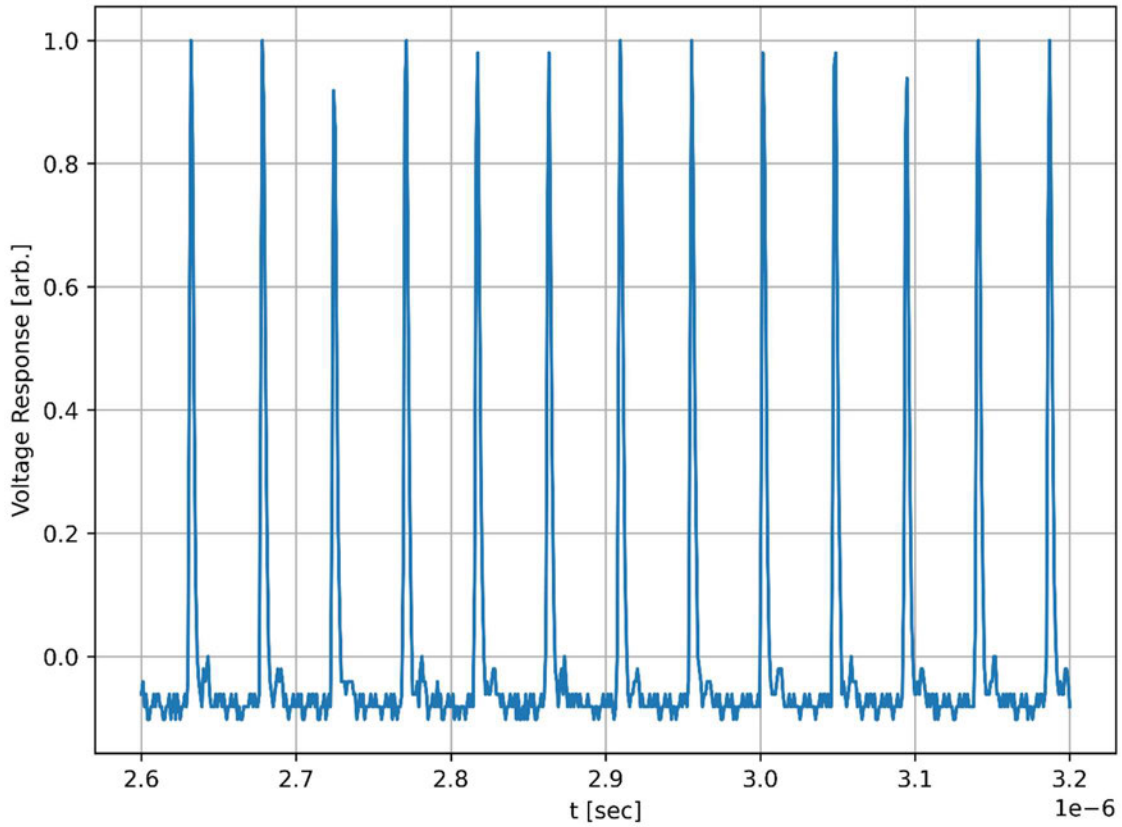

Figure 4.4.4: Oscilloscope trace of stable laser in CML regime, 50 ns timebase.

Despite the poor resolution and thus high digitisation noise present in Figure 4.4.4 above, conservation of energy permits the oscilloscope to measure the total energy of the pulses in the pulse train at the laser output. The RIN of Figure 4.4.4 is 8.2%, approximately three to four times less than that observed in any of the alternate cavity designs in Section 4.3 previously. As seen in this section, further characterisation methods confirm the relative stability of this laser cavity design. This result is in good agreement with the simulation, both displaying RIN around 10% in the steady state.

The optical spectrum of the output pulses in the CML regime is shown in Figure 4.4.5 below:

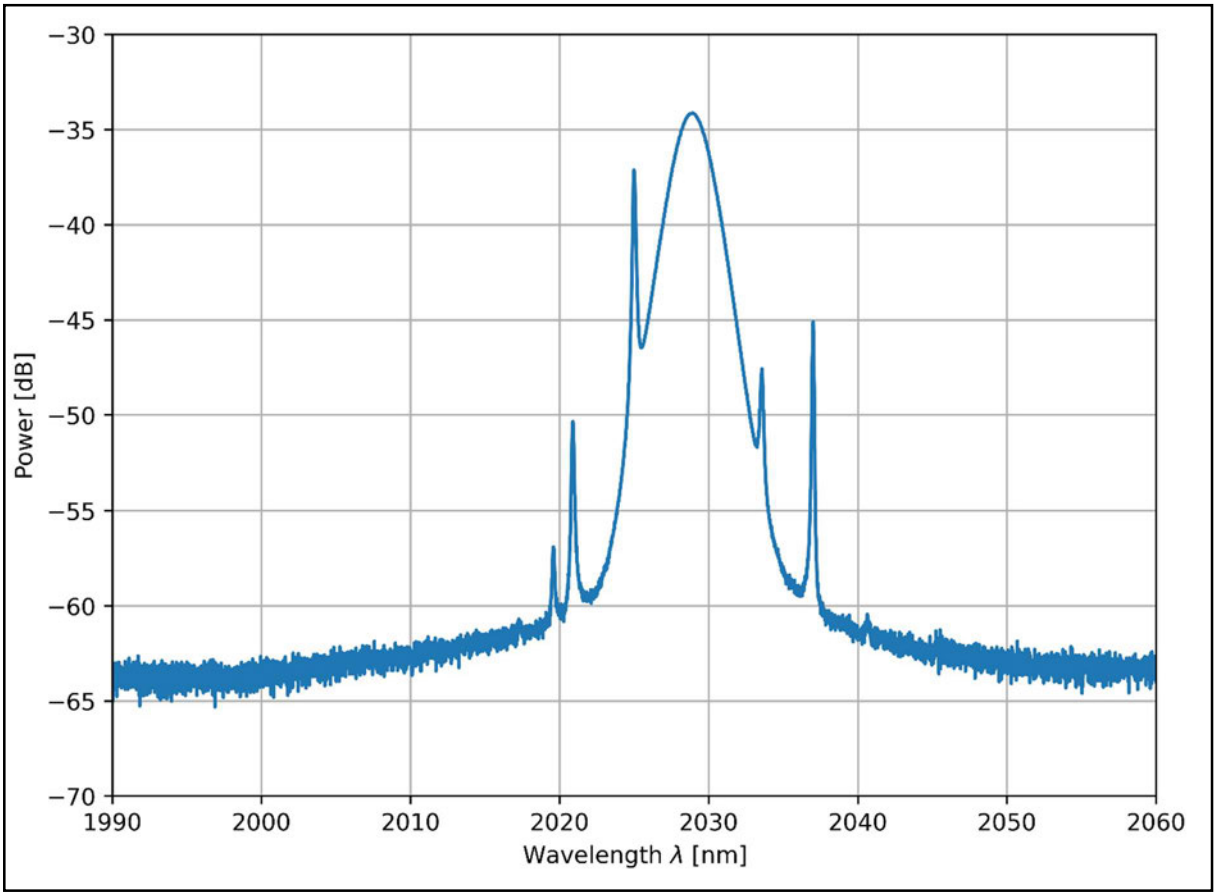

Figure 4.4.5: Optical spectrum of the stable laser in a CML regime, 1 GHz span.

CML operation results in a spectrum with a 3 dB FWHM of approximately 4 nm. In addition to the smooth, broad structure, there exists several Kelly sidebands located symmetrically in pairs about the central wavelength of 2029.1 nm.

Note that there is an apparently unpaired peak located at ~2020 nm which could be symmetrically paired with the small peak located past ~2040 nm, or possibly buried by noise (as these sidebands vary by around -5 dB in a pair). Otherwise, these sideband positions largely match those of the three pairs shown in the simulated data of Figure 4.4.2c.

Interestingly the laser output tends much more toward the shorter wavelengths at 2030 nm, as opposed to the simulation's prediction around 2070 nm as expected due to the choice of components (all of which have passbands around 2000 or 2100 nm, the net region of least loss/most gain lying somewhere closer toward 2100 nm, in agreement with the results in Section 4.3).

The RF spectrum over 1 GHz is shown in the Figure 4.4.6 below.

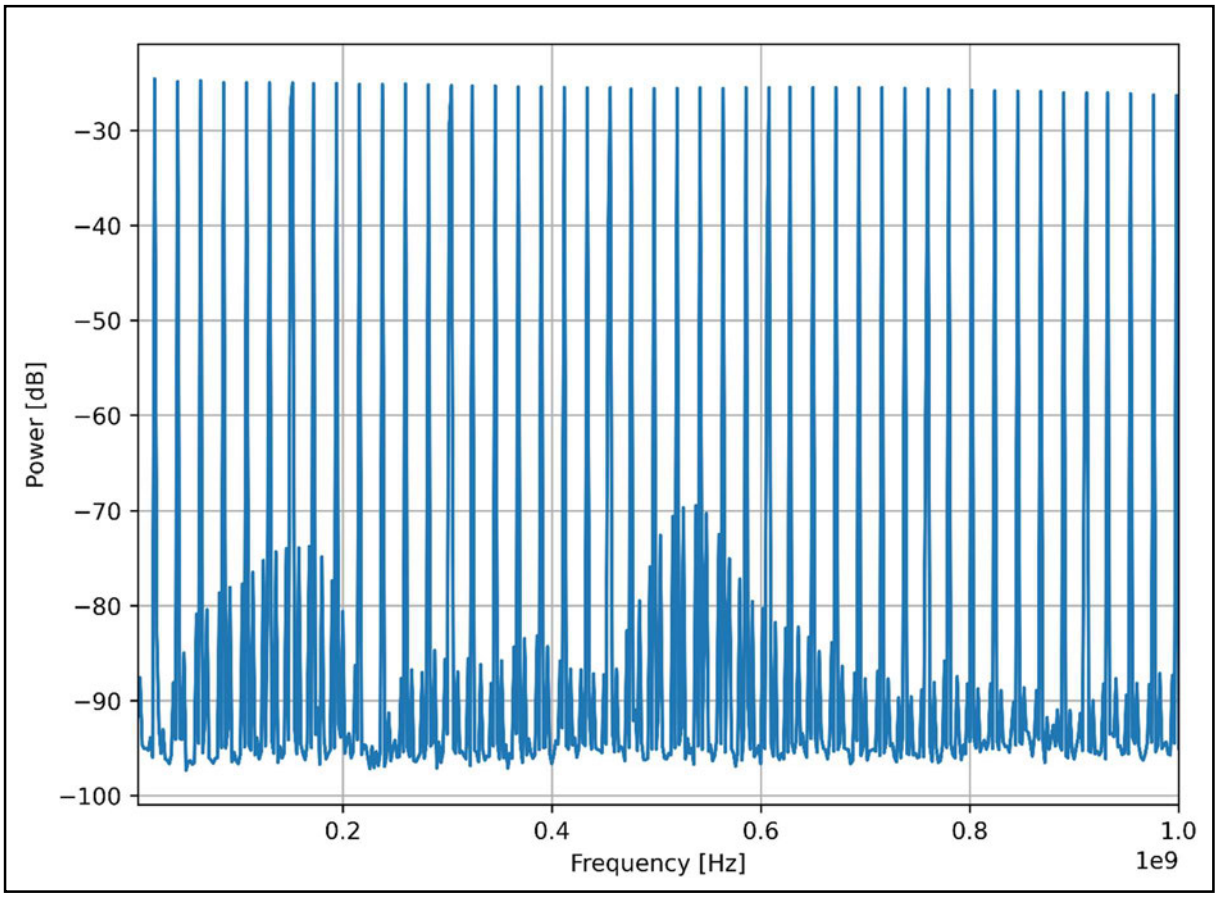

Figure 4.4.6: RF spectrum of the stable laser in a CML regime, 1 GHz span

The RF spectrum of the CML regime over a 1 GHz span displays satisfactory stability, displaying a shallow RF power roll-off of only ~ 1.76 dB, indicating the notably high stability of this cavity layout. The SNR of the fundamental laser repetition rate peak is ~63 dB, located at ~20 MHz, the repetition rate.

In addition to these two features there also appears to be some frequency sub-structure fluctuating below -70 dB, similar to that observed in Section 4.3. Again, such sideband structures are associated with timing noise between the pulses, discussed in Chapter 3 previously.

Lastly, an intensity ACF of the pulsed output is shown in Figure 4.4.7 below.

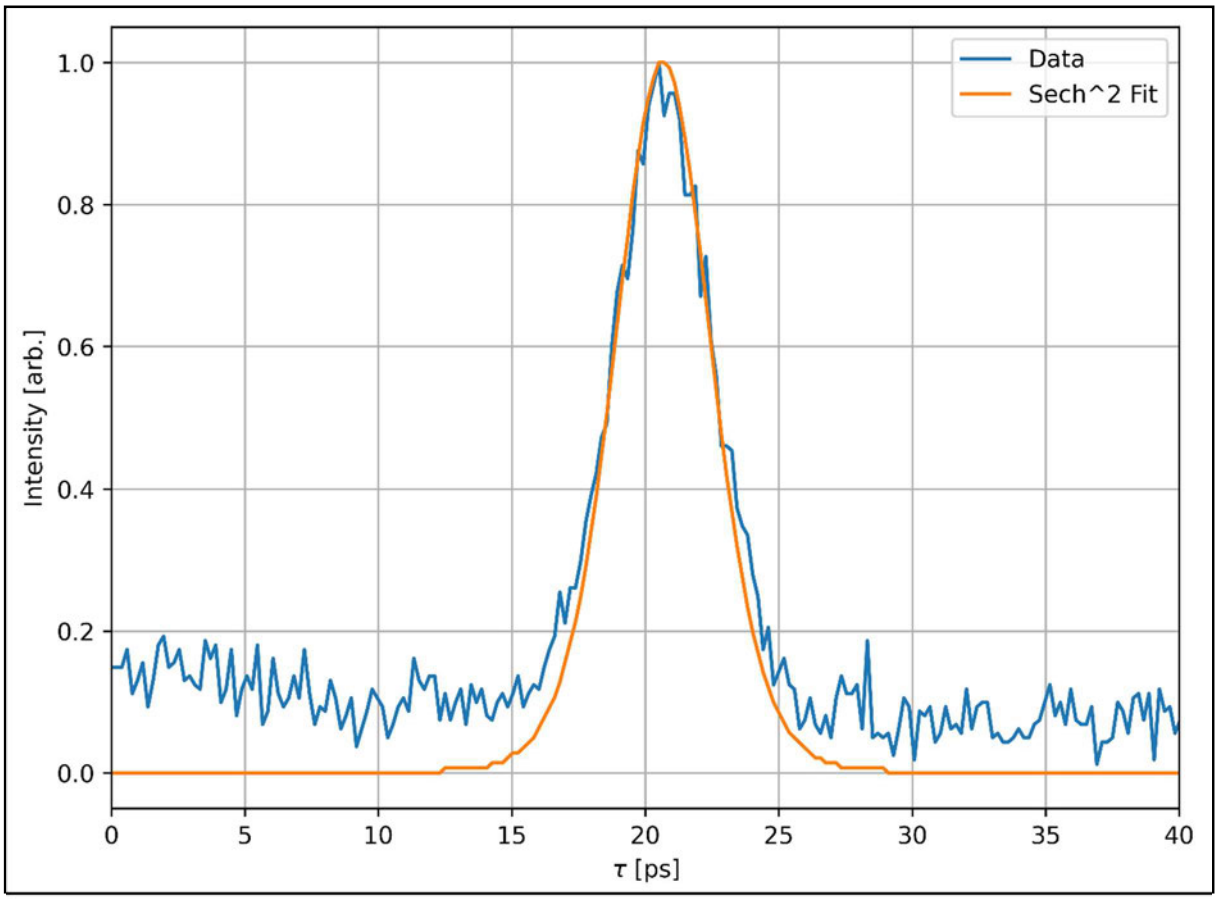

Figure 4.4.7: ACF of the stable laser in a CML regime 50 ps scan range.

A $sech^2$ function was fitted to the data numerically. This is the general functional form of a conventional soliton pulse, which displays dispersive wave features such as Kelly sidebands in its spectrum and is thus the assumed pulse shape for the ACF [40, 41]. The FWHM of the autocorrelation data was found to be 4.49 ps. Applying the deconvolution factor of 1.54 (0.647^{-1}) for $sech^2$ pulses this gives a true temporal FWHM of 2.92 ps [42].

4.4.5 Discussion

Firstly, the oscilloscope trace provides a simple measure of this designs stability, with a RIN 8.2%, the lowest of all cavity designs tested in this project. This indicates the importance of maintaining pulse energies above QML threshold whilst avoiding MPML through overdriven nonlinear effects, as given by the singularly pumped Ho:fibre design.

The RF spectrum displayed extremely low roll-off of only 1.76 dB across a 1 GHz band, again indicating the superior stability of this design. Interestingly the SNR is only 63, which is superseded only by Design #7 (~70 dB SNR) from Section 4.3. However, due to the small RIN and RF roll-off, and lack of multipulsing in the oscilloscope trace, this design is considerably more stable.

Recall that Figure 4.4.6 (RF spectrum) possessed a distinct, ~100 MHz scale sub-structure of RF sidebands about the harmonics. These small 'spurs' appear symmetrically about the harmonic RF peaks and are likely further related to the phase-noise generated by pulse train instabilities such as timing jitter or simply produced by photodiode saturation [43, 44]. The structure is persistent, in that repeat measurements preserve the structure, in addition to appearing in differing forms throughout the RF traces in the alternate designs shown in Section 4.3.

The optical spectrum in Figure 4.4.4 possesses several key, near ideal characteristics, indicating good performance for this cavity arrangement. Firstly, the Kelly sidebands are confirmation that the holmium doped laser in this experiment is mode-locking through SESAM stabilisation of conventional solitons [45, 46]. However, it should be noted that the sidebands themselves are considered undesirable as adjacent soliton Kelly sidebands (i.e. dispersive waves) may interfere to destabilise mode-locked operation [45, 47, 48]. The next step, removing (or effectively 'pushing out') the sidebands in the spectrum, is addressed through dispersion compensation in Section 4.5.

Lastly, an intensity autocorrelation reveals a symmetrical, sech^2 pulse shape with a true temporal FWHM of 2.92 ps. The most notable features are a lack of multipulse instabilities such as satellite pulses or the tendency to a broad feature with a noise-coherence spike, in tandem with the somewhat long pulse FWHM as compared to the other designs. The discrepancy in FWHM is likely due to multiple nonlinear effects, most notably the strength of the driven SPM in the different laser designs. As this cavity utilised only one pump with one gain fibre, with an estimated intracavity average power of ~ 80 mW, the nonlinearity

experienced and generated by the pulse peak power is much smaller compared to the average intracavity power utilised in many of the alternate designs (~up to 160 mW intracavity), i.e. Kerr nonlinearity depends on the cube of intensity.

As discussed in Chapter 2, the nonlinearly induced positive chirp of SPM is key to balancing dispersion, and thus pulse duration in the anomalous dispersion regime, thus we may expect that low intracavity power will lead to unbalanced nonlinear phase (from SPM) and thus uncompensated pulse broadening in the time domain.

Furthermore, the spectral bandwidth of the pulse is only 4 nm, as opposed to the bandwidths seen in the other designs of approx. 10 nm. Again, the explanation leads back to SPM: for an initially down-chirped pulse, SPM will always lead to spectral narrowing, not broadening. The comparably narrow bandwidth and broad temporal FWHM is indicative of inadequate dispersion compensation against a weakly driven SPM effect. The importance of experimentally optimised dispersion is explored in the proceeding section.

However, it should be noted that the weakly driven nonlinearity leads to a stable, apparently multipulse-free CML operation. The pump diode current was unable to be tuned below ~700 mA without the laser falling into QML, and eventually QS operation, with a small region of mode-locking hysteresis around 700 – 800 mA driver current.

4.5 Dispersion Compensation

4.5.1 Overview

The balancing of SPM versus GVD is crucial in mode-locking ultrafast pulses [49-51]. As discussed in Chapter 2, soliton formation and propagation depend on the balance of these phase shifts, providing inherent stability and pulse shaping [52-55]. The approximate amount of DCF required to offset GVD alone (not including SPM) was determined by Equation 4.5.1, a rearrangement of Equation 2.2.17 [56]:

$$D_p l_p + D_a l_a + D_D l_D = 0 \qquad (4.5.1)$$

where D_p, D_a and D_D are the dispersion coefficients and l_p, l_a and l_D are the fibre lengths for the passive, active and dispersion compensating fibres respectively. Equation 4.5.1 allows for an initial estimate of net cavity dispersion, which is offset by the nonlinear phase induced by SPM and a selected length l_D of DCF. Using this equation, the approximate DCF length required would range around 10 m, and thus this served as a starting point for the experiments in this section. Naturally, the true length required would be shorter as SPM is neglected in Equation 4.5.1, in addition to the small normal dispersion caused by the 0.5 mm propagation through the SESAM, and therefore this section seeks to experimentally determine this length via DCF cutbacks.

To experimentally determine the optimal cavity dispersion and compress the pulse, a 13 m reel of DCF was spliced to the cavity. Lengths of 1 m were removed, with the laser characterised at each length from 13 m to 5 m. Measurements were repeated with a new length of 9 m of DCF with 20 cm decrements in the DCF length.

A schematic of the dispersion-compensated laser is shown in Figure 4.5.1 below:

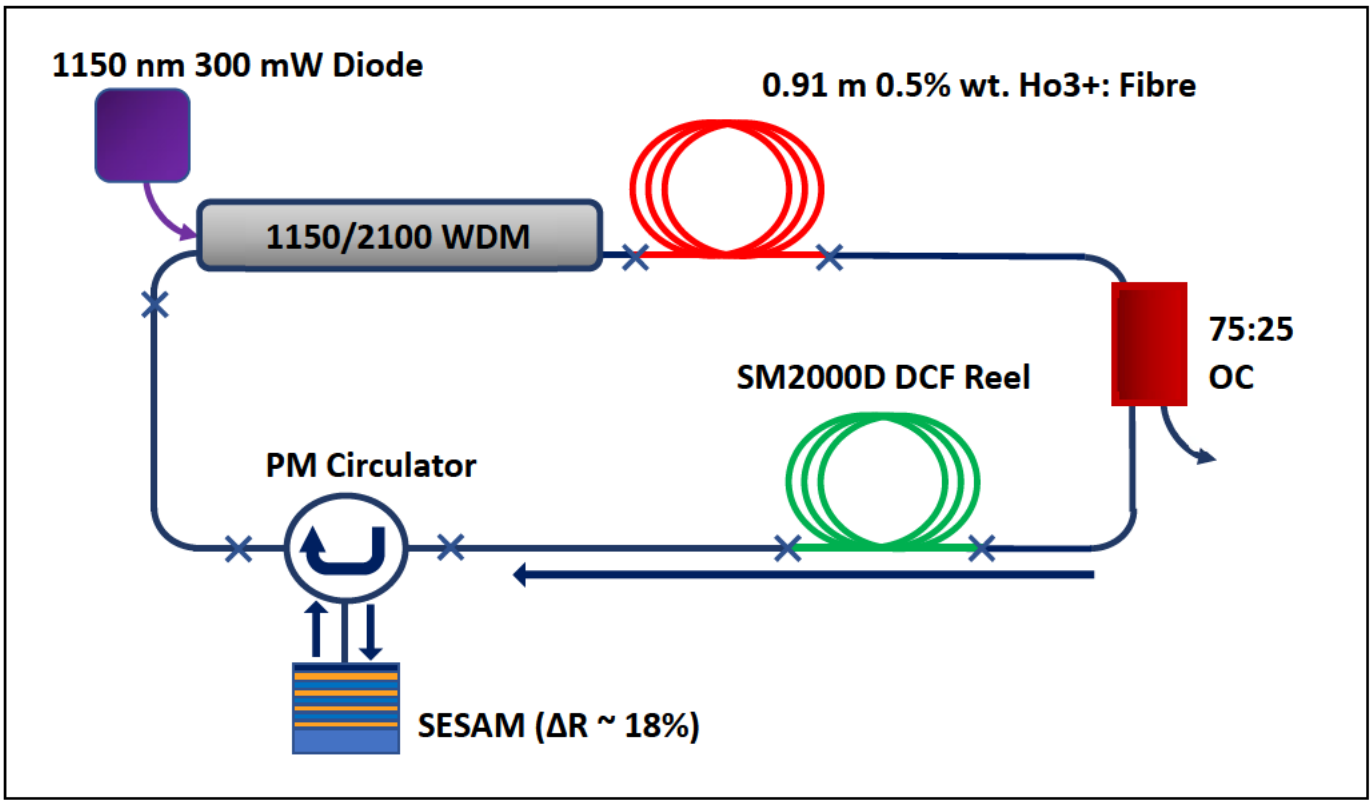

Figure 4.5.1: A schematic of the dispersion-compensated Ho-doped SESAM-mode-locked fibre laser. Fusion splices are marked with an 'X', and propagation direction is indicated by the arrows.

Note that this cavity design is identical to that in Section 4.4 but with the addition of a reel of SM2000D DCF before the circulator to provide the dispersion offset for the whole cavity, the length estimated by Equation 4.5.1. In the experiment this length varied from 5 to 13 m.

4.5.2 Numerical Results

The length of DCF in the cavity simulation was simply handled via the same routine as that used by the SMF, with appropriately tuned numerical aperture, mode field diameter and GVD. The length of the fibre was then set to lengths of 3–11 m in 2 m increments, providing five simulated datasets analysed herein, with the data recorded after 600 cavity round-trips.

As before, the code is available in Appendix D, with transient behaviour from 2–600 round trips available in Appendix H. The DCF was simulated as a single mode fibre with custom NA, core diameter and dispersion. The parameters used for simulated the DCF are summarised in Appendix F.

The effect of introducing even a small, 'undercompensating' length of 3 m DCF is immediately apparent, with noisy pulse splitting and satellite features abundant in the time domain in Figure 4.5.2(a). The pulse durations of the two main pulses (30 arbitrary intensity units high) are 1.05 ps and 2.99 ps respectively. The spectrum displays familiar interference patterns common to all multipulse regimes observed. No Kelly sidebands are predicted, as expected for dispersion managed regimes [6].

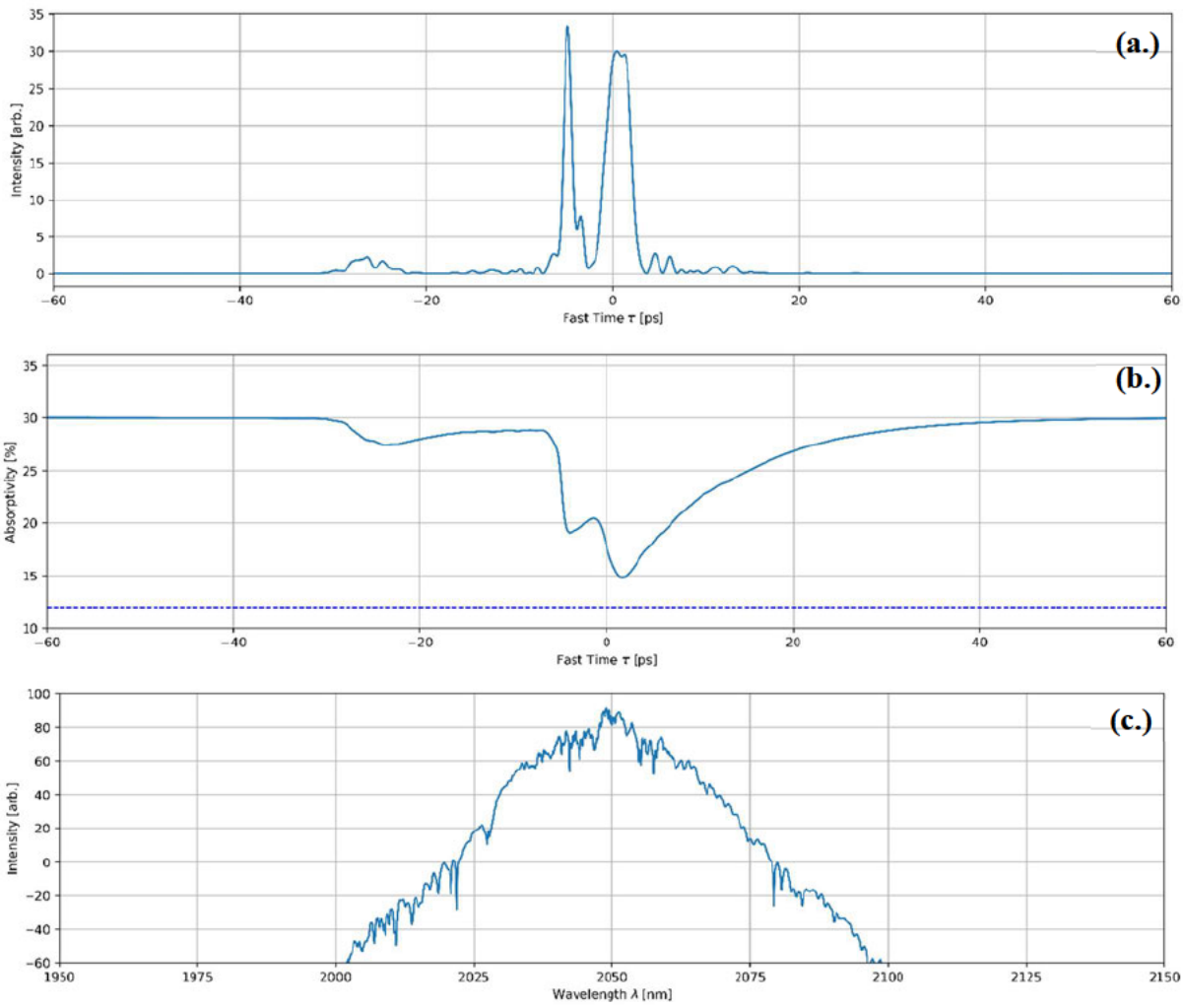

Figure 4.5.2: Simulation results for 3 m DCF length, (a.) time domain intensity, (b.) SESAM absorptivity and (c.) optical power spectral density.

The simulation results for 5 m DCF are shown in Figure 4.5.3 below. The time domain intensity, Figure 4.5.3a, shows the presence of pulse splitting, with a significant pedestal or ripple feature as is expected with unbalanced dispersion compensation [57-59]. The leftmost, primary pulse has a temporal FWHM of 1.11 ps, whereas the trailing sidepulse feature to its right is 693 fs long.

Again, the spectrum displays a lack of Kelly sidebands and the presence of complex, distorted features due to the presence of multiple pulses.

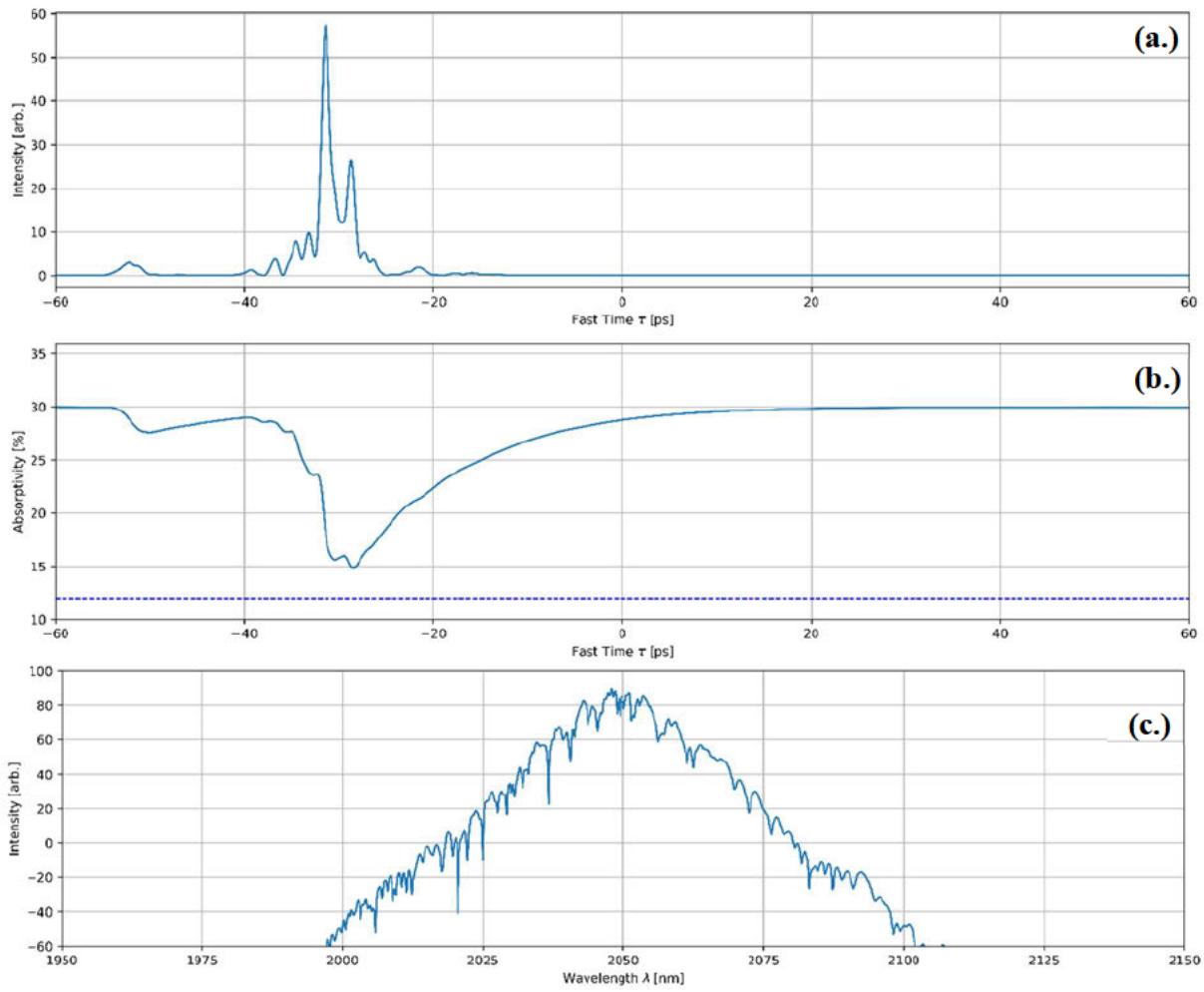

Figure 4.5.3: Simulation results for 5 m DCF length, (a.) time domain intensity, (b.) SESAM absorptivity and (c.) optical power spectral density.

The simulation for 7 m DCF generates one of the highest pulse qualities for the simulated results, shown in Figure 4.5.4 below, with only small pedestal features and a leading sidepulse of ~ 15% of the primary pulse intensity. The corresponding temporal FWHM in the time domain for the primary and side pulse are 1.04 ps and 1.66 ps respectively. This is the minimal primary pulse duration of any of the simulated results, although the experimental data shows a much stronger trend as seen in the section below.

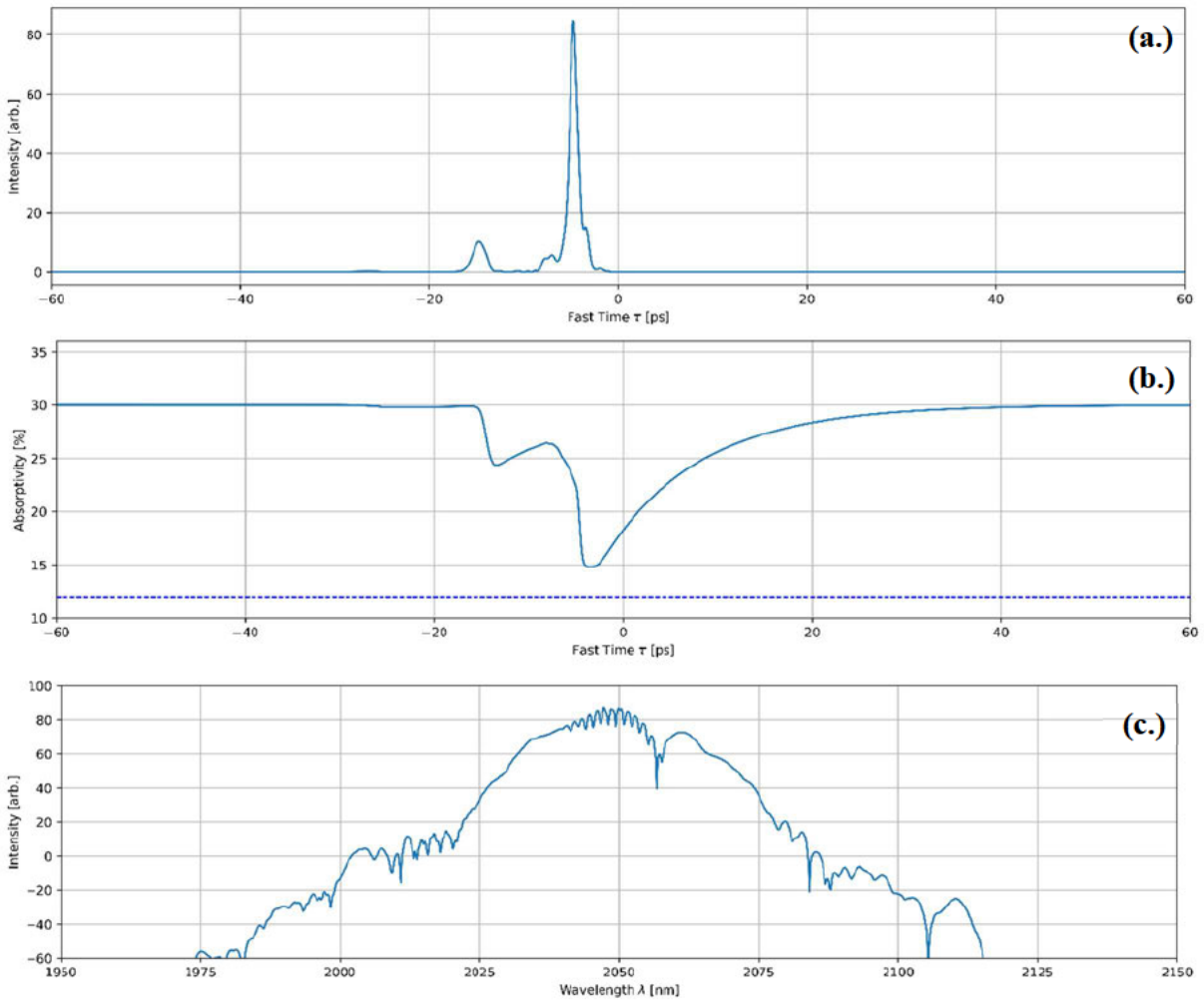

Figure 4.5.4: Simulation results for 7 m DCF length, (a.) time domain intensity, (b.) SESAM absorptivity and (c.) optical power spectral density.

At 9 m, the simulation predicts that pulse breakup begins to occur once more, with what appears to be at least seven distinct peaks in the time domain intensity of Figure 4.5.5a. The most energetic, 'primary' pulse bunch at the trailing edge (40 – 60 ps) of Figure 4.5.5a has a FWHM of 2.21 ps, whereas the second-tallest pulse has a FWHM of 1.89 ps. Lastly, the FWHM of the third tallest is 1.26 ps. The interference of such a noisy pulse bunch leads to the familiar distorted spectral features in the PSD of Figure 4.5.5c.

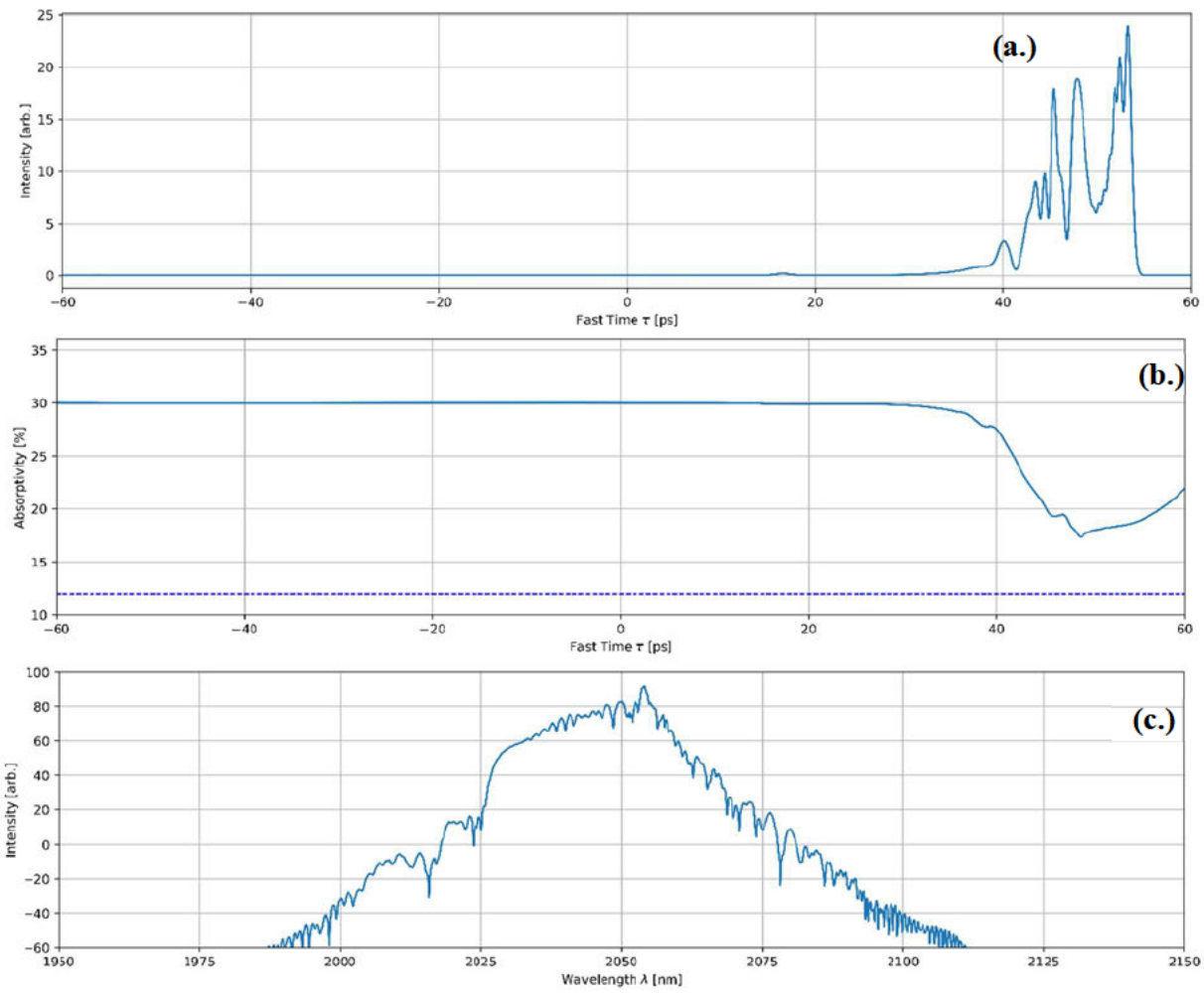

Figure 4.5.5: Simulation results for 9 m DCF length, (a.) time domain intensity, (b.) SESAM absorptivity and (c.) optical power spectral density.

Lastly, the simulation for 11 m DCF leads to an abrupt increase in pulse duration, but also a significant reduction in multipulse and side-pulse instabilities. The pulse in Figure 4.5.6a has a FWHM of 6.93 ps, over six times longer than those produced by smaller lengths of DCF. Simulations beyond 11 m yield similar results, with a steadily increasing relation in pulse duration with lengths longer than 11 m. This indicates that the normal dispersion introduced by this much DCF is leading to dispersion more than the anomalous dispersion present. Thus, pulses are no longer adequately compensated and broaden in time.

Interestingly, the spectrum in Figure 4.5.6c becomes largely flat with several peaks towards the longer wavelengths. This agrees with previous literature, where the interplay between SPM and normal GVD in the DCF leads to a flat-top spectrum, with SPM-induced spectral peaks towards the longer wavelengths as is visible in Figure 4.5.6c below [60, 61].

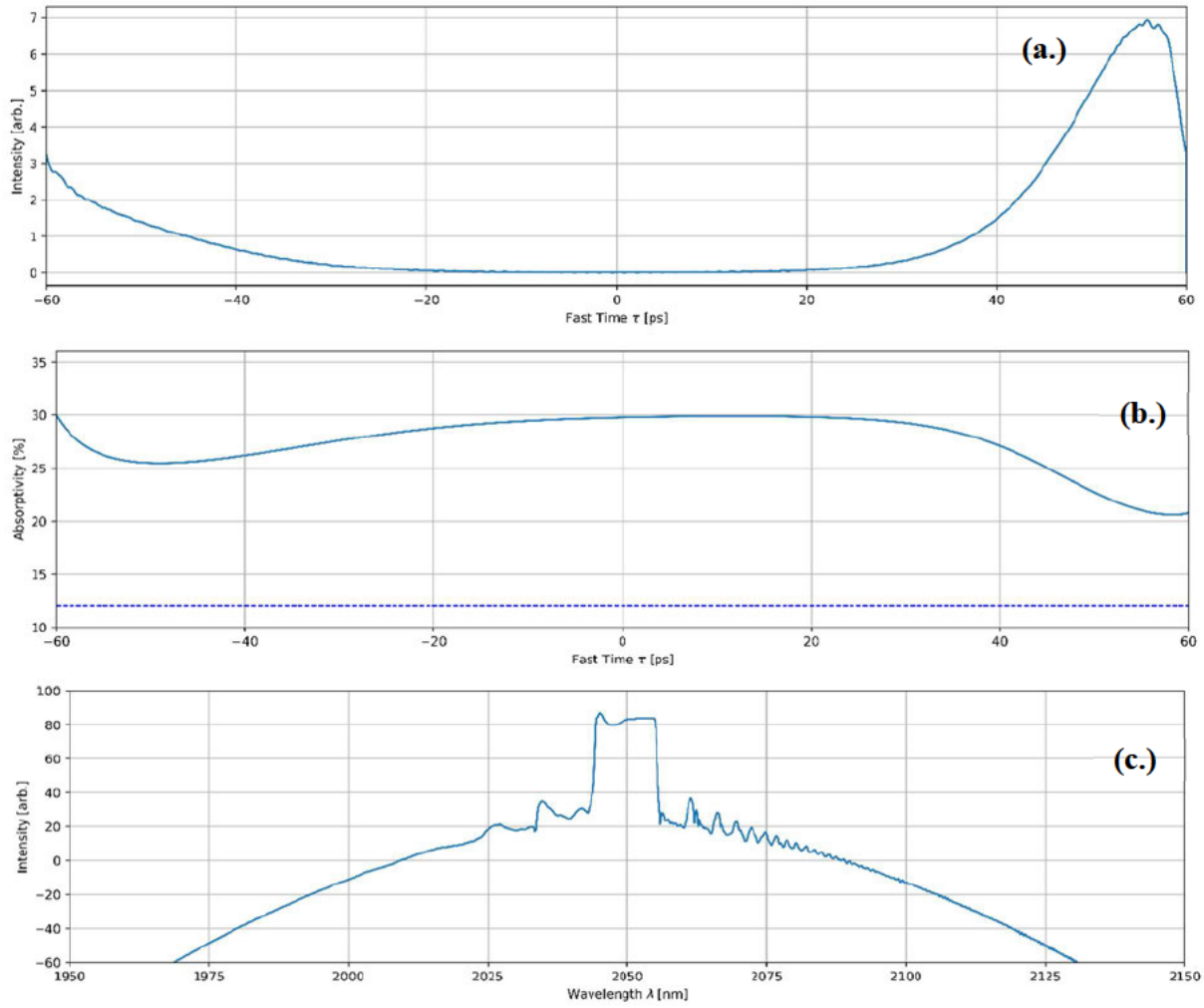

Figure 4.5.6: Simulation results for 11 m DCF length, (a.) time domain intensity, (b.) SESAM absorptivity and (c.) optical power spectral density.

Recall that the preliminary calculations from Equation 4.5.1 indicate that net zero dispersion should be at approximately 10 m of DCF for this cavity. Furthermore, the simulation results of Figure 4.5.6 strongly indicate that the laser is operating in a regime of small net normal dispersion, in agreement with the preliminary calculations. This implies that a longer length of (normal dispersion) DCF would only lead to excess normal dispersion and that the anomalous dispersion has been overcompensated. Therefore, the experiment investigates lengths from 5 to 13 m as this is the region of interest as indicated by these simulation results, around which normal and anomalous dispersion approximately cancel out.

4.5.3 Relative Intensity Noise vs. DCF Length

The interpulse RIN at each DCF length was measured using an oscilloscope as before for each length, excluding lengths where ML was unobtainable (see discussion). It was observed to vary largely, with no clear regression, with longer lengths displaying the lowest RIN, and shorter lengths displaying high RIN. Plots of lowest RIN and highest RIN pulse trains viewed on the oscilloscope are shown in Figures 4.5.7a and 4.5.7b. below respectively:

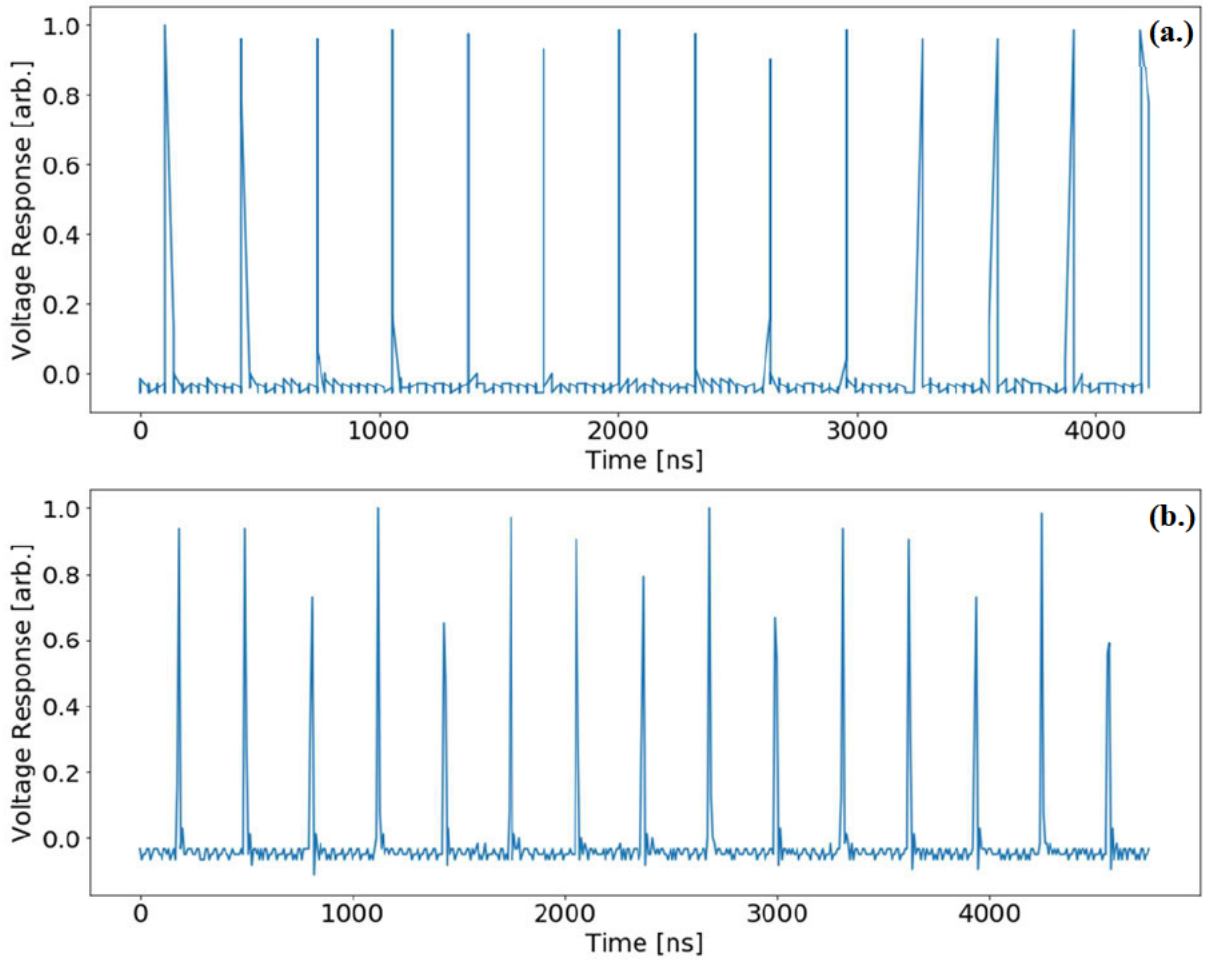

Figure 4.5.7: Example oscilloscope traces for (a.) low RIN at 8.6 m DCF and (b.) high RIN at 6.6 m DCF.

Note that the modulation of pulse height (energy) is somewhat chaotic for 6.6 m of DCF, indicating the relative pulse train instability at that short of a DCF length.

The depth of modulation from the height of the most energetic pulse to the height of the least at a 100 ns timebase was calculated from this data. A DCF length of 8.6 m showed the

shallowest modulation overall of 9.86%, only 2% more than the uncompensated design in Section 4.4, whereas the largest modulation of 39.8% was seen at a DCF length of 6.4 m, where a small, periodic fluctuation in pulse energy was observed, seen in Figure 4.5.7b. above.

The RIN of the peak heights was plotted against DCF length, fitted with a linear regression in Figure 4.5.8 below. It should be noted that at 8.6 m the datapoint is somewhat of an outlier from the predicted, linear trend, with a majority of data points lying in the region of ~ 30% RIN.

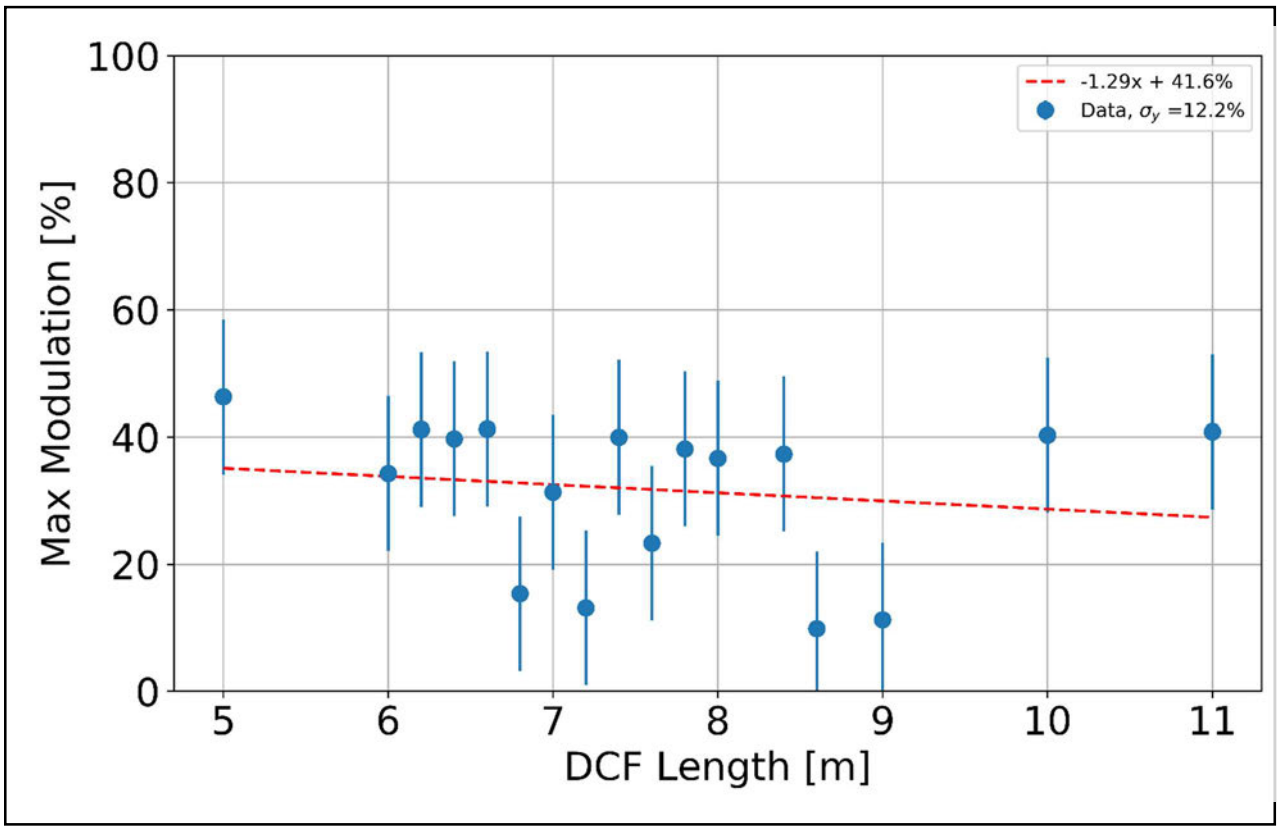

Figure 4.5.8: Plot of DCF length versus the RIN observed on the oscilloscope.

As shown in Figure 4.5.8 above, there appears to be a weak linear relation over this region at around 30% RIN, however the presence of several outliers and high variance makes it difficult to confirm the relation. Naively, there seems to be a tendency toward longer lengths to stably pulse, somewhere in the region of ~ 7 – 9 m of DCF serves as the optimum.

To confirm this, we look to the RF spectrum to obtain further stability metrics on laser diagnostics for the different DCF lengths.

4.5.4 RF Roll-off and SNR vs. DCF Length

The RF spectrum of the laser output was measured across a 1 GHz span for all lengths of DCF tested. As before, maximum value of 3 dB drop over the 1 GHz span was used as a benchmark for pulse train stability. An example of an RF spectrum for 9.0 m DCF is shown in Figure 4.5.9 below:

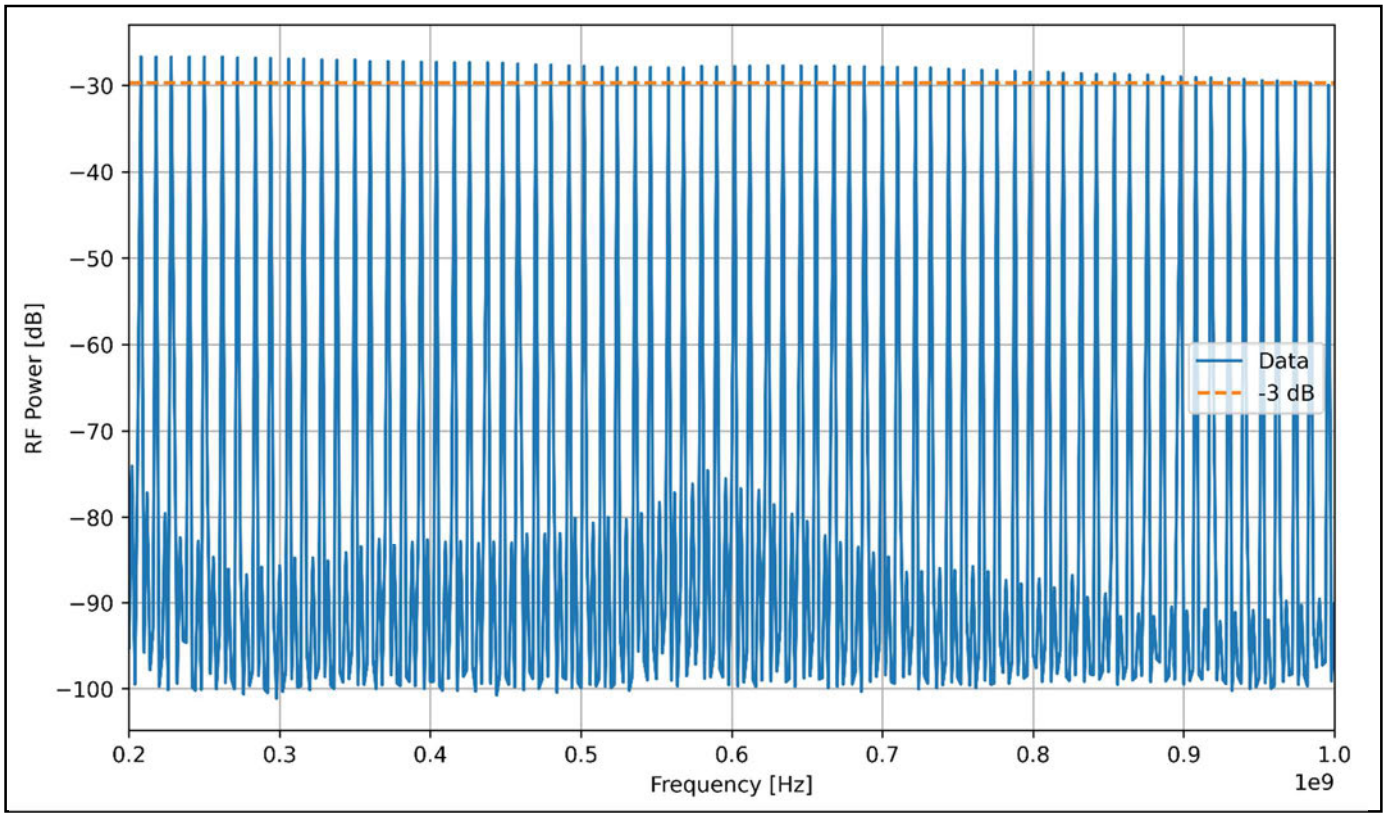

Figure 4.5.9: Example plot of the RF spectrum for 9.0 m DCF. Note the presence of a spur-like structure at -80 dB due to phase noise.

The largest (i.e. worst) RF roll-off observed was at a DCF length of 5.4 m, with a drop of 4.27 dB of RF power across the 1 GHz RF span. Such a result is expected as the laser was largely inoperable at DCF lengths approaching and below 5.4 m, where the cavity would often fall into QS or QML regimes with only seconds of semi-stable CML operation being achieved.

Curiously, smallest RF roll-off was obtained at a DCF length of 6.2 m, with a drop in power of only 2.06 dB over the 1 GHz span, close to the edge of the range of DCF lengths for which the laser was still stable.

An ordinary least squares fit is performed on the roll-off data, with the fit and roll-off variance displayed in the legend of Figure 4.5.10. According to the figure, RF roll-off appears to trend slightly downwards toward 6.0 m, before sharply increasingly at 5.4 m, at which shorter lengths caused the laser to no longer mode-lock. The above low-points in the roll-off plot may indicate a trade-off between pulse stability and temporal FWHM minimisation.

It should be noted that the shortest ACF FWHM (at 7.2 m) and the lowest RF roll-off (at 6.2 m) did not occur at the same length of DCF, indicating that there may exist some sort of trade-off between stability and pulse duration over only 1 m difference in DCF used. The instability observed may be due to a variety of factors involved with a change of non-PM DCF length, such as polarisation mode dispersion changes, splicing and fibre losses and more. However, it should be noted that all splice losses were monitored and kept to a constant (estimated) minimum of 0.01 dB, automatically calculated on the FITEL fusion splicer via the methods outlined in Chapter 2. Any discrepancies in the data related to splice quality are therefore minimised as a source of systemic decrease in laser performance.

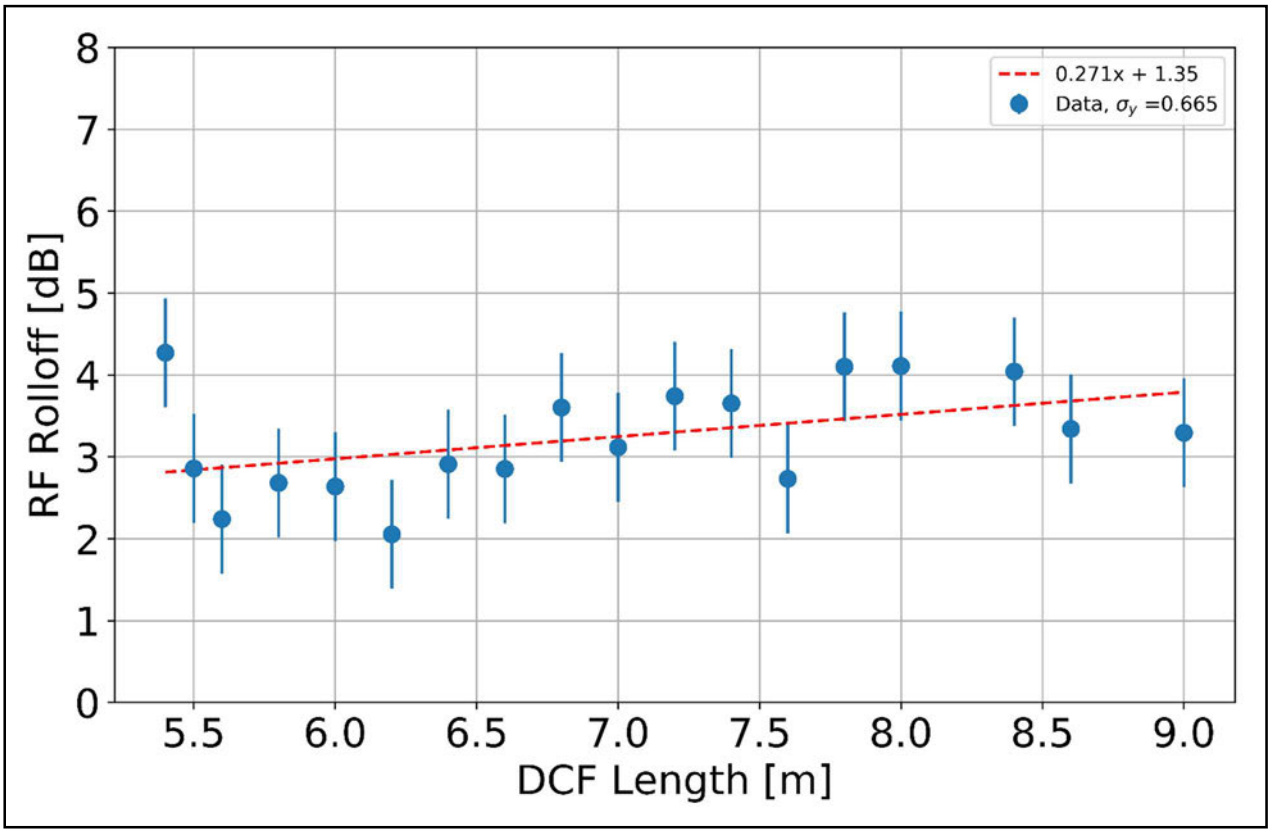

Figure 4.5.10: Plot of RF roll-off vs. DCF length.

While the relation between roll-off and DCF length shows several valleys and crests in a nearly noise-like fashion, a positive linear fit accounts for much of the data barring the sharp jump in instability (high roll-off) at 5.4 m DCF, beyond which the laser would no longer mode-lock long enough for measurements to be taken.

Otherwise, this seems to indicate a tendency for stability toward shorter lengths above ~ 5.4 – 5.5 m DCF, whereas the RIN measure in Figure 4.5.8 shows a negative slope instead, minimising toward 8 – 9 m. This may indicate that the true stability region lies between these points of interest, somewhere in the 6 – 8 m region. This is further indicated by Figure 4.5.11 below, which in agreement with Figure 4.5.8, a plot of RF SNR vs. DCF length, shows an increasing stability toward longer lengths.

Again, this shows a positive linear trend toward longer DCF lengths, ie. higher stability toward 9 m DCF, with the only significant outliers at 6.8 and 7.2 m.

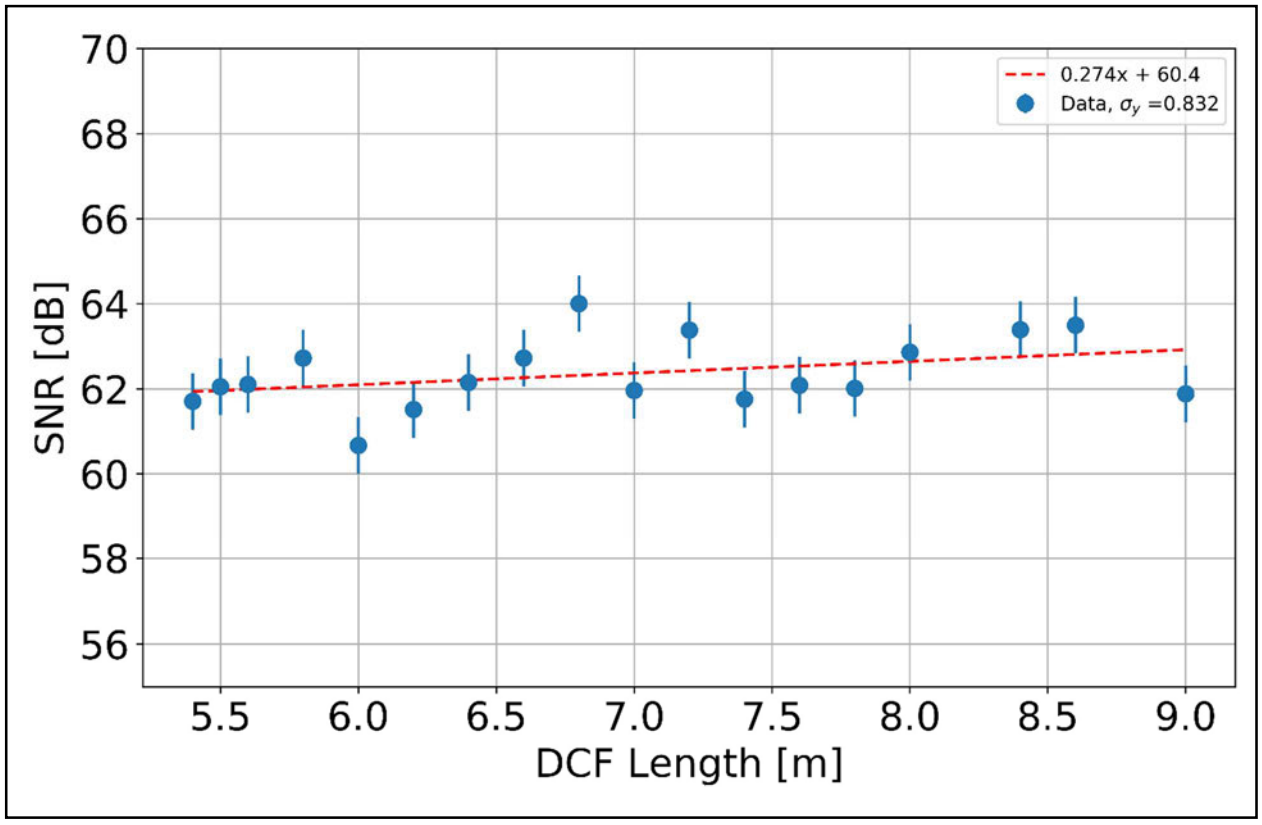

Figure 4.5.11: Plot of RF SNR vs. DCF length.

4.5.5 Optical Spectrum FWHM vs. DCF Length

The optical spectrum FWHM was determined by measuring the width of the spectrum at the 3 dB point. It was found that the smallest spectral width of 1.69 nm was obtained at 5.4 m of DCF, indicating a relative lack of broadband spectral content within the cavity during mode-locked operation.

Such a small spectral FWHM was likely caused by the distortion of the spectrum due to the presence of small, peak-like sidebands and wave-breaking crests in the spectrum, both related to soliton propagation in the dispersive regime (as opposed to the dispersion managed regime where no sidebands are present). By contrast, the largest spectral FWHM of 18.6 nm was obtained at a DCF length of 8.2 m. The spectral FWHM vs. DCF length is plotted in Figure 4.5.12 below.

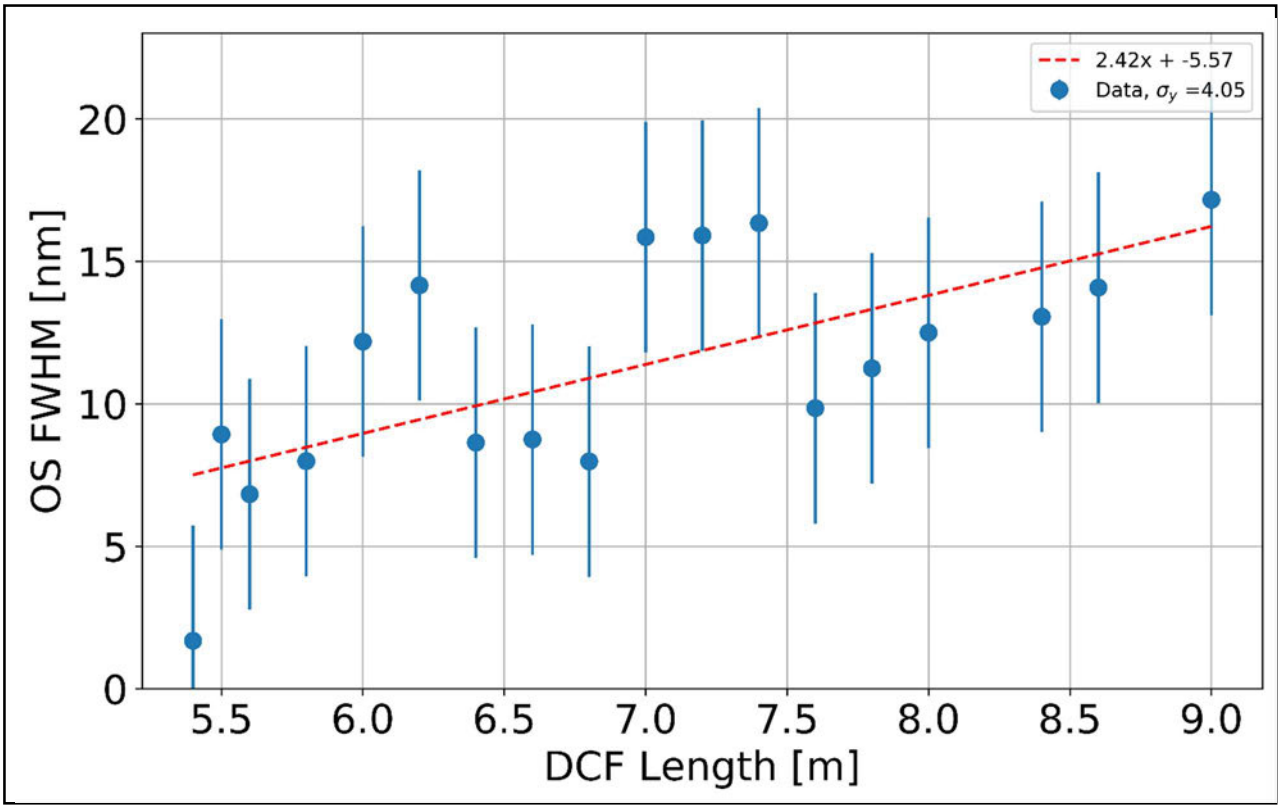

Figure 4.5.12: Plot of optical spectral FWHM vs. DCF length.

The relationship of spectral FWHM and DCF length shows several crests and troughs as DCF length varies, but most notably the overall trend of the relationship shows that longer DCF

lengths (i.e. more positive intracavity dispersion) gives rise to a broader spectrum. However, notable peaks in this relation showing increases in spectral FWHM are located at 6.0 m, 7.0 m to 7.4 m and 8.2 m, indicating that there may be lurking parameters and effects that are introduced with the increase or decrease of DCF length.

This could be due to effects such as polarisation mode dispersion (PMD) introduced with additional non-PM DCF length combined with the polarisation gating of the PM circulator or other gain/loss dynamics introduced with specific amounts of DCF.

4.5.6 Autocorrelation FWHM vs. DCF Length

The autocorrelation FWHM was approximated by fitting a sech^2 function to the primary pulse observed in each ACF trace. Satellite pulses were removed from the data where appropriate to get a better fit for the sech^2 function, and then added back to the data after the primary peak was fitted. In some cases, the side-pulsing would occur so close to the primary pulse peak that the primary pulse would develop a pedestal-like structure about its base, causing the measured ACF FWHM to be much larger than it otherwise. The estimated ACF FWHM vs. DCF length is plotted in Figure 4.5.13 below.

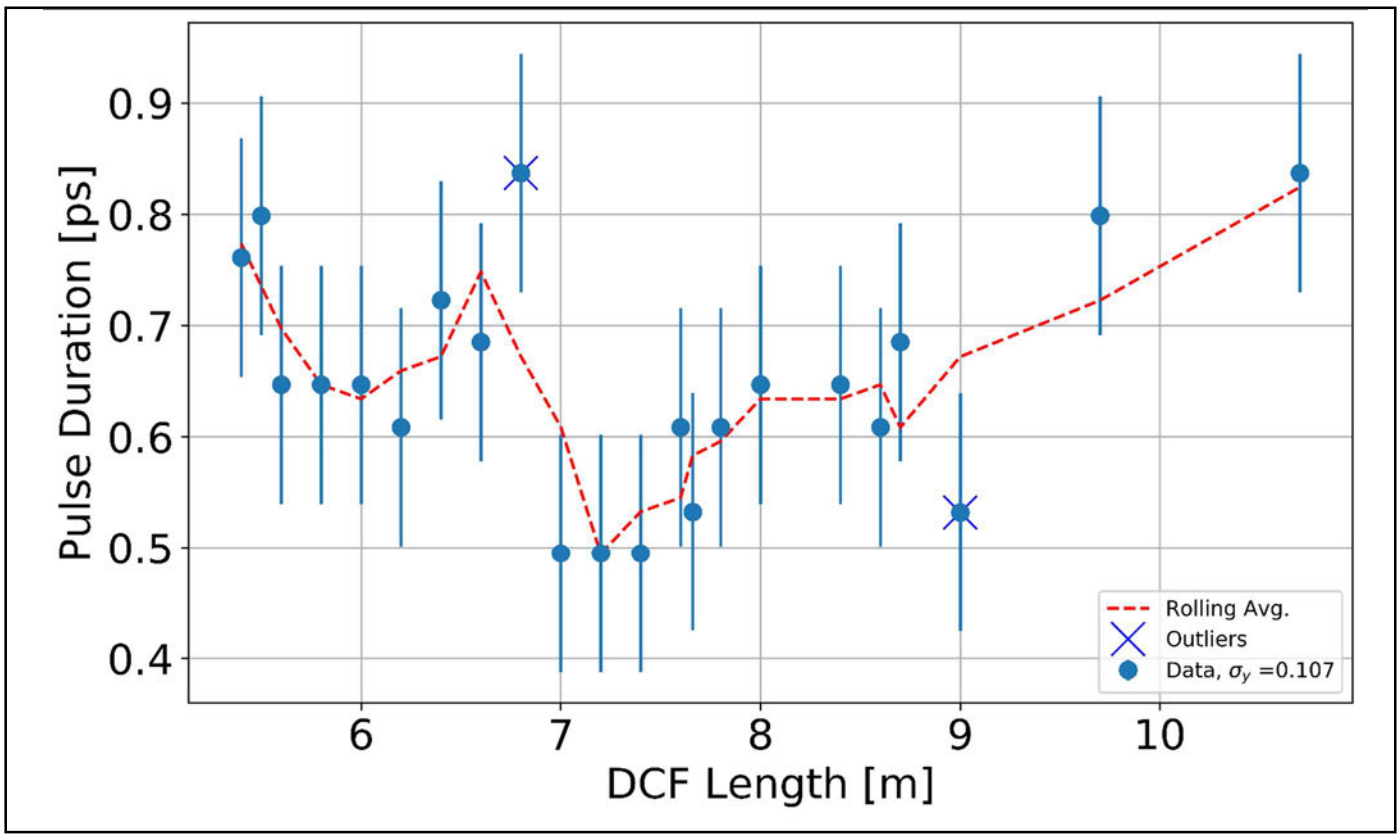

Figure 4.5.13: Plot of DCF length versus temporal FWHM estimate obtained from the ACF.

The ACF FWHM demonstrated the clearest relationship of all characterisation instruments when plotted against DCF length, demonstrating a noticeable minimum in pulse duration in the 7.0 m to 7.4 m region. This is indicative of the strong effect of second order dispersion on pulse shaping and thus pulse duration in the cavity via tuning the DCF length, and in good agreement with previous literature [54]. Furthermore, recall the simulation results for pulse formation from 3 – 11 m DCF. At 7 m it was found that the pulse FWHM was 1.06 ps, with side-pulsing minimised versus the other lengths simulated.

In particular, while continual decrease of the DCF (and thus the negative dispersion) may, in theory, shape and produce shorter pulses, having too short of a pulse (i.e. not enough negative dispersion) can destabilise soliton pulses [62]. In Figure 4.5.13 we see that pulse duration sharply increases beyond 7.0 m of DCF. This was due to the growth of pedestal-like features in the time domain, due to the low negative dispersion permitting the background continuum to grow, broadening the temporal FWHM [50].

While the ACF trace only provides an estimation of pulse width, it may be combined with the spectral FWHM to determine if a pulse is close to the time-bandwidth limit, a fundamental limit of pulse duration vs. spectral width (and is thus a good indicator of ultrashort pulse duration).

Lastly, two outliers are notable here: DCF length at 6.8 m and 9 m, both of which have far longer and far shorter ACF FWHM than their neighbouring counterparts respectively. This error may be attributed to the cavity setup and its relative sensitivity to mechanical perturbations as the SESAM was left un-epoxied to the flat-cleaved PMF from the circulator, which was mounted to a three-axis stage for SESAM fluence adjustments. However, acoustic foam was used to partially isolate the oscillator and the amplifier from any vibrations coupled from the optical table. Any perturbations from one set of measurements to the next may cause a slight change in cavity energetics due to this setup.

Furthermore, the ACF algorithm only provides an estimate of the true pulse temporal FWHM, and may explain the strange, digitization-like distortions at 5.6 – 6 m and 7 – 7.4 m DCF where there is no change whatsoever to the ACF FWHM, before abruptly continuing to change after these breakpoints.

4.5.7 Time-bandwidth Product vs. DCF Length

Recall that optical pulses are limited in duration for a given spectrum. This is a fundamental result of Fourier theory, whereby the minimum achievable duration is set by the spectral width and a constant factor associated with the assumed pulse shape [63]. In the case of solitons, we are generally concerned with hyperbolic secant squared pulses, which have a minimum time-bandwidth product (TBP) given by Equation 4.5.2 [64]:

$$\Delta v \Delta \tau \approx 0.315 \qquad (4.5.2)$$

Where Δν is the spectral bandwidth of the pulse and Δτ is the temporal FWHM. For pulses near the TBP limit, a decrease in temporal duration must correspond to an increase in spectral width, and vice versa [63]. Producing an ultrashort pulse close to the TBP (in this case 0.315) requires careful dispersion management to eliminate chirp and prevent spectral distortions which will, in turn, distort the temporal profile.

Pulses produced by the laser, at almost all lengths of DCF, came within approximately 0.1-0.3 of the minimum TBP value of 0.315, demonstrating that it can produce nearly transform limited pulses. Further dispersion management will likely be required to not only bring the TBP of the laser output closer to the minimum of 0.315, but to possibly eliminate spurious side and multi-pulsing seen in the ACF traces above.

The TBP and the DCF length are plotted against one another in Figure 4.5.14, with a least-squares linear fit plotted over the data.

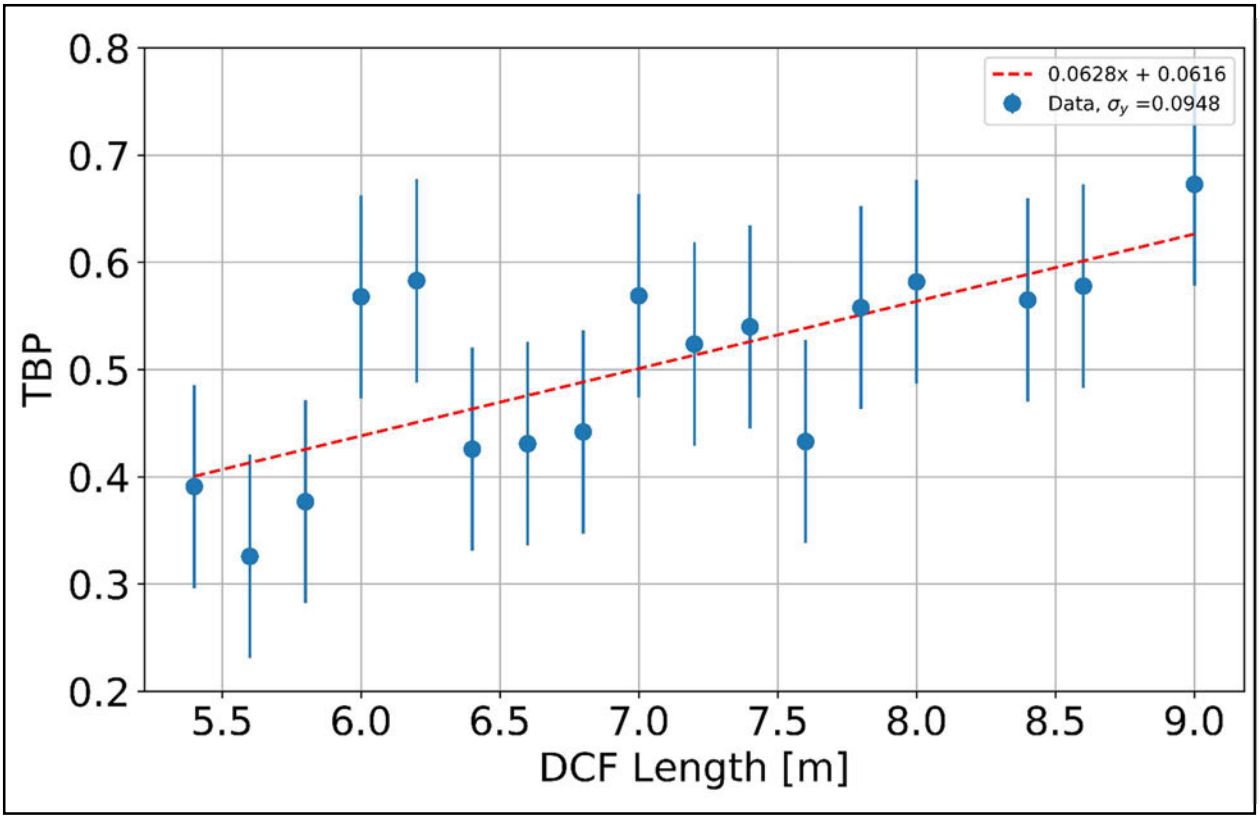

Figure 4.5.14: Plot of DCF length versus the time-bandwidth product.

It appears from Figure 4.5.14 that the overall dispersion in the cavity is relatively low, and thus chirp is relatively low. Furthermore, it appears that there is a slight positive trend with DCF length, with smaller lengths giving lower TBP values toward 5.4 m DCF (beyond which the laser no longer mode-locks). This indicates that DCF lengths toward 8–9 m introduce excess chirp, and therefore cause longer pulse durations, in good agreement with Figure 4.5.13.

However, from the simulations earlier in this section it should be noted that the relative sensitivity of the system to considerable, but not extreme changes in GVD can lead to pulse splitting. Furthermore, despite DCF lengths from 7.0 to 7.4 m giving the shortest pulses, their corresponding TBP values are somewhat middling, fluctuating about 0.4 indicating the presence of some form of chirp. This contrasts with the minimum recorded TBPs, which occur around 5.6 m DCF. The difference in dispersion apparently present could be some form of instrumental noise, miscalibration, or a true representation of so-far uncompensated effects of higher order dispersion such as third-order dispersion (TOD).

4.5.8 Discussion

Overall, desirable operation of the laser was generally seen with lengths of DCF ranging between 6.0 m and 8.0 m. In some cases, a favourable pulse FWHM (spectral or temporal) was obtained whereas in others the pulse train stability seen in the RF spectrum roll-off and oscilloscope peak-to-peak modulation was optimised.

This array of differing laser operation characteristics (all reaching optimal values at relatively different DCF lengths) presents an interesting problem in that temporal narrowness may be traded-off for additional stability and may result from tweaking the overall round-trip dispersion via the DCF of by the interplay of many different effects inherently introduced by using different fibre lengths, such as splicing/bending losses, PMD or TOD.

However, most desirable length of DCF for this cavity was determined to be around 7.2 m, where the ACF FWHM was minimised while maintain a RF roll-off around only 3 dB. Compared to 7.0 m and 7.4 m of DCF, this length demonstrated a slightly smaller TBP value (see Figure 4.5.14), however this was within standard error of the neighbouring data points and does not appear statistically significant.

4.5.9 Optimal DCF Length

The characteristic measurements of the laser with 7.2 m of DCF are displayed in Figure 4.5.15 below. The oscilloscope trace as seen in Figure 4.5.15 (a) shows a relatively little but present amount of instability, with pulse energy varying by ~10–15% across a 1 μs time window. While useful, we may also look to the RF spectrum in Figure 4.5.15 (c) to gauge the stability of the pulse train.

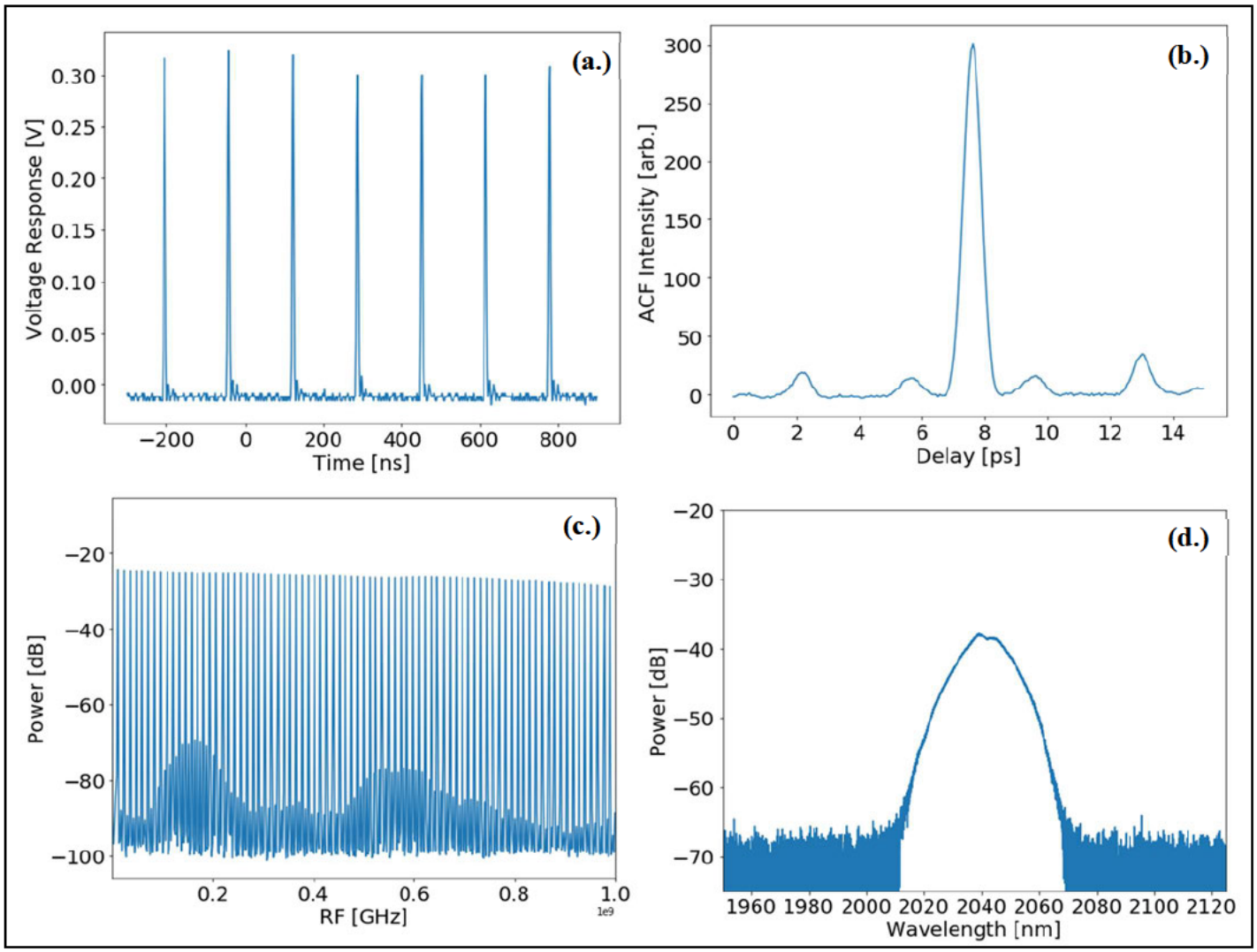

Figure 4.5.15: Characterisation of laser output with 7.2 m DCF. (a) Oscilloscope trace, (b) ACF trace , (c) RF spectrum, (d) Optical spectrum.

Note the presence of multiple pulses in Figure 4.5.15 (b). Operation at all lengths of DCF showed that multiple pulses were present within the cavity but changed position relative to the primary pulse based on the amount of DCF present. Interestingly, the sidepulse is located approximately 7 ps away from the primary pulse, in good agreement with the simulation

result of the time-domain intensity shown in Figure 4.5.4, where a similar sidepulse is approximately 10 ps away from the primary pulse. Such features were not observed experimentally or predicted numerically in Sections 4.3 and 4.4, where no normal dispersion was introduced. This indicates that the introduction of a large reel of normal dispersion DCF leads to pulse splitting of the dispersion-managed soliton. Note that the simulation results in Figure 4.5.4a overestimate the primary pulse duration at 1.04 ps, compared to the measured experimental value of approximately 500 fs. Overestimation of the pulse temporal FWHM was also common amongst all numerical results. This consistent discrepancy may indicate that the estimated intracavity energy, and therefore nonlinear pulse shaping, was too small, or the estimated third order dispersion parameter used in the simulation was too small, as discussed further in Appendix F.

Apart from the side-pulse structure, the ACF reveals a sharp peak with a hyperbolic secant-squared profile with an estimated FWHM of 494 fs.

Similarly, Figure 4.5.15 (c) shows, like every other measurement, the presence of an underlying harmonic sub-structure at -75 dB familiar to many results in Chapter 4, largely due to timing instability. The overall envelope that dictates the power in these harmonics seems to vary somewhat randomly, spiking at 200 MHz and 600 MHz, indicating the relative instability of the harmonic content at this level. This further motivates the mitigation and eventual removal of these pulses from an ideal, optimised laser seed design, the methods of which are discussed in Chapter 5.

The optical spectrum in Figure 4.5.15 (d) shows few distinct features, following a smooth Voigt (or Lorentzian if discounting broadening effects) spectral profile. There are, however, two points of interest. Firstly, the Kelly sidebands that were present in the laser's output in Section 4.4 have been removed entirely. This is typical for soliton-like pulses in the 'dispersion-managed' regime, whereby the sideband formation is supressed [65, 66].

The second structure of interest is at the peak of the spectrum, where there is an apparent 1 dB double-peak atop the spectral profile. Such structure typically results from multipulse interaction and is visible in the simulation results when such regimes occur. This clearly matches observations in Figure 4.5.15 (b) where multiple pulses are indeed present. This presents another possible avenue of multi-pulse identification within the cavity and may be used as a metric to study multi-pulse instabilities.

Chapter 5: Conclusion

5.1 Outline

This thesis presented an all-fibre mode-locked laser source at 2 μm, utilising a SESAM-soliton based mode-locked system in a variety of dispersion-managed, bidirectional, and unidirectional pumping schemes. The resulting operating characteristics were measured, and the performance both from expected numerical projections and experimental work were compared amongst the designs.

To summarise, this involved:

- Design, construction, and demonstration of eight separate Ge-silica, active Ho-doped single-mode fibre laser, six of which were successfully mode-locked with a SESAM to produce picosecond pulses, both through numerical simulations and experiments.

- Design, construction, and demonstration of a single-pass amplifier stage based on the same Ho-doped fibre arrangement to achieve up to 10 dB amplification.

- Demonstration of a stable (sub 2 dB RF roll-off) picosecond Ho:fibre laser design.

- Optimisation of second order dispersion of this laser design utilising dispersion compensating fibre cutbacks.

To the best of our knowledge, this is the first comprehensive numerical and experimental review of optimising a holmium fibre mode-locked source within the literature.

Chapter 1 outlined the problems and prospects cited within the literature, and the wide range of applications that this projects results may be applied to. Furthermore, a review of many similar studies in developing mode-locked MIR sources was presented. Lastly, the key points and objectives of this project were outlined.

Chapter 2 reviewed the theory behind optical fibre, devices and the underlying physics relevant to the experimental aims of the project, in addition to laying the foundational

knowledge to understanding the Runge-Kutta 4th order interaction-picture pulse propagation model.

Chapter 3 explored preliminary results of the project in the context of operating regimes such as Q-switched, Q-switched mode-locked, continuous-wave mode-locked and multi-pulse mode-locked, in addition to an overview of characterisation equipment and methods, and the justification thereof of these methods. A discussion of mode-locking instabilities was also included, with an overview of pulse breakup due to higher order dispersion and nonlinearity provided.

Chapter 4 presented the experimental and numerical results of this project. In order, this involved designing multiple Ho:fibre laser designs guided by the numerical model, utilising different component orders and arrangements to achieve different operating performance, with full characterisation and discussion thereof for each. Secondly, the most stable result was presented alongside the corresponding numerical result, schematic and the design of the single-pass bidirectionally pumped Ho:fibre amplifier for the master oscillator output. Lastly, dispersion compensating fibre cutbacks were utilised to tune the balance of GVD and SPM to achieve minimised pulse dispersion and thus optimise the duration, with the full stability performance characteristics discussed as a result.

5.2 Results Summary

5.2.1 Section 4.3 Results

Section 4.3 explored seven different cavity designs, exploring the effect of component order relative to SESAM position within the ring cavity. Five of the seven designs were successfully mode-locked, with a variety of average power, RIN, RF SNR and roll-off, ACF FWHM and optical FWHM obtained.

A summary of the performance of the seven designs is given in Table 4.3.2:

	RIN	OS FWHM [nm]	Central Wavelength [nm]	ACF FWHM [ps]	TBP	RF roll-off [dB]	RF SNR [dB]	Rep. Rate [MHz]	Avg. Power [mW]
Design 1	39.1%	12.3	2075.7	1.99	1.69	9.0	62.5	18.0	13.2
Design 2	42.6%	6.74	2058.1	1.57	0.748	7.0	69.2	19.8	23.6
Design 3	45.0%	12.3	2085.3	1.44	1.22	5.5	59.6	13.8	25.4
Design 4	49.1%	4.64	2063.4	~	~	20.2	28.8	90.0	20.5
Design 5	26.7%	~	2069.3	~	~	8.1	31.9	98.0	20.6
Design 6	38.3%	5.55	2074.2	1.78	0.677	5.4	69.1	15.4	43.0
Design 7	39.4%	5.71	2072.5	1.66	0.66	7.7	70.6	11.8	35.8

Table 4.3.2: Tabulated summary of performance of designs 1 – 7.

Overall, it was found that designs that placed the gain close to the SESAM (i.e. higher SESAM saturation) saw comparable or higher to those that did not, and showed over double the average power output of those that did not. This indicates a trade-off between stability and pulse energy due to the nonlinear absorption of the SESAM for designs that utilise a SESAM-adjacent gain.

Note that these designs still had considerably more RIN than that presented in Section 4.4, the results of which are summarised in Section 5.2.2.

5.2.2 Section 4.4 Results

Section 4.4 demonstrated the first successful cavity design of Chapter 4, using a simple singly pumped ring cavity design, shown in Figure 4.4.1 below. Recall that this design, shown in Figure 4.4.1 below, served as a basis for the results of Section 4.5:

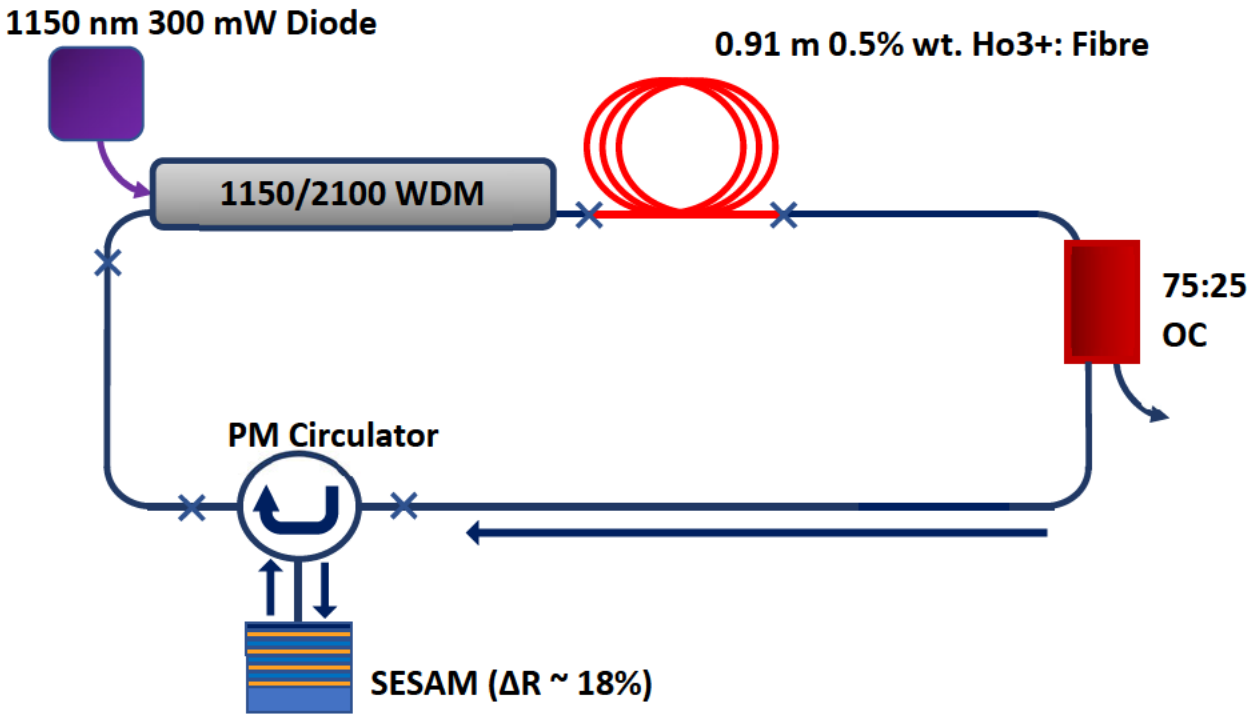

Figure 4.4.1: A diagrammatic representation of the Ho-doped SESAM-mode-locked fibre laser. Fusion splices are marked with an 'X', and propagation direction is indicated by the arrows.

The output consisted of 2.92 ps hyperbolic secant-squared pulses, at a repetition rate of 20 MHz and a central wavelength of 2029.1 nm (4 nm FWHM). The stability of the laser was indicated by 8.2% RIN, RF roll-off of 1.76 dB and RF SNR of 63 dB. These stability metrics indicate that the design presented in Section 4.4 is the most stable of all eight designs tested, including both those tested in Section 4.3 and the dispersion-compensated design in Section 4.5.

5.2.3 Section 4.5 Results

Section 4.5 focussed on numerical and experimental methods to optimise the dispersion of the laser presented in Section 4.4. Recall Figure 4.5.8, the key result of Section 4.5, shown below:

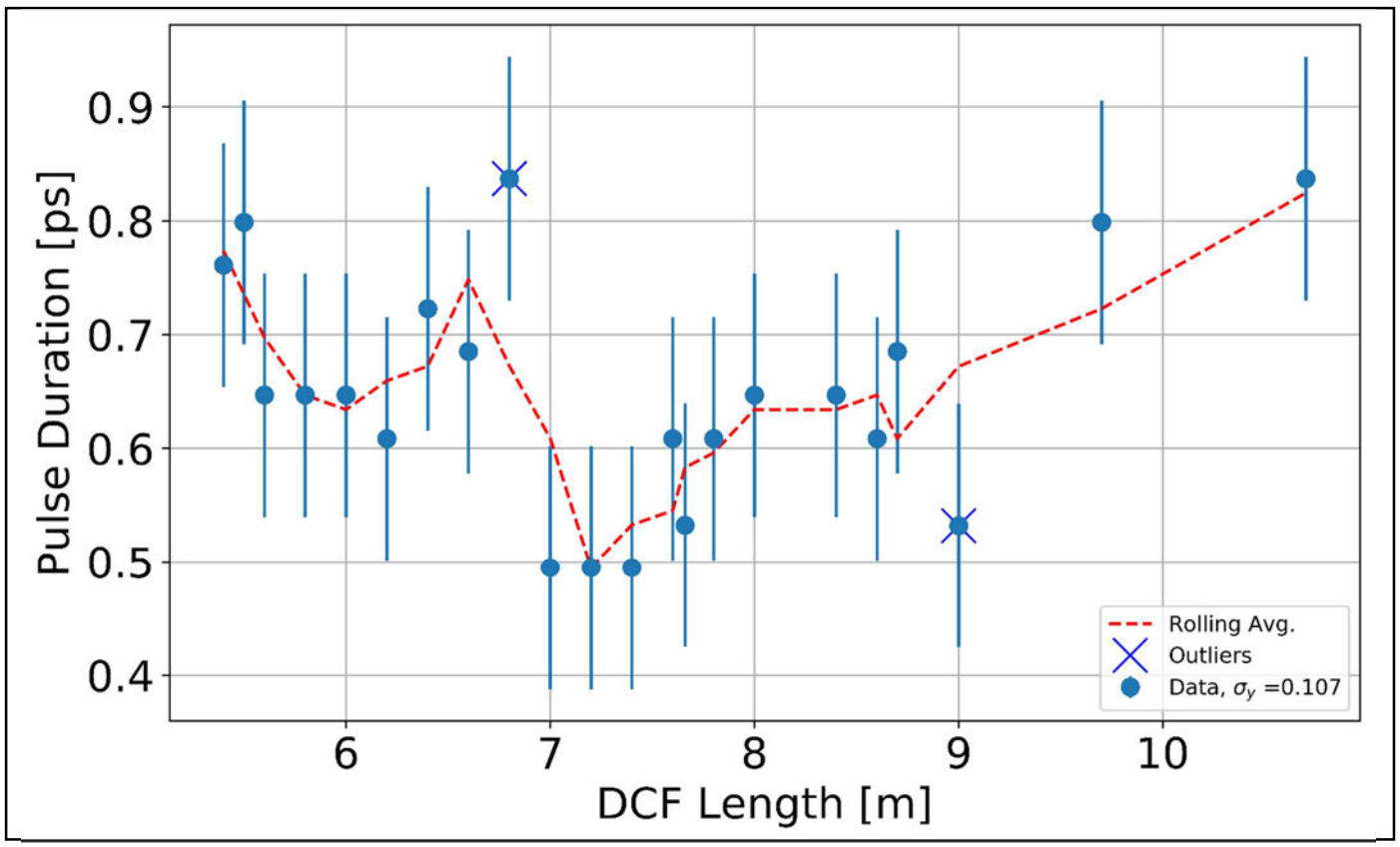

Figure 4.5.8: Plot of DCF length versus temporal FWHM estimate obtained from the ACF.

It was found through experimental DCF cutbacks that the pulse duration was minimised at DCF lengths from ~ 7.0 to 7.4 m. This was in good agreement with the numerical results, which demonstrated dispersive pulse spreading and instability away from this region of DCF length, for lengths both significantly shorter or longer than approximately 7 m of DCF.

Other performance characteristics such as RF SNR and roll-off, optical FWHM and interpulse RIN were also investigated, but no clear relation was observed, unlike the simulations which predict chaotic pulse breakup.

5.3 Future Work

5.3.1 Preamble

While the above goals were that which fit within the scope of the project, further steps were considered and may be taken to improve upon the designs and work of this thesis in future. These methods are outlined below.

5.3.2 Pulse Picking and Active Mode-lockers

Recall the presence of a persistent, phase-noise like structure about -90 dB in many RF spectra in Chapter 4. A close-up of the sidebands in the RF spectrum from Section 4.4 is shown in Figure 5.3.1 below:

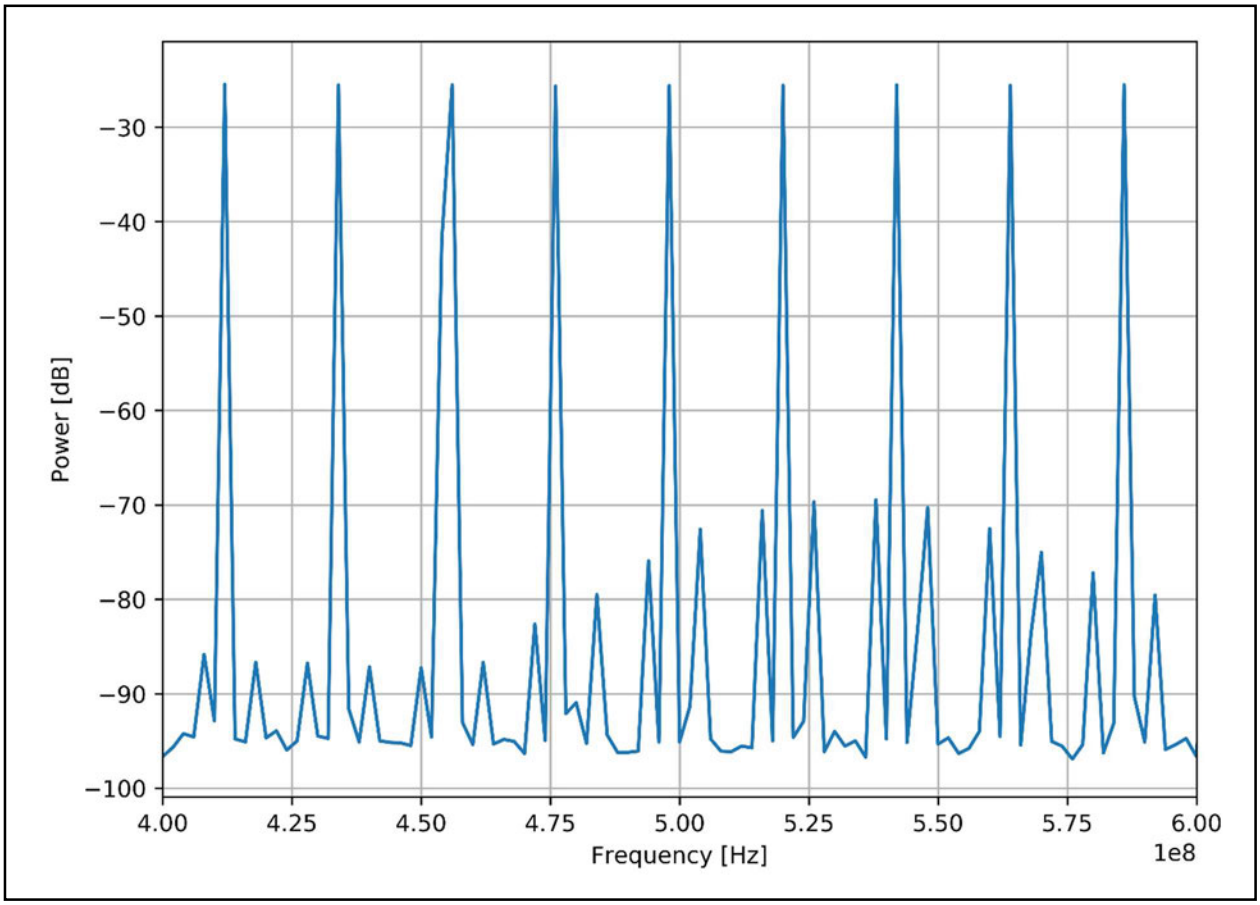

Figure 5.3.1: Example RF trace with phase noise sidebands at -70 dB and below.

As discussed prior in Chapter 3, these sidebands of the harmonics are born out of the noise in pulse timing from the oscillator. One such method to remove these timing instabilities is to

introduce an active element to force repetition rates to synchronise with an optoelectronic device, known as pulse picking. Devices such as acousto-optic or electro-optic modulators (AOMs, EOMs) are often employed to achieve this for a variety of cavity designs [1-5].

Future cavity designs could utilise an external electronic RF timing source to synchronise to the repetition rate of the oscillator, ensuring electronically controlled timing phase to reduce or remove these sidebands.

5.3.3 SESAM Fabrication and Optimisation

Recall the discussion in Section 4.2, where a brief review of literature showed that SESAM parameters may be tailored to further improve mode-locked laser performance [6-10]. Due to the lack of local infrastructure and capability, along with budgetary and time constraints, this was one such potential optimisation region that was relatively unexplored.

A handful of SESAMs (BATOP GmbH), 2 μm, SMF coupled were used in this thesis, with absorptivities ranging from 2% to 30% being tested. However, it was found that mode-locking could only be achieved at 30%. Furthermore, recovery time was only available as τ = 10 ps. In particular, having as fast a recovery time as is possible is most desirable for controllable pulse shaping [9-12].

In future, for a project with further scope, collaborative efforts could be established locally to produce SAM devices with customised parameters in-house, opening a wide berth of new options for laser optimisation for a variety of different intracavity powers.

5.3.4 Simulation Improvements

The MATLAB modelling undertaken in Chapter 4 was crucial to better understanding the nonlinear dynamics as governed by the GNLSE. While this served as a useful and computationally efficient tool to guide experimental design and discussion, and there were several improvements to be made that fell outside the scope of the thesis that would otherwise improve the accuracy of the model.

Firstly, and most importantly, the MATLAB script, while efficient, used a simple model for gain and gain saturation that assumes the gain given by Equation 5.3.1 [13, 14]:

$$g = \frac{g_0}{1 + \left(\frac{P}{P_{sat}}\right)} \qquad (5.3.1)$$

where g_0 is the small signal gain, P is the optical power and P_{sat} is the saturation power.

While this allowed for ease-of-use regarding predictions of net intracavity energy and lasing thresholds versus losses, they neglect to account for more complicated gain relaxation dynamics, such as the gain relaxation oscillations discussed in Chapter 3 that give rise to SAM-based Q-switching [15]. Such modelling would provide further parity between experiment and theory.

Furthermore, the model does not account for the complicated nonlinear optics regarding polarisation states due to NLPR, as discussed in Section 2.3. As the circulator used in the experiments was polarisation based, it would undoubtedly provide some artificial saturable absorption via preferentially passing a certain nonlinear evolution of the polarisation, i.e. it can be configured to preferentially pass pulse-like signals. Note that in experiments the use of a manual polarisation controller revealed no drastic changes in laser behaviour, and the SESAM and soliton-like pulse propagation and shaping appeared to dominate intracavity dynamics.

This was ignored as modelling of NLPR effects in such a model would further increase computation time, turning the simplified 1D GNLSE into a 2D problem to account for this nonlinear birefringence. The coupled PDEs are given below in Equation 5.3.2 [16]:

$$\frac{\partial A_{x,y}}{\partial Z} + \frac{\delta \partial A_{x,y}}{\partial T} + \frac{\beta_2 i}{2}\frac{\partial^2 A_{x,y}}{\partial T^2} - \frac{\beta_3}{6}\frac{\partial^3 A_{x,y}}{\partial T^3} =$$
$$i\gamma\left(\left|A_{x,y}\right|^2 + \frac{2}{3}\left|A_{y,x}\right|^2\right)A_{x,y} + \frac{i\gamma}{2}A_{x,y}^* A_{y,x}^2\, exp(-i2\Delta\beta z) \qquad (5.3.2)$$

where $A_{x,y}$ is the amplitude that experiences birefringent index $n_{x,y}$ respectively.

5.4 Concluding Statement

5.4.1 Conclusion

This chapter provided a full summary and review of the objectives and contents of this thesis, in addition to the most promising future prospects to further improve the work therein. As a result, a robust, stable, ultrashort all-fibre MIR source was developed. In-house manufacturing or further optimisation of cavity components such as WDMs, SESAMs, gain fibre and more would unlock the potential for both selectivity of lasing wavelength, in addition to reduction of phase and power noise.

Appendix A
Free Space SESAM Mode-locked Sources from the Literature

Table A-1 below contains a summary of all free-space SESAM mode-locked cavities from the literature review in Section 1.2.

Primary author	Mode-locker	Active dopant	Centre wavelength λ_0 [nm]	Pulse duration $\Delta\tau$ [ps]	Pulse energy [nJ]	Avg. power [W]	Peak power [kW]	Rep. rate [MHz]
Hou et. al. (2013) [1]	Double SESAMs	Nd	1064.48	9.97	23.46	2.98	2.35	127
Bu et. al. (2017) [2]	SESAM	Cr	2415	2.08	2.71	0.342	1.30	126.4
Bu et. al. (2017) [2]	SESAM-Soliton	Cr	2420	0.408	3.17	0.403	7.78	127
Wang et. al. (2019) [3]	SESAM	Tm-Ho	2015	52	4.40	0.378	0.08	86
Sorokina et. al. (2006) [4]	SESAM	Cr	2450	1.1	0.83	0.125	0.76	150
Yang et. al. (2021) [5]	SESAM	Yb	1041	0.247	139.47	10	564.66	71.7
Saraceno et. al. (2012) [6]	SESAM	Yb	1040	0.096	65.81	5.1	685.48	77.5
Wang et. al. (2021) [7]	SESAM	Tm-Ho	2033	0.046	1.55	0.121	33.72	78
Gaponenko et. al. (2014) [8]	SESAM	Pr	639.5	18	0.18	0.015	0.01	85.6
Zeng et. al. (2021) [9]	SESAM – KLM - Soliton	Yb	976 – 1054	0.094	17.80	1.05	189.33	59

Quarterman et. al. (2009) [10]	SESAM	InGaAs Disk	1037	0.06	0.04	0.035	0.58	1000
Kowalczyk et. al. (2021) [11]	SESAM	Yb	1050	0.093	0.38	0.03	4.12	78.3
Kowalczyk et. al. (2018) [12]	SESAM-Soliton	Yb	1049	0.063	0.36	0.028	5.70	78
Kowalczyk et. al. (2016) [13]	SESAM	Yb	1029.4	0.191	2.55	0.160	13.34	62.81
Kowalczyk et. al. (2016) [13]	SESAM-KLM	Yb	1036.5	0.059	0.99	0.062	16.76	62.71
Kim et. al. (2011) [14]	SESAM outcoupler	Nd	1064	12	12.44	1.55	1.04	124.6
Ghanbari et. al. (2018) [15]	SESAM	Alexandrite	774	0.420	4.06	0.325	9.67	80
Sverre (2017) [16]	SESAM	InGaAs Disk	997	0.452	0.03	0.03	0.06	1080
Leonov et. al. (2021) [17]	SESAM-Soliton	Cr	2462	1.4	0.15	0.02	0.11	129.5
Lederer et. al. (1999) [18]	SESAM-KLM-Soliton	Ti	828 - 865	0.155	6.71	0.510	43.29	76
Wang et. al. (2017) [19]	SESAM-KLM	Yb	1030	0.63	3.93	0.385	6.24	98
Crombie (2013) [20]	SESAM	Cr	1248 - 1312	0.263	0.17	0.027	0.63	162

Table A-1: Extended summary table of free-space SESAM mode-locked sources from the literature.

Appendix B
Fibre SESAM Mode-locked Sources from the Literature

Table B-1 below contains a summary of all fibre based SESAM mode-locked cavities from the literature review in Section 1.2.

Primary author	Mode-locker	Active dopant	Centre wavelength λ_0 [nm]	Pulse duration $\Delta\tau$ [ps]	Pulse energy [nJ]	Avg. power [W]	Peak power [kW]	Rep. rate [MHz]
Qi et. al. (2021) [21]	SESAM	Yb	1064	57	14.42	0.015	0.25	1.04
Huang et. al. (2015) [22]	SESAM-Soliton	Tm	1918	0.58	4.94	0.158	8.53	32
Wang et. al. (2012) [23]	SESAM-soliton	Tm	1980	2.65	0.76	0.01	0.29	13.2
Krylov et. al. (2008) [24]	SESAM	Yb	1160	50	0.71	0.0078	0.01	11
Xu et. al. (2017) [25]	SESAM	Tm	1860 – 2020 (tunable)	208	1.79	0.0071	0.01	3.97
Bharathan (2020) [26]	SA nanomaterial	Er-doped ZBLAN	2796	10	20.10	0.603	2.01	30
Herda & Okhotnikov (2004) [27]	SESAM	Yb	1032	11	0.06	0.005	0.01	80
Xu et. al. (2016) [28]	SESAM	Yb	1030.93	8	0.32	0.006	0.04	18.5
Liu et. al. (2012) [29]	SESAM	Yb	1064.1	21	0.03	0.017	0.00	490
Tolstik et. al. (2017) [30]	SESAM-soliton	Ho	2134.7	1.26	0.3353	0.005103	250	15.22

Al-Masoodi et. al. (2018) [31]	SbTe SA	Yb	1072.7	18.8	0.77	0.0186	0.04	24.2
Zhiguo et. al. (2018) [32]	SESAM	Yb	1032	20.6	1.24	0.0359	0.06	29
Wang et. al. (2011) [33]	SESAM-soliton	Tm-Ho codoped	2060	1.1	0.00		0.00	24.4
Hirooka et. al. (2016) [34]	SESAM-soliton	Er	1560	0.48	0.00	0.015, 0.045	0.01	9200
Hinkelmann et. al. (2017) [35]	SESAM-soliton	Ho	2052	1.2	0.18	0.005	0.15	27.3
Okhotnikov et. al. (2004) [36]	SESAM	Yb	1040	11	0.01	~0.001	0.00	80
Chamorovskiy et. al. (2012) [37]	SESAM + carbon nanotube SA, soliton	Ho	2085	0.89	2.93	0.046	3.29	15.7
Zhang et. al. (2014) [38]	SESAM	Yb	1034	24	2.05	0.053	0.09	25.8
Gou et. al. (2013) [39]	SESAM	Yb	1033.4 – 1069.7 (tuneable)	34.85	0.00	0.00447	0.00	25.4
Soltanian et. al. (2020) [40]	SESAM	Er	1550 (1200nm BW, SC source)	17	16600	0.32464	1300	13.8 kHz
Stoliarov et. al. (2020) [41]	SESAM-soliton	Er	1553	10.4	10 pJ	0.0003	0.0009	1060.9
Huang et. al. (2019) [42]	SESAM	Tm	1940	3.93	38.84	0.672	9.88	17.3

Afifi et. al. (2016) [43]	SESAM-NLPR	Er	1560	0.206	0.89	0.07	4.30	79
Jiménez-Rodriguez et. al. (2017) [44]	SESAM	Er	1500	0.230	9.04	0.047	39.30	5.2
Grześ et. al. (2018) [45]	SESAM	Tm	1994.3	23	0.21	0.017	0.01	81
Wang et. al. (2017) [46]	SESAM-soliton (similariton)	Yb	1030	4.8	0.53	0.037	0.11	70
Li et. al. (2015) [47]	SESAM-NLPR	Yb	1030	0.96	37.63	3.15	39.20	83.7
Tolstik et. al. (2016) [48]	SESAM-soliton	Ho	2100	2.23	4.00	0.03	1.79	7.5
Mashiko et. al. (2016) [49]	SESAM	Tm	1928	0.28	8.59	0.176	30.66	20.5
Gomes et. al. (2004) [50]	SESAM	Yb	1023	1.5	14.42	0.001	0.25	95
Gomes et. al. (2004) [50]	SESAM	Yb	1020	14.4	4.94	0.001	8.53	140
Gumenyuk et. al. (2012) [51]	PbS SA – Soliton	Tm-Ho Codoped	1990	0.98	0.76	-	0.29	22.75
Li et. al. (2021) [52]	SESAM	Yb	1040	012	0.71	0.007	0.01	43.2
Zhang et. al. (2014) [53]	SESAM	Tm	2054.67	20.2	1.79	0.056	0.01	10.22

Table B-1: Extended summary table of fibre-based SESAM mode-locked sources from the literature.

Appendix C
Resonant and Anti-resonant SESAMs

Appendix C contains a brief discussion on the two key SESAM architectures broadly seen in the literature: resonant and anti-resonant SESAMs. Recall that a SESAM is comprised of a substrate, the Bragg reflector and a saturable semiconductor material at the topmost layer, possibly with a dielectric coating. The reflection from the Bragg reflector and the back-reflection from the topmost coating-air interface provides feedback for light passing through the SESAM, leading to a microcavity.

As shown in Figure C-1(a) below, resonant SESAMs produce an intensity node at the air-surface interface, whereas anti-resonant SESAMs produce an anti-node at the air-surface interface (Figure C-1(b)):

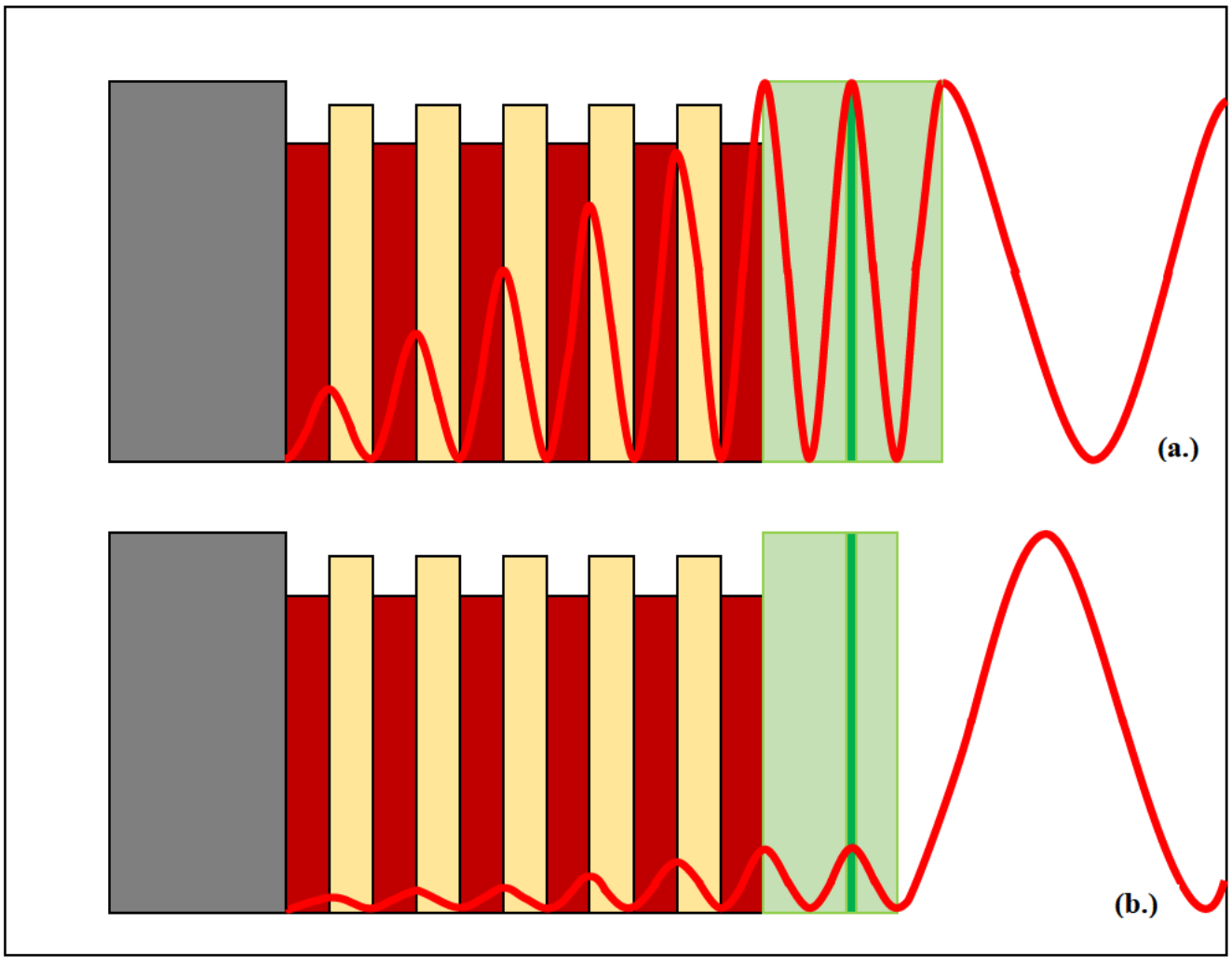

Figure C-1: Typical structures of (a.) resonant and (b.) anti-resonant SESAMs, with the incident field intensity represented by the red trace.

The effect of the architecture on the local field intensity and hence operative SESAM parameters is characterised by a field enhancement factor, ξ, which relates to the modulation depth and saturation fluence by Equations C.1 and C.2 respectively [54]:

$$\Delta R \approx \frac{n_r \alpha_0 (1 - \alpha_c) \Lambda}{2} \xi \qquad (C.1)$$

$$F_{sat} = \frac{h\nu}{2\sigma_{abs}\xi} \qquad (C.2)$$

Where n_R is the real refractive index and σ_{abs} is the absorption cross-section. Wang et. al. (2015) report that resonant SESAMs may have enhancement factors at least one order of magnitude larger than that of anti-resonant SESAMs, thus anti-resonant SESAMs exhibit modulation depths ten times more and saturation fluences at least ten times less than resonant ones [55].

While a larger wavelength-averaged enhancement factor (resonant-like) is desirable for providing higher pulse shaping via Equation C.1, such SESAM devices present peak-like GDD and spectral properties by nature of being highly resonant [56-58]. This not only makes resonant SESAMs narrowband but display quickly wavelength-varying dispersion around their operation wavelength, magnifying the deleterious effects of growth defects and thermal issues whereas anti-resonant designs are considerably less sensitive [54, 56].

Note that an even wider variety of alternative, novel SESAM architectures exists in the literature, such as the so-called ‘low-field-enhancement resonant-like SESAMs’ (LOFERS) and enhanced SESAM (ESESAM) devices, however these are outside the scope of this thesis [54-56].

Appendix D
MATLAB RK45IP Laser Cavity Simulation Code

Appendix D contains the code for the simulation work used in Chapter 4.

The MATLAB script overleaf utilises a Runge-Kutta 4th order numerical routine to solve the Generalised Nonlinear Schrödinger Equation discussed in Chapter 2. The code records the calculated time domain intensity, SESAM absorption and optical spectrum after every full code loop.

The base code is a combination of work from many authors in addition to many modifications [59-61]. The original script was written by Dan Nguyen (2021) [62].

```
close all
clear all
clc

if ~exist('RESULTS','dir')
    mkdir('RESULTS');
end

global t N      % vector time, globally used (including functions)
global f        % global freq. def.
global lambdaP  % DEBUG

tol = 1e-3;          % tolerance

c0 = 2.99792458e8;    %%%% speed of light [m/s]
h = 6.62607015e-34;   %%%% Planck's constant [m^2 kg/s]

% Time domain
N = 2^17;                              % #pts in time domain
Tmax = 60e-12;         % half width of time window [s]
Tmin = -Tmax;          % other side of time window Tmin<t<Tmax
deltat = 2*Tmax/(N-1);                 % Time res. [s]
t = linspace(Tmin, Tmax - deltat, N); %time array

% Freq/Wavelength domain
lambdaP = 2050e-9;    %%%% lasing wavelength [m]
wP = 2*pi*c0/lambdaP; % angular freq of central @2100nm

deltaf = 1/(2*Tmax); % Frequency res. (step)
f = [0:deltaf:(N/2-1)*deltaf, -N*deltaf/2:deltaf:-deltaf]; % vector freq

w = 2*pi*f;          % Angular freq
wshift = -w + wP;    % plus the freq with its central freq
                     % with minus sign to compensate for definition of
                     % FFT in MATLAB having opposite sign to that in
                      % the GNLSE

wl = 1e9 * 2 * pi * c0 ./wshift; % shift nm to present [nm]
tm = 1e12 * t; %shift ps to present [ps]

%////////////////////////////////////////
%-----------------------RAMAN FUNCTION
fR = 0.18 ;    %%%% Raman coeff in silica glass fibre
%fR = 0.0;
```

```
43 -    fR = 0.18 ;     %%%% Raman coeff in silica glass fibre
44      %fR = 0.0;
45 -    t1 = 12.2e-15; %%%% appx parameter in silica glass [s]
46 -    t2 = 32e-15;   %%%% appx parameter in silica glass [s]
47
48 -    t_shock = 1/wP; % self-steepening parameter [s]
49
50 -    tr = t - t(1); % shift time array to start at 0
51
52      % Raman response function by Blow & Wood (1989)
53 -    hR = (t1^2 + t2^2) / t1 / t2^2 *exp(-tr/t2) .*sin(tr/t1);
54
55 -    hR = hR./trapz(tr,hR); % normalized of integ_0^inf hR = 1
56 -    hR_f = fft(hR);
57
58      %//////////////////////////////////////////
59      %-----------------------HOLMIUM DOPED FIBRE
60      %tt = 50e-15; % contribution to effect of gain in dispersion value [Agr.
61      %1991]
62 -    n2 = 2.7e-20;                  %%%% nonlinear refr index [m^2/W]
63
64 -    crossSec_ems = 2.2e-25;    %%% sigma_ems(lasing wavelength) [m^-2]
65 -    crossSec_abs  = 0.6e-25;   %%% sigma_abs(lasing wavelength) [m^-2]
66
67 -    L_hdf1 = 0.87;                  %%%% Length of HDF [m]
68 -    L_hdf2 = 0.91;                  %%%% Length of HDF [m]
69      %L_hdf2 = 0.97;                  %%%% Length of HDF [m]
70
71
72      %~~~~~~~~~~~~~~~~~~~~~~
73 -    coreR_hdf = 5e-6; %%%% 10 micron diam core [m] > % From Hemming (2014)
74 -    NA_hdf = 0.12;    %%%%                          > % """
75 -    Vnum_hdf  = 2*pi/(lambdaP) * coreR_hdf * NA_hdf;
76 -    MFD_hdf  = 2*coreR_hdf*(0.65 + 1.619/(Vnum_hdf^(3/2)) + 2.879/(Vnum_hdf^6))
77 -    Aeff_hdf = pi*(MFD_hdf/2)^2;             % effective mode area in core
78
79 -    gamma_hdf = 2*pi * n2/lambdaP/Aeff_hdf; % 0.0013/(2^2)
80
81
82      %~~~~~~~~~~~~~~~~~~~~~~
83
84 -    delta_wl = 50e-9; %%% gain bandwidth [nm]
85 -        Omega = (2*pi*c0/lambdaP^2)*delta_wl;
86 -        tt = 1/Omega;
```

```matlab

    D_hdf = 52e6; %%% dispersion [ps m^-2]
    b2_hdf = - lambdaP^2/(2*pi*c0*1e-12)*D_hdf;
    b3_hdf = -0.001960807;

    % [beta1, beta2, beta3, ...] in ps^k/m
beta_hdf = [0, b2_hdf, b3_hdf];

for ii = 1:length(beta_hdf)
    beta_hdf(ii) = (1e-12)^(ii)*beta_hdf(ii);
end

%Esat = 5e-11; % Nguyen
%Esat = 6e-11;
Esat = 1e-10;
%Esat = 5e-10; %BEST
%Esat = 1e-9;
disp('HDF saturation energy [J]')
disp(Esat)

%AdB_hdf = 4.5;                 %%%% net loss [db/m]
%AdB_hdf = 10;                 %%%% net loss [db/m]

AdB_hdf = 0.03;                 %%%% net loss [db/m]
%^^^^^^^^^^^^^^^^^^^^^^^^^^^^^^^^^^^^^^^^^^^^^^^^^^^^^^^^^^^^^

alfa_hdf = AdB_hdf/4.343;     % loss CONVERTED [1/m]

%GdB = 15;           %%%% HDF total gain in dB
%GdB2 = 25.0; % Best

GdB2 = 15.0; % Best
%GdB2 = 20.0; % Best

%^^^^^^^^^^^^^^^^^^^^^^^^^^^^^^^^^^^^^^^^^^^^^^^^^^^^^^^^^^^^^


%GdB2 = 30.0;           %%%% HDF total gain in dB
%GdB2 = 40.0;           %%%% HDF total gain in dB
%GdB1 = 45.0;           %%%% HDF total gain in dB

%gain1 = GdB1/L_hdf1/4.343; % gain [1/m]
gain2 = GdB2/L_hdf2/4.343; % gain [1/m]
```

```
129
130     %//////////////////////////////////////////
131     %-----------------------PASSIVE FIBRE
132
133 -   L_smf1 = 3.3; %%%% 1st SMF length: 0.1(after NP) + 2 both side ISO
134 -   L_smf2 = 3.3; %%%% Length of SMF before OC
135 -   L_smf3 = 3.3; %%%% Length of SMF after OC
136
137 -   AdB_smf = 0.03;             %%%% loss of silica fibre [dB/m]
138 -   alfa_smf = AdB_smf/4.343;    % loss [1/m]
139
140 -   coreR_smf = 4.1e-6;                              %%%% 8.2 micron diam core [m]
141 -   NA_smf    = 0.12;                                %%%%
142
143 -   Vnum_smf  = 2*pi/(lambdaP) * coreR_smf * NA_smf;
144 -   MFD_smf   = 2*coreR_smf*(0.65 + 1.619/(Vnum_smf^(3/2)) + 2.879/(Vnum_smf^6));
145
146 -   Aeff_smf  = pi*(MFD_smf/2)^2;             % effective mode area in core
147
148
149     %MFD_smf = 13e-6;                              %%%% MFD of the fibre
150     %Aeff_smf = pi*(MFD_smf/2)^2;                  % effective core area
151 -   gamma_smf = 2*pi*n2 / lambdaP / Aeff_smf;     % nonlinear coeff [1/W/m]
152
153
154
155 -   D_smf = 40e6; %%%%% dispersion of SMF in ps/(m*m)
156 -   b2_smf = -lambdaP^2 / (2*pi*c0*1e-12)*D_smf;
157 -   b3_smf = -0.001960807;
158     % [beta1, beta2, beta3, ...] in ps^2/m
159 -   beta_smf = [0, b2_smf, b3_smf];
160
161 -   for ii = 1:length(beta_smf) % change units to s^k/m
162 -       beta_smf(ii) = (1e-12)^(ii) * beta_smf(ii);
163 -   end
164
165
166     %//////////////////////////////////////////////////////
167     %-----------------------DISPERSION COMPENSATING FIBRE
168
```

```
169 -    L_dcf = 0.0;
170      %L_dcf  = 10.0; %%%% Length of DCF
171
172 -    AdB_dcf = 0.03;                 %%%% [dB/m] loss of silica fibre
173 -    alfa_dcf = AdB_dcf/4.343;       % [1/m] loss
174
175 -    coreR_dcf = 2.1e-6;                              %%%% 8.2 micron diam core [m]
176 -    NA_dcf    = 0.37;                                %%%%
177
178 -    Vnum_dcf  = 2*pi/(lambdaP) * coreR_dcf * NA_dcf;
179 -    MFD_dcf   = 2*coreR_dcf*(0.65 + 1.619/(Vnum_dcf^(3/2)) + 2.879/(Vnum_dcf^6));
180
181 -    Aeff_dcf  = pi*(MFD_dcf/2)^2;            % effective mode area in core
182
183      %MFD_dcf = 4.0e-6;                %%%% MFD of the fibre, assume 10um CHECK
184      %Aeff_dcf = pi*(MFD_dcf/2)^2;                % effective core area
185 -    gamma_dcf = 2*pi*n2 / lambdaP / Aeff_dcf;   % nonlinear coeff [1/W/m]
186
187 -    D_dcf = -55e6; %%%% dispersion of DCF [ps/(m*m)]
188 -    b2_dcf = -lambdaP^2 / (2*pi*c0*1e-12)*D_dcf;
189 -    b3_dcf = -0.001960807;
190
191      % [beta1, beta2, beta3, ...] in ps^2/m
192 -    beta_dcf = [0, b2_dcf, b3_dcf];
193
194 -    for ii = 1:length(beta_dcf) % change units to s^k/m
195 -        beta_dcf(ii) = (1e-12)^(ii) * beta_dcf(ii);
196 -    end
197
198      %//////////////////////////////////////////
199      %-----------------------NOISE SEED
200
201 -    phase = pi*rand([1,N]);
202 -    Unoise = 1e-4.*randn(1,N).*exp(-1i*phase); % small noise seed
203 -    Unoise_f = fft(Unoise);
204 -    It0 = abs(Unoise.^2);
205 -    If0 = abs(Unoise_f).^2;
206 -    Uin0 = Unoise;
207
208      %//////////////////////////////////////////
209      %-----------------------SATURABLE ABSORBER
210
```

```
211
212      % SAM dispersion
213 -    L_dsam = 1e-3; %'length' of SESAM propagation
214 -    AdB_dsam = 0.0; % Loss already handled by alfa func.
215 -    alfa_dsam = AdB_dsam/4343; % loss m^-1
216
217 -    coreR_dsam = 4.1e-6;                                %%%% from SMF [m]
218 -    NA_dsam    = 0.12;                                  %%%%
219 -    Vnum_dsam  = 2*pi/(lambdaP) * coreR_dsam * NA_dsam;
220 -    MFD_dsam   = 2*coreR_dsam*(0.65 + 1.619/(Vnum_dsam^(3/2)) + 2.879/(Vnum_dsam^6));
221 -    Aeff_dsam  = pi*(MFD_dsam/2)^2;             % effective mode area in core
222
223 -    gamma_dsam = 2*pi*n2 / lambdaP / Aeff_dsam;    % nonlinear coeff [1/W/m]
224
225
226
227 -    D_dsam = -528e6 ; %%%%% dispersion of SAM in ps/(m*m)
228 -    b2_dsam = -lambdaP^2 / (2*pi*c0*1e-12)*D_dsam;
229      %b3_dsam = -0.001960807;
230
231      % [beta1, beta2, beta3, ...] in ps^2/m
232 -    beta_dsam = [0, b2_smf];
233
234 -    for ii = 1:length(beta_dsam) % change units to s^k/m
235 -        beta_dsam(ii) = (1e-12)^(ii) * beta_dsam(ii);
236 -    end
237
238
239      %-----------------------------------------
240 -    a0 = 0.18;        %%% mod depth
241 -    abb = 0.3;        %%% absorbtance
242 -    ac = abb - a0;    %%% linear abs
243      %``````````````````````
244
245 -    Ts = 10e-12;      %%%% 10 ps recovery time
246
247 -    F_saSat = 7e-1;  %%%% saturation FLUENCE [J/m^2]
248 -    Es = F_saSat * Aeff_smf ; %%%% sat energy at SESAM %best
249      %Es = 7e-11;
250      %Es = 5e-12; % NGUYEN
251 -    disp('SESAM sat energy [J] ')
252 -    disp(Es)
253 -    alfa0 = SA(Uin0, a0, ac, Ts, Es);
254
```

```
255     %//////////////////////////////////////////
256     %-----------------------MISC. PARAMETERS
257
258 -   FB = 75/100;     % outcoupler coeff
259 -   CL1 = 99.8/100; % splice coupling coeff: loss = (1-CL)*100%
260 -   CL2 = 99.8/100; % splice coupling coeff: loss = (1-CL)*100%
261
262
263     % Loop integers
264 -   indc = 0; % loop index
265 -   indx = 0;
266 -   loopmax = 600; % max no. of round trips.
267
268     % filter params
269     % ===== WAVELENGTH DIVISION MULTIPLEXERS =====
270 -   dw_WDM = 50.0;                          % WDM filter bandwidth
271     %dw_WDM = 40.0;                          % best<----------------------
272     %lambdaF_WDM = lambdaP;                  % WDM central wavelength
273 -   lambdaF_WDM = 2070e-9;                  % WDM central wavelength
274
275 -   FL_WDM = 0.912 ;                           % WDM filter insertion loss
276     %FL_WDM = 1 ;                            % best<----------------------
277 -   GF_WDM = Filter(lambdaF_WDM,dw_WDM); % WDM filter func.
278
279     % ===== SESAM =====
280 -   dw_SAM = 300.0;                         % SESAM filter bandwidth
281 -   lambdaF_SAM = 2000e-9;                  % SESAM central wavelength
282 -   FL_SAM = 1 ;                            % SESAM filter insertion loss
283 -   GF_SAM = Filter(lambdaF_SAM,dw_SAM); % SESAM filter func.
284
285     % ===== CIRCULATOR =====
286 -   dw_CIRC = 70.0;                            % Circulator bandwidth
287     %dw_CIRC = 60.0;                            % best<----------------------
288     %lambdaF_CIRC = lambdaP;                     % Circulator wavelength
289 -   lambdaF_CIRC = 2070e-9;                    % Circulator wavelength
290 -   FL_CIRC = 0.708 ;                          % Circulator insertion loss
291     %FL_CIRC = 1 ;                             % best<----------------------
292 -   GF_CIRC = Filter(lambdaF_CIRC,dw_CIRC); % Circulator func.
293
294     % ===== OUTCOUPLER =====
```

```
295     %dw_OC = 300.0;                          % OC filter bandwidth
296     %lambdaF_OC = 2000e-9;                   % OC central wavelength
297 -   FL_OC = 0.63 ;                             % OC filter insertion loss
298     %FL_OC = 1 ;                              % best<--------------------
299     %GF_OC = Filter(lambdaF_OC,dw_OC); % OC filter func.
300
301     %%%%%%%%%%%%%%%%%%%%%%%%%%%%%%%%%%%%%%%%%%%%%%%%%%%%%%%%%%%%%%%%%%%
302     %-----------------------MAIN LOOP
303
304 -   for loop = 1:loopmax
305 -       indc = indc + 1;
306
307         % --> propagation through (1st) component = HDF
308 -       Uin_hdf2 = Uin0; % set input to this component
309 -       Uout_hdf2 = Propagation_HDFL(Uin_hdf2, tol, L_hdf2, gain2, Esat, ...
310             alfa_hdf, beta_hdf, gamma_hdf, t_shock, fR, hR_f);% propagate
311
312         % --> propagation through (2nd) component = SMF
313 -       Uin_smf1 = sqrt(CL1)*Uout_hdf2; % set input to this component
314 -       Uout_smf1 = Propagation_SMF(Uin_smf1, tol, L_smf1, alfa_smf, ...
315             beta_smf, gamma_smf, t_shock, fR, hR_f);% propagate
316
317         %+++++++++++++++++++++++++++++++++++++++++++++++++++++++++++++++++%
318         % --> propagation through (3rd) component = outcoupler
319 -       Uout_loop = sqrt(FL_OC)*sqrt(1-FB)*Uout_smf1;
320 -       Uouf_loop = fft(Uout_loop);
321 -       Iout = abs(Uout_loop).^2;
322 -       Iouf = 10*log10(abs(Uouf_loop).^2);
323         %+++++++++++++++++++++++++++++++++++++++++++++++++++++++++++++++++%
324
325         % --> propagation through (4th) component = DCF
326 -       Uin_dcf = sqrt(FL_OC)*sqrt(FB)*Uout_smf1; % set input to this component
327 -       Uout_dcf = Propagation_SMF(Uin_dcf, tol, L_dcf, alfa_dcf, ...
328             beta_dcf,gamma_dcf,t_shock,fR,hR_f);% propagate
329
330         % --> propagation through (5th) component = SMF
331         % Uin_smf2 = sqrt(FB)*Uout_smf1; % set input to this component
332 -       Uin_smf2 = sqrt(CL1)*Uout_dcf; % set input to this component
333 -       Uout_smf2 = Propagation_SMF(Uin_smf2, tol, L_smf2, alfa_smf, ...
334             beta_smf,gamma_smf,t_shock,fR,hR_f);% propagate
335
336         % --> propagation through (6th) component = CIRC
337 -       Uin_circ  = Uout_smf2;
338 -       Uout_circ = sqrt(FL_CIRC)*ifft(GF_CIRC.*fft(Uin_circ));
```

```
339
340         % --> propagation through (9th) component = SA
341 -       alfa = SA(Uout_circ, a0, ac, Ts, Es);
342 -       Uout_sa = sqrt(1-alfa).*Uout_circ;
343 -       Uouf_sa = fft(Uout_sa);
344
345         % --> propagation through (10th) component = SESAM filter
346         %\\\\\\\\\\\\\\\%
347 -       Uin_saF  = Uout_sa;
348 -       Uout_saF = sqrt(FL_SAM)*ifft(GF_SAM.*fft(Uin_saF));
349
350          % --> propagation through (10th) component = SESAM dispersion
351         %\\\\\\\\\\\\\\\%
352 -       Uin_dsam  = Uout_saF;
353 -       Uout_dsam = Propagation_SMF(Uin_dsam, tol, L_dsam, alfa_dsam, ...
354             beta_dsam,gamma_dsam,t_shock,fR,hR_f);
355
356         %\\\\\\\\\\\\\\\%
357         % --> propagation through (14th) component = SMF
358 -       Uin_smf3 = sqrt(CL2)*Uout_dsam; % set input to this component
359 -       Uout_smf3 = Propagation_SMF(Uin_smf3, tol, L_smf3, alfa_smf, ...
360             beta_smf,gamma_smf,t_shock,fR,hR_f);% propagate
361
362         % --> propagation through (14th) component = WDM filter
363         %\\\\\\\\\\\\\\\%
364 -       Uin_wdmF1  = Uout_smf3;
365 -       Uout_wdmF1 = sqrt(FL_WDM)*ifft(GF_WDM.*fft(Uin_wdmF1));
366
367 -       Uin0 = sqrt(CL1)*Uout_wdmF1;
368
369         %=========================================================
370 -       figure(1);
371         % Time domain intensity
372 -       subplot(3, 1, [1]) % Time domain intensity
373 -       plot(tm, It0, 'r', 'LineWidth', 2);
374 -       hold on
375 -       plot(tm, Iout, 'b','LineWidth', 1);
376 -       xlabel('Time (ps)','FontSize', 14);
377 -       xlim([-60,60])
378 -       set(gca,'XTick',-60:10:60)
379 -       ylim([0,2*(max(It0)+10)])
380 -       set(gca,'YTick',0:4:20)
```

```
381        %legend('input','out');
382 -      ylabel('Power (a.u.)','FontSize',12);
383 -      grid on;
384 -      set(gca,'FontSize',12);
385 -      hold off
386
387        %============================================================
388        % SA
389 -      subplot(3, 1, [2])
390 -      plot(tm, alfa0*100, 'r', 'LineWidth',2);
391 -      hold on
392 -      plot(tm, alfa*100,  'b', 'LineWidth',1);
393 -      xlabel('Time [ps]','FontSize', 14);
394 -      xlim([-60 60])
395 -      set(gca,'XTick',-60:10:60)
396 -      ylim([0 41])
397        %set(gca, 'YTick', 0:2:40)
398 -      set(gca, 'YTick', 0:3:42)
399        %legen('\alpha(t)');
400 -      ylabel('Absorption (%)','FontSize',12);
401 -      grid on;
402 -      set(gca,'FontSize',12);
403 -      hold off
404
405        %============================================================
406        % Frequency domain intensity
407        % old log
408 -      subplot(3, 1, [3])
409 -      plot(wl, 10*log10(If0), 'LineWidth',2,'Color','r');
410 -      hold off
411 -      plot(wl, Iouf, 'b', 'LineWidth',1);
412 -      text(2020,10,num2str(indc),'FontSize',20)
413 -      xlabel('Wavelength [nm]');
414 -      ylabel('Power [dB]');
415 -      xlim([1980, 2140])
416 -      set(gca,'XTick',1980:10:2140)
417 -      ylim([-80 100])
418 -      set(gca,'YTick',-80:40:100)
419 -      grid on;
420 -      set(gca,'FontSize',12);
421 -      hold off
422
```

```
423         %drawnow
424 -       if mod(indc,2)==0
425 -           indx = indx + 1;
426 -           cd RESULTS
427 -           saveas(gcf, strcat('file',num2str(indx),'.png'));
428 -           cd ../
429 -       end
430 -   end
431
432     % pack data into arrays for export
433     %
434 -   tmArr  = transpose(tm);
435 -   wlArr  = transpose(wl);
436
437 -   IArr   = transpose(Iout);
438 -   SAMArr = transpose(alfa*100);
439 -   IFArr  = transpose(Iouf);
440
441     % time tm Iout
442     %
443 -   TimeData = cat(2,tmArr,IArr);
444     %writematrix(TimeData,'TimeData.txt','Delimiter','tab')
445 -   dlmwrite('TimeData.txt',TimeData,'delimiter',' ')
446     % SAM tm alfa*100
447     %
448 -   SAMData  = cat(2,tmArr,SAMArr);
449     %writematrix(SAMData,'SAMData.txt','Delimiter','tab')
450 -   dlmwrite('SAMData.txt',SAMData,'delimiter',' ')
451     % Spect wl Iouf
452     %
453 -   FreqData = cat(2,wlArr,IFArr);
454     %writematrix(FreqData,'FreqData.txt','Delimiter','tab')
455 -   dlmwrite('FreqData.txt',FreqData,'delimiter',' ')
456     %+++++++++++++++++++++++++++++++++++++++++++++++++++++++++++++++++++++++++
457     % FUNCTIONS
458     %+++++++++++++++++++++++++++++++++++++++++++++++++++++++++++++++++++++++++
459
460     %/////////////////////////////////////////
461     %------------------------D^ OPERATOR
462     % calculates "exp(hD) . A" in NLSE
463
```

```
464     function Aout = D_op(Ain,dz,beta,alpha,omega)
465     %dispersion term in NLSE
466 -   Dw = zeros(1,length(omega));
467
468     %Dw = sum(i*beta(i)*(-w)^i/(i!))
469 -   for jl = 1:length(beta)
470 -       Dw = Dw - 1i.*beta(jl)/factorial(jl).*(-omega).^(jl);
471 -   end
472
473 -   Aout = ifft(exp(dz* (-Dw - alpha/2)).*fft(Ain));
474 -   end
475
476
477     %//////////////////////////////////////////
478     %------------------------N^ OPERATOR
479
480     function Aout = N_op(Ain, dz, gamma, t_shock, fR, hR_w)
481 -   global t
482 -   dt = abs((t(2) - t(1)));
483
484         % convolution term int_0^inf(hR(t)|A(z,T-t)|^2 dt
485         % ie. Eq.7 Hult 2007 or ifft(hR_w.*fft(abs(A)^2)
486
487 -   hR_A2 = ifft(hR_w.*fft(abs(Ain).^2))*dt;
488
489     % 1st term
490 -   N1 = 1i*gamma*((1-fR).*Ain.*abs(Ain).^2 + fR*Ain.*hR_A2);
491
492     % 2nd term
493 -   N2 = -gamma*t_shock.*gradient(((1-fR).*Ain.*abs(Ain).^2 ...
494         + fR.*Ain.*hR_A2),dt);
495
496 -   Aout = dz*(N1+N2);
497
498 -   end
499
500
501     %//////////////////////////////////////////////////////
502     %------------------------PROPAGATE HDFL
503     % Hult JLT 2007 & Sinkin JLT 2003
504     %--------------
505     %INPUTS
```

```
506     % Ei    - impulses, starting field amplitude (vector)
507     % tol   - local error limitation
508     % long  - length of fibre
509     % alpha - linear loss coeff i.e. Pz=P0*exp(-alpha*z)
510     % betap - dispersion polynomial coeffs beta1, ... etc.
511     % gam   - nonlinearity coeff
512     % ts    - self steepening term (t_shock)
513     % fR    - fraction of Raman effect
514     % hR    - the response fn of Raman in freq domain
515     %
516     %--------------
517     % OUTPUT
518     % Uout - field at the output
519     %--------------
520     %
521     function Uout = Propagation_HDFL(Uin,tol,L,g0,Es,alpha,beta,gam,ts,fR,hR)
522 -   global f t
523 -   delta_t = abs(t(2) - t(1));
524 -   omega = 2*pi*f;
525 -   c0 = 3e8;
526 -   lambdaP = 2050e-9; % PUMP WAVELENGTH
527 -   wP = 2*pi*c0/lambdaP;
528 -   delta_wl = 50e-9;
529 -   OmegaP = (2*pi*c0/lambdaP^2)*delta_wl;
530
531 -   Efield = Uin;
532
533 -   fprintf(1, '\nCalculation in process ...   ');
534
535 -       dz = L / 10e4; % trial for 1st step
536
537 -       alpha0 = alpha;
538 -       beta0 = beta;
539 -       gamma0 = gam;
540 -       Z_prop = 0;
541 -       ii = 0;
542
543 -   while Z_prop<L
544 -       ii = ii + 1;
545 -       if Z_prop + dz > L
546 -           dz = L - Z_prop;
547 -       end
548 -       Z_prop = Z_prop + dz;
```

```
549
550         % change parameters as Z_propgatation change
551         %tt = 40e-15; % T2 in Agrawal 1990 PTL
552 -       tt = 1/OmegaP;
553
554         % g = g0*exp(-sum(abs(E_z).^2)*delta_t/E_sat) (Agrawal 1991)
555         % or approximation as:
556 -       g = g0./(1 + sum(abs(Efield).^2)*delta_t/Es);
557
558 -       alpha = alpha0 - g; % loss and gain in NLSE
559 -       beta(2) = beta0(2) + 1i*tt*tt*g; % from eqn. (2) Agrawal PTL 1991
560
561 -       m = 0;
562 -       gam = gamma0*(1 + m*Z_prop);
563
564         % ----- optimisation of local error (SINKIN 2003)
565
566 -       Uf = rk4ip(rk4ip(Efield, omega, dz/2, beta, alpha, gam, ts, fR, hR),...
567             omega, dz/2, beta, alpha, gam, ts, fR, hR);
568 -       Uc = rk4ip(Efield, omega, dz, beta, alpha, gam, ts, fR, hR);
569
570 -       error = sqrt(sum(abs(Uf-Uc).^2))/sqrt(sum(abs(Uf.^2)));
571
572 -       factor = tol/error;
573 -       if error > 2*tol
574 -               Z_prop = Z_prop - dz;
575 -       else
576 -           Efield = 16/15*Uf - 1/15*Uc;
577 -       end
578 -       dz = dz* factor^(1/5);
579
580 -   end
581 -   Uout = Efield;
582 -   end
583
584     %//////////////////////////////////////////////////
585     %-----------------------PROPAGATE SMF
586     % Hult JLT 2007 & Sinkin JLT 2003
587     %--------------
588     %INPUTS
```

```
589     % Ei    - impulses, starting field amplitude (vector)
590     % tol   - local error limitation
591     % long  - length of fibre
592     % alpha - linear loss coeff i.e. Pz=P0*exp(-alpha*z)
593     % betap - dispersion polynomial coeffs betal, ... etc.
594     % gam   - nonlinearity coeff
595     % ts    - self steepening term (t_shock)
596     % fR    - fraction of Raman effect
597     % hR    - the response fn of Raman in freq domain
598     %
599     %--------------
600     % OUTPUT
601     % Uout - field at the output
602     %--------------
603     %
604     function [Uout,numFFT] = Propagation_SMF(imp,tol,long,alpha,beta,gamma,ts,fR,hR)
605 -   global f t
606     %delta_t = abs(t(2) - t(1));
607 -   omega = 2*pi*f;
608
609 -   E_z = imp;
610
611 -   fprintf(1, '\nCalculation in process ...   ');
612
613 -       dz = long / 10e4; % trial for 1st step
614
615 -       alpha0 = alpha;
616 -       beta0 = beta;
617 -       gamma0 = gamma;
618 -       Z_prop = 0;
619 -       ii = 0;
620
621 -   while Z_prop<long
622 -       ii = ii + 1;
623 -       if Z_prop + dz > long
624 -           dz = long - Z_prop;
625 -       end
626 -       Z_prop = Z_prop + dz;
627
628         % change parameters as Z_propgatation change
629 -       m = 0;
630 -       alpha = alpha0*(1 + m*Z_prop);
```

```
631 -       beta = beta0*(1 + m*Z_prop);
632 -       gamma = gamma0*(1 + m*Z_prop);
633         %-----------
634
635 -       Uf = rk4ip(rk4ip(E_z, omega, dz/2, beta, alpha, gamma, ts, fR, hR), ...
636             omega, dz/2, beta, alpha, gamma, ts, fR, hR);
637 -       Uc = rk4ip(E_z, omega, dz, beta, alpha, gamma, ts, fR, hR);
638
639 -       error = sqrt(sum(abs(Uf-Uc).^2))/sqrt(sum(abs(Uf).^2));
640 -       factor = tol/error;
641
642         % discard the solution and recalculate with a half of old stepsize
643 -       if error > 2*tol
644 -           Z_prop = Z_prop-dz;
645 -       else
646 -           E_z = 16/15*Uf - 1/15*Uc; % improve the accuracy of the solution
647 -       end
648 -       dz = dz*factor^(1/5);
649
650 -       fprintf(1, '\b\b\b\b\b\b%5.2f%%', Z_prop* 100.0 /long);
651 -   end
652
653 -   Uout = E_z;
654 -   numFFT = 3*16*ii;
655
656 -   end
657
658     %////////////////////////////////////////////////////
659     %-----------------------RK4IP SOLVER
660     % Hult JLT 2007 & Sinkin JLT 2003
661     %--------------
662     function Eout = rk4ip(A0,omega,dz,beta,alpha,gamma,ts,fR,hR)
663 -   Efield = A0;
664     % Aip: interaction presentation
665
666 -   Aip = D_op(Efield, dz/2, beta, alpha, omega);
667 -   k1 = D_op( N_op(Efield, dz, gamma, ts, fR, hR), dz/2, beta, alpha, omega);
668 -   k2 = N_op(Aip + k1/2, dz, gamma, ts, fR, hR);
669 -   k3 = N_op(Aip + k2/2, dz, gamma, ts, fR, hR);
670 -   k4 = N_op(D_op(Aip + k3, dz/2, beta, alpha, omega), dz, gamma, ts, fR, hR);
671
672 -   Eout = D_op( Aip + k1/6 + k2/3 + k3/3, dz/2, beta, alpha, omega) + k4/6;
673 -   end
```

```
674
675       %////////////////////////////////////////////////////
676       %-----------------------SATURABLE ABSORBER
677
678       function alfa = SA(Ei, a0, ac, Ts, Es)
679       % calculate and display 'alfa_SA(|A|)'
680       % dalfa(t)/dt = (a0 - alfa(t))/ts - |A(t)|^2 / Esat*alfa(t)
681
682 -     global N t
683 -     deltat = abs(t(2) - t(1));
684
685       % This part constructs the pump @975nm
686 -     Et = zeros(size(t));
687
688 -     alfal = zeros(size(t));
689 -     intga = zeros(size(t));
690 -     intga0 = 0;
691 -     intgal = 0;
692
693 -     for k = 1:N
694 -         Et(k) = Ei(k);
695 -         intga(k) = deltat*(1/Ts + abs(Et(k))^2/Es); % a = a0/(1 + I/Isat)
696 -         intga0 = intga0 + intga(k);
697
698 -         intgal = intgal + a0/Ts * deltat*exp(+intga0);
699 -         alfal(k) = ac + exp(-intga0)*(intgal + a0);
700
701 -     end
702 -     alfa = alfal;
703 -     end
704
705
706
707       %////////////////////////////////////////////////////
708       %-----------------------FILTERS
709       function v = Filter(lambda0,dw)
710
711 -     c0 = 2.99792458e8; % speed of light in vac. [ms^-1]
712 -     lamb0 = lambda0;   % FILTER wavelength [m]
713
714 -     global f    % PULSE wavelength/freq.
715 -     global lambdaP
716 -     disp(lambdaP)
```

```
717
718 -    wP = 2*pi*c0/lambdaP; % angular freq. of signal
719 -    w= 2*pi*f;            % array of angular freqs
720
721 -    wshift = -w + wP;         % neg sign for FFT in MATLAB, shifted freq vector
722 -    lambda = 2*pi*c0./wshift; % shift wavelength too
723 -    lambdaD = lambda - lamb0; % difference between wavelengths and filter
724
725 -    v = exp(-(1.3e9*(lambdaD)/dw).^2); % filter func.
726
727 -    end
```

Ready

Appendix E
Frequency Resolved Optical Gating (FROG)

E.1 Frequency Resolved Optical Gating (FROG)

Appendix E reviews a third pulse shape characterisation technique not discussed in Chapter 3, known as frequency resolved optical gating (FROG), a technique to resolve ambiguities over pulse phase information [63]. Recall that a spectrogram is a power mapping of the pulse intensity, plotting frequency against delay in the hybridised frequency-time domain, as shown in Figure E-1 below [64]:

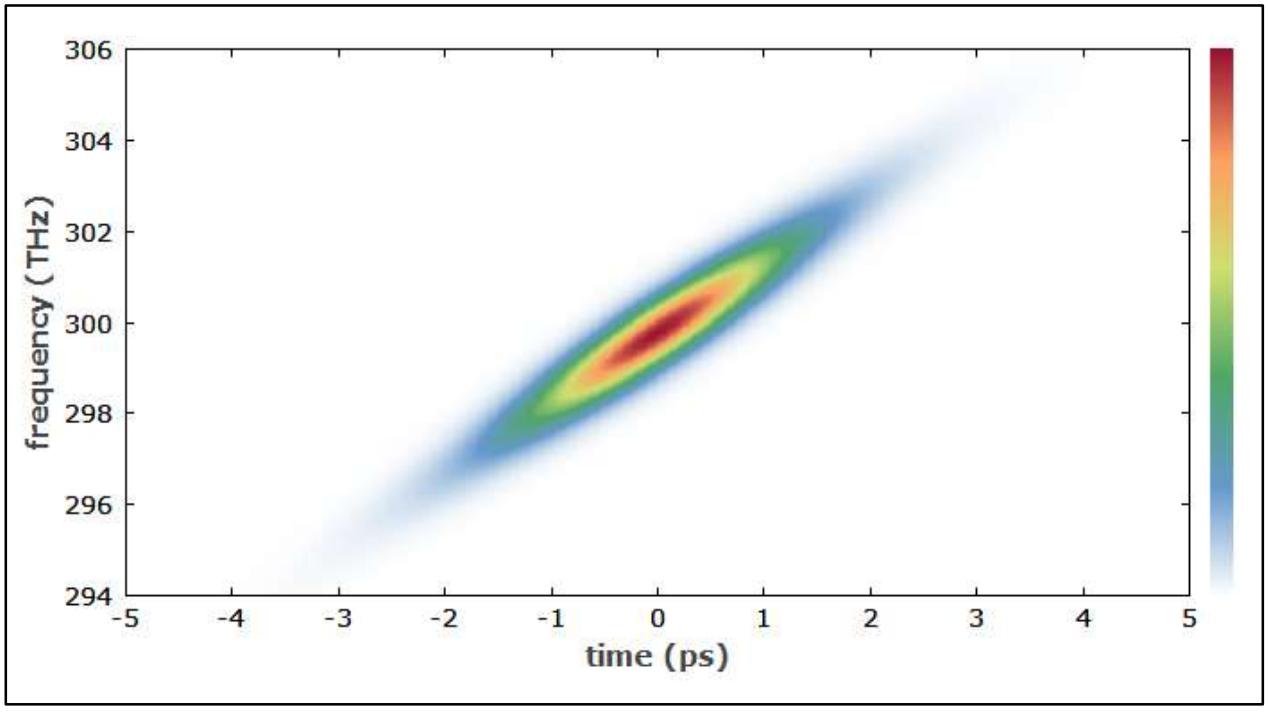

Figure E-1: An example spectrogram (FROG trace) of a linearly up-chirped pulse.

FROG may utilise a variety of geometries, with the SHG FROG scheme being the most widely used, analogous to a spectrally resolved non-colinear autocorrelation geometry. Note that SHG FROG provides highly sensitive detection down to the 0.001 nJ range, desirable for characterising low-power ultrafast fibre oscillators [65]. This increased sensitivity is owed to

using a 2nd order nonlinearity as opposed to the alternative FROG geometries involving 3rd order nonlinearities. SHG FROG geometry follows the geometry for a non-collinear autocorrelation with the photodetector replaced with a spectrometer, and is shown in Figure E-2 below [63]:

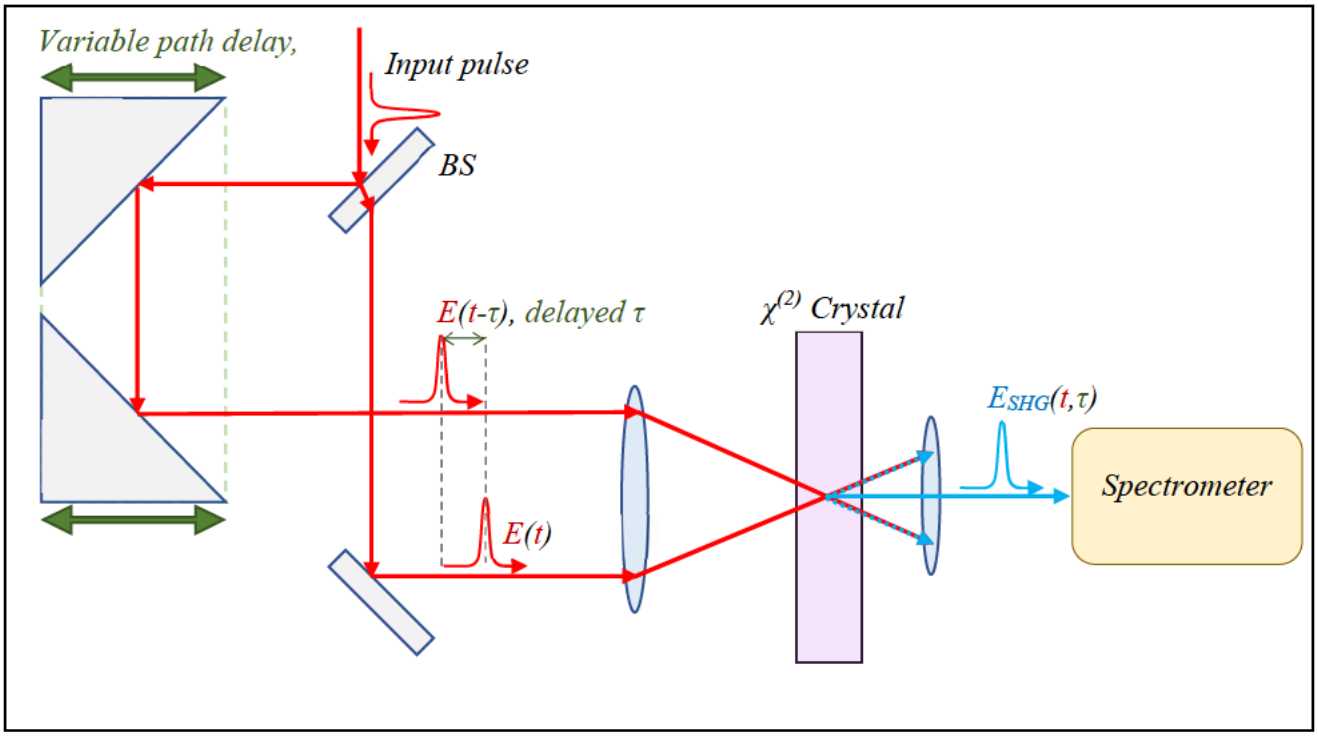

Figure E-2: Architecture of a SHG FROG geometry.

The two mutually-delayed beams are overlapped in the $\chi^{(2)}$ material using the beam geometry shown in Figure E-2 above. The resulting SHG signal is then spectrally resolved at the spectrometer to obtain the signal given by Equation E.1 [63]:

$$I_{FROG}^{SHG}(\omega,\tau) = \left| \int_{-\infty}^{\infty} E(t)E(t-\tau)\, exp(-i\omega t)\, dt \right|^2 \qquad (E.1)$$

Retrieval of the spectrogram is sufficient to fully describe a pulse outside of a few trivial ambiguities, with the only notable disadvantage being ambiguity in time [66, 67].

Appendix F
Simulation Parameters

Appendix F outlines the basic calculations and justifications for the parameters used in the simulation from various sources from the literature and relevant manufacturers.

F.1 Single Mode Fibre

The loss per metre at 2000 nm, A_{dB_SMF}, core radius R_{SMF}, core and cladding indices n_1 and n_2 and dispersion coefficient at 2000 nm, D_{SMF}, used are given in Table F-1 below. The numerical aperture, NA, is then trivially calculated by Equation F.1 [68]:

$$NA = \sqrt{n_1^2 - n_2^2} \approx 0.1201 \qquad (F.1)$$

Parameter	Value	Source
Loss per metre, $A_{dB,\ SMF}$	0.03 dB/m	[68]
Core radius, R_{SMF}	4.1 µm	[69]
Core index, n_1	1.444	[70]
Cladding index, n_2	1.439	[70]
Numerical aperture, NA	0.1201	Calculated from n_1, n_2
Dispersion coeff., D_{SMF}	40 ps/nmkm @ 2000 nm	[71]
Kerr coefficient, $\overline{n_2}$	2.8e-20 m^2/W	[72]

Table F-1: Summary table of SMF parameters used for simulation work.

F.2 Dispersion Compensating Fibre

The specifications of the simulated DCF are based on the Nufern SM2000D DCF used in the experimental work of Chapter 4. Assuming similar propagation losses as SMF (both Ge-Silica fibre), parameters are listed from the manufacturer specifications in Table F-2 below:

Parameter	**Value**	**Source**
Loss per metre, $A_{dB,\,DCF}$	0.03 dB/m	[68]
Core radius, R_{DCF}	2.1 µm	[73]
Numerical aperture, NA	0.37	[73]
Dispersion coeff., D_{DCF}	-55 ps/nmkm @ 2000 nm	[73]
Kerr coefficient, $\overline{n_2}$	2.8e-20 m^2/W	[72]

Table F-2: Summary table of DCF parameters used for simulation work

F.3 Holmium Doped Fibre and Gain

Saturation energy of the gain for a single pass amplifier is estimated using Equation F.2 [74]:

$$E_{sat} = \frac{A_{eff}\, h\nu}{\sigma_{em}(2050\ nm) + \sigma_{abs}(2050\ nm)} \qquad (F.2)$$

Where A_{eff} is the effective mode area σ_{abs}(2050 nm) and σ_{em}(2050 nm) are the absorption and emission cross-sections at 2050 nm respectively. A correction factor is applied accounting for multiple passes per second, i.e. the repetition rateto obtain E_{sat} = 100 pJ [75].

Also note that the lasing manifolds used, the $^5I_6$ to $^5I_7$ transition for Ho^{3+}, is a quasi-three-level system there are reabsorption losses on the lasing wavelength in addition to the OH^- impurities etc. Estimates range from 5 – 10 dB total loss over 1 m at 2050 nm due to reabsorption [76, 77]. Note that in the code in Appendix D it is factored in by setting gain to 15 dB and loss to ~0 dB, which is equivalent to setting gain to 25 dB and loss to 10 dB for ease of use.

Assuming 10 dB absorption [76], and emission and absorption cross-sections at the lasing wavelength of 2050 nm are 0.6 * 10^{-25} m^2 and 2.2 * 10^{-25} m^2 respectively, we can calculate the small signal gain [78, 79]:

$$g_0 = \alpha_{Ho}.\left(\frac{\sigma_{ems}}{\sigma_{abs}}\right) \qquad (F.3)$$

$$g_0 \approx 15\ dB$$

Parameter	Value	Source
Core radius, R_{HDF}	2.5 µm	[80]
Dispersion coeff., D_{HDF}	51.8 ps/nmkm @ 2000 nm	[81]
Kerr coefficient, $\overline{n_2}$	2.8e-20 m^2/W	[72]
Absorption cross-section at 2050 nm, $\sigma_{abs}(2050\ nm)$	0.6 * 10^-25 m^2	[79]
Emission cross-section at 2050 nm, $\sigma_{em}(2050\ nm)$	2.2 * 10^-25 m^2	[79]
Small-signal gain, g_0	15 - 35 dB	Calculations from $\sigma_{em,\ abs}$, [82]
Reabsorption losses, L_{re}	5 – 10 dB	[76, 77]
Saturation Energy, E_{sat}	100 pJ	Calculations from $\sigma_{em,\ abs}$
Gain Bandwidth, $\Delta\lambda$	50 nm	[80]

Table F-3: Summary table of HDF parameters used for simulation work

F.4 SESAM

A BATOP GmbH 2 μm, 10 ps recovery time, 30% absorptivity SESAM was used for the project. From the manufacturer we have the following specifications listed in Table F-4:

Parameter	Value	Source
Modulation depth, ΔR	18%	[83]
Absorptance, α	30%	[83]
Recovery time, τ	10 ps	[83]
Saturation fluence, F_{sat}	70 μJ/cm^2	[83]
Operating bandwidth, $\Delta\lambda$	1910 – 2080 nm	[83]
Dispersion, *GDD*	+1200 fs^2	[83]

Table F-4: Summary table of SESAM parameters used for simulation work

F.5 Raman Coefficients of Ge-Silica Fibre

Recall that the delayed Raman response was given by Equation 2.3.7 [84] [84]:

$$h_R(t) = \frac{\tau_1^2 + \tau_2^2}{\tau_1 \tau_2^2} \exp\left(-\frac{t}{\tau_2}\right) \sin\left(\frac{t}{\tau_1}\right) \tag{2.3.7}$$

Where τ_1 and τ_2 are inverse time scales that represent the phonon frequency and the linewidth. For silica fibre, the inverse time scales and Raman response coefficient, f_R, are summarised in Table F-5 below:

Parameter	Value	Source
Inverse timescale (photon frequency), τ_1	12.2e-15 s	[85]
Inverse timescale (linewidth), $\tau 2$	32e-15 s	[85]
Raman coefficient, f_R	0.18	[86]

Table F-5: Summary table of Raman parameters used for simulation work

F.6 Calculating Third-order Dispersion in Silica Glass

Lastly, the TOD of the simulated fibres was estimated by using the method described by Marcuse (1980) [87]. Marcuse (1980) relates the first, second and third orders of dispersion through the respective derivatives of the propagation constant, β:

$$\dot{\beta} = \frac{1}{c}\left(n - \lambda\frac{dn}{d\lambda}\right) \tag{F.4}$$

$$\ddot{\beta} = \frac{\lambda^3}{2\pi c^2}\frac{d^2n}{d\lambda^2} \tag{F.5}$$

$$\dddot{\beta} = -\frac{\lambda^2}{(2\pi)^2 c^3}\left(3\lambda^2\frac{d^2n}{d\lambda^2} + \lambda^3\frac{d^3n}{d\lambda^3}\right) \tag{F.6}$$

This requires calculating the derivatives of the refractive index of the material at the lasing wavelength (2 μm). To calculate the derivatives of *n*, we look to the work of Miyagi & Nishida (1979). By utilising the Sellmeier equation, Equation F.7 we obtain expressions for the wavelength derivatives F.8 – F.10 [88]:

$$n^2 = 1 + \sum_{i=1}^{3}\frac{a_i\lambda^2}{\lambda^2 - b_i} \tag{F.7}$$

$$\frac{dn}{d\lambda} = -\frac{\lambda}{n}\left(\sum_{i=1}^{3}\frac{a_i b_i}{(\lambda^2 - b_i)^2}\right) \tag{F.8}$$

$$\frac{d^2n}{d\lambda^2} = \frac{1}{n}\left(\sum_{i=1}^{3}\frac{a_i b_i(3\lambda^2 + b_i)}{(\lambda^2 - b_i)^3}\right) - \frac{1}{n}\left(\frac{dn}{d\lambda}\right)^2 \tag{F.9}$$

$$\frac{d^3n}{d\lambda^3} = -\frac{12}{n}\left(\sum_{i=1}^{3}\frac{a_i b_i(3\lambda^2 + b_i)}{(\lambda^2 - b_i)^4}\right) - \frac{3}{n}\left(\frac{dn}{d\lambda}\frac{d^2n}{d\lambda^2}\right) \tag{F.10}$$

Where a_i and b_i are the Sellmeier coefficients for silica fibre [88]:

$$a_1 = 0.6961663, \qquad b_1 = 0.004679148$$

$$a_2 = 0.4079426, \qquad b_2 = 0.01351206$$

$$a_3 = 0.8974994, \qquad b_3 = 97.934002$$

Using Equations F.4 – F.10, it was possible to calculate the TOD propagation constant term for λ = 2050 nm, yielding $\ddot{\beta} \approx -0.00196\ \mathrm{ps}^2/\mathrm{m}$. Note that this value only reflects the material contribution, and neglects the other contributions (e.g. modal, PMD) to TOD, thus this value is an underestimate. Nonetheless, it is included in the simulation work of Chapter 4 for completeness.

F.7 Effects of Simulated TOD

The effects on the simulated laser cavity presented in Section 4.4 are done again, with and without TOD. The results are shown in Figure F-1a,b,c and F-2a,b,c respectively:

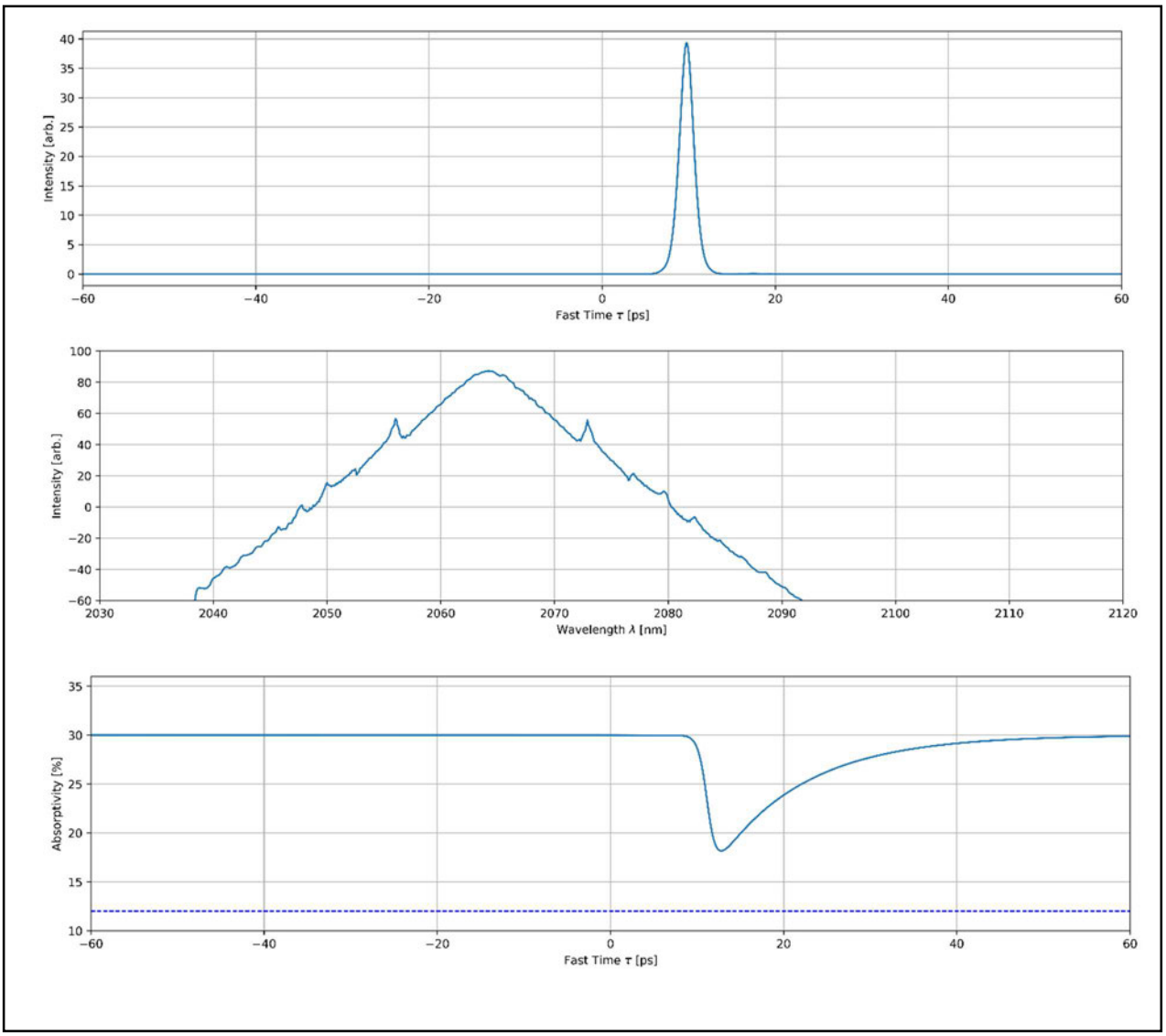

Figure F-1: Simulation results for TOD enabled.

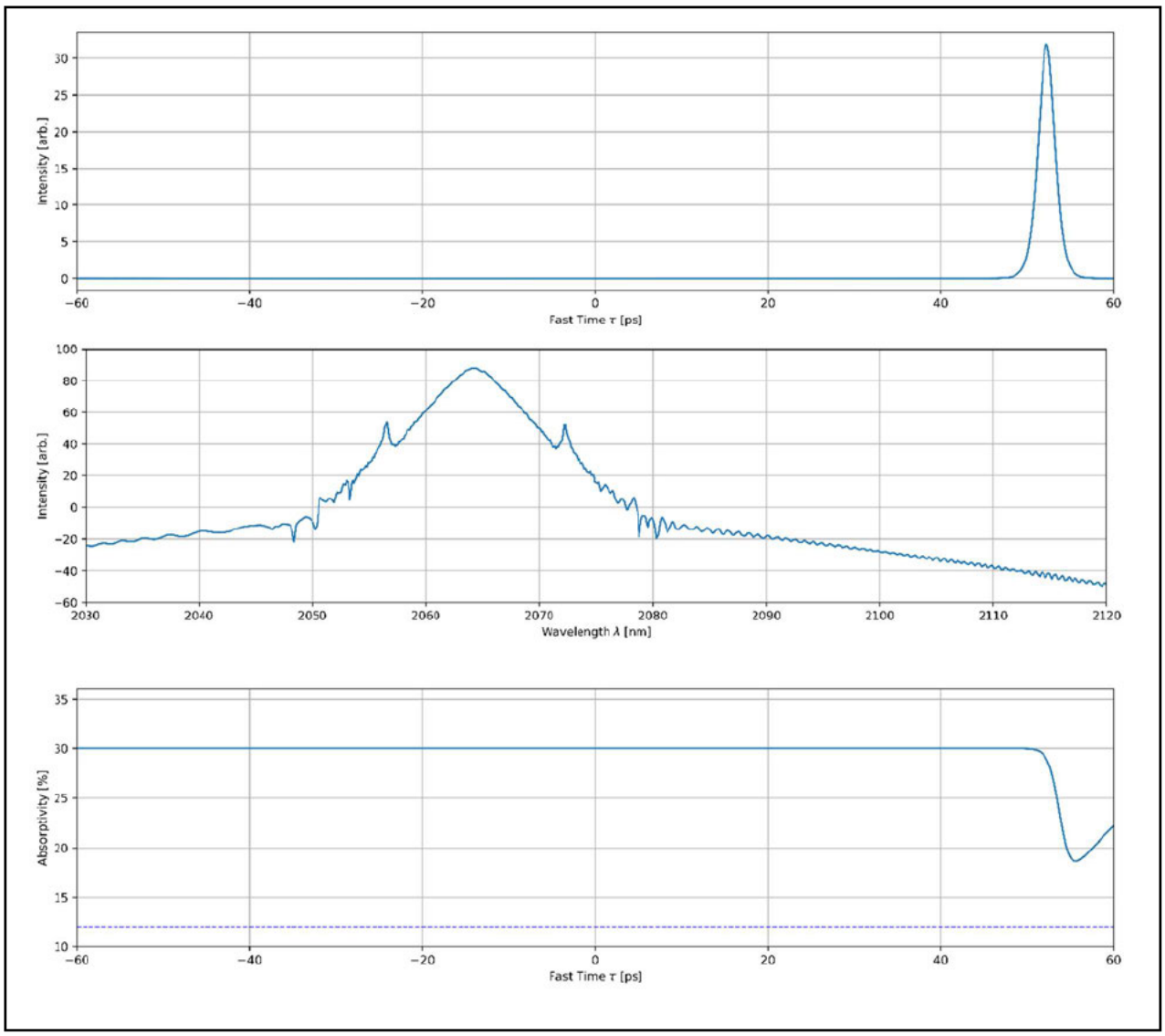

Figure F-2: Simulation results for TOD disabled.

Figures F-1 and F-2 have performance characteristics summarised in Table F-6 below:

	SESAM Absorption	Central Wavelength [nm]	OS FWHM [nm]	Temporal FWHM [ps]
TOD Enabled	18.2%	2064.2	2.7	1.8877
TOD Disabled	18.6%	2064.2	2.0	2.237

Table F-6: Summary of simulation results for Figures F-1, F-2.

As expected, there is approximately no change in the SESAM's nonlinear absorption, with the TOD enabled and disabled simulations demonstrating 18.2% and 18.6% respectively. Any difference can be explained by the difference in pulse temporal FWHM, which was 1.89 and 2.24 ps for the TOD and non-TOD simulations respectively. This result is particularly interesting as it implies that some pulse compression is occurring due to the introduction of TOD. In particular, this aligns with the earlier calculations through Equations F.4 – F.10 above, as the sign of the dispersion is opposite to that of the anomalous dispersion in the cavity; the TOD is small and normal. Thus, according to the results in Figures F-1 and F-2, the small normal dispersion from TOD slightly counteracts the GVD in the fibre. In line with the pulse durations we see a slightly larger bandwidth for the TOD simulation, but we expectantly see that the central wavelengths remain the same at 2064.2 nm.

It would be enlightening to further investigate this effect by more carefully determining the total TOD for the various fibres, either by considering waveguide, modal, polarisation, etc. contributions to the TOD in the calculations, or by experimental characterisation of the fibres used. This is of particular import due to the discrepancy in pulse duration that arose in the simulation of the 7 m DCF cavity in Section 4.5, whereby the simulation overestimated the pulse temporal FWHM by a factor of two. A more accurate calculation of the TOD may yield more accurate dispersion compensation predictions in future. Unfortunately, this is outside the scope of this thesis. However, this will be crucial to optimising lasers of similar design to those in this project in future work, particularly as such designs are scaled further toward femto, or possibly attosecond pulse durations.

Appendix G
Time Evolution of Laser Cavity Designs

Appendix G consists of eight pages containing printouts of the time domain intensity, SESAM absorptivity and pulse spectrum for simulations Designs 1 – 8 from Sections 4.3 and 4.4. Each simulation is started from a packet of random (quantum) spectral noise generated via MATLABs normal distribution function, as can be seen in the 2nd round trip printout on Figures G-1 to G-8.

G.1 Design #1 Simulation

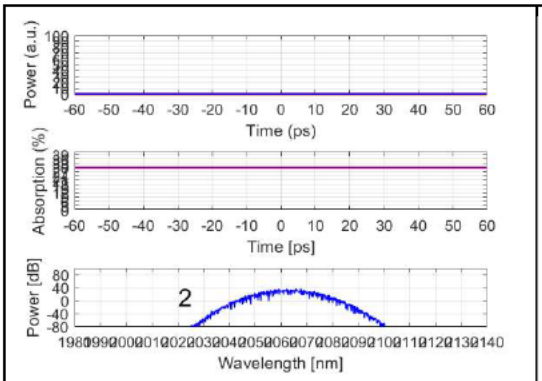

Figure G-1: (From top to bottom in each square) simulations of the time domain intensity, SESAM saturable absorption and the pulse spectrum at 2 to 600 round trips for Design #1 from Section 4.3.

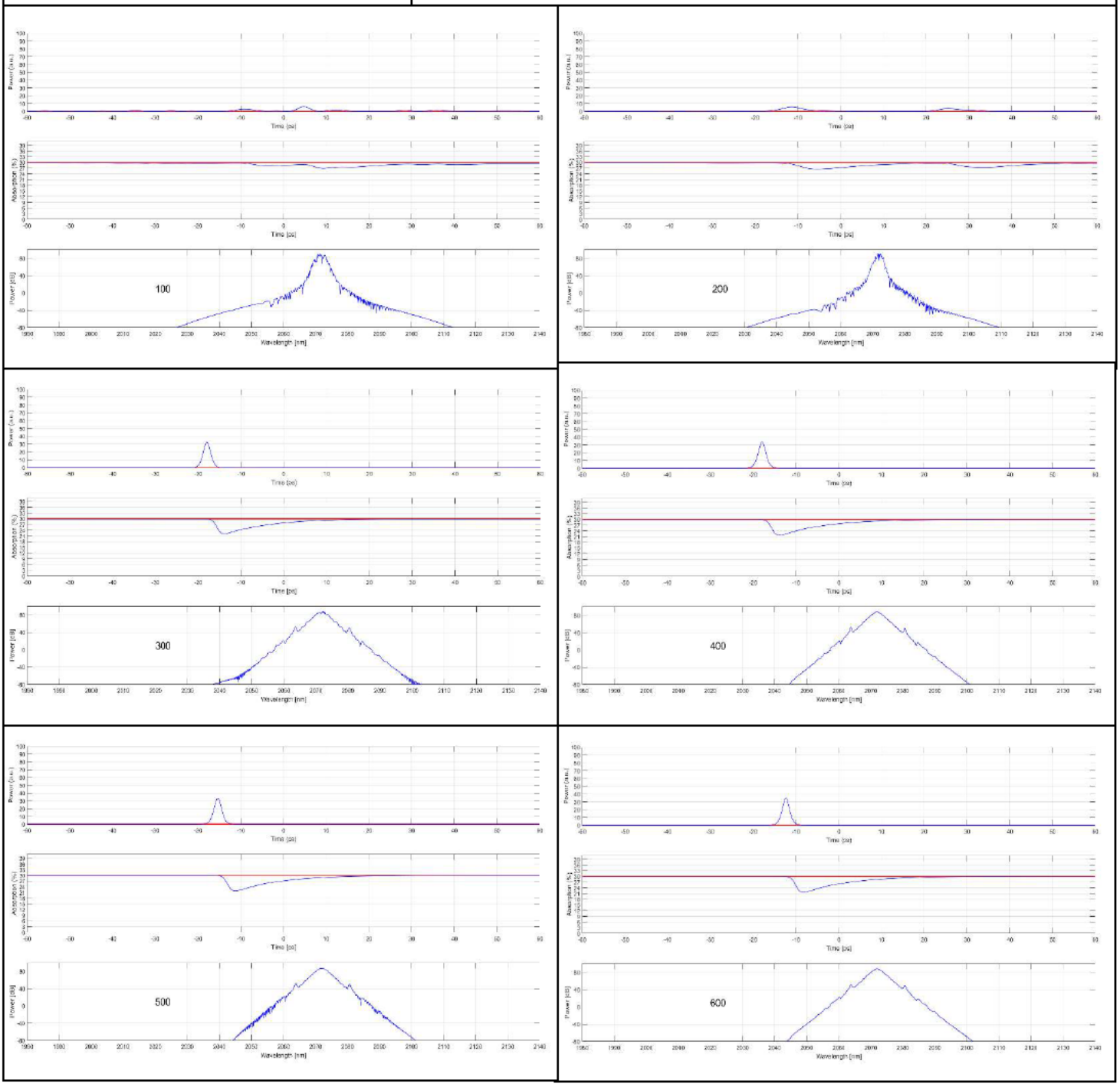

G.2 Design #2 Simulation

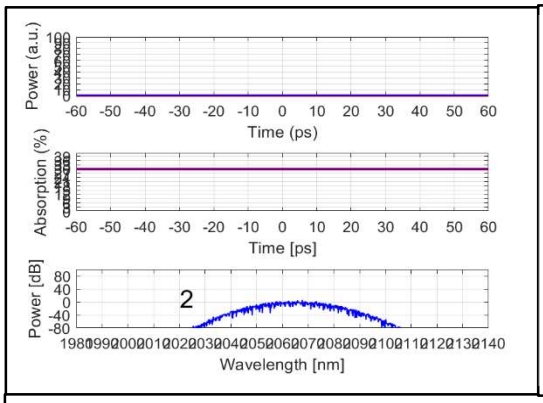

Figure G-2: (From top to bottom in each square) simulations of the time domain intensity, SESAM saturable absorption and the pulse spectrum at 2 to 600 round trips for Design #2 from Section 4.3.

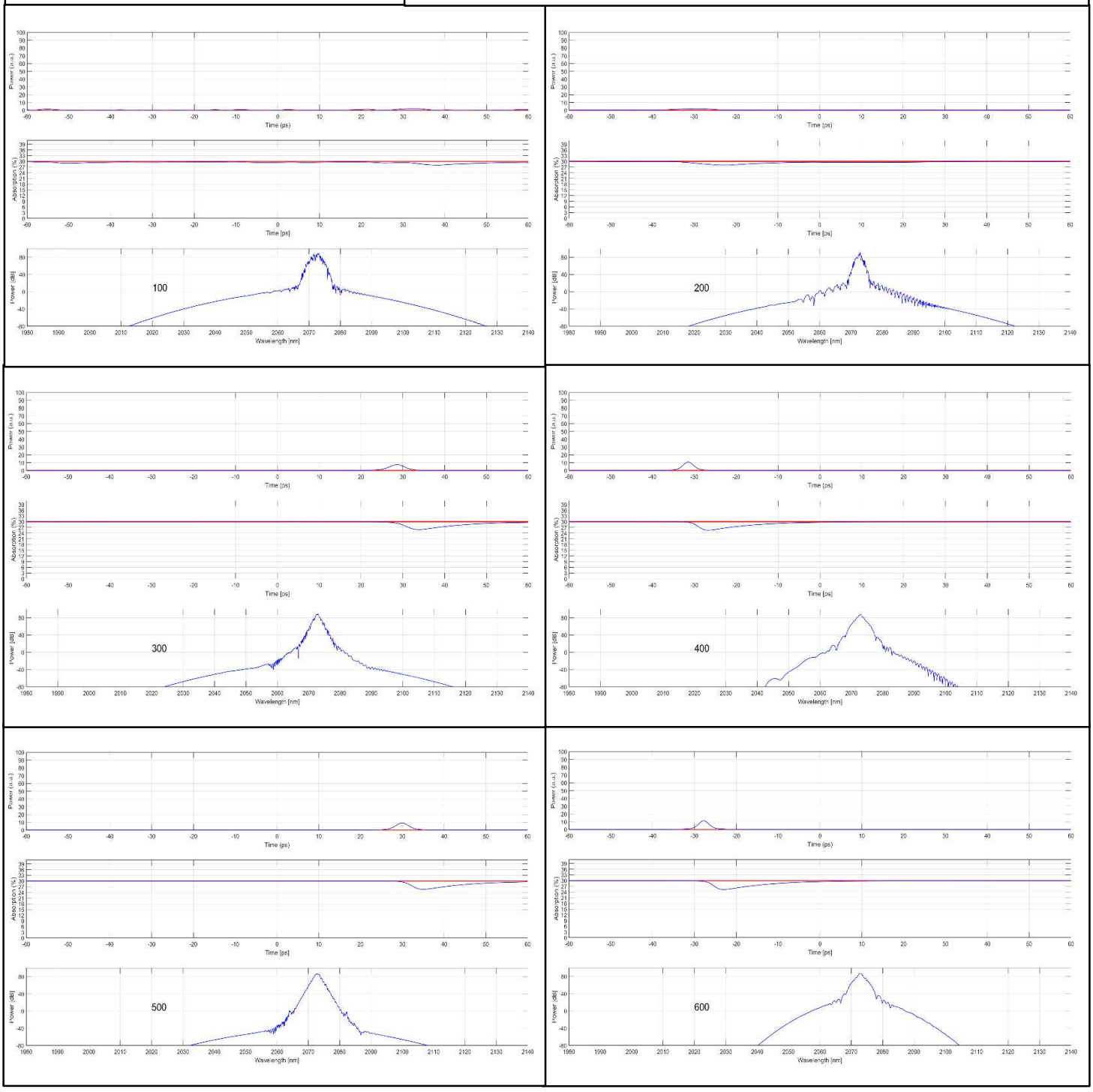

G.3 Design #3 Simulation

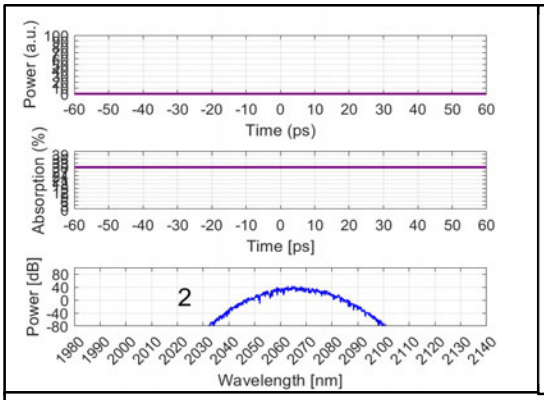

Figure G-3: (From top to bottom in each square) simulations of the time domain intensity, SESAM saturable absorption and the pulse spectrum at 2 to 600 round trips for Design #3 from Section 4.3.

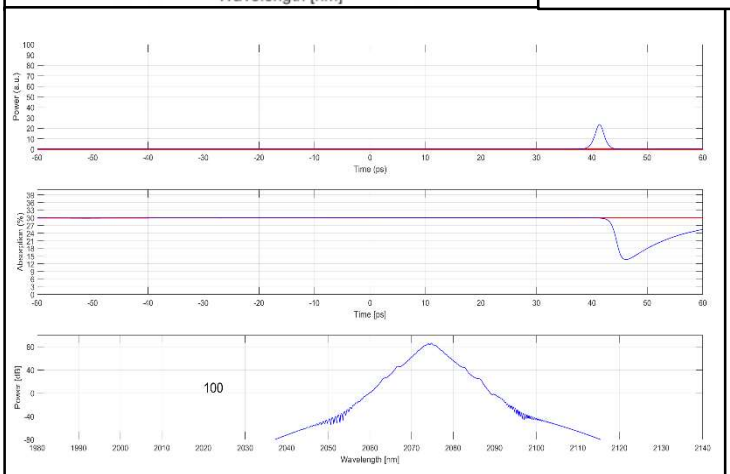

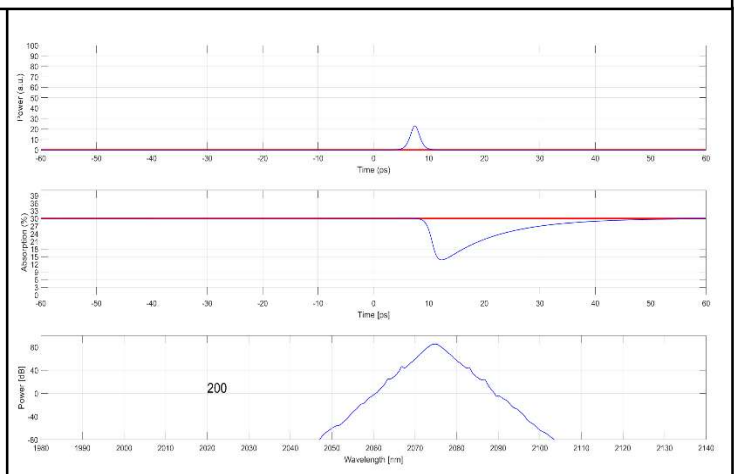

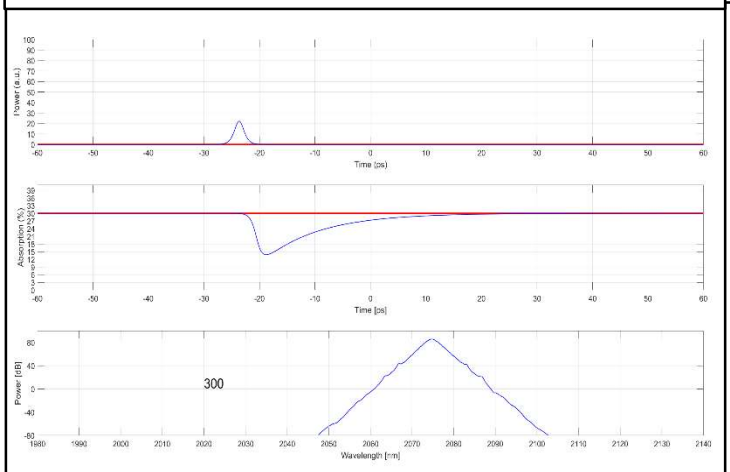

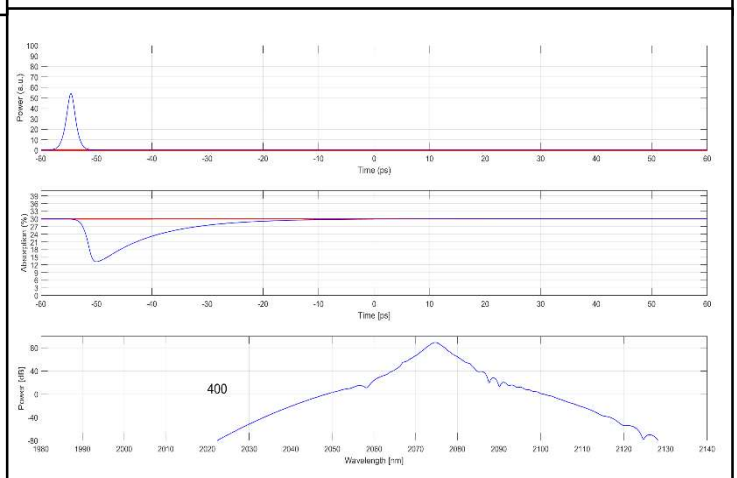

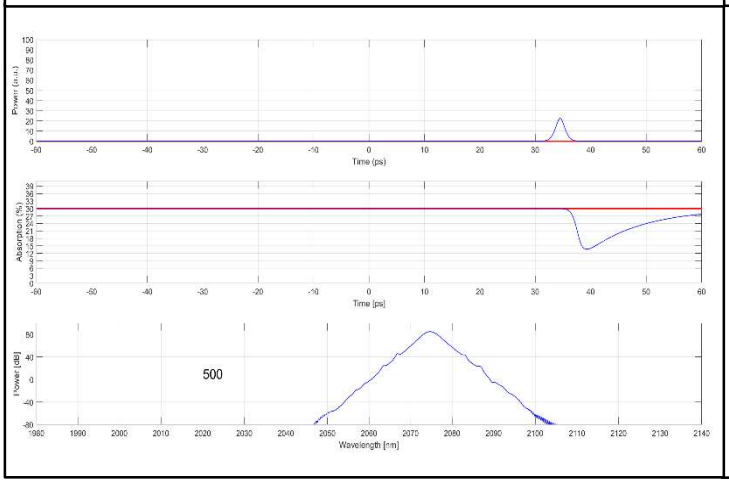

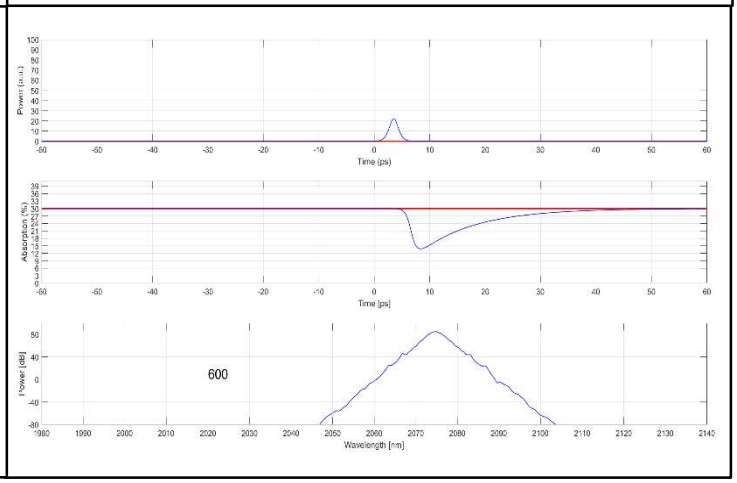

G.4 Design #4 Simulation

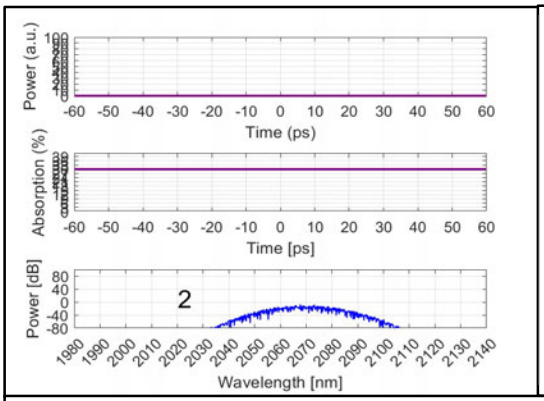

Figure G-4: (From top to bottom in each square) simulations of the time domain intensity, SESAM saturable absorption and the pulse spectrum at 2 to 600 round trips for Design #4 from Section 4.3.

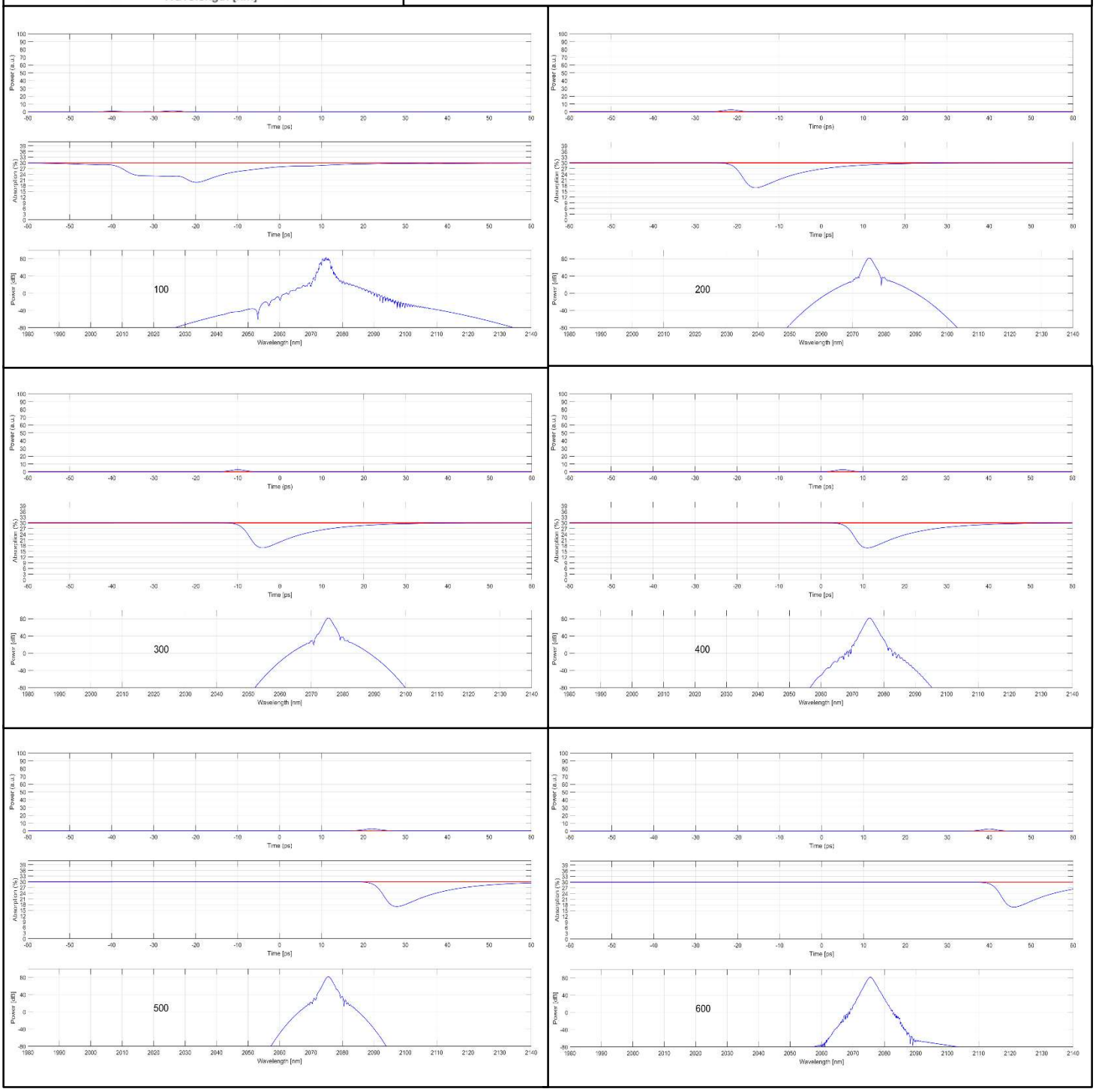

G.5 Design #5 Simulation

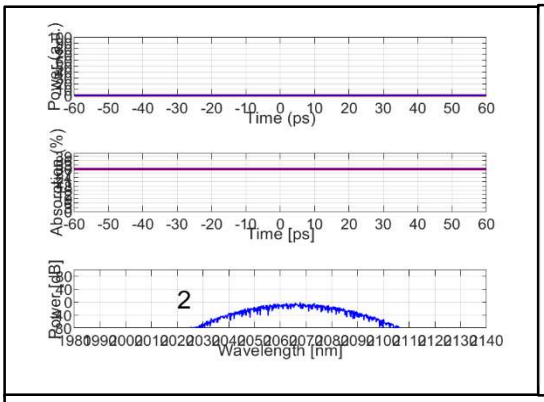

Figure G-5: (From top to bottom in each square) simulations of the time domain intensity, SESAM saturable absorption and the pulse spectrum at 2 to 600 round trips for Design #5 from Section 4.3.

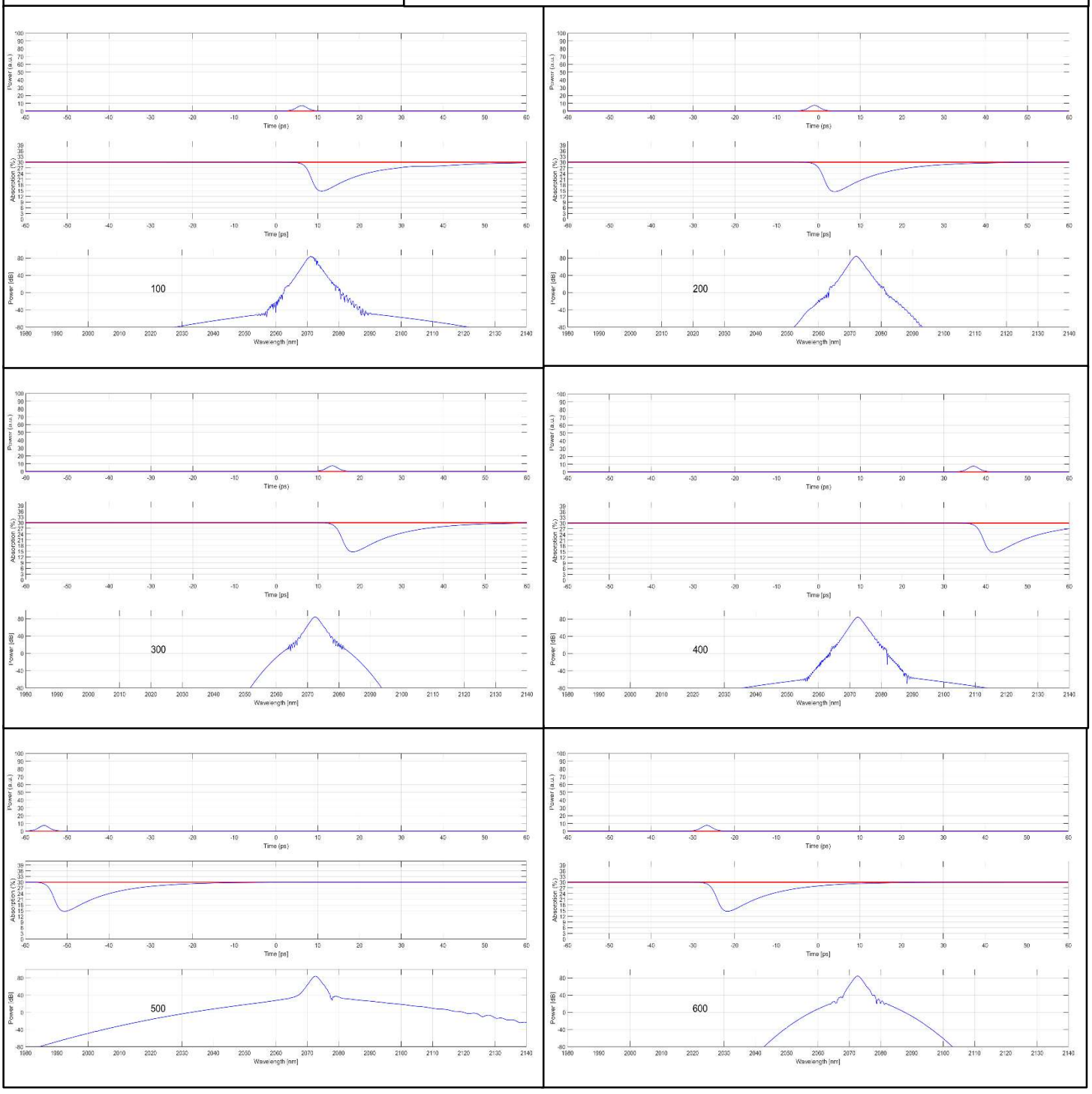

G.6 Design #6 Simulation

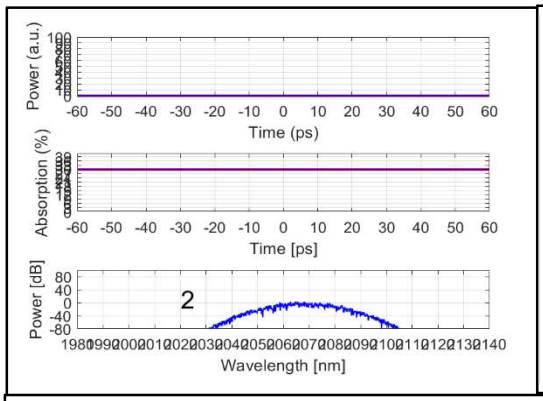

Figure G-6: (From top to bottom in each square) simulations of the time domain intensity, SESAM saturable absorption and the pulse spectrum at 2 to 600 round trips for Design #6 from Section 4.3.

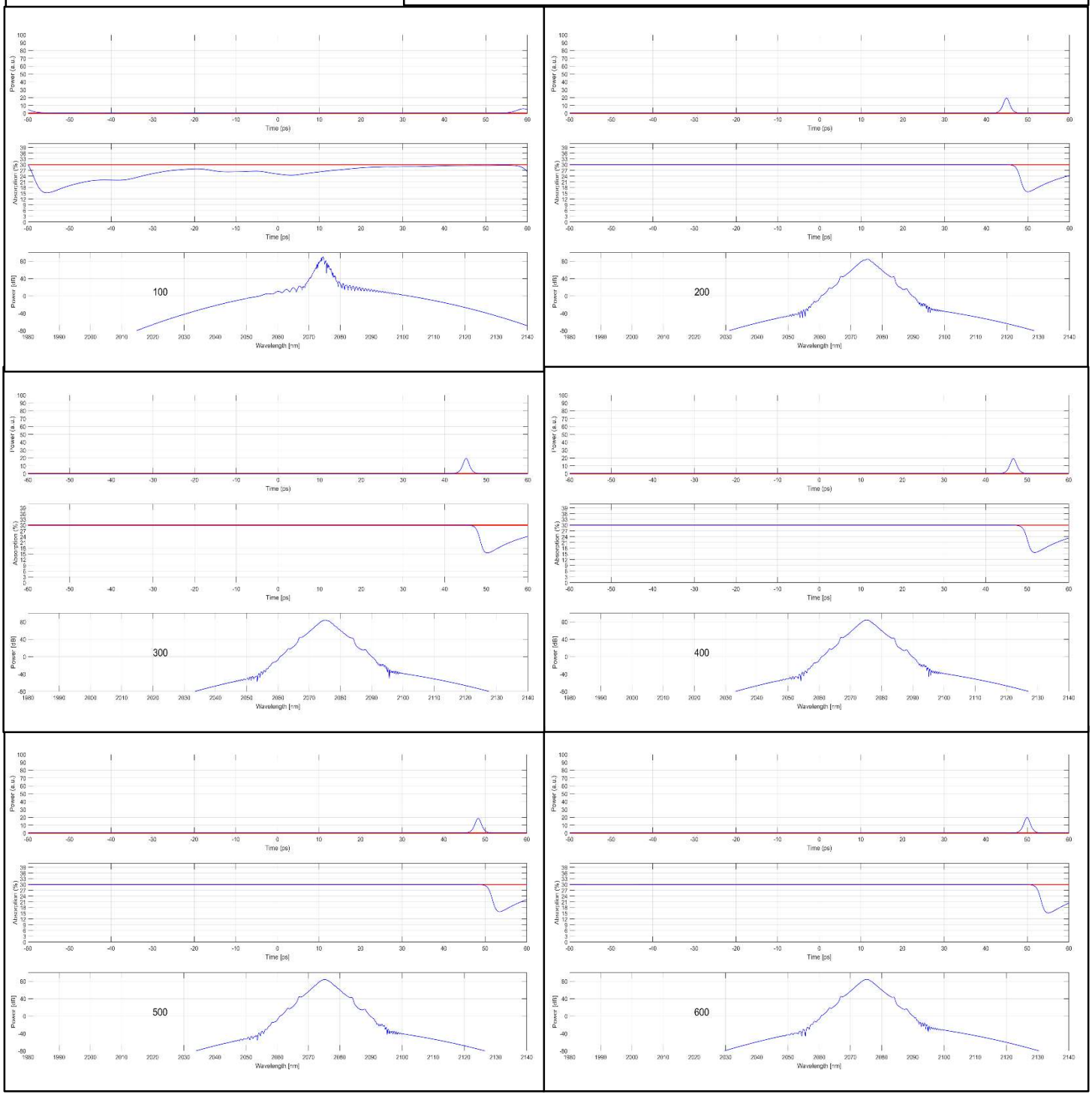

G.7 Design #7 Simulation

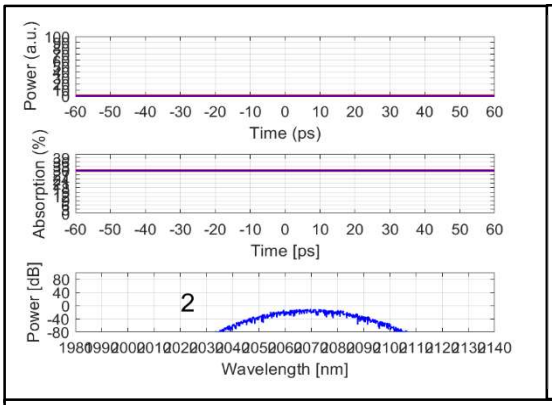

Figure G-7: (From top to bottom in each square) simulations of the time domain intensity, SESAM saturable absorption and the pulse spectrum at 2 to 600 round trips for Design #7 from Section 4.3

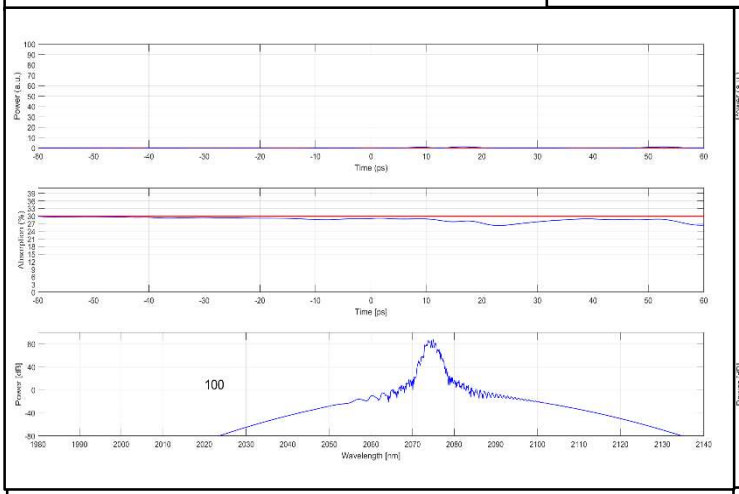

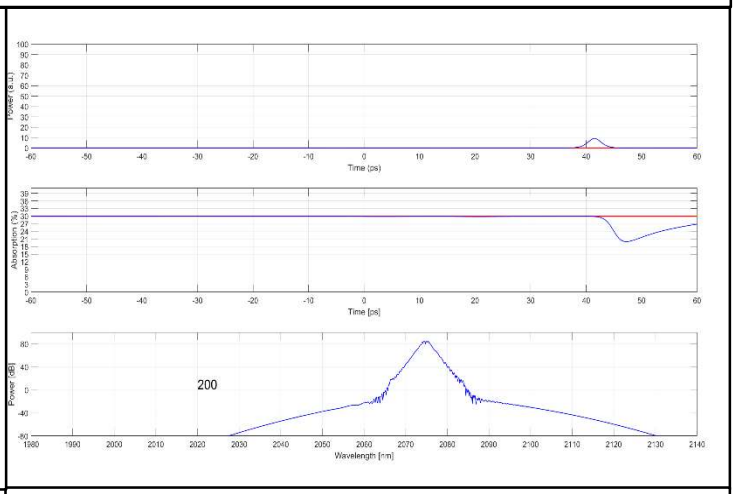

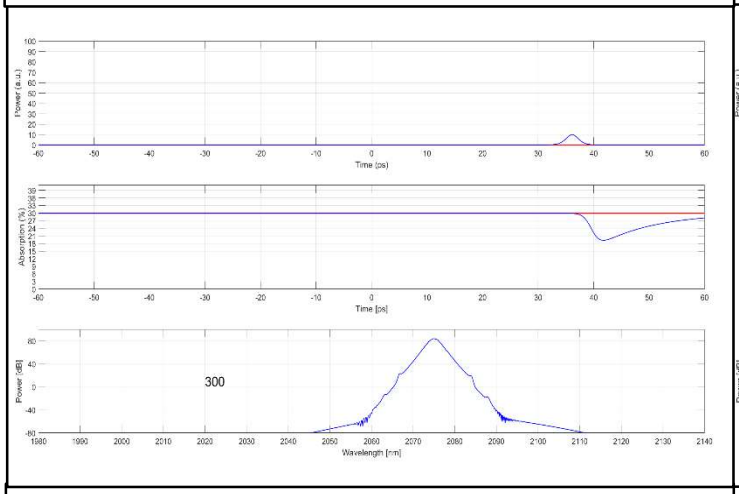

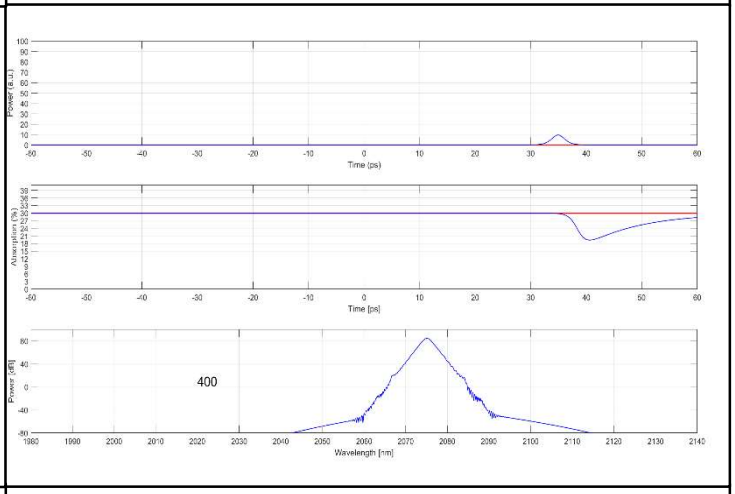

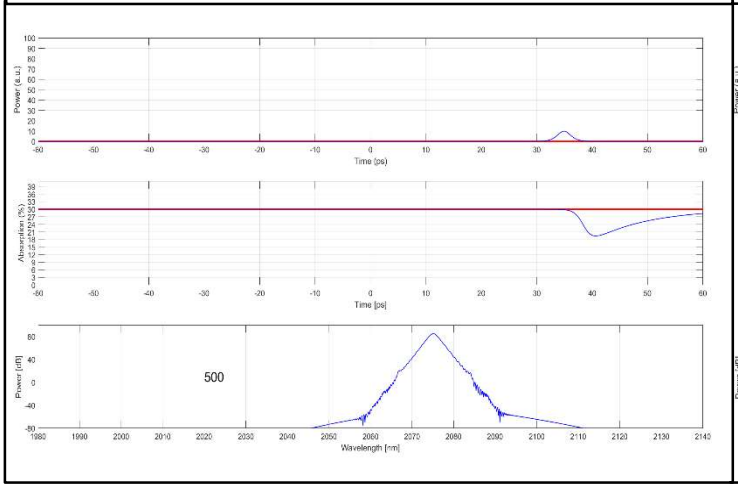

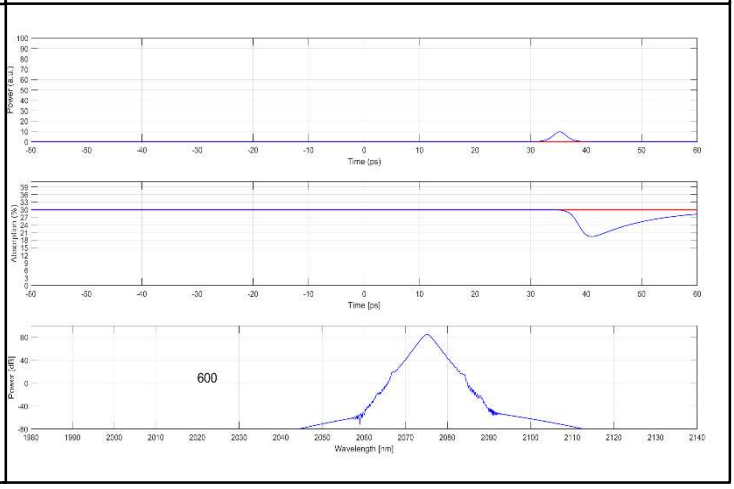

G.8 Design #8 Simulation

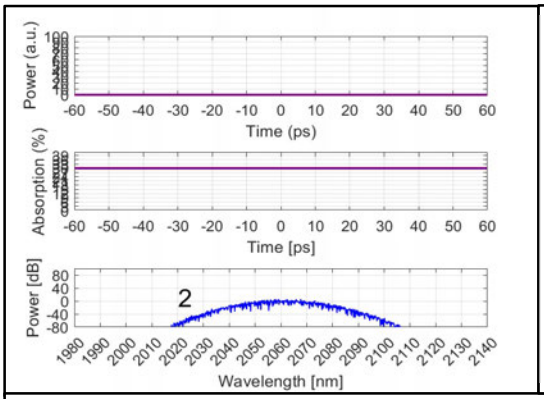

Figure G-8: (From top to bottom in each square) simulations of the time domain intensity, SESAM saturable absorption and the pulse spectrum at 2 to 600 round trips for Design #8 from Section 4.4.

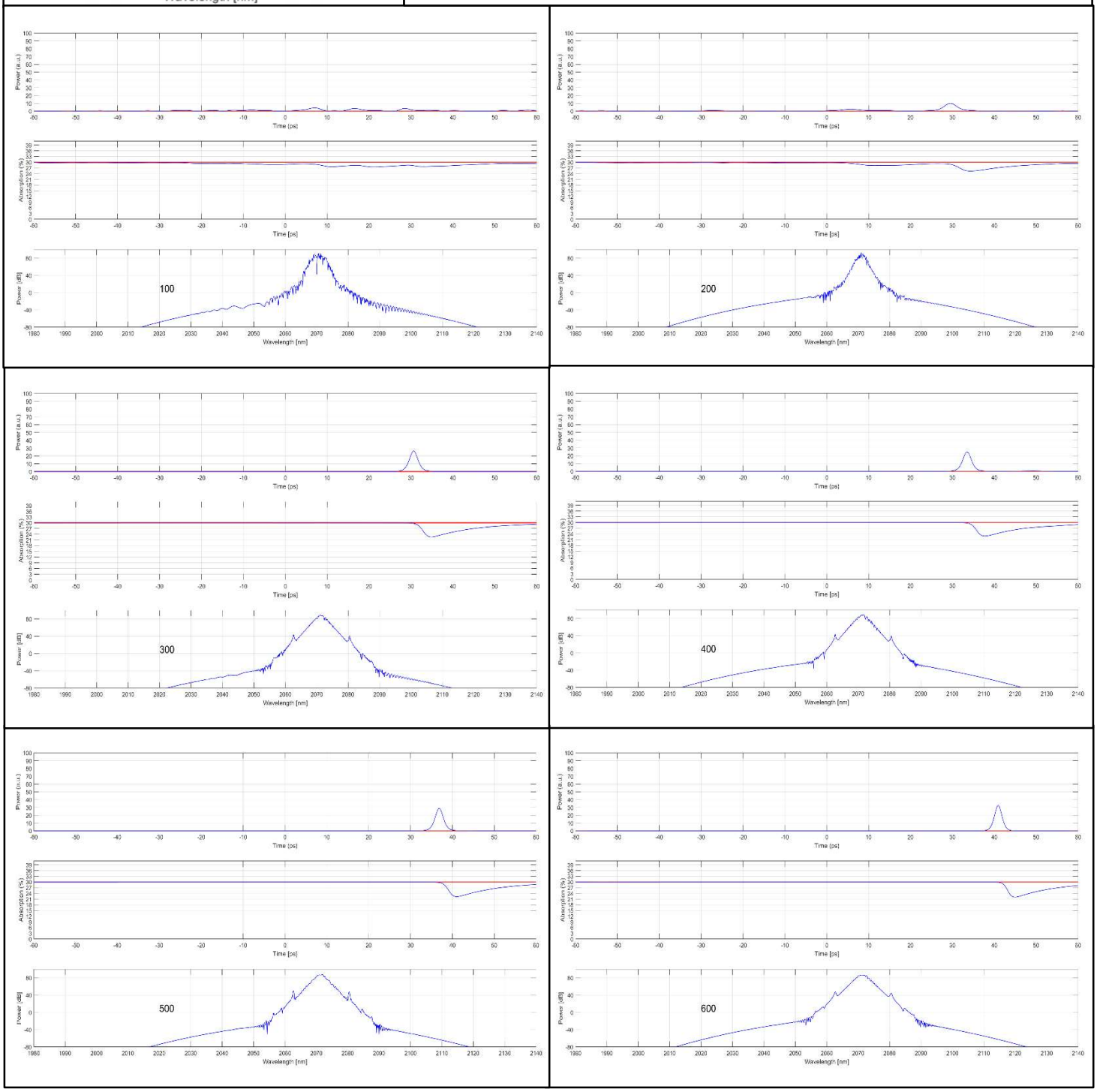

Appendix H
Time Evolution of DCF-spliced Cavity Simulations

Appendix H consists of five pages of printouts of the time domain intensity, SESAM absorptivity and pulse spectrum for simulations of 3, 5, 7, 9 and 11 m of DCF spliced into the cavity. Each simulation is started from a packet of random (quantum) of spectral noise generated via MATLABs normal distribution function, as can be seen in the 2nd round trip printout on Figures H-1 to H-5.

H.1 3 m DCF Simulation

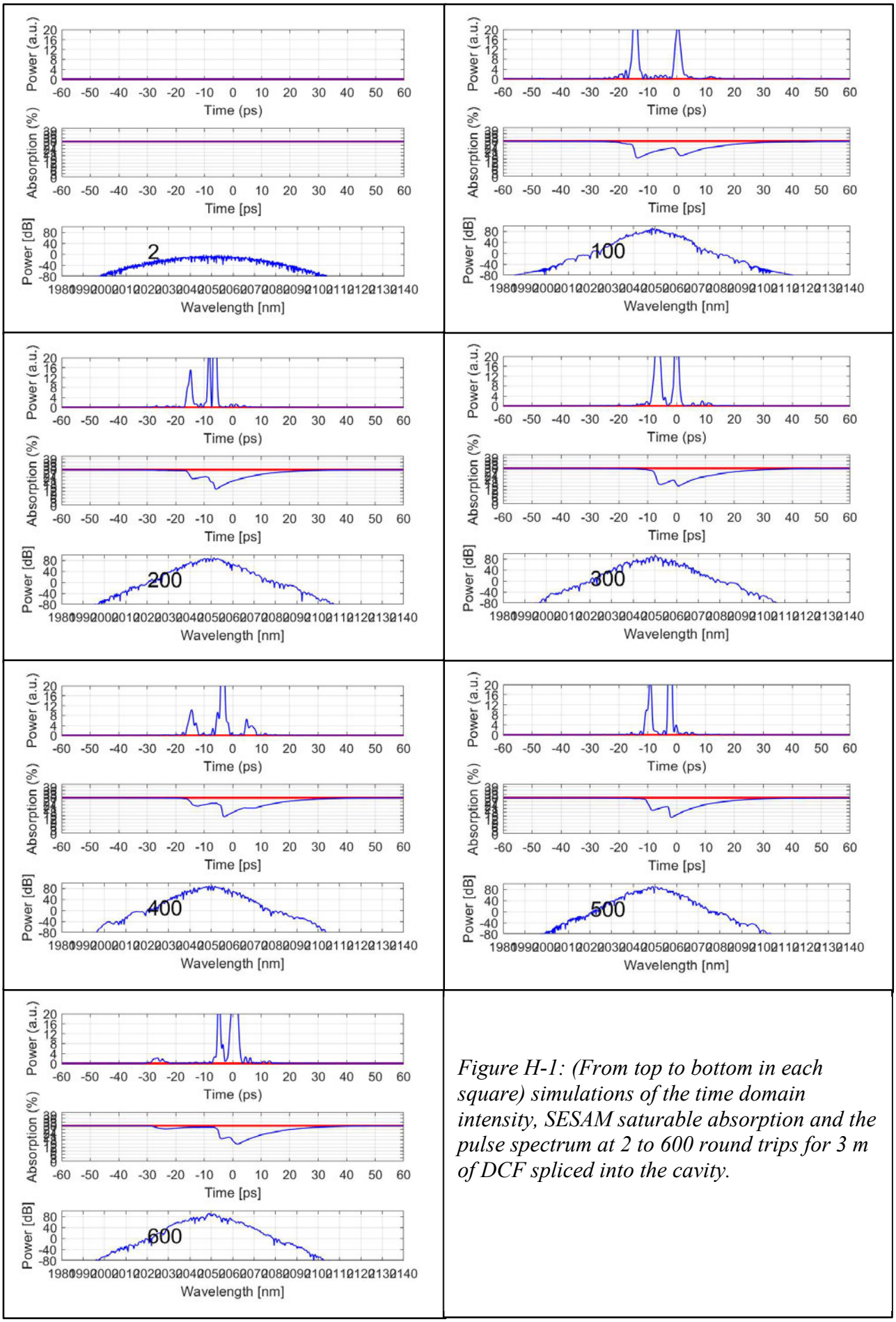

Figure H-1: (From top to bottom in each square) simulations of the time domain intensity, SESAM saturable absorption and the pulse spectrum at 2 to 600 round trips for 3 m of DCF spliced into the cavity.

H.2 5 m DCF Simulation

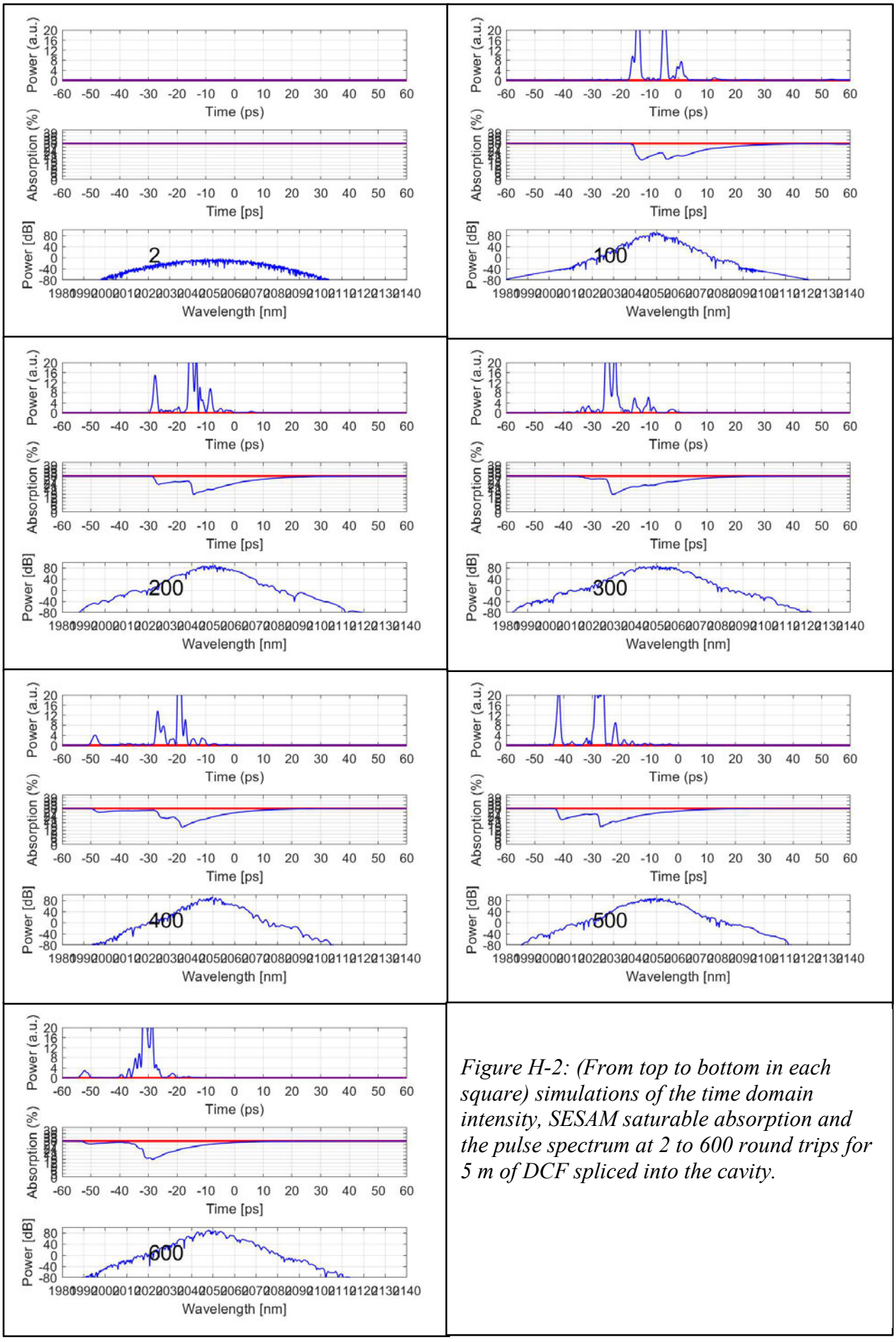

Figure H-2: (From top to bottom in each square) simulations of the time domain intensity, SESAM saturable absorption and the pulse spectrum at 2 to 600 round trips for 5 m of DCF spliced into the cavity.

H.3 7 m DCF Simulation

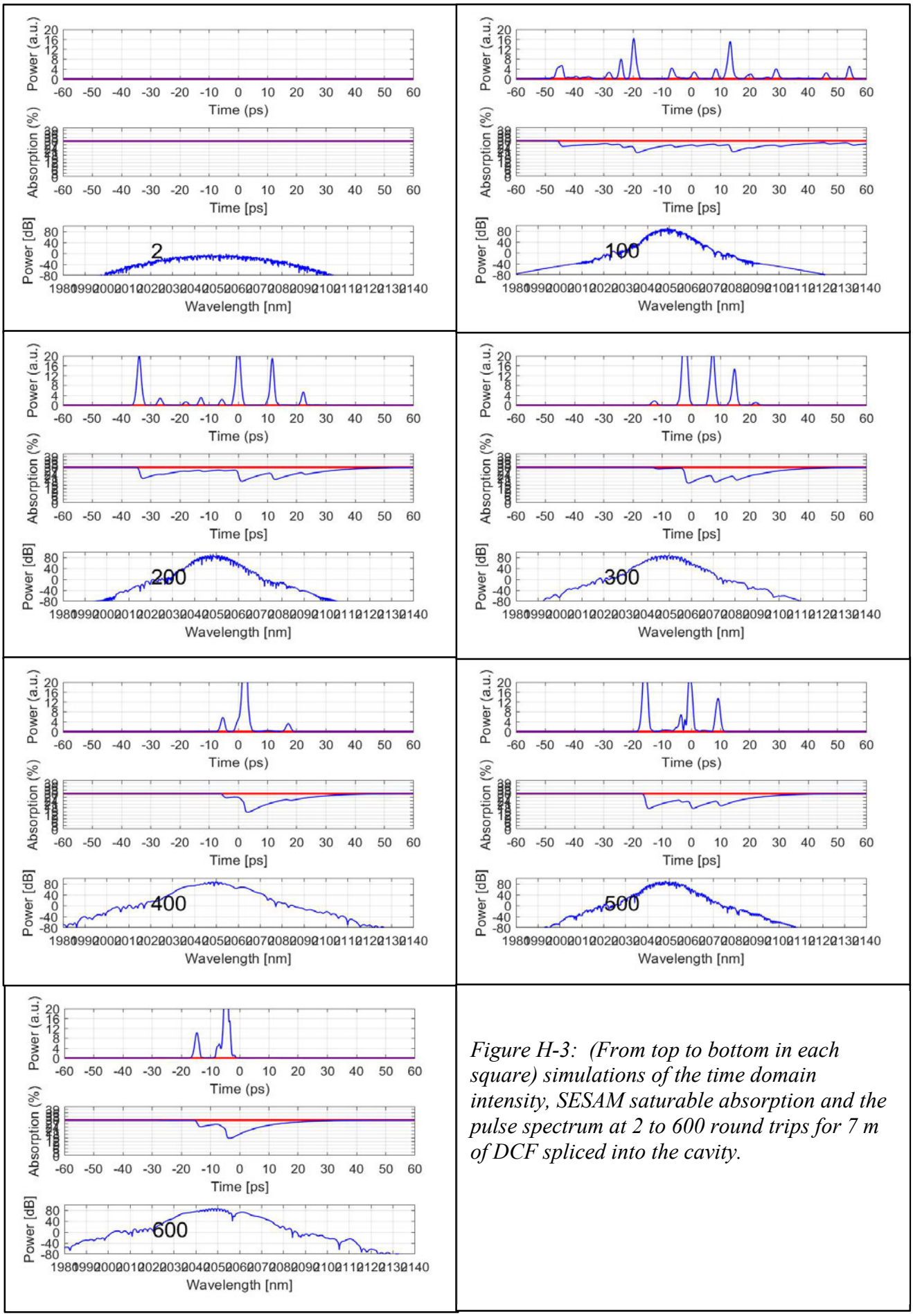

Figure H-3: (From top to bottom in each square) simulations of the time domain intensity, SESAM saturable absorption and the pulse spectrum at 2 to 600 round trips for 7 m of DCF spliced into the cavity.

H.4 9 m DCF Simulation

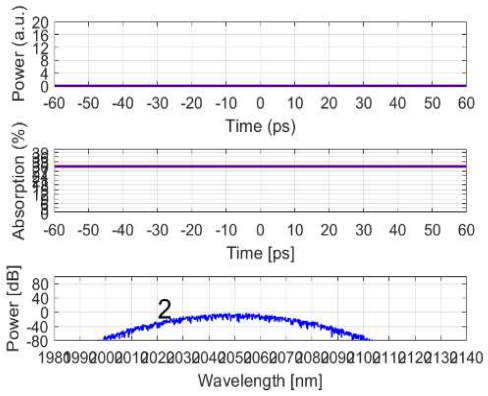

Figure H-4: (From top to bottom in each square) simulations of the time domain intensity, SESAM saturable absorption and the pulse spectrum at 2 to 600 round trips for 9 m of DCF spliced into the cavity.

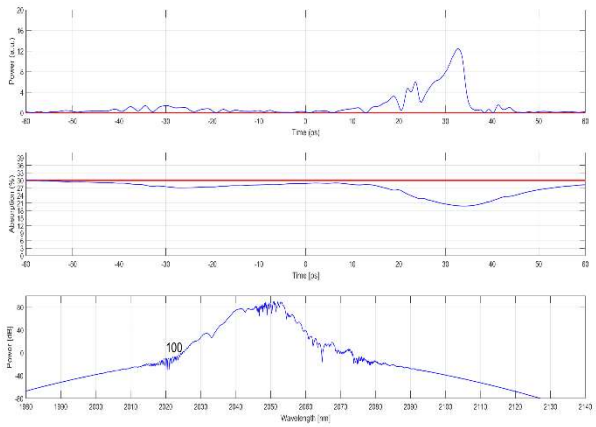

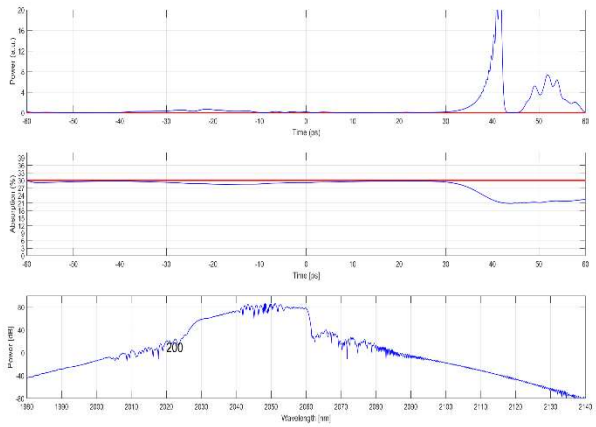

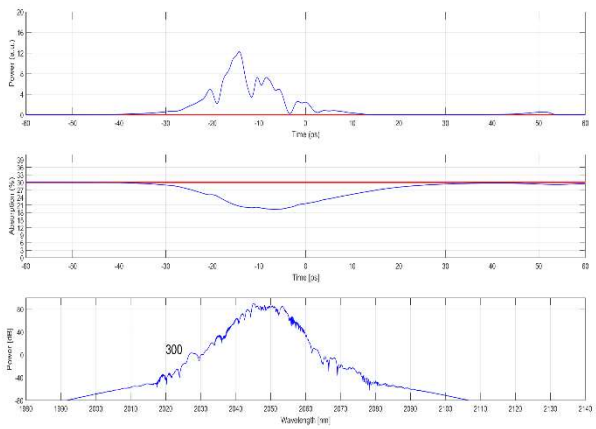

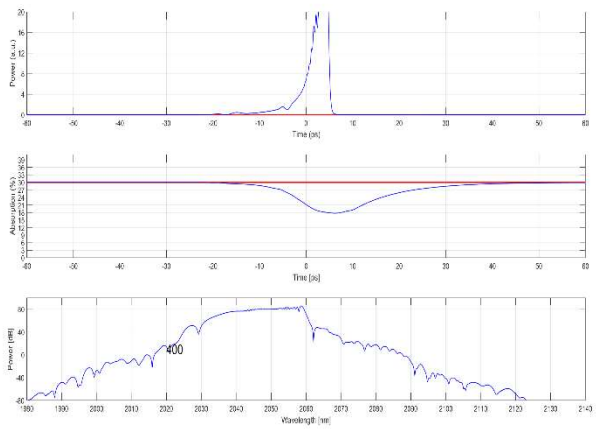

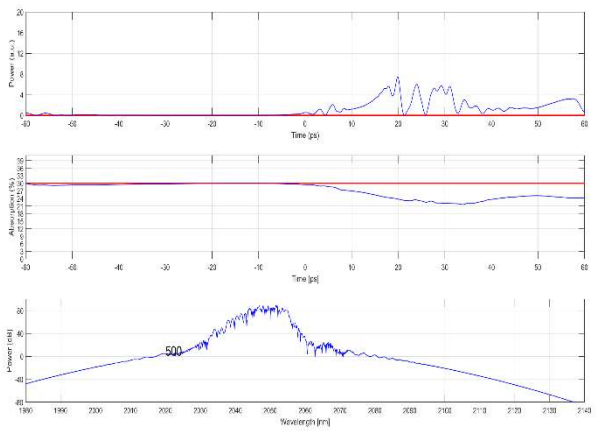

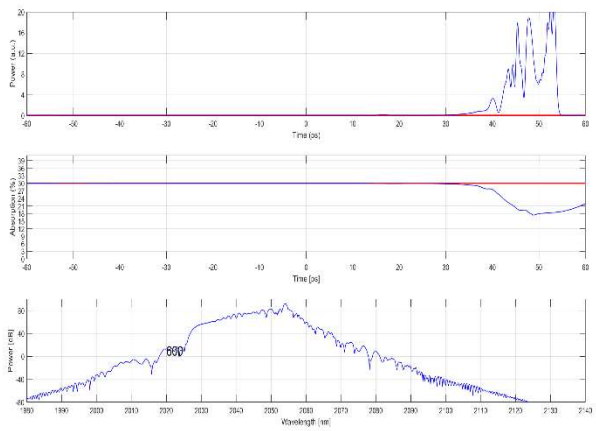

H.5 11 m DCF Simulation

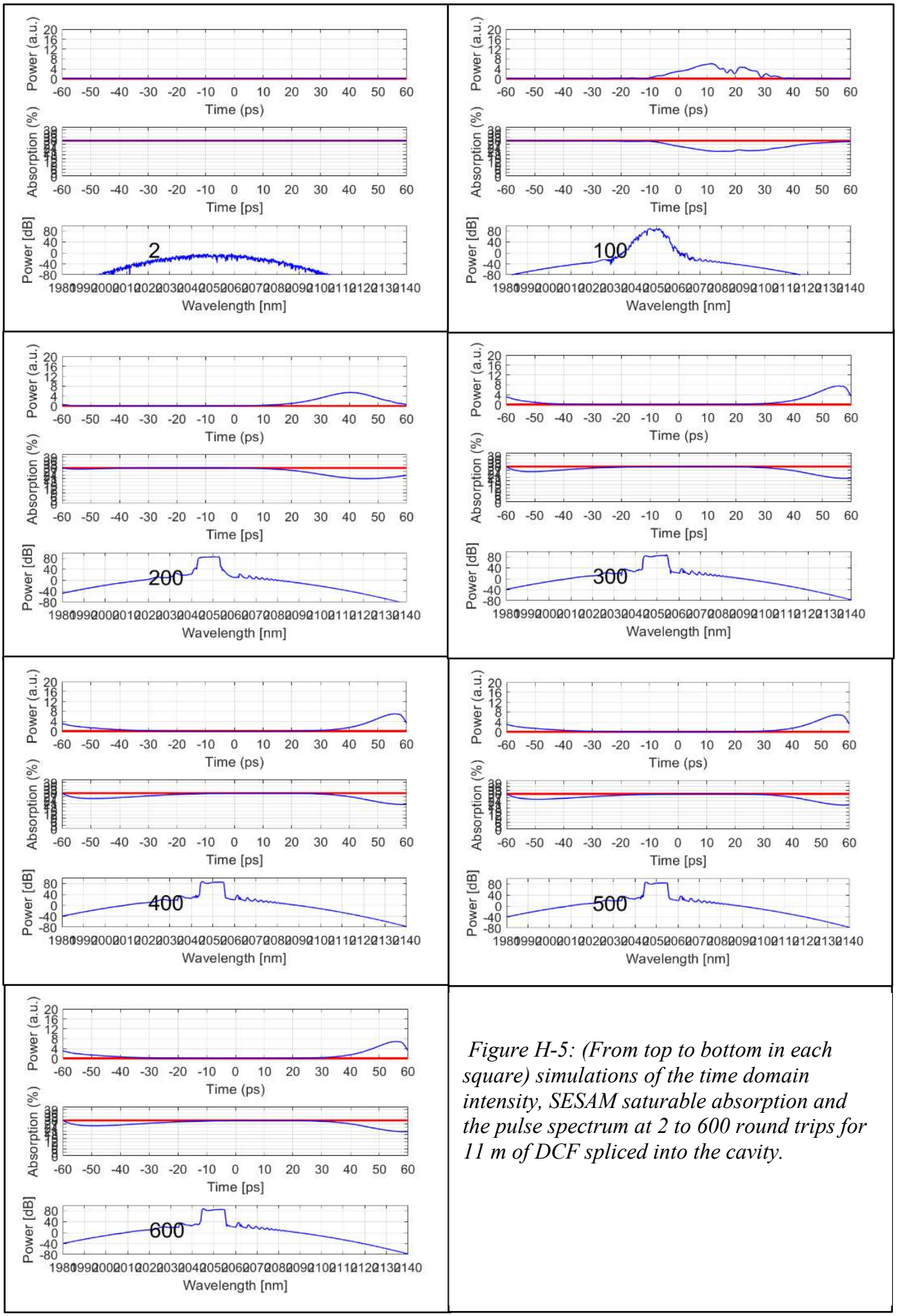

Figure H-5: (From top to bottom in each square) simulations of the time domain intensity, SESAM saturable absorption and the pulse spectrum at 2 to 600 round trips for 11 m of DCF spliced into the cavity.

Appendix I
Publications and Presentations

Kolovinos, A, Boyd, K, McAfee, D, Ganija, M & Veitch, P 2021, 'Optimisation of a Dispersion Compensating Fibre Length in a SESAM Mode-locked Cavity', presented at Australian and New Zealand Conference on Optics and Photonics (ANZCOP), online, 18 – 19 November

Kolovinos, A, Boyd, K, McAfee, D & Ganija, M 2022, 'Experimental Investigation of Ring Cavity Architecture on Holmium Fibre Laser Mode-locked Stability', presented at Australian and New Zealand Conference on Optics and Photonics (ANZCOP), Adelaide, South Australia, 12 – 15 December

References

Chapter 1

1. Haus, H.A., *Mode-locking of lasers.* IEEE journal of selected topics in quantum electronics, 2000. **6**(6): p. 1173-1185.

2. Ippen, E.P., *Principles of passive mode locking.* Applied physics. B, Lasers and optics, 1994. **58**(3): p. 159-170.

3. Ippen, E.P., *Principles of passive mode locking.* Applied Physics B, 1994. **58**(3): p. 159-170.

4. Kuizenga, D. and A. Siegman, *FM and AM mode locking of the homogeneous laser-Part I: Theory.* IEEE Journal of Quantum Electronics, 1970. **6**(11): p. 694-708.

5. Paschotta, R., *Mode Locking*, in *RP Encyclopedia of Laser Physics and Technology*, R. Paschotta, Editor. 2008, Wiley-VCH.

6. Pires, H., et al., *Ultrashort pulse generation in the mid-IR.* Progress in Quantum Electronics, 2015. **43**: p. 1-30.

7. Wang, Z., et al., *Recent developments in mid-infrared fiber lasers: Status and challenges.* Optics & Laser Technology, 2020. **132**: p. 106497.

8. Sorokina, I.T., et al., *Mid-IR Ultrashort Pulsed Fiber-Based Lasers.* IEEE Journal of Selected Topics in Quantum Electronics, 2014. **20**(5): p. 99-110.

9. Tian, K., et al. *Mid-Infrared Few-Cycle Pulse Generation and Amplification*. Photonics, 2021. **8**, DOI: 10.3390/photonics8080290.

10. Weigl, P., A. Kasenbacher, and K. Werelius, *Dental Applications*, in *Femtosecond Technology for Technical and Medical Applications*, F. Dausinger, H. Lubatschowski, and F. Lichtner, Editors. 2004, Springer Berlin Heidelberg: Berlin, Heidelberg. p. 167-187.

11. Schwab, B., et al., *The Use of Femtosecond Technology in Otosurgery*, in *Femtosecond Technology for Technical and Medical Applications*, F. Dausinger, H. Lubatschowski, and F. Lichtner, Editors. 2004, Springer Berlin Heidelberg: Berlin, Heidelberg. p. 211-226.

12. Kirsch, D.C., et al., *Short-wave IR ultrafast fiber laser systems: Current challenges and prospective applications.* Journal of Applied Physics, 2020. **128**(18): p. 180906.

13. Pierce, M., et al., *Development and application of fiber lasers for medical applications.* Proc SPIE, 2001. **4253**.

14. Waynant, R., I. Ilev, and I. Gannot, *Mid-infrared laser applications in medicine and biology.* Philosophical Transactions of The Royal Society B: Biological Sciences, 2001. **359**.

15. Colley, C.S., et al., *Mid-infrared optical coherence tomography.* Review of Scientific Instruments, 2007. **78**(12): p. 123108.

16. Richard, L.B., M.F. Nathaniel, and B.I. Pierce, *Comparison of holmium:YAG and thulium fiber laser lithotripsy: ablation thresholds, ablation rates, and retropulsion effects.* Journal of Biomedical Optics, 2011. **16**(7): p. 071403.

17. Geng, J. and S. Jiang, *Fiber Lasers: The 2 μm Market Heats Up.* Optics and Photonics News, 2014. **25**(7): p. 34-41.

18. Jackson, S. and A. Lauto, *Diode-pumped fiber lasers: A new clinical tool?* Lasers in surgery and medicine, 2002. **30**: p. 184-90.

19. Pierce, M.C., et al., *Laser-tissue interaction with a high-power 2-microm fiber laser: preliminary studies with soft tissue.* Lasers in surgery and medicine, 1999. **25**(5): p. 407.

20. Fried, N. and K. Murray, *High-Power Thulium Fiber Laser Ablation of Urinary Tissues at 1.94 μm.* Journal of endourology / Endourological Society, 2005. **19**: p. 25-31.

21. Fried, N., *Thulium fiber laser lithotripsy: An in vitro analysis of stone fragmentation using a modulated 110-watt Thulium fiber laser at 1.94 μm.* Lasers in surgery and medicine, 2005. **37**: p. 53-8.

22. Bouma, B.E., et al., *Self-phase-modulated Kerr-lens mode-locked Cr:forsterite laser source for optical coherence tomography.* Optics letters, 1996. **21**(22): p. 1839-1841.

23. Bouma, B.E., et al., *Optical coherence tomographic imaging of human tissue at 1.55 μM and 1.81 μM using ER- and TM-doped fiber sources.* Journal of biomedical optics, 1998. **3**(1): p. 76-79.

24. Nomura, Y., H. Murakoshi, and T. Fuji, *Short-wavelength, ultrafast thulium-doped fiber laser system for three-photon microscopy.* OSA Continuum, 2020. **3**(6): p. 1428-1435.

25. Horton, N.G., et al., *In vivo three-photon microscopy of subcortical structures within an intact mouse brain.* Nature Photonics, 2013. **7**(3): p. 205-209.

26. Horton, N.G. and C. Xu, *Dispersion compensation in three-photon fluorescence microscopy at 1,700 nm.* Biomedical Optics Express, 2015. **6**(4): p. 1392-1397.

27. Udem, T., et al., *Optical frequency-comb generation and high-resolution laser spectroscopy*, in *Few-Cycle Laser Pulse Generation and Its Applications*. 2004, Springer. p. 295-317.

28. Cundiff, S.T. and J. Ye, *Colloquium: Femtosecond optical frequency combs.* Reviews of Modern Physics, 2003. **75**(1): p. 325.

29. Udem, T., R. Holzwarth, and T.W. Hänsch, *Optical frequency metrology.* Nature, 2002. **416**(6877): p. 233-237.

30. Menzel, R., *Metrological Applications*, in *Femtosecond Technology for Technical and Medical Applications*, F. Dausinger, H. Lubatschowski, and F. Lichtner, Editors. 2004, Springer Berlin Heidelberg: Berlin, Heidelberg. p. 257-285.

31. Schliesser, A., N. Picqué, and T.W. Hänsch, *Mid-infrared frequency combs.* Nature Photonics, 2012. **6**(7): p. 440-449.

32. Duval, S., et al., *Femtosecond fiber lasers reach the mid-infrared.* Optica, 2015. **2**: p. 623-626.

33. Corkum, P.B., C. Rolland, and T. Srinivasan-Rao, *Supercontinuum Generation in Gases.* Physical Review Letters, 1986. **57**(18): p. 2268-2271.

34. Dudley, J.M. and J.R. Taylor, *Supercontinuum Generation in Optical Fibers*. 2010, Cambridge: Cambridge University Press.

35. Dudley, J.M., G. Genty, and S. Coen, *Supercontinuum generation in photonic crystal fiber.* Reviews of Modern Physics, 2006. **78**(4): p. 1135-1184.

36. Birks, T.A., W.J. Wadsworth, and P.S.J. Russell, *Supercontinuum generation in tapered fibers.* Optics Letters, 2000. **25**(19): p. 1415-1417.

37. Grassani, D., et al., *Mid infrared gas spectroscopy using efficient fiber laser driven photonic chip-based supercontinuum.* Nature Communications, 2019. **10**(1): p. 1553.

38. Scurria, G., et al., *7 W mid-infrared supercontinuum generation up to 4.7 μm in an indium-fluoride optical fiber pumped by a high-peak power thulium-doped fiber single-oscillator.* Optics Express, 2020. **28**(5): p. 7672-7677.

39. Taczak, T.M. and D.K. Killinger, *Development of a tunable, narrow-linewidth, cw 2.066-μm Ho:YLF laser for remote sensing of atmospheric CO2 and H2O.* Applied Optics, 1998. **37**(36): p. 8460-8476.

40. Hudson, D.D., *Invited paper: Short pulse generation in mid-IR fiber lasers.* Optical Fiber Technology, 2014. **20**(6): p. 631-641.

41. Thorpe, M.J., et al., *Cavity-ringdown molecular spectroscopy based on an optical frequency comb at 1.45-1.65 μm.* Optics Letters, 2007. **32**(3): p. 307-309.

42. Kadwani, P., et al. *Atmospheric gas detection using broadband mid-IR thulium fiber-based sources*. in *Defense + Commercial Sensing*. 2011.

43. Dixit, U.S., S.N. Joshi, and J.P. Davim, *Application of Lasers in Manufacturing: Select Papers from AIMTDR 2016*. 2018: Springer Singapore.

44. Lenzner, M., et al., *Femtosecond Optical Breakdown in Dielectrics.* Physical Review Letters, 1998. **80**(18): p. 4076-4079.

45. Wolfgang, K. and K. Joerg. *Femtosecond pulse laser ablation of metallic, semiconducting, ceramic, and biological materials*. in *Proc.SPIE*. 1994.

46. Kautek, W., et al., *Laser ablation of dielectrics with pulse durations between 20 fs and 3 ps.* Applied Physics Letters, 1996. **69**(21): p. 3146-3148.

47. Stuart, B.C., et al., *Laser-Induced Damage in Dielectrics with Nanosecond to Subpicosecond Pulses.* Physical Review Letters, 1995. **74**(12): p. 2248-2251.

48. Hertwig, A., et al., *Primary Hazards and Reliability of Protective Materials*, in *Femtosecond Technology for Technical and Medical Applications*, F. Dausinger, H. Lubatschowski, and F. Lichtner, Editors. 2004, Springer Berlin Heidelberg: Berlin, Heidelberg. p. 287-308.

49. Korte, F., et al., *Far-field and near-field material processing with. femtosecond laser pulses.* Applied Physics A, 1999. **69**(1): p. S7-S11.

50. Dausinger, F. and S. Nolte, *Introduction to Femtosecond Technology*, in *Femtosecond Technology for Technical and Medical Applications*, F. Dausinger, H. Lubatschowski, and F. Lichtner, Editors. 2004, Springer Berlin Heidelberg: Berlin, Heidelberg. p. 1-6.

51. Weikert, M. and F. Dausinger, *Cutting of Diamond*, in *Femtosecond Technology for Technical and Medical Applications*, F. Dausinger, H. Lubatschowski, and F. Lichtner, Editors. 2004, Springer Berlin Heidelberg: Berlin, Heidelberg. p. 155-165.

52. Mielke, M., et al., *Ultrafast fiber laser platform for advanced materials processing.* JLMN-Journal of Laser Micro/Nanoengineering, 2010. **5**.

53. Li, X., et al., *High-power graphene mode-locked Tm/Ho co-doped fiber laser with evanescent field interaction.* Scientific Reports, 2015. **5**(1): p. 16624.

54. Voisiat, B., et al., *Material processing with ultra-short pulse lasers working in 2μm wavelength range.* Proceedings of SPIE - The International Society for Optical Engineering, 2015. **9350**.

55. Mingareev, I., et al., *Welding of polymers using a 2μm thulium fiber laser.* Optics & Laser Technology, 2012. **44**(7): p. 2095-2099.

56. Breitling, D., et al., *Drilling of Metals*, in *Femtosecond Technology for Technical and Medical Applications*, F. Dausinger, H. Lubatschowski, and F. Lichtner, Editors. 2004, Springer Berlin Heidelberg: Berlin, Heidelberg. p. 131-156.

57. Nikogosyan, D.N., *Nonlinear Optical Crystals: A Complete Survey*. 2006: Springer New York.

58. Gebhardt, M., et al., *High peak-power mid-infrared ZnGeP2 optical parametric oscillator pumped by a Tm:fiber master oscillator power amplifier system.* Optics Letters, 2014. **39**(5): p. 1212-1215.

59. Menzies, R.T. and R.M. Hardesty, *Coherent Doppler lidar for measurements of wind fields.* Proceedings of the IEEE, 1989. **77**(3): p. 449-462.

60. Targ, R., et al., *Coherent lidar airborne windshear sensor: performance evaluation.* Applied optics, 1991. **30**(15): p. 2013-2026.

61. Collis, R., *Lidar.* Applied optics, 1970. **9**(8): p. 1782-1788.

62. Dubayah, R.O. and J.B. Drake, *Lidar remote sensing for forestry.* Journal of forestry, 2000. **98**(6): p. 44-46.

63. Henderson, S.W. and S.M. Hannon. *Advanced coherent lidar system for wind measurements*. in *Lidar Remote Sensing for Environmental Monitoring VI*. 2005. SPIE.

64. Lagatsky, A., et al., *2 μm solid-state laser mode-locked by single-layer graphene.* Applied Physics Letters, 2013. **102**(1): p. 013113.

65. Targ, R., et al., *Coherent lidar airborne wind sensor II: flight-test results at 2 and 10 μm.* Applied optics, 1996. **35**(36): p. 7117-7127.

66. Koch, G., et al., *High-energy 2 μm Doppler lidar for wind measurements.* Optical Engineering - OPT ENG, 2007. **46**.

67. Ambrico, P.F., et al., *Sensitivity analysis of differential absorption lidar measurements in the mid-infrared region.* Applied Optics, 2000. **39**(36): p. 6847-6865.

68. De Young, R.J. and N.P. Barnes, *Profiling atmospheric water vapor using a fiber laser lidar system.* Applied optics, 2010. **49**(4): p. 562-567.

69. Jackson, S.D., *Towards high-power mid-infrared emission from a fibre laser.* Nature photonics, 2012. **6**(7): p. 423-431.

70. Rottwitt, K., et al., *Scaling of the Raman gain coefficient: applications to germanosilicate fibers.* Journal of lightwave technology, 2003. **21**(7): p. 1652-1662.

71. Corkum, P.B., *Plasma perspective on strong field multiphoton ionization.* Physical review letters, 1993. **71**(13): p. 1994.

72. Marangos, J.P., *Solid progress.* Nature Physics, 2011. **7**(2): p. 97-98.

73. McPherson, A., et al., *Studies of multiphoton production of vacuum-ultraviolet radiation in the rare gases.* JOSA B, 1987. **4**(4): p. 595-601.

74. Popmintchev, T., et al., *The attosecond nonlinear optics of bright coherent X-ray generation.* Nature Photonics, 2010. **4**(12): p. 822-832.

75. Schafer, K.J., et al., *Above threshold ionization beyond the high harmonic cutoff.* Physical review letters, 1993. **70**(11): p. 1599-1602.

76. Sorokin, E., S. Naumov, and I.T. Sorokina, *Ultrabroadband infrared solid-state lasers.* IEEE Journal of Selected Topics in Quantum Electronics, 2005. **11**(3): p. 690-712.

77. Emelina, A.S., M.Y. Emelin, and M.Y. Ryabikin, *Wavelength scaling laws for high-order harmonic yield from atoms driven by mid- And long-wave infrared laser fields.* Journal of the Optical Society of America. B, Optical physics, 2019. **36**(11): p. 3236-3245.

78. Tate, J., et al., *Scaling of wave-packet dynamics in an intense midinfrared Field.* Physical review letters, 2007. **98**(1): p. 013901-013901.

79. Gibson, E.A., et al., *Coherent soft x-ray generation in the water window with quasi-phase matching.* Science, 2003. **302**(5642): p. 95-98.

80. Chang, Z., et al., *Generation of coherent soft X rays at 2.7 nm using high harmonics.* Physical Review Letters, 1997. **79**(16): p. 2967.

81. Spielmann, C., et al., *Generation of coherent X-rays in the water window using 5-femtosecond laser pulses.* Science, 1997. **278**(5338): p. 661-664.

82. Solem, J.C. and G.C. Baldwin, *Microholography of living organisms.* Science, 1982. **218**(4569): p. 229-235.

83. Seres, J., et al., *Source of coherent kiloelectronvolt X-rays.* Nature, 2005. **433**(7026): p. 596-596.

84. Schoenlein, R., et al., *Recent advances in ultrafast X-ray sources.* Philosophical Transactions of the Royal Society A, 2019. **377**(2145): p. 20180384.

85. Ebrahim-Zadeh, M. and I.T. Sorokina, *Mid-infrared coherent sources and applications*. 2007: Springer Science & Business Media.

86. Ebrahim-Zadeh, M. and K. Vodopyanov, *Mid-infrared coherent sources and applications: introduction.* JOSA B, 2016. **33**(11): p. MIC1-MIC1.

87. Corrigan, P., et al., *Quantum cascade lasers and the Kruse model in free space optical communication.* Optics Express, 2009. **17**(6): p. 4355-4359.

88. Li, Z., et al., *Thulium-doped fiber amplifier for optical communications at 2 μm.* Optics Express, 2013. **21**(8): p. 9289-9297.

89. Alfano, R.R. and S.L. Shapiro, *Ultrashort phenomena.* Phys. Today, 1975. **28**: p. 30-37.

90. Zewail, A.H., *Femtochemistry: Atomic-scale dynamics of the chemical bond.* The Journal of Physical Chemistry A, 2000. **104**(24): p. 5660-5694.

91. Cowan, M., et al., *Ultrafast memory loss and energy redistribution in the hydrogen bond network of liquid H2O.* Nature, 2005. **434**(7030): p. 199-202.

92. Mokhtari, A., et al., *Direct femtosecond mapping of trajectories in a chemical reaction.* Nature, 1990. **348**(6298): p. 225-227.

93. Ribessi, R.L., et al., *Quantification of Carbon Dioxide (CO2), Methane (CH4), and Nitrous Oxide (N2O) Using Near Infrared Spectroscopy and Multivariate Calibration in High Humidity Levels.* Journal of the Brazilian Chemical Society, 2022. **33**(4): p. 340-347.

94. Harris, S., et al., *N2O isotopocule measurements using laser spectroscopy: analyzer characterization and intercomparison.* Atmospheric Measurement Techniques, 2020. **13**.

95. Paschotta, R., *Passive mode locking*, in *RP Encyclopedia of Laser Physics and Technology*, R. Paschotta, Editor. 2017, Wiley-VCH.

96. Kobtsev, S.M., *Artificial saturable absorbers for ultrafast fibre lasers.* Optical Fiber Technology, 2022. **68**: p. 102764.

97. Vladimirov, A.G. and D. Turaev, *Model for passive mode locking in semiconductor lasers.* Physical Review A, 2005. **72**(3): p. 033808.

98. Keller, U., et al., *Semiconductor saturable absorber mirrors (SESAM's) for femtosecond to nanosecond pulse generation in solid-state lasers.* IEEE Journal of selected topics in QUANTUM ELECTRONICS, 1996. **2**(3): p. 435-453.

99. Paschotta, R., *Semiconductor Saturable Absorber Mirrors*, in *RP Encyclopedia of Laser Physics and Technology*, R. Paschotta, Editor. 2010, Wiley-VCH.

100. Rohrbacher, A., et al., *Multiphoton imaging with blue-diode-pumped SESAM-modelocked Ti: sapphire oscillator generating 5 nJ 82 fs pulses.* Optics Express, 2017. **25**(9): p. 10677-10684.

101. Tsuda, S., et al., *Low-loss intracavity AlAs/AlGaAs saturable Bragg reflector for femtosecond mode locking in solid-state lasers.* Optics Letters, 1995. **20**(12): p. 1406-1408.

102. Gaponenko, M., et al., *SESAM mode-locked red praseodymium laser.* Optics letters, 2014. **39**(24): p. 6939-6941.

103. Sorokina, I.T., et al. *A SESAM passively mode-locked Cr: ZnS laser*. 2006.

104. Wang, L., et al., *Sub-50 fs pulse generation from a SESAM mode-locked Tm,Ho-codoped calcium aluminate laser.* Optics letters, 2021. **46**(11): p. 2642-2645.

105. Saraceno, C.J., et al., *Sub-100 femtosecond pulses from a SESAM modelocked thin disk laser.* Applied physics. B, Lasers and optics, 2012. **106**(3): p. 559-562.

106. Bu, X., et al. *408-fs SESAM mode locked Cr: ZnSe laser*. in *2017 International Conference on Optical Instruments and Technology: Advanced Laser Technology and Applications*. 2018. SPIE.

107. Yang, J., et al., *Diode-pumped 10 W femtosecond Yb:CALGO laser with high beam quality.* High Power Laser Science and Engineering, 2021. **9**: p. e33.

108. Hou, J., et al., *High-stability passively mode-locked laser based on dual SESAM.* Applied Physics B, 2014. **116**(2): p. 347-351.

109. Kowalczyk, M., J. Sotor, and K.M. Abramski, *59 fs mode-locked Yb:KGW oscillator pumped by a single-mode laser diode.* Laser Physics Letters, 2016. **13**(3): p. 035801.

110. Leonov, S.O., et al., *Bound soliton formation in a SESAM mode-locked Cr:ZnSe laser with birefringent plates.* Applied Physics B, 2021. **127**(4): p. 56.

111. Kowalczyk, M., et al., *Dual-Comb Lasers: Dual-Comb Femtosecond Solid-State Laser with Inherent Polarization-Multiplexing.* Laser & photonics reviews, 2021. **15**(8).

112. Ghanbari, S., et al. *InP/InGaP quantum-dot SESAM mode-locked Alexandrite laser*. in *Solid State Lasers XXVII: Technology and Devices*. 2018.

113. Kowalczyk, M. and J. Sotor, *Investigation on dispersion regimes in Yb:KGW solid-state laser.* Laser Physics Letters, 2018. **15**(6): p. 065003.

114. Kim, H.-N., et al., *Mode Evolution and Lasing Characteristics of a Passively Mode-locked Nd:YAG Laser with a Saturable Output Coupler (SOC).* Journal- Korean Physical Society, 2011. **59**: p. 3210.

115. Lederer, M.J., et al., *Multipulse operation of a Ti:sapphire laser mode locked by an ion-implanted semiconductor saturable-absorber mirror.* Journal of the Optical Society of America B, 1999. **16**(6): p. 895-904.

116. Quarterman, A.H., et al., *A passively mode-locked external-cavity semiconductor laser emitting 60-fs pulses.* Nature Photonics, 2009. **3**(12): p. 729-731.

117. Zeng, H.-J., et al., *SESAM mode-locked Yb:SrLaAlO4 laser.* Optics Express, 2021. **29**(26): p. 43820-43826.

118. Chen-Sverre, T., *Ultrafast mode-locked semiconductor disk lasers for frequency domain measurement systems*. 2017.

119. Wang, Q., et al., *2μm Mode-locked fiber lasers.* Progress in Biomedical Optics and Imaging - Proceedings of SPIE, 2012. **8237**: p. 40.

120. Xu, Z., et al., *All-fiber wavelength-tunable Tm-doped fiber laser mode locked by SESAM with 120 nm tuning range.* Applied Optics, 2017. **56**: p. 5978.

121. Bharathan, G., et al. *All-fibre Ultrafast Mid-infrared Laser*. 2020.

122. Huang, C., et al., *Developing high energy mode-locked fiber laser at 2 micron.* 2015.

123. Herda, R. and O.G. Okhotnikov, *Dispersion compensation-free fiber laser mode-locked and stabilized by high-contrast saturable absorber mirror.* IEEE Journal of Quantum Electronics, 2004. **40**(7): p. 893-899.

124. Crombie, C., *Electronic and optical SESAM control in Cr^{4+}: forsterite lasers*. 2013, University of St Andrews.

125. Qi, Y., et al., *Low repetition rate, narrow-linewidth, all-fiber 1064 nm laser system.* Infrared Physics & Technology, 2021. **119**: p. 103930.

126. Krylov, A.A., et al., *Mode locking in a bismuth fibre laser by using a SESAM.* Quantum Electronics, 2008. **38**(3): p. 233.

127. Wang, Y., et al., *SESAM combined Kerr lens mode locked Yb:CALGO laser pumped by a 1.2 W single mode fiber coupled laser diode.* Laser Physics Letters, 2017. **14**: p. 055003.

128. Zhao, L.M., et al. *Soliton trapping in a Tm fiber laser*. in *CLEO: 2014*. 2014. San Jose, California: Optica Publishing Group.

129. Hirooka, T., et al., *A 440 fs, 9.2 GHz Hybrid Mode-Locked Erbium Fiber Laser with a Combination of Higher-Order Solitons and a SESAM Saturable Absorber*. 2016. STu1P.4.

130. Tolstik, N.A., et al., *Diode-pumped mode-locked holmium fiber laser at 2.138 μm*. 2017. 1-1.

131. Xu, Z.-w., et al. *Dual-wavelength mode-locked Yb-doped fiber laser with SESAM*. in *Asia Communications and Photonics Conference 2016*. 2016. Wuhan: Optica Publishing Group.

132. Chamorovskiy, A., et al., *Femtosecond mode-locked holmium fiber laser pumped by semiconductor disk laser.* Optics Letters, 2012. **37**(9): p. 1448-1450.

133. Liu, J., J. Xu, and P. Wang, *High Repetition-Rate Narrow Bandwidth SESAM Mode-Locked Yb-Doped Fiber Lasers.* IEEE Photonics Technology Letters, 2012. **24**(7): p. 539-541.

134. Hinkelmann, M., et al., *Mode-locked Ho-doped laser with subsequent diode-pumped amplifier in an all-fiber design operating at 2052 nm.* Optics Express, 2017. **25**(17): p. 20522-20529.

135. Wang, Q., et al. *Mode-locked Tm-Ho Fiber Laser with a Sb-based SESAM*. in *CLEO:2011 - Laser Applications to Photonic Applications*. 2011. Baltimore, Maryland: Optica Publishing Group.

136. Harun, S.W., et al., *Q-switched and mode-locked Ytterbium-doped fiber lasers With Sb2Te3 topological insulator saturable absorber.* IET Optoelectronics, 2018. **12**.

137. Lv, Z., et al., *SESAM mode-locked all-polarization-maintaining fiber linear cavity ytterbium laser source with spectral filter as pulse shaper.* Laser Physics, 2018. **28**(12): p. 125103.

138. Okhotnikov, O., A. Grudinin, and M. Pessa, *Ultra-fast fibre laser systems based on SESAM technology: new horizons and applications.* New Journal of Physics, 2004. **6**(1): p. 177.

139. Soltanian, M.R.K., et al., *All-fiber sub-20 ps ultra low repetition rate high peak power mode-locked fiber laser to generate supercontinuum.* Laser Physics Letters, 2020. **17**(2): p. 025104.

140. Stoliarov, D.A., et al., *Linear cavity fiber laser harmonically mode-locked with SESAM.* Laser Physics Letters, 2020. **17**(10): p. 105102.

141. Grześ, P., M. Michalska, and J. Świderski, *Picosecond mode-locked tm-doped fibre laser and amplifier system providing over 20 W of average output power at 1994 nm.* Metrology and Measurement Systems, 2018. **vol. 25**(No 4): p. 649–658-649–658.

142. Aleksandr, A.K., et al., *Picosecond pulse generation in a passively mode-locked Bi-doped fibre laser.* Quantum Electronics, 2009. **39**(10): p. 882.

143. Huang, C., et al., *Selectively mode-locked high-order-mode 2-μm thulium fiber laser.* Optics Communications, 2019. **440**: p. 95-99.

144. Zhang, L., et al., *SESAM Mode-Locked, Environmentally Stable, and Compact Dissipative Soliton Fiber Laser.* IEEE Photonics Technology Letters, 2014. **26**(13): p. 1314-1316.

145. Doudou, G., et al. *SESAM-based ring-cavity all-normal-dispersion tunable Ytterbium mode-locked fiber laser*. in *2013 18th OptoElectronics and Communications Conference held jointly with 2013 International Conference on Photonics in Switching (OECC/PS)*. 2013.

146. Wang, H., et al. *Stable SESAM-mode-locked Yb fiber laser in the similariton regime*. in *Laser Congress 2017 (ASSL, LAC)*. 2017. Nagoya, Aichi: Optica Publishing Group.

147. Jiménez-Rodríguez, M., et al. *Sub-200 fs mode-locked fiber laser with InN-based SESAM*. in *2017 Conference on Lasers and Electro-Optics Europe & European Quantum Electronics Conference (CLEO/Europe-EQEC)*. 2017.

148. Afifi, G., et al., *Timing stability enhancement of an Erbium Doped mode locked Fiber Laser using SESAM mirror.* Optical Fiber Technology, 2016. **29**: p. 74-83.

149. Zhang, B., et al., *All-fiberized polarized mode-locked thulium-doped fibre laser.* Laser Physics Letters, 2015. **12**(1): p. 015102.

150. Tolstik, N., et al. *Compact Diode-pumped Dispersion-managed SESAM-mode-locked Ho:fiber Laser*. in *High-Brightness Sources and Light-Driven Interactions*. 2016. Long Beach, California: Optica Publishing Group.

151. Gomes, L.A., et al., *Picosecond SESAM-based ytterbium mode-locked fiber lasers.* IEEE Journal of Selected Topics in Quantum Electronics, 2004. **10**(1): p. 129-136.

152. Li, Y., et al., *Sub-Femtosecond Timing Jitter From a SESAM Mode-Locked Yb-Fiber Laser.* IEEE Photonics Technology Letters, 2021. **33**(23): p. 1309-1312.

153. Li, P., et al., *Subpicosecond SESAM and nonlinear polarization evolution hybrid mode-locking ytterbium-doped fiber oscillator.* Applied Physics B, 2015. **118**(4): p. 561-566.

154. Mashiko, Y., E. Fujita, and M. Tokurakawa, *Tunable noise-like pulse generation in mode-locked Tm fiber laser with a SESAM.* Optics Express, 2016. **24**(23): p. 26515-26520.

155. Gumenyuk, R., et al., *Vector Soliton Bunching in Thulium-Holmium Fiber Laser Mode-Locked With PbS Quantum-Dot-Doped Glass Absorber.* Quantum Electronics, IEEE Journal of, 2012. **48**: p. 903-907.

156. Wang, Y., et al. *52-fs SESAM Mode-Locked Tm,Ho:CALGO Laser*. in *Laser Congress 2019 (ASSL, LAC, LS&C)*. 2019. Vienna: Optica Publishing Group.

157. Lecourt, J.-B., et al., *All-normal dispersion, all-fibered PM laser mode-locked by SESAM.* Optics Express, 2012. **20**(11): p. 11918-11923.

158. Hasegawa, A. and F. Tappert, *Transmission of stationary nonlinear optical pulses in dispersive dielectric fibers. I. Anomalous dispersion.* Applied Physics Letters, 1973. **23**(3): p. 142-144.

159. Pawliszewska, M., et al., *Wavelength-and dispersion-tunable ultrafast holmium-doped fiber laser with dual-color operation.* Optics Letters, 2020. **45**(4): p. 956-959.

Chapter 2

1. Goure, J.-P. and I. Verrier, *Optical fibre devices*. 2016: CRC Press.

2. Yan, Y. and R. Pitchumani, *Numerical study on the dopant concentration and refractive index profile evolution in an optical fiber manufacturing process.* International journal of heat and mass transfer, 2006. **49**(13-14): p. 2097-2112.

3. Blair, S 2008,'Wave propagation in fibers', lecture notes in the topic ECE 5411 Electrical Engineering for Nonmajors, University of Utah, viewed 11/02/2023

4. Petermann, K., *Constraints for fundamental-mode spot size for broadband dispersion-compensated single-mode fibres.* Electronics Letters, 1983. **18**(19): p. 712-714.

5. Marcuse, D., *Loss analysis of single-mode fiber splices.* Bell system technical journal, 1977. **56**(5): p. 703-718.

6. Paschotta, R., *Fibre Joints*, in *RP Encyclopedia of Laser Physics and Technology*, R. Paschotta, Editor. 2008, Wiley-VCH.

7. Cui, Z., et al., *Modeling the splice loss of single-mode optical fibers affected by altitude.* IEEE Access, 2019. **7**: p. 99283-99289.

8. Paschotta, R., *Chromatic dispersion*, in *RP Encyclopedia of Laser Physics and Technology*, R. Paschotta, Editor. 2008, Wiley-VCH.

9. Paschotta, R. *Field guide to optical fiber technology*. 2010. SPIE.

10. Wemple, S., *Material dispersion in optical fibers.* Applied Optics, 1979. **18**(1): p. 31-35.

11. Saleh, B.E. and M.C. Teich, *Fundamentals of photonics*. 2019: john Wiley & sons.

12. Tariyal, B. and A. Cherin, *Optical fiber communications.* 2003.

13. Willner, A.E. and B. Hoanca, *Fixed and tunable management of fiber chromatic dispersion*, in *Optical Fiber Telecommunications IV-B*. 2002, Elsevier. p. 642-724.

14. Agrawal, G.P., *Nonlinear fiber optics*, in *Nonlinear Science at the Dawn of the 21st Century*. 2000, Springer. p. 195-211.

15. Okamoto, K., *Fundamentals of optical waveguides*. 2021: Elsevier.

16. Marfice, J.P. and O.R. Baiocchi, *Dispersion approximation using higher-order Taylor series terms.* Applied optics, 1987. **26**(19): p. 4043-4045.

17. Ramaswami, R., K. Sivarajan, and G. Sasaki, *Optical networks: a practical perspective*. 2009: Morgan Kaufmann.

18. Paschotta, R., *Chirp*, in *RP Encyclopedia of Laser Physics and Technology*, R. Paschotta, Editor. 2007, Wiley-VCH.

19. Grüner-Nielsen, L., et al., *Dispersion compensating fibers.* Optical fiber technology, 2000. **6**(2): p. 164-180.

20. Cao, B., et al., *Dispersion compensating fibers with improved splicing performance.* Physics Procedia, 2013. **48**: p. 96-101.

21. Webb, C. and J.D. Jones, *Handbook of Laser Technology and Applications: Volume 3: Applications*. 2020: CRC Press.

22. Thomson, R., C. Leburn, and D. Reid, *Ultrafast nonlinear optics*. Vol. 33. 2013: Springer.

23. Kodama, Y., et al., *Role of third-order dispersion on soliton instabilities and interactions in optical fibers.* Optics letters, 1994. **19**(3): p. 165-167.

24. Desaix, M., D. Anderson, and M. Lisak, *Solitons emerging from pulses launched in the vicinity of the zero-dispersion point in a single-mode optical fiber.* Optics Letters, 1990. **15**(1): p. 18-20.

25. Agrawal, G., *Nonlinear fiber optics*. Sixth edition. ed. 2019, London, England: Academic Press.

26. Agrawal, G.P. and M. Potasek, *Nonlinear pulse distortion in single-mode optical fibers at the zero-dispersion wavelength.* Physical Review A, 1986. **33**(3): p. 1765.

27. Dakova, D., et al., *Soliton regime of propagation of optical pulses in isotropic medium under the influence of third order of linear dispersion and dispersion of nonlinearity.* nonlinearity, 2016. **4**(10): p. 10.

28. Porsezian, K. and K. Nakkeeran, *Optical solitons in presence of Kerr dispersion and self-frequency shift.* Physical review letters, 1996. **76**(21): p. 3955.

29. Gangwar, R., S. Singh, and N. Singh, *Soliton based optical communication.* Progress In Electromagnetics Research, 2007. **74**: p. 157-166.

30. Nair, S.S. and V. Prem, *Solitons: a promising technology in optical communication.* International J of Science and Research, 2014. **3**(1).

31. Gardner, C.S. and G. Papen, *Optical communications*, in *Reference Data for Engineers*. 2002, Elsevier. p. 22-1-22-28.

32. Paschotta, R., *Intermodal Dispersion*, in *RP Encyclopedia of Laser Physics and Technology*, R. Paschotta, Editor. 2007, Wiley-VCH.

33. Hui, R. and M. O'Sullivan, *Fiber optic measurement techniques*. 2009: Academic Press.

34. Zhou, L., et al., *Generation of stretched pulses from an all-polarization-maintaining Er-doped mode-locked fiber laser using nonlinear polarization evolution.* Applied Physics Express, 2019. **12**(5): p. 052017.

35. Varnham, M., et al., *Analytic solution for the birefringence produced by thermal stress in polarization-maintaining optical fibers.* Journal of lightwave technology, 1983. **1**(2): p. 332-339.

36. Paschotta, R., *Polarization-maintaining fibers*, in *RP Encyclopedia of Laser Physics and Technology*, R. Paschotta, Editor. 2007, Wiley-VCH.

37. Guan, R., et al., *Stress birefringence analysis of polarization maintaining optical fibers.* Optical Fiber Technology, 2005. **11**(3): p. 240-254.

38. *Polarization-Maintaining Fiber Tutorial* in *FiberStore Community*. 2015.

39. Cheng, Y., *Optical Isolators, Circulators.* 2003.

40. Ryabochkina, P.A.e., et al., *Absorption and luminescence characteristics of transitions of the holmium ion in-doped aluminosilicate preforms and fibres.* Quantum Electronics, 2015. **45**(2): p. 102.

41. Hemming, A., et al., *A review of recent progress in holmium-doped silica fibre sources.* Optical Fiber Technology, 2014. **20**(6): p. 621-630.

42. Várallyay, Z. and J. Jasapara, *Comparison of amplification in large area fibers using cladding-pump and fundamental-mode core-pump schemes.* Optics express, 2009. **17**(20): p. 17242-17252.

43. *Core pumping and cladding pumping*. 2021.

44. Hemming, A., et al., *High power operation of cladding pumped holmium-doped silica fibre lasers.* Optics express, 2013. **21**(4): p. 4560-4566.

45. Jackson, S.D., *Midinfrared holmium fiber lasers.* IEEE journal of quantum electronics, 2006. **42**(2): p. 187-191.

46. Kurkov, A.S., et al., *Holmium fibre laser with record quantum efficiency.* Quantum Electronics, 2011. **41**(6): p. 492.

47. Eilchi, M. and P. Parvin, *Heat generation and removal in fiber lasers.* Fiber Laser, 2016: p. 321-344.

48. Stucky, G.D., S.R. Marder, and J.E. Sohn, *Linear and nonlinear polarizability: A primer*. 1991, ACS Publications.

49. Boyd, R.W., *Nonlinear optics*. 2020: Academic press.

50. Sheik-Bahae, M. and M.P. Hasselbeck, *Third-order optical nonlinearities.* Handbook of Optics, 2000. **4**: p. 16.1-16.36.

51. Belanger, P.-A. and C. Pare, *Self-focusing of Gaussian beams: an alternate derivation.* Applied Optics, 1983. **22**(9): p. 1293-1295.

52. Crespo, H.M. and C.C. Rosa. *Femtosecond lasers for optical coherence tomography*. in *1st Canterbury Workshop on Optical Coherence Tomography and Adaptive Optics*. 2008. SPIE.

53. Pandit, S., *Fundamentals of Femtosecond LASER*. 2015.

54. Ait-Ameur, K., *Kerr lens effect induced by a super-Gaussian laser beam.* Optik, 2021. **241**: p. 167250.

55. Giovanni, D., *Optical-spin Dynamics in Organic-inorganic Hybrid Lead Halide Perovskites*. 2017, Nanyang Technological University.

56. Paschotta, R., *Kerr lens*, in *RP Encyclopedia of Laser Physics and Technology*, R. Paschotta, Editor. 2008, Wiley-VCH.

57. Shimizu, F., *Frequency broadening in liquids by a short light pulse.* Physical Review Letters, 1967. **19**(19): p. 1097.

58. Stolen, R.H. and C. Lin, *Self-phase-modulation in silica optical fibers.* Physical Review A, 1978. **17**(4): p. 1448.

59. Suda, A. and T. Takeda, *Effects of nonlinear chirp on the self-phase modulation of ultrashort optical pulses.* Applied Sciences, 2012. **2**(2): p. 549-557.

60. Washburn, B.R., J.A. Buck, and S.E. Ralph, *Transform-limited spectral compression due to self-phase modulation in fibers.* Optics Letters, 2000. **25**(7): p. 445-447.

61. Pinault, S.C. and M. Potasek, *Frequency broadening by self-phase modulation in optical fibers.* JOSA B, 1985. **2**(8): p. 1318-1319.

62. Tomlinson, W., R. Stolen, and C. Shank, *Compression of optical pulses chirped by self-phase modulation in fibers.* JOSA B, 1984. **1**(2): p. 139-149.

63. Minkovski, N., et al., *Nonlinear polarization rotation and orthogonal polarization generation experienced in a single-beam configuration.* JOSA B, 2004. **21**(9): p. 1659-1664.

64. Cao, X.D. and D.D. Meyerhofer. *Nonlinear birefringence of optical fibers*. in *Conference on Lasers and Electro-Optics*. 1993. Baltimore, Maryland: Optica Publishing Group.

65. Yang, Z., et al. *Numerical analysis of the nonlinear polarization rotation mode-locked pulses in fiber*. in *2011 Asia Communications and Photonics Conference and Exhibition (ACP)*. 2011. IEEE.

66. Koechner, W., *Solid-state laser engineering*. Vol. 1. 2013: Springer.

67. Jones, R.R., et al., *Raman techniques: fundamentals and frontiers.* Nanoscale research letters, 2019. **14**(1): p. 1-34.

68. Bloembergen, N., *The stimulated Raman effect.* American Journal of Physics, 1967. **35**(11): p. 989-1023.

69. Paschotta, R., *Raman Scattering*, in *RP Encyclopedia of Laser Physics and Technology*, R. Paschotta, Editor. 2007, Wiley-VCH.

70. Mukherjee, S., *The science of clays.* Netherlands: Springer Science and Business Media, 2013.

71. Blow, K.J. and D. Wood, *Theoretical description of transient stimulated Raman scattering in optical fibers.* IEEE Journal of Quantum Electronics, 1989. **25**(12): p. 2665-2673.

72. Santhanam, J. and G.P. Agrawal, *Raman-induced spectral shifts in optical fibers: general theory based on the moment method.* Optics Communications, 2003. **222**(1-6): p. 413-420.

73. Mitschke, F.M. and L.F. Mollenauer, *Discovery of the soliton self-frequency shift.* Optics letters, 1986. **11**(10): p. 659-661.

74. Nguyen, D.T., *Modeling and Design Photonics by Examples Using MATLAB®*. 2021: IOP Publishing.

75. Lin, Q. and G.P. Agrawal, *Raman response function for silica fibers.* Optics Letters, 2006. **31**(21): p. 3086-3088.

76. Paschotta, R., 2015. Resonator Modes. *Encyclopedia of Laser Physics and Technology. Web*, *11*.

77. Silfvast, WT 2004, *Laser fundamentals*, Second edition., Cambridge University Press, Cambridge.

78. Svelto, O. and D.C. Hanna, *Principles of lasers*. Vol. 4. 1998: Springer.

79. Melchert, O. and A. Demircan, *A generalized nonlinear Schr\" odinger Python module implementing different models of input pulse quantum noise.* arXiv preprint arXiv:2206.07526, 2022.

80. Balac, S., et al., *The Interaction Picture method for solving the generalized nonlinear Schrödinger equation in optics.* ESAIM: Mathematical Modelling and Numerical Analysis, 2016. **50**(4): p. 945-964.

81. Dudley, J.M., G. Genty, and S. Coen, *Supercontinuum generation in photonic crystal fiber.* Reviews of modern physics, 2006. **78**(4): p. 1135.

82. Ma, W.-X. and M. Chen, *Direct search for exact solutions to the nonlinear Schrödinger equation.* Applied Mathematics and Computation, 2009. **215**(8): p. 2835-2842.

83. Si-Liu, X., L. Jian-Chu, and Y. Lin, *Exact soliton solutions to a generalized nonlinear Schrödinger equation.* Communications in Theoretical Physics, 2010. **53**(1): p. 159.

84. Sarma, A.K., *Solitary wave solutions of higher-order NLSE with Raman and self-steepening effect in a cubic–quintic–septic medium.* Communications in Nonlinear Science and Numerical Simulation, 2009. **14**(8): p. 3215-3219.

85. Lu, D., et al., *Soliton solutions of the generalised third-order nonlinear Schrödinger equation by two mathematical methods and their stability.* Pramana, 2019. **93**(3): p. 1-9.

86. Sarma, A.K., *Solitary wave solution to the generalized nonlinear Schrodinger equation for dispersive permittivity and permeability.* arXiv preprint arXiv:1001.0727, 2010.

87. Liu, S., et al., *Novel wave solutions to a generalized third-order nonlinear Schrödinger's equation.* Results in Physics, 2022. **37**: p. 105457.

88. Ishii, Y., *Numerical computation of the nonlinear Schrödinger equation with higher order group velocity dispersion and frequency-dependent gain using the differential method.* Optical Review, 2021. **28**(4): p. 462-470.

89. Hasegawa, A. and F. Tappert, *Transmission of stationary nonlinear optical pulses in dispersive dielectric fibers. I. Anomalous dispersion.* Applied Physics Letters, 1973. **23**(3): p. 142-144.

90. Paschotta, R., *Soliton Mode Locking*, in *RP Encyclopedia of Laser Physics and Technology*, R. Paschotta, Editor. 2008, Wiley-VCH.

91. Paschotta, R., *Self-phase Modulation*, in *RP Encyclopedia of Laser Physics and Technology*, R. Paschotta, Editor. 2007, Wiley-VCH.

92. Paschotta, R., *Group velocity dispersion*, in *RP Encyclopedia of Laser Physics and Technology*, R. Paschotta, Editor. 2008, Wiley-VCH.

93. Hasegawa, A. and M. Matsumoto, *Optical solitons in fibers*, in *Optical Solitons in Fibers*. 2003, Springer. p. 41-59.

94. Keller, U., *Physics@FOM Veldhoven 2014, Masterclass*. 2014.

95. Lee, C.-C. and T. Schibli, *Intrinsic power oscillations generated by the backaction of continuum on solitons and its implications on the transfer functions of a mode-locked laser.* Physical Review Letters, 2014. **112**(22): p. 223903.

96. Jung, I., et al., *Experimental verification of soliton mode locking using only a slow saturable absorber.* Optics letters, 1995. **20**(18): p. 1892-1894.

97. Haus, H.A., W.S. Wong, and F.I. Khatri, *Continuum generation by perturbation of soliton.* JOSA B, 1997. **14**(2): p. 304-313.

98. Paschotta, R. and U. Keller, *Passive mode locking with slow saturable absorbers.* Applied Physics B, 2001. **73**(7): p. 653-662.

99. Paschotta, R., *Saturable absorbers*, in *RP Encyclopedia of Laser Physics and Technology*, R. Paschotta, Editor. 2015, Wiley-VCH.

100. Choi, M.-T., *Ultrashort, high power, and ultralow noise mode-locked optical pulse generation using quantum-dot semiconductor lasers.* 2006.

101. Gomes, L., *Ultrafast Ytterbium Fiber Sources Based on SESAM Technology.* 2006.

102. *SAM - Saturable Absorber Mirror*. 2021; Available from: https://www.batop.de/information/SAM_infos.html.

103. Hirooka, T., et al., *440 fs, 9.2 GHz regeneratively mode-locked erbium fiber laser with a combination of higher-order solitons and a SESAM saturable absorber.* Optics Express, 2016. **24**(21): p. 24255-24264.

104. Qingsong, J., et al., *Mode-locking thulium-doped fiber laser with 1.78-GHz repetition rate based on combination of nonlinear polarization rotation and semiconductor saturable absorber mirror.* IEEE Photonics Journal, 2017. **9**(3): p. 1-8.

105. Koechner, W., *Mode Locking*, in *Solid-State Laser Engineering*, W. Koechner, Editor. 2006, Springer New York: New York, NY. p. 534-586.

106. Keller, U., et al., *Semiconductor saturable absorber mirrors (SESAM's) for femtosecond to nanosecond pulse generation in solid-state lasers.* IEEE Journal of selected topics in QUANTUM ELECTRONICS, 1996. **2**(3): p. 435-453.

107. Diebold, A., et al. *Optimized SESAMs for Kilowatt Ultrafast Lasers*. in *CLEO: Science and Innovations*. 2015. Optical Society of America.

108. Paschotta, R., *Semiconductor Saturable Absorber Mirrors*, in *RP Encyclopedia of Laser Physics and Technology*, R. Paschotta, Editor. 2010, Wiley-VCH.

109. Kwon, S.-H., et al., *Operating characteristics of a SESAM-assisted mode-locked laser oscillator with the location of the SESAM position.* Optics & Laser Technology, 2021. **133**: p. 106560.

110. Wang, Y., et al., *SESAM mode-locked Tm: CALGO laser at 2 μm.* Optical Materials Express, 2016. **6**(1): p. 131-136.

111. Maas, D., et al., *High precision optical characterization of semiconductor saturable absorber mirrors.* Optics express, 2008. **16**(10): p. 7571-7579.

112. Quarterman, A.H., et al., *A passively mode-locked external-cavity semiconductor laser emitting 60-fs pulses.* Nature Photonics, 2009. **3**(12): p. 729-731.

113. Kivistö, S., et al., *Pulse dynamics of a passively mode-locked Bi-doped fiber laser.* Optics Express, 2010. **18**(2): p. 1041-1048.

114. Li, H., et al. *Passively mode-locked femtosecond fiber laser using a SESAM*. in *2009 International Conference on Optical Instruments and Technology: Optoelectronic Devices and Integration*. 2009. SPIE.

115. Lecourt, J.-B., et al., *All-normal dispersion, all-fibered PM laser mode-locked by SESAM.* Optics Express, 2012. **20**(11): p. 11918-11923.

116. Okhotnikov, O., A. Grudinin, and M. Pessa, *Ultra-fast fibre laser systems based on SESAM technology: new horizons and applications* New journal of physics, 2004. **6**(1): p. 177.

117. Härkönen, A., et al., *1.34 μm VECSEL mode-locked with a GaSb-based SESAM.* Optics Letters, 2018. **43**(14): p. 3353-3356.

118. Kim, M.J., et al., *Investigation of InGaAs quantum-well parameters of a semiconductor saturable absorber mirror used for mode locking of a Yb-doped fiber laser.* Journal of the Korean Physical Society, 2013. **63**(10): p. 1919-1924.

119. Lederer, M.J., et al., *Ion-implanted InGaAs single quantum well semiconductor saturable absorber mirrors for passive mode-locking.* Journal of Physics D: Applied Physics, 2001. **34**(16): p. 2455.

120. Alaydin, B.O., et al. *Mid-infrared type-I InGaSb/GaSb quantum well SESAM*. in *The European Conference on Lasers and Electro-Optics*. 2021. Optical Society of America.

121. Garnache, A., et al. *A new kind of fast quantum-well semiconductor saturable-absorber mirror with low losses for ps pulse generation*. in *International Conference onIndium Phosphide and Related Materials, 2003.* 2003. IEEE.

122. Liu, X., et al., *Quantum well saturable absorber mirror with electrical control of modulation depth.* Applied Physics Letters, 2010. **97**(5): p. 051103.

123. Rubtsova, N., et al. *Semiconductor quantum well based shutters for NIR laser mode-locking with ~ GHz repetition rate*. in *Journal of Physics: Conference Series*. 2021. IOP Publishing.

124. Sorokina, I.T., et al. *A SESAM passively mode-locked Cr: ZnS laser*. in *Advanced Solid-State Photonics*. 2006. Optica Publishing Group.

125. Zhang, Z., et al., *1.55 μm InAs/GaAs quantum dots and high repetition rate quantum dot SESAM mode-locked laser.* Scientific reports, 2012. **2**(1): p. 1-5.

126. Resan, B., et al., *10 GHz pulse repetition rate Er: Yb: glass laser modelocked with quantum dot semiconductor saturable absorber mirror.* Applied optics, 2016. **55**(14): p. 3776-3780.

127. Wittwer, V., et al. *Free-running quantum dot SESAM modelocked VECSEL with record-low timing jitter*. in *2011 Conference on Lasers and Electro-Optics Europe and 12th European Quantum Electronics Conference (CLEO EUROPE/EQEC)*. 2011. IEEE.

128. Maas, D., et al., *Growth parameter optimization for fast quantum dot SESAMs.* Optics express, 2008. **16**(23): p. 18646-18656.

129. Bellancourt, A.-R., et al., *Low saturation fluence antiresonant quantum dot SESAMs for MIXSEL integration.* Optics express, 2009. **17**(12): p. 9704-9711.

130. Finke, T., et al., *Temperature resistant fast In x Ga 1− x As/GaAs quantum dot saturable absorber for the epitaxial integration into semiconductor surface emitting lasers.* Optics express, 2020. **28**(14): p. 20954-20966.

131. Donodin, A., et al., *Numerical model of hybrid mode-locked Tm-doped all-fibre laser.* Scientific Reports, 2020. **10**(1): p. 1-9.

132. Jang, H., *SESAM Design and Characterization*. 2010, Stockholm Royal Institute of Technology.

133. AbouElEz, A.E., et al., *Modelling and simulation of pin quantum dot semiconductor saturable absorber mirrors.* Progress In Electromagnetics Research C, 2018. **82**: p. 39-53.

134. Shtyrina, O., et al., *Evolution and stability of pulse regimes in SESAM-mode-locked femtosecond fiber lasers.* JOSA B, 2009. **26**(2): p. 346-352.

135. Haus, H.A., *Theory of mode locking with a fast saturable absorber.* Journal of Applied Physics, 1975. **46**(7): p. 3049-3058.

136. Nussbaum-Lapping, A., et al., *Absolute SESAM characterization via polarization-resolved non-collinear equivalent time sampling.* Applied Physics B, 2022. **128**(2): p. 1-12.

137. Spühler, G., et al., *Semiconductor saturable absorber mirror structures with low saturation fluence.* Applied Physics B, 2005. **81**(1): p. 27-32.

138. Haiml, M., R. Grange, and U. Keller, *Optical characterization of semiconductor saturable absorbers.* Applied Physics B, 2004. **79**(3): p. 331-339.

139. Saraceno, C.J., et al. *SESAM designs for ultrafast lasers*. in *Fiber Lasers X: Technology, Systems, and Applications*. 2013. SPIE.

140. Zhang, Y., et al., *Study of the influence of SESAM parameters on the evolution of mode-locked pulses at different repetition rates.* Applied Physics B, 2021. **127**(8): p. 1-10.

141. Yan, P., et al., *Passively mode-locked fiber laser by a cell-type WS2 nanosheets saturable absorber.* Scientific reports, 2015. **5**(1): p. 1-7.

142. Kwon, S.-H. and D.-K. Ko, *Pulse formation and stability of a SESAM mode-locked laser depending on the SESAM position.* Journal of the Korean Physical Society, 2020. **77**(12): p. 1153-1158.

143. Yan, D., et al., *Route to stable dispersion-managed mode-locked Yb-doped fiber lasers with near-zero net cavity dispersion.* Optics Express, 2020. **28**(20): p. 29766-29774.

144. Herda, R. and O.G. Okhotnikov, *Effect of amplified spontaneous emission and absorber mirror recovery time on the dynamics of mode-locked fiber lasers.* Applied physics letters, 2005. **86**(1): p. 011113.

145. Ippen, E.P., *Principles of passive mode locking.* Applied Physics B, 1994. **58**(3): p. 159-170.

146. New, G., *Mode-locking of quasi-continuous lasers.* Optics Communications, 1972. **6**(2): p. 188-192.

147. Haus, H., *Theory of mode locking with a slow saturable absorber.* IEEE Journal of Quantum Electronics, 1975. **11**(9): p. 736-746.

148. Kärtner, F. and U. Keller, *Stabilization of solitonlike pulses with a slow saturable absorber.* Optics letters, 1995. **20**(1): p. 16-18.

149. Kurtner, F.X., J.A. der Au, and U. Keller, *Mode-locking with slow and fast saturable absorbers-what's the difference?* IEEE Journal of Selected Topics in Quantum Electronics, 1998. **4**(2): p. 159-168.

150. Woodward, R. and E.J. Kelleher, *Towards 'smart lasers': self-optimisation of an ultrafast pulse source using a genetic algorithm.* Scientific reports, 2016. **6**(1): p. 1-9.

151. Genty, G., et al., *Machine learning and applications in ultrafast photonics.* Nature Photonics, 2021. **15**(2): p. 91-101.

152. Dudley, J.M. and J.R. Taylor, *Supercontinuum generation in optical fibers*. 2010: Cambridge University Press.

153. Bonetti, J., et al. *Quasi-analytical perturbation analysis of the generalized nonlinear Schrödinger equation*. in *Proceedings of the 5th International Conference on Applications in Nonlinear Dynamics*. 2019. Springer.

154. Ablowitz, M.J., M. Ablowitz, and P.A. Clarkson, *Solitons, nonlinear evolution equations and inverse scattering*. Vol. 149. 1991: Cambridge university press.

155. Sheng, Q., A. Khaliq, and E. Al-Said, *Solving the generalized nonlinear Schrödinger equation via quartic spline approximation.* Journal of Computational Physics, 2001. **166**(2): p. 400-417.

156. Boscolo, S., J.M. Dudley, and C. Finot, *Modelling self-similar parabolic pulses in optical fibres with a neural network.* Results in Optics, 2021. **3**: p. 100066.

157. Salmela, L., et al., *Predicting ultrafast nonlinear dynamics in fibre optics with a recurrent neural network.* Nature Machine Intelligence, 2021. **3**(4): p. 344-354.

158. Suarez, P., *An introduction to the split step Fourier method using MATLAB*. 2016.

159. Hult, J., *A fourth-order Runge–Kutta in the interaction picture method for simulating supercontinuum generation in optical fibers.* Journal of Lightwave Technology, 2007. **25**(12): p. 3770-3775.

160. Schuttrups, B., *Modelling nonlinear optical pulse propagation using pseudo-spectral methods*. 2020, University of Twente.

161. Sternberg, S., *Lie algebras.* 2004.

162. Washburn, B., *Numerical Solutions to the Nonlinear Schrödinger Equation*. 2002, University of Atlanta: Georgia. p. 134 - 157.

163. Anderson, M., *Introduction to NLSE simulation / supercontinuum generation*, in *K-LAB lecture series*. 2020.

164. MathWorks. *Solve Stiff ODEs*. MATLAB Documentation 2021; Available from: https://au.mathworks.com/help/matlab/math/solve-stiff-odes.html.

165. Li, H. *Solving Stiff ODEs*. 2009; Available from: http://lh3lh3.users.sourceforge.net/solveode.shtml.

166. Agger, C.S. and O. Bang, *Infrared supercontinuum generation in soft-glass fibers*. 2013: Citeseer.

167. Zhang, Z., L. Chen, and X. Bao, *A fourth-order Runge-Kutta in the interaction picture method for numerically solving the coupled nonlinear Schrödinger equation.* Optics Express, 2010. **18**(8): p. 8261-8276.

168. Mamyshev, P. and S.V. Chernikov, *Ultrashort-pulse propagation in optical fibers.* Optics letters, 1990. **15**(19): p. 1076-1078.

Chapter 3

1. Pi, Y., et al., *Timing Jitter and Intensity Noise Characterization of a 122-MHz All-PM NALM Mode-Locked Fiber Laser.* IEEE Photonics Technology Letters, 2021. **33**(24): p. 1439-1442.

2. Smith, C.R., R.D. Engelsholm, and O. Bang, *Pulse-to-pulse relative intensity noise measurements for ultrafast lasers.* Optics Express, 2022. **30**(5): p. 8136-8150.

3. Paschotta, R., *Timing Jitter*, in *RP Encyclopedia of Laser Physics and Technology*, R. Paschotta, Editor. 2007, Wiley-VCH.

4. Zhang, J., et al., *Generation of 100 nJ pulse, 1 W average power at from an intermode beating mode-locked all-fiber laser.* High power laser science and engineering, 2019. **7**.

5. Paschotta, R., *Gordon–Haus Jitter*, in *RP Encyclopedia of Laser Physics and Technology*, R. Paschotta, Editor. 2007, Wiley-VCH.

6. Wang, Y., et al., *Timing jitter reduction through relative intensity noise suppression in high-repetition-rate mode-locked fiber lasers.* Optics express, 2019. **27**(8): p. 11273-11280.

7. Vasa, P. and D. Mathur, *Ultrafast Biophotonics*. 2016: Springer.

8. Rulliere, C., *Femtosecond laser pulses*. 2005: Springer.

9. Lauterborn, W. and T. Kurz, *Coherent optics: fundamentals and applications*. 2003: Springer Science & Business Media.

10. *Pulsed Signals Spectrum Analysis: How to measure pulsed signals using a spectrum analyzer - some of the key concepts and techniques*. 2022.

11. Kues, M., et al., *Passively mode-locked laser with an ultra-narrow spectral width.* Nature Photonics, 2017. **11**(3): p. 159-162.

12. Ferrera, M., et al. *Characterization of ultra-high repetition rate mode-locked lasers with an integrated all-optical RF spectrum analyzer*. in *CLEO: Science and Innovations*. 2014. Optica Publishing Group.

13. Green, E.I., *The story of Q.* American Scientist, 1955. **43**(4): p. 584-594.

14. Howe, D.A., *Frequency domain stability measurements: A tutorial introduction.* 1976.

15. Dúill, S.P.Ó., et al., *Analytical approach to assess the impact of pulse-to-pulse phase coherence of optical frequency combs.* IEEE Journal of Quantum Electronics, 2015. **51**(11): p. 1-8.

16. Clays, K., et al., *Alternative Experimental Determination of Weak Localization of Light in Nanostructured Materials.* Journal of Nonlinear Optical Physics & Materials - JNOPM, 2002. **11**: p. 261-274.

17. Lv, R.-d., et al., *Carboxyl graphene oxide solution saturable absorber for femtosecond mode-locked erbium-doped fiber laser.* Chinese Physics B, 2018. **27**(11): p. 114214.

18. Wilson, J., *Timing Jitter Dictionary and Measurement*. 2022, Skyworks Inc.

19. Kester, W. *Converting Oscillator Phase Noise to Time Jitter*. DigiKey Electronics Article Library 2010; Available from: https://www.digikey.co.nz/en/articles/converting-oscillator-phase-noise-to-time-jitter.

20. *Understanding Frequency Performance Specifications*. 2022; Available from: https://www.ni.com/en-au/support/documentation/supplemental/06/understanding-frequency-performance-specifications.html.

21. *AQ6370 Series Optical Spectrum Analyzer - an introduction*. 2021, Yokogawa Electric Corporation.

22. Paschotta, R., *Time-bandwidth product*, in *RP Encyclopedia of Laser Physics and Technology*, R. Paschotta, Editor. 2007, Wiley-VCH.

23. Keller, U., *Physics@FOM Veldhoven 2014, Masterclass*. 2014.

24. Paschotta, R., *Kelly Sidebands*, in *RP Encyclopedia of Laser Physics and Technology*, R. Paschotta, Editor. 2007, Wiley-VCH.

25. Dennis, M.L. and I.N. Duling, *Experimental study of sideband generation in femtosecond fiber lasers.* IEEE Journal of Quantum electronics, 1994. **30**(6): p. 1469-1477.

26. Li, J., et al., *Kelly sideband suppression and wavelength tuning of a conventional soliton in a Tm-doped hybrid mode-locked fiber laser with an all-fiber Lyot filter.* Photonics Research, 2019. **7**(2): p. 103-109.

27. Trebino, R., *Frequency-Resolved Optical Gating: The Measurement of Ultrashort Laser Pulses: The Measurement of Ultrashort Laser Pulses*. 2000: Springer Science & Business Media.

28. Pollock, C.R., *Ultrafast optical pulses.* Progress in optics, 2008. **51**: p. 211-249.

29. Paschotta, R., *Field guide to laser pulse generation (SPIE, 2008)*. 2008.

30. Takao, Y., et al., *Autocorrelation and Frequency-Resolved Optical Gating Measurements Based on the Third Harmonic Generation in a Gaseous Medium.* Applied Sciences, 2015. **5**(2): p. 136-144.

31. Paschotta, R., *Autocorrelators*, in *RP Encyclopedia of Laser Physics and Technology*, R. Paschotta, Editor. 2007, Wiley-VCH.

32. Trebino, R. *Swamp Optics Tutorial: Intensity Autocorrelation*. 2015.

33. Huang, S., *Femtosecond first-order autocorrelation measurement based one-photon induced photocurrent in Si Schottky diodes.* Optics & Laser Technology, 2008. **40**(8): p. 1051-1054.

34. Trebino, R. *Swamp Optics Tutorial: Interferometric Autocorrelation*. 2015.

35. DeLong, K., et al., *Frequency-resolved optical gating with the use of second-harmonic generation.* JOSA B, 1994. **11**(11): p. 2206-2215.

36. Kolokolnikov, T., et al., *The Q-switching instability in passively mode-locked lasers.* Physica D: Nonlinear Phenomena, 2006. **219**(1): p. 13-21.

37. Yu, Y., et al., *Spectral-temporal dynamics of multipulse mode-locking.* Applied physics letters, 2017. **110**(20): p. 201107.

38. Paschotta, R., *Continuous-wave Operation*, in *RP Encyclopedia of Laser Physics and Technology*, R. Paschotta, Editor. 2008, Wiley-VCH.

39. Lazaridis, P., G. Debarge, and P. Gallion, *Time–bandwidth product of chirped sech 2 pulses: application to phase–amplitude-coupling factor measurement.* Optics letters, 1995. **20**(10): p. 1160-1162.

40. Zakharov, V.E. and S. Wabnitz, *Optical Solitons: Theoretical Challenges and Industrial Perspectives: Les Houches Workshop, September 28–October 2, 1998*. Vol. 12. 2013: Springer Science & Business Media.

41. Yu, T., et al., *Dispersion-managed soliton interactions in optical fibers.* Optics letters, 1997. **22**(11): p. 793-795.

42. Li, X., et al., *Investigation of regime switching from mode locking to Q-switching in a 2 μm InGaSb/AlGaAsSb quantum well laser.* Optics Express, 2018. **26**(7): p. 8289-8295.

43. Ismail, M.A., et al., *Passive Q-switched and mode-locked fiber lasers using carbon-based saturable absorbers*, in *Fiber Laser*. 2016, IntechOpen. p. 43-69.

44. Wang, P. and C. Zhu, *Passively Q-Switched and Mode-Locked Fiber Laser Based on a Zeolitic Imidazolate Framework-67 Saturable Absorber.* Frontiers in Physics, 2022: p. 505.

45. Schibli, T., et al., *Suppression of Q-switched mode locking and break-up into multiple pulses by inverse saturable absorption.* Applied Physics B, 2000. **70**(1): p. S41-S49.

46. Paschotta, R., *Q-switching*, in *RP Encyclopedia of Laser Physics and Technology*, R. Paschotta, Editor. 2011, Wiley-VCH.

47. Paschotta, R., *Q-switched Mode Locking*, in *RP Encyclopedia of Laser Physics and Technology*, R. Paschotta, Editor. 2011, Wiley-VCH.

48. Hönninger, C., et al., *Q-switching stability limits of continuous-wave passive mode locking.* JOSA B, 1999. **16**(1): p. 46-56.

49. Agrawal, G., *Nonlinear fiber optics*. Sixth edition. ed. 2019, London, England: Academic Press.

50. Paschotta, R., *Rp photonics encyclopedia.* Available online: www. rp-photonics. com (accessed on 4 January 2021), 2013.

51. Kaminow, I.P. and T. Koch, *Advanced multiaccess lightwave networks.* Optical Fiber Telecommunications IIIA, 1997: p. 560-593.

52. DeMartini, F., et al., *Self-steepening of light pulses.* Physical Review, 1967. **164**(2): p. 312.

53. Do Thanh, T., T. Nguyen, and D. Bui, *Influence of self-steepening and higher dispersion effects on the propagation characteristics of solitons in optical fibers.* CMST, 2016. **22**(4): p. 239-243.

54. Miyagi, M. and S. Nishida, *Pulse spreading in a single-mode fiber due to third-order dispersion.* Applied optics, 1979. **18**(5): p. 678-682.

55. Luo, Y., et al., *Group-velocity-locked vector soliton molecules in fiber lasers.* Scientific Reports, 2017. **7**(1): p. 1-8.

56. Zhou, R., et al., *Versatile multi-soliton patterns of noise-like pulses in a passively mode-locked fiber laser.* Optics Express, 2020. **28**(2): p. 912-923.

Chapter 4

1. Li, J.-F. and S.D. Jackson, *Theoretical study and optimization of a high power mid-infrared erbium-doped ZBLAN fibre laser.* Chinese Physics B, 2011. **20**(3): p. 034205.

2. Obronov, I.V., V.E.e. Sypin, and S.V. Larin, *Optimisation of thulium fibre laser parameters with generation of pulses by pump modulation.* Quantum Electronics, 2015. **45**(7): p. 617.

3. Andrianov, A.V., et al., *Tapered erbium-doped fibre laser system delivering 10 MW of peak power.* Quantum Electronics, 2019. **49**(12): p. 1093.

4. Sigonya, A., *Design and optimisation of a linear cavity Erbium-doped Fibre Laser for Fibre-Optic Communication Systems*. 2020: University of Johannesburg (South Africa).

5. Woodward, R. and E.J. Kelleher, *Towards 'smart lasers': self-optimisation of an ultrafast pulse source using a genetic algorithm.* Scientific reports, 2016. **6**(1): p. 1-9.

6. Wu, X., et al., *Intelligent breathing soliton generation in ultrafast fibre lasers.* arXiv preprint arXiv:2108.09869, 2021.

7. Wang, S., et al., *Obtaining more energetic modelocked pulses from a SESAM-based fiber laser.* Optics Express, 2020. **28**(14): p. 20345-20361.

8. Asaki, M.T., et al., *Generation of 11-fs pulses from a self-mode-locked Ti: sapphire laser.* Optics letters, 1993. **18**(12): p. 977-979.

9. Nelson, L.E., et al., *Ultrashort-pulse fiber ring lasers.* Applied Physics B: Lasers & Optics, 1997. **65**(2).

10. Zhou, X., et al., *Generation of 28-fs pulses from a mode-locked ytterbium fiber oscillator.* Optics express, 2008. **16**(10): p. 7055-7059.

11. Spielmann, C., et al., *Ultrabroadband femtosecond lasers.* IEEE Journal of quantum electronics, 1994. **30**(4): p. 1100-1114.

12. Balzer, J.C., et al., *Passively mode-locked diode laser with optimized dispersion management.* IEEE Journal of Selected Topics in Quantum Electronics, 2015. **21**(6): p. 16-23.

13. Yanovsky, V., et al., *Generation of 25-fs pulses from a self-mode-locked Cr: forsterite laser with optimized group-delay dispersion.* Optics letters, 1993. **18**(18): p. 1541-1543.

14. Balzer, J., et al., *High peak power pulses from dispersion optimised modelocked semiconductor laser.* Electronics letters, 2013. **49**(13): p. 838-839.

15. Saleh, B.E. and M.C. Teich, *Fundamentals of photonics*. 2019: john Wiley & sons.

16. Grüner-Nielsen, L., et al., *Dispersion compensating fibers.* Optical fiber technology, 2000. **6**(2): p. 164-180.

17. Cao, B., et al., *Dispersion compensating fibers with improved splicing performance.* Physics Procedia, 2013. **48**: p. 96-101.

18. Jauregui, C., J. Limpert, and A. Tünnermann, *High-power fibre lasers.* Nature photonics, 2013. **7**(11): p. 861-867.

19. Kurkov, A.S., et al., *Effect of active-ion concentration on holmium fibre laser efficiency.* Quantum electronics, 2010. **40**(5): p. 386.

20. Kamynin, V.A., et al., *Holmium-doped fibre amplifier operating at.* Quantum Electronics, 2014. **44**(2): p. 161.

21. Plotskii, A.Y., et al., *Amplifying properties of heavily erbium-doped active fibres.* Quantum Electronics, 2005. **35**(6): p. 559.

22. Okhotnikov, O. and J. Sousa. *High power single-transverse-mode amplifier based on a multimode Er-doped fibre*. in *24th European Conference on Optical Communication. ECOC'98 (IEEE Cat. No. 98TH8398)*. 1998. IEEE.

23. Kim, T.K., et al., *Sub-100-as timing jitter optical pulse trains from mode-locked Er-fiber lasers.* Optics letters, 2011. **36**(22): p. 4443-4445.

24. Feehan, J.S., et al., *Computer-automated design of mode-locked fiber lasers.* Optics express, 2022. **30**(3): p. 3455-3473.

25. Nady, A., F. Mathkoor, and S.W. Harun, *Theoretical study on passively mode-locked fiber lasers with saturable absorber.* Fiber and Integrated Optics, 2019. **38**(1): p. 76-89.

26. Kokhanovskiy, A., et al., *Inverse design of mode-locked fiber laser by particle swarm optimization algorithm.* Scientific reports, 2021. **11**(1): p. 1-9.

27. Shtyrina, O., et al., *Impact of the order of cavity elements in all-normal dispersion ring fiber lasers.* IEEE Photonics Journal, 2015. **7**(2): p. 1-7.

28. Andral, U., et al., *Fiber laser mode locked through an evolutionary algorithm.* Optica, 2015. **2**(4): p. 275-278.

29. Zhang, G., et al., *A dual-loss-modulated Q-switched and mode-locked Nd: GdVO4 laser with AOM and V3+: YAG saturable absorber at 1.34 μm.* Journal of Optics, 2011. **13**(3): p. 035202.

30. Kim, K.H., et al., *Gain Dependent Optimum Pulse Generation Rates of a Hybrid-Type Actively and Passively Mode-Locked Fiber Laser.* ETRI journal, 1996. **18**(1): p. 1-14.

31. Jasik, A., et al., *Low-temperature grown near surface semiconductor saturable absorber mirror: Design, growth conditions, characterization, and mode-locked operation.* Journal of Applied Physics, 2009. **106**(5): p. 053101.

32. Maas, D., et al., *Growth parameter optimization for fast quantum dot SESAMs.* Optics express, 2008. **16**(23): p. 18646-18656.

33. Jasik, A., et al., *Ultrashort pulses supported by SESAM absorber.* Bulletin of the Polish Academy of Sciences. Technical Sciences, 2010. **58**(4): p. 477-483.

34. Zeng, Y., W. Fan, and X. Wang, *The combined effects of intra-cavity spectral filtering on the fiber mode-locked laser.* Optics Communications, 2020. **474**: p. 126152.

35. Zhang, X., et al., *Impact of spectral filtering on multipulsing instability in mode-locked fiber lasers.* IEEE Journal of Selected Topics in Quantum Electronics, 2017. **24**(3): p. 1-9.

36. *2 μm Fused Wavelength Division Multiplexer (WDM Series)*. 2022: Advanced Fiber Resources Ltd.

37. Keller, U., et al., *Semiconductor saturable absorber mirrors (SESAM's) for femtosecond to nanosecond pulse generation in solid-state lasers.* IEEE Journal of selected topics in QUANTUM ELECTRONICS, 1996. **2**(3): p. 435-453.

38. Wang, S., et al., *Digital-wavelength ytterbium fiber laser mode-locked with MoS2.* Laser Physics Letters, 2016. **13**(5): p. 055102.

39. Fang, Z., et al., *Fundamentals of optical fiber sensors*. Vol. 226. 2012: John Wiley & Sons.

40. Guan, J., et al., *Generation and propagation of hyperbolic secant solitons, Peregrine solitons, and breathers in a coherently prepared atomic system.* Optics Express, 2020. **28**(21): p. 31287-31296.

41. Paschotta, R., *Sech2-shaped Pulses*, in *RP Encyclopedia of Laser Physics and Technology*, R. Paschotta, Editor. 2008, Wiley-VCH.

42. Aljunid, S.A., *Optical Autocorrelation using Non-Linearity in a Simple Photodiode.* National University of Singapore Department of Physics, 2007.

43. Wu, K. and P. Shum, *Phase Noise and Intensity Noise of the Pulse Train Generated from Mode-locked Lasers in the Demodulation Measurement.* arXiv preprint arXiv:1007.5367, 2010.

44. Wilson, J., *Timing Jitter Tutorial & Measurement Guide*, S. Labs, Editor. 2019.

45. Li, J., et al., *Kelly sideband suppression and wavelength tuning of a conventional soliton in a Tm-doped hybrid mode-locked fiber laser with an all-fiber Lyot filter.* Photonics Research, 2019. **7**(2): p. 103-109.

46. Du, Y., et al., *Pulsating soliton with broadened Kelly sidebands in an ultrafast fiber laser.* Optics Letters, 2019. **44**(16): p. 4087-4090.

47. Weill, R., et al., *Spectral sidebands and multipulse formation in passively mode-locked lasers.* Physical Review A, 2011. **83**(4): p. 043831.

48. Wang, C., et al., *High energy and low noise soliton fiber laser comb based on nonlinear merging of Kelly sidebands.* Optics Express, 2022. **30**(13): p. 23556-23567.

49. Jung, I., et al., *Experimental verification of soliton mode locking using only a slow saturable absorber.* Optics letters, 1995. **20**(18): p. 1892-1894.

50. Kartner, F., I. Jung, and U. Keller, *Soliton mode-locking with saturable absorbers.* IEEE Journal of Selected Topics in Quantum Electronics, 1996. **2**(3): p. 540-556.

51. Kärtner, F. and U. Keller, *Stabilization of solitonlike pulses with a slow saturable absorber.* Optics letters, 1995. **20**(1): p. 16-18.

52. Chen, Y., et al., *Dispersion-managed mode locking.* JOSA B, 1999. **16**(11).

53. Kurtner, F.X., J.A. der Au, and U. Keller, *Mode-locking with slow and fast saturable absorbers-what's the difference?* IEEE Journal of Selected Topics in Quantum Electronics, 1998. **4**(2): p. 159-168.

54. Ippen, E.P., *Principles of passive mode locking.* Applied Physics B, 1994. **58**(3): p. 159-170.

55. Haus, H.A., J.G. Fujimoto, and E.P. Ippen, *Structures for additive pulse mode locking.* JOSA B, 1991. **8**(10): p. 2068-2076.

56. Agrawal, G.P., *Nonlinear fiber optics*, in *Nonlinear Science at the Dawn of the 21st Century*. 2000, Springer. p. 195-211.

57. Chen, Y., et al., *All-fiber low-pedestal spectral compression in a novel architecture based on an SMF cascading an HNLF-NOLM.* IEEE Photonics Journal, 2014. **6**(5): p. 1-9.

58. Steinmeyer, G., *Brewster-angled chirped mirrors for high-fidelity dispersion compensation and bandwidths exceeding one optical octave.* Optics express, 2003. **11**(19): p. 2385-2396.

59. Chen, Y., et al. *Numerical Investigation of a Novel Two-stage Structure to Compress Spectrum and Suppress Pedestal Employing a DIF Interconnected with a HNLF-NOLM*. in *PIERS Proceedings*. 2014.

60. Huang, C., et al., *Developing high energy dissipative soliton fiber lasers at 2 micron.* Scientific Reports, 2015. **5**(1): p. 1-7.

61. Heidt, A.M., *Pulse preserving flat-top supercontinuum generation in all-normal dispersion photonic crystal fibers.* JOSA B, 2010. **27**(3): p. 550-559.

62. Kalashnikov, V. and E. Sorokin, *Mode-locked oscillators in the positive and negative dispersion regimes: scenarios of destabilization.* 2008.

63. Diels, J.-C. and W. Rudolph, *Ultrashort laser pulse phenomena*. 2006: Elsevier.

64. Lazaridis, P., G. Debarge, and P. Gallion, *Time–bandwidth product of chirped sech 2 pulses: application to phase–amplitude-coupling factor measurement.* Optics letters, 1995. **20**(10): p. 1160-1162.

65. Woodward, R.I., *Dispersion engineering of mode-locked fibre lasers.* Journal of Optics, 2018. **20**(3): p. 033002.

66. Tamura, K., et al., *Soliton versus nonsoliton operation of fiber ring lasers.* Applied physics letters, 1994. **64**(2): p. 149-151.

Chapter 5

1. Zhang, G., et al., *A dual-loss-modulated Q-switched and mode-locked Nd: GdVO4 laser with AOM and V3+: YAG saturable absorber at 1.34 μm.* Journal of Optics, 2011. **13**(3): p. 035202.

2. Kim, K.H., et al., *Gain Dependent Optimum Pulse Generation Rates of a Hybrid-Type Actively and Passively Mode-Locked Fiber Laser.* ETRI journal, 1996. **18**(1): p. 1-14.

3. Saleh, K., G. Lin, and Y.K. Chembo, *Effect of laser coupling and active stabilization on the phase noise performance of optoelectronic microwave oscillators based on whispering-gallery-mode resonators.* IEEE Photonics Journal, 2014. **7**(1): p. 1-11.

4. van Dijk, F., et al., *Phase noise reduction of a quantum dash mode-locked laser in a millimeter-wave coupled opto-electronic oscillator.* Journal of Lightwave Technology, 2008. **26**(15): p. 2789-2794.

5. Hjelme, D.R. and A.R. Mickelson, *Theory of timing jitter in actively mode-locked lasers.* IEEE journal of Quantum Electronics, 1992. **28**(6): p. 1594-1606.

6. Maas, D., et al., *Growth parameter optimization for fast quantum dot SESAMs.* Optics express, 2008. **16**(23): p. 18646-18656.

7. Jasik, A., et al., *Low-temperature grown near surface semiconductor saturable absorber mirror: Design, growth conditions, characterization, and mode-locked operation.* Journal of Applied Physics, 2009. **106**(5): p. 053101.

8. Jasik, A., et al., *Ultrashort pulses supported by SESAM absorber.* Bulletin of the Polish Academy of Sciences. Technical Sciences, 2010. **58**(4): p. 477-483.

9. Guina, M., N. Xiang, and O. Okhotnikov, *Stretched-pulse fiber lasers based on semiconductor saturable absorbers.* Applied Physics B, 2002. **74**(1): p. s193-s200.

10. Okhotnikov, O., A. Grudinin, and M. Pessa, *Ultra-fast fibre laser systems based on SESAM technology: new horizons and applications* New journal of physics, 2004. **6**(1): p. 177.

11. Kurtner, F.X., J.A. der Au, and U. Keller, *Mode-locking with slow and fast saturable absorbers-what's the difference?* IEEE Journal of Selected Topics in Quantum Electronics, 1998. **4**(2): p. 159-168.

12. Suomalainen, S., et al., *Semiconductor saturable absorbers with recovery time controlled by lattice mismatch and band-gap engineering.* Materials Science and Engineering: B, 2008. **147**(2-3): p. 156-160.

13. Paschotta, R., *Gain Saturation*, in *RP Encyclopedia of Laser Physics and Technology*, R. Paschotta, Editor. 2008, Wiley-VCH.

14. Nguyen, D.T., *Modeling and Design Photonics by Examples Using MATLAB®*. 2021: IOP Publishing.

15. Paschotta, R., *Q-switching*, in *RP Encyclopedia of Laser Physics and Technology*, R. Paschotta, Editor. 2011, Wiley-VCH.

16. Wu, J., et al., *Soliton polarization dynamics in fiber lasers passively mode-locked by the nonlinear polarization rotation technique.* Physical Review E, 2006. **74**(4): p. 046605.

Appendices

1. Hou, J., et al., *High-stability passively mode-locked laser based on dual SESAM.* Applied Physics B, 2014. **116**(2): p. 347-351.

2. Bu, X., et al. *408-fs SESAM mode locked Cr: ZnSe laser*. in *2017 International Conference on Optical Instruments and Technology: Advanced Laser Technology and Applications*. 2018. SPIE.

3. Wang, Y., et al. *52-fs SESAM Mode-Locked Tm,Ho:CALGO Laser*. in *Laser Congress 2019 (ASSL, LAC, LS&C)*. 2019. Vienna: Optica Publishing Group.

4. Sorokina, I.T., et al. *A SESAM passively mode-locked Cr: ZnS laser*. 2006.

5. Yang, J., et al., *Diode-pumped 10 W femtosecond Yb:CALGO laser with high beam quality.* High Power Laser Science and Engineering, 2021. **9**: p. e33.

6. Saraceno, C.J., et al., *Sub-100 femtosecond pulses from a SESAM modelocked thin disk laser.* Applied physics. B, Lasers and optics, 2012. **106**(3): p. 559-562.

7. Wang, L., et al., *Sub-50 fs pulse generation from a SESAM mode-locked Tm,Ho-codoped calcium aluminate laser.* Optics letters, 2021. **46**(11): p. 2642-2645.

8. Gaponenko, M., et al., *SESAM mode-locked red praseodymium laser.* Optics letters, 2014. **39**(24): p. 6939-6941.

9. Zeng, H.-J., et al., *SESAM mode-locked Yb:SrLaAlO4 laser.* Optics Express, 2021. **29**(26): p. 43820-43826.

10. Quarterman, A.H., et al., *A passively mode-locked external-cavity semiconductor laser emitting 60-fs pulses.* Nature Photonics, 2009. **3**(12): p. 729-731.

11. Kowalczyk, M., et al., *Dual-Comb Lasers: Dual-Comb Femtosecond Solid-State Laser with Inherent Polarization-Multiplexing.* Laser & photonics reviews, 2021. **15**(8).

12. Kowalczyk, M. and J. Sotor, *Investigation on dispersion regimes in Yb:KGW solid-state laser.* Laser Physics Letters, 2018. **15**(6): p. 065003.

13. Kowalczyk, M., J. Sotor, and K.M. Abramski, *59 fs mode-locked Yb:KGW oscillator pumped by a single-mode laser diode.* Laser Physics Letters, 2016. **13**(3): p. 035801.

14. Kim, H.-N., et al., *Mode Evolution and Lasing Characteristics of a Passively Mode-locked Nd:YAG Laser with a Saturable Output Coupler (SOC).* Journal- Korean Physical Society, 2011. **59**: p. 3210.

15. Ghanbari, S., et al. *InP/InGaP quantum-dot SESAM mode-locked Alexandrite laser*. in *Solid State Lasers XXVII: Technology and Devices*. 2018.

16. Chen-Sverre, T., *Ultrafast mode-locked semiconductor disk lasers for frequency domain measurement systems*. 2017.

17. Leonov, S.O., et al., *Bound soliton formation in a SESAM mode-locked Cr:ZnSe laser with birefringent plates.* Applied Physics B, 2021. **127**(4): p. 56.

18. Lederer, M.J., et al., *Multipulse operation of a Ti:sapphire laser mode locked by an ion-implanted semiconductor saturable-absorber mirror.* Journal of the Optical Society of America B, 1999. **16**(6): p. 895-904.

19. Wang, Y., et al., *SESAM combined Kerr lens mode locked Yb:CALGO laser pumped by a 1.2 W single mode fiber coupled laser diode.* Laser Physics Letters, 2017. **14**: p. 055003.

20. Crombie, C., *Electronic and optical SESAM control in Cr^{4+}: forsterite lasers*. 2013, University of St Andrews.

21. Qi, Y., et al., *Low repetition rate, narrow-linewidth, all-fiber 1064 nm laser system.* Infrared Physics & Technology, 2021. **119**: p. 103930.

22. Huang, C., et al., *Developing high energy mode-locked fiber laser at 2 micron.* 2015.

23. Wang, Q., et al., *2μm Mode-locked fiber lasers.* Progress in Biomedical Optics and Imaging - Proceedings of SPIE, 2012. **8237**: p. 40.

24. Krylov, A.A., et al., *Mode locking in a bismuth fibre laser by using a SESAM.* Quantum Electronics, 2008. **38**(3): p. 233.

25. Xu, Z., et al., *All-fiber wavelength-tunable Tm-doped fiber laser mode locked by SESAM with 120 nm tuning range.* Applied Optics, 2017. **56**: p. 5978.

26. Bharathan, G., et al. *All-fibre Ultrafast Mid-infrared Laser*. 2020.

27. Herda, R. and O.G. Okhotnikov, *Dispersion compensation-free fiber laser mode-locked and stabilized by high-contrast saturable absorber mirror.* IEEE Journal of Quantum Electronics, 2004. **40**(7): p. 893-899.

28. Xu, Z.-w., et al. *Dual-wavelength mode-locked Yb-doped fiber laser with SESAM*. in *Asia Communications and Photonics Conference 2016*. 2016. Wuhan: Optica Publishing Group.

29. Liu, J., J. Xu, and P. Wang, *High Repetition-Rate Narrow Bandwidth SESAM Mode-Locked Yb-Doped Fiber Lasers.* IEEE Photonics Technology Letters, 2012. **24**(7): p. 539-541.

30. Tolstik, N.A., et al., *Diode-pumped mode-locked holmium fiber laser at 2.138 μm*. 2017. 1-1.

31. Harun, S.W., et al., *Q-switched and mode-locked Ytterbium-doped fiber lasers With Sb2Te3 topological insulator saturable absorber.* IET Optoelectronics, 2018. **12**.

32. Lv, Z., et al., *SESAM mode-locked all-polarization-maintaining fiber linear cavity ytterbium laser source with spectral filter as pulse shaper.* Laser Physics, 2018. **28**(12): p. 125103.

33. Wang, Q., et al. *Mode-locked Tm-Ho Fiber Laser with a Sb-based SESAM*. in *CLEO:2011 - Laser Applications to Photonic Applications*. 2011. Baltimore, Maryland: Optica Publishing Group.

34. Hirooka, T., et al., *A 440 fs, 9.2 GHz Hybrid Mode-Locked Erbium Fiber Laser with a Combination of Higher-Order Solitons and a SESAM Saturable Absorber*. 2016. STu1P.4.

35. Hinkelmann, M., et al., *Mode-locked Ho-doped laser with subsequent diode-pumped amplifier in an all-fiber design operating at 2052 nm.* Optics Express, 2017. **25**(17): p. 20522-20529.

36. Okhotnikov, O., A. Grudinin, and M. Pessa, *Ultra-fast fibre laser systems based on SESAM technology: new horizons and applications.* New Journal of Physics, 2004. **6**(1): p. 177.

37. Chamorovskiy, A., et al., *Femtosecond mode-locked holmium fiber laser pumped by semiconductor disk laser.* Optics Letters, 2012. **37**(9): p. 1448-1450.

38. Zhang, L., et al., *SESAM Mode-Locked, Environmentally Stable, and Compact Dissipative Soliton Fiber Laser.* IEEE Photonics Technology Letters, 2014. **26**(13): p. 1314-1316.

39. Doudou, G., et al. *SESAM-based ring-cavity all-normal-dispersion tunable Ytterbium mode-locked fiber laser*. in *2013 18th OptoElectronics and Communications Conference held jointly with 2013 International Conference on Photonics in Switching (OECC/PS)*. 2013.

40. Soltanian, M.R.K., et al., *All-fiber sub-20 ps ultra low repetition rate high peak power mode-locked fiber laser to generate supercontinuum.* Laser Physics Letters, 2020. **17**(2): p. 025104.

41. Stoliarov, D.A., et al., *Linear cavity fiber laser harmonically mode-locked with SESAM.* Laser Physics Letters, 2020. **17**(10): p. 105102.

42. Huang, C., et al., *Selectively mode-locked high-order-mode 2-μm thulium fiber laser.* Optics Communications, 2019. **440**: p. 95-99.

43. Afifi, G., et al., *Timing stability enhancement of an Erbium Doped mode locked Fiber Laser using SESAM mirror.* Optical Fiber Technology, 2016. **29**: p. 74-83.

44. Jiménez-Rodríguez, M., et al. *Sub-200 fs mode-locked fiber laser with InN-based SESAM*. in *2017 Conference on Lasers and Electro-Optics Europe & European Quantum Electronics Conference (CLEO/Europe-EQEC)*. 2017.

45. Grześ, P., M. Michalska, and J. Świderski, *Picosecond mode-locked tm-doped fibre laser and amplifier system providing over 20 W of average output power at 1994 nm.* Metrology and Measurement Systems, 2018. **vol. 25**(No 4): p. 649–658-649–658.

46. Wang, H., et al. *Stable SESAM-mode-locked Yb fiber laser in the similariton regime*. in *Laser Congress 2017 (ASSL, LAC)*. 2017. Nagoya, Aichi: Optica Publishing Group.

47. Li, P., et al., *Subpicosecond SESAM and nonlinear polarization evolution hybrid mode-locking ytterbium-doped fiber oscillator.* Applied Physics B, 2015. **118**(4): p. 561-566.

48. Tolstik, N., et al. *Compact Diode-pumped Dispersion-managed SESAM-mode-locked Ho:fiber Laser*. in *High-Brightness Sources and Light-Driven Interactions*. 2016. Long Beach, California: Optica Publishing Group.

49. Mashiko, Y., E. Fujita, and M. Tokurakawa, *Tunable noise-like pulse generation in mode-locked Tm fiber laser with a SESAM.* Optics Express, 2016. **24**(23): p. 26515-26520.

50. Gomes, L.A., et al., *Picosecond SESAM-based ytterbium mode-locked fiber lasers.* IEEE Journal of Selected Topics in Quantum Electronics, 2004. **10**(1): p. 129-136.

51. Gumenyuk, R., et al., *Vector Soliton Bunching in Thulium-Holmium Fiber Laser Mode-Locked With PbS Quantum-Dot-Doped Glass Absorber.* Quantum Electronics, IEEE Journal of, 2012. **48**: p. 903-907.

52. Li, Y., et al., *Sub-Femtosecond Timing Jitter From a SESAM Mode-Locked Yb-Fiber Laser.* IEEE Photonics Technology Letters, 2021. **33**(23): p. 1309-1312.

53. Zhang, B., et al., *All-fiberized polarized mode-locked thulium-doped fibre laser.* Laser Physics Letters, 2015. **12**(1): p. 015102.

54. Jang, H., *SESAM Design and Characterization*. 2010, Stockholm Royal Institute of Technology.

55. Wang, S., G.-y. Feng, and S.-h. Zhou, *SESAM fabrication errors and its influence on ultrafast laser cavity design.* Journal of Zhejiang University-SCIENCE A, 2015. **16**(4): p. 326-334.

56. Spühler, G., et al., *Semiconductor saturable absorber mirror structures with low saturation fluence.* Applied Physics B, 2005. **81**(1): p. 27-32.

57. Koechner, W., *Mode Locking*, in *Solid-State Laser Engineering*, W. Koechner, Editor. 2006, Springer New York: New York, NY. p. 534-586.

58. *SAM - Saturable Absorber Mirror*. 2021; Available from: https://www.batop.de/information/SAM_infos.html.

59. Dudley, J.M. and J.R. Taylor, *Supercontinuum generation in optical fibers*. 2010: Cambridge University Press.

60. Hult, J., *A fourth-order Runge–Kutta in the interaction picture method for simulating supercontinuum generation in optical fibers.* Journal of Lightwave Technology, 2007. **25**(12): p. 3770-3775.

61. Mamyshev, P. and S.V. Chernikov, *Ultrashort-pulse propagation in optical fibers.* Optics letters, 1990. **15**(19): p. 1076-1078.

62. Nguyen, D.T., *Modeling and Design Photonics by Examples Using MATLAB®*. 2021: IOP Publishing.

63. Trebino, R., *Frequency-Resolved Optical Gating: The Measurement of Ultrashort Laser Pulses*. 1st ed. 2000. ed. 2000, New York, NY: Springer US.

64. Paschotta, R., *Spectrograms*, in *RP Encyclopedia of Laser Physics and Technology*, R. Paschotta, Editor. 2008, Wiley-VCH.

65. Kärtner, F., *Pulse Characterization: Autocorrelation, FROG and SPIDER*. 2005, MITOpenCourseware: Massachusetts Institute of Technology.

66. Trebino, R. *Swamp Optics Tutorial: FROG*. 2015.

67. Trebino, R., et al., *Measuring ultrashort laser pulses in the time-frequency domain using frequency-resolved optical gating.* Review of Scientific Instruments, 1997. **68**(9): p. 3277-3295.

68. Mashinsky, V., et al., *Germania-glass-core silica-glass-cladding modified chemical-vapor deposition optical fibers: optical losses, photorefractivity, and Raman amplification.* Optics letters, 2004. **29**(22): p. 2596-2598.

69. Campanella, C., et al., *Photobleaching effect on infrared radiation-induced attenuation of germanosilicate optical fibers at MGy dose levels.* IEEE Transactions on Nuclear Science, 2021. **68**(8): p. 1688-1693.

70. Boilard, T., R. Vallée, and M. Bernier, *Probing the dispersive properties of optical fibers with an array of femtosecond-written fiber Bragg gratings.* Scientific Reports, 2022. **12**(1): p. 1-8.

71. Ciąćka, P., et al., *Dispersion measurement of ultra-high numerical aperture fibers covering thulium, holmium, and erbium emission wavelengths.* JOSA B, 2018. **35**(6): p. 1301-1307.

72. Ensley, T.R. and N.K. Bambha, *Ultrafast nonlinear refraction measurements of infrared transmitting materials in the mid-wave infrared.* Optics express, 2019. **27**(26): p. 37940-37951.

73. *Dispersion tailored fibers for 2 micron pulsed applications*. 2021: Coherent Inc.

74. Paschotta, R., *Saturation energy.* RP Photonics-Encyclopedia of Laser Physics and Technology, 2007.

75. Paschotta, R., *Gain Saturation*, in *RP Encyclopedia of Laser Physics and Technology*, R. Paschotta, Editor. 2008, Wiley-VCH.

76. *IXF-HDF-8-125 Single Clad Holmium Fiber*. 2022, iXblue.

77. Kir'yanov, A., Y. Barmenkov, and I.V. Garcia, *2.05 μm holmium-doped all-fiber laser diode-pumped at 1.125 μm.* Laser Physics, 2017. **27**(8): p. 085101.

78. Le Gouët, J., et al., *Realization and simulation of high-power holmium doped fiber lasers for long-range transmission.* Optics Express, 2020. **28**(15): p. 22307-22320.

79. Simakov, N., et al., *High gain holmium-doped fibre amplifiers.* Optics Express, 2016. **24**(13): p. 13946-13956.

80. Hemming, A., et al., *A review of recent progress in holmium-doped silica fibre sources* Optical Fiber Technology, 2014. **20**(6): p. 621-630.

81. Filatova, S.A., et al., *Spectral and temporal dynamics of ultrashort pulses in a holmium-doped fibre amplifier.* Quantum Electronics, 2019. **49**(12): p. 1108.

82. Filatova, S., et al., *Gain spectrum of the Ho-doped fiber amplifier.* Laser Physics Letters, 2015. **12**(9): p. 095105.

83. *SAM Data Sheet SAM-2000-30-10ps-x, 2000 nm*, B. Optoelectronics, Editor. 2022.

84. Andre, P.S., et al., *Raman gain characterization in standard single mode optical fibres for optical simulation purposes.* Optica Applicata, 2003. **33**(4): p. 559-574.

85. Hollenbeck, D. and C.D. Cantrell, *Multiple-vibrational-mode model for fiber-optic Raman gain spectrum and response function.* JOSA B, 2002. **19**(12): p. 2886-2892.

86. Stolen, R.H., et al., *Raman response function of silica-core fibers.* JOSA B, 1989. **6**(6): p. 1159-1166.

87. Marcuse, D., *Pulse Distortion in Single-mode Fibers* Applied Optics, 1980. **19**(10): p. 1653-1660.

88. Miyagi, M. and S. Nishida, *Pulse spreading in a single-mode fiber due to third-order dispersion.* Applied optics, 1979. **18**(5): p. 678-682.